The Pennsylvania State University

The Graduate School

The Department of Energy and Geo-Environmental Engineering

A GENERALIZED 2-D HYPERBOLIC SOLVER WITH

APPLICATION TO ORIFICE METERING

A Thesis in

Petroleum and Natural Gas Engineering

by

Daniel Eduardo León E.

Submitted in Partial Fulfillment
of the Requirements
for the Degree of

Doctor of Philosophy

December 2006

The thesis of Daniel Eduardo León E. was reviewed and approved* by the following:

Michael A. Adewumi
Professor of Petroleum and Natural Gas Engineering
Quentin E. and Louis L. Wood University
  Endowed Fellow
Thesis Advisor
Chair of Committee

Turgay Ertekin
Professor and George E. Trimble Chair in EMS
Chair of Petroleum and Natural Gas Engineering

Robert W. Watson
Associate Professor of Petroleum and Natural Gas
and Geo-Environmental Engineering

Luis F. Ayala
Assistant Professor of Petroleum and
Natural Gas Engineering

John F. Mahaffy
Associate Professor of Mechanical and
Nuclear Engineering

*Signatures are on file in the Graduate School

ABSTRACT

Hyperbolic systems of PDEs arise in many practical problems. This study presents the description, validation and application of a generalized 2-D solver. The Essentially Non-Oscillatory (ENO) Scheme is used to solve the homogeneous PDEs, while the forcing functions are solved using the Fifth Order Runge-Kutta Method. Prior to the deployment of the numerical methods for actual application, their performance was assessed by solving many benchmark problems with exact or reliable numerical solutions, which have the essential features of the actual PDEs that we desire to solve. After benchmarking, the solver is applied to a single pipeline to obtain a solution for the sudden valve closure problem and a comparison between the 1-D and 2-D models is conducted. Additionally, 2-D flow through a horizontal pipeline was simulated until a fully developed turbulent flow was achieved.

More than 80% of gas metering is still performed by orifice meters and considering the actual price of natural gas, a small error of 1% can amount to a loss of millions of dollars per year. Measurements of flow rate are obtained using a semi-empirical equation recommended by the AGA which is known to generate an error of up to 3%. An improved model based on the fundamental conservation laws is presented for flow of natural gas through an orifice meter. The solution of the Navier-Stokes equations considers the viscous effects of the flow and the turbulent effects are accounted by using the Large-Eddy-Simulation (LES) approach.

A final validation was achieved by matching experimental data of the mean velocity vector field for air. The maximum error in the axial velocity upstream the orifice-plate between the experimental data and the numerical results is within 3.5%. Moreover, a cross plot for the comparison downstream the plate shows a very good match between the measured data and the numerical predictions. Given the successful validation process, numerical predictions were made for the case of natural gas and a parametric study was conducted varying the Reynolds number, the specific gravity of the fluid and the Beta ratio. Among the most important accomplishments is the successful capturing of the recirculation phenomenon that takes place downstream of the plate. Additionally, the model predicts the flow rate by numerical integration of the axial velocity at a location where a fully developed flow exists. The error between the predicted flow rate and the specified value at the inlet is less than 1%. Moreover, the predictions obtained using the AGA-3 equation produced errors above 4% for most of the cases, with a maximum of 6.41% for the case of specific gravity equal to 0.77.

TABLE OF CONTENTS

LIST OF FIGURES

LIST OF TABLES

NOMENCALTURE

a : Speed of sound

a_i^F : Constant coefficient given by Cash and Karp. Table 3.1

$(a\alpha)_m$: Mixture parameter in the Peng-Robinson EOS

a_n : Constant (n=1,2, etc) (AGA-8 equation)

A_{pd} : Passut and Danner coefficient

b_m : Mixture parameter in the Peng-Robinson EOS

b_n : Constant (n=13,14, etc.) (AGA-8 equation)

B_r : Constant for tuning roughness at the boundary (wall model)

B : Second virial coefficient (AGA-8 equation)

BCs : Boundary Conditions

B_{pd} , : Passut and Danner coefficient

B_{nij}^* : Binary characterization coefficient (AGA-8 equation)

c_i : Mole fraction of component i.

c : Constant

c_p : Specific heat at constant pressure

c_{cp} : Pressure coefficient

c_v : Specific heat at constant volume

c_n : Constant (n=13,14, etc.) (AGA-8 equation)

C : Sutherland's constant (120 for air)

C' : Orifice flow constant (AGA-3 equation)

CFL : CFL coefficient

C_{pd} : Passut and Danner coefficient

C_n^* : Coefficients which are functions of compositions (AGA-8 equation)

d : Molar density (AGA-8 equation)

det : Determinant

d_{ij}^F : Constant coefficient given by Cash and Karp. Table 3.1

D : Diameter of the pipe

D_r :   Reduced density (AGA-8 equation)

D_{pd} :   Passut and Danner coefficient

e :   Specific internal energy

E :   Total energy per unit volume

E_{pd} :   Passut and Danner coefficient

E_i :   Characteristic energy parameter for i[th] component (AGA-8 equation)

E_j :   Characteristic energy parameter for j[th] component (AGA-8 equation)

E_{ij} :   Second virial coefficient binary energy parameter (AGA-8 equation)

E_{ij}^* :   Second virial coefficient energy binary interaction parameter (AGA-8 equation)

f_w :   Friction factor

f_n :   Constant (n=1,2, etc) (AGA-8 equation)

$\vec{F}(U)$:   Vector of physical fluxes

F_i :   High temperature parameter for i[th] component (AGA-8 equation)

F_j :   Physical flux of jth equation

F_{pd} :   Passut and Danner coefficient

F_{gr} :   Gravitational force in the r-direction per unit volume

F_{gz} :   Gravitational force in the z-direction per unit volume

F_{wz} :   Wall friction force per unit volume

$F_{i+\frac{1}{2}}^n$:   Numerical flux at the intercell $(i,i+1)$ at time level n

F_i^F :   Functions in the Runge-Kutta method. Equation (3.56)

F_n :   Numeric conversion factor (AGA-3 equation)

F_c :   Basic orifice factor (AGA-3 equation)

F_{sl} :   Orifice slope factor (AGA-3 equation)

F_{pb} :   Pressure base factor (AGA-3 equation)

F_{tb} :   Temperature base factor (AGA-3 equation)

F_{tf} :   Flowing temperature factor (AGA-3 equation)

F_{gr} :   Real gas relative density factor (AGA-3 equation)

F_{pv} :   Supercompressibility factor (AGA-3 equation)

F_{ht} :   Mixture high temperature parameter (AGA-8 equation)

g_c :   Conversion factor, 32.17 [(lbm.ft/s^2) / lbf]

g :   Gravity acceleration

g_n :   Constant (n=1,2, etc) (AGA-8 equation)

G :   Filter function

G_i :   Orientation parameter for ith component (AGA-8 equation)

G_j :   Orientation parameter for jth component (AGA-8 equation)

G_{ij} :   Binary orientation parameter (AGA-8 equation)

G_o :   Orientation parameter (AGA-8 equation)

G_{ij}^* :   Binary interaction parameter for orientation (AGA-8 equation)

h_w :   Differential pressure, in inches of water at 60 ºF (AGA-3 equation)

h_r :   Specific enthalpy

h_{r0} :   Reference specific enthalpy, (-9.098244 kJ/kg)

H :   Specific enthalpy of phase "p"

$\tilde{H}$:   Enthalpy of departure

H^* :   Ideal enthalpy

I :   Identity matrix

ICs :   Initial Conditions

$J(U)$:   Jacobian matrix

k :   Thermal conductivity

k_w :   Molecular kinetic energy (wall model)

k_{ij} :   Binary interaction coefficient between components i and j

k_n :   Constants (n=13,14, etc.) (AGA-8 equation)

K :   Mixture size parameter (AGA-8 equation)

K_i :   Size parameter for ith component (AGA-8 equation)

K_j :   Size parameter for jth component (AGA-8 equation)

K_{ij} :   Binary interaction parameter for size (AGA-8 equation)

lw :   work energy lost due to frictional effects (Bernoulli's equation)

LHS :   Left hand side

$L^{(p)}$:   pth left eigenvector of the system

MW_i :   Molecular weight of the ith component

MW_g :   Molecular Weight of the gas phase

n_c :   Number of components in the hydrocarbon mixture.

N :   Number of grid points

N_{Re} :   Reynolds Number

$O^{(\Delta t)}$:   ODE operator applied on a time step Δt

p :   Pressure

p_r :   Reduced pressure

p_f :   Static pressure (AGA-3 equation)

p_{ci} :   Critical Pressure of the component i

p_{ri} :   Reduced Pressure of the component i

p_{pc} :   Pseudocritical Pressure

p_{pr} :   Pseudo reduced pressure

PCB :   Polychlorinated Biphenyls

$P^{(\Delta t)}$:   PDE operator applied on a time step Δt

Pr :   Molecular Prandlt number (wall model)

q_h :   Flow rate at base conditions (AGA-3 equation)

q_w :   Wall heat transfer (wall model)

$\vec{Q}(U)$:   Vector of forcing functions

Q_t :   Total heat transfer between the system and its surroundings per unit volume

Q_i :   Quadrupole parameter for ith component (AGA-8 equation)

Q_j :   Quadrupole parameter for jth component (AGA-8 equation)

Q_p :   Quadrupole parameter (AGA-8 equation)

r :   Radial distance from the pipe axis, [ft]

r_f :   Recovery factor, $\mathrm{Pr}^{1/3}$

R :   Universal Gas Constant, (10.7315 psia-ft^3/lbmol-°R = 1.9858 Btu/ lbmol-°R)

$R^{(p)}$:   pth right eigenvector of the system

$\tilde{R}^{(p)}$:   pth right eigenvector of the average Jacobian $\tilde{A}$

$R_j^{(p)}$:   Component jth of the pth right eigenvector

RHS :   Right hand side

s_n :   Constant (n=1,2, etc) (AGA-8 equation)

S_i :   Dipole parameter for ith component (AGA-8 equation)

S_j :   Dipole parameter for jth component (AGA-8 equation)

SGS :   Subgrid scale

t :   Time

T :   Temperature

T_r :   Reduced temperature

T_{ci} :   Critical Temperature of the component i

T_{ri} :   Reduced Temperature of the component i

T_{pc} :   Pseudocritical temperature

T_{pr} :   Pseudo reduced temperature

T_s :   Surroundings temperature

T_o :   Reference temperature (524.07 °R for air)

u :   Average linear-flow velocity

u^+ :   Velocity parallel to the wall (wall model)

u_n :   Constant (n=13,14, etc.) (AGA-8 equation)

$\vec{U}$:   Vector of conservative variables

U_j :   Conservative variable of jth equation

U_{ij} :   Binary interaction parameter for conformal energy (AGA-8 equation)

U_i^n :   Conservative variable in the ith grid point at time level n

U_{ht} :   Overall heat transfer coefficient

U_e :   Mixture energy parameter (AGA-8 equation)

v_g :   Gas Velocity

v_r : Radial velocity

v_z : Axial velocity

V : Volume

w : work done by flowing fluid (Bernoulli's equation)

w_i : Pitzer's acentric factor of the component i

w_n : Constant (n=1,2, etc) (AGA-8 equation)

W_i : Association parameter for i^{th} component (AGA-8 equation)

W_j : Association parameter for j^{th} component (AGA-8 equation)

x : Axial-coordinate

x_j : Mole fraction of jth component (AGA-8 equation)

y_i : Mole composition of the ith component in the gas mixure

y^+ : Velocity parallel to the wall (wall model)

Y_1 : Expansion factor based on upstream static pressure (AGA-3 equation)

z_i : Mole composition of the ith component in the overall mixture

z : Compressibility factor of phase

Z : Vertical distance above datum

Greek Letters

ε_j : Epsilon corresponding to the jth conservative variable

ξ : Roughness of the pipe

γ : Ratio of specific heats

λ : Eigenvalue

λ_j : j^{th} eigenvalue of the system

λ_{max}^n : Largest wave speed in the domain at time level n

ρ : Density

η : Constant parameter in Equation (3.42).

Δt : Uniform time step

Δx : Uniform grid cell size

υ :   Specific volume

μ :   viscosity

μ_o :   reference viscosity at reference temperature, (0.01827 cp for air)

Γ :   Nondimensional parameter for compressibility effects (wall model)

κ :   Constant for tuning roughness at the boundary (wall model)

Subscripts

$j + \frac{1}{2}$:   Intercell between the j and $j+1$ grid points

o :   Initial conditions

w :   Wall

Superscripts

k : k^{th} iteration level

m :   Number of equations

n : n^{th} time level

p :   Referring to the pth eigenvalue

ACKNOWLEDGEMENTS

Chapter 1

INTRODUCTION

Throughout the 20th century, dedicated efforts were focused on developing numerical schemes for solving differential equations. This is because of the inability of solving complex equations analytically. In parallel, the development of the computer during this period has had a great impact on the way principles from the sciences of fluid dynamics and heat transfer are applied to design problems in modern engineering practice. As a result, a new methodology for attacking these complex problems using numerical techniques, known as Computational Fluid Dynamics (CFD), was born.

Different physical processes governing a variety of problems can be modeled by hyperbolic partial differential equations (PDEs). In the Petroleum and Natural Gas Engineering field, classical problems involve the flow of natural gas in pipelines. In order to solve this kind of problems numerically, we need to have the mathematical formulation of the governing equations and the numerical schemes to solve the equations. Note, that fully-transient problems are modeled by PDEs since they have at least two independent variables, namely time and one spatial dimension.

The idea of a generalized solver using conserved variables, allow us to solve different problems without the need to write a new program for every specific case. Therefore, an efficient and useful solver was developed for 2-D hyperbolic PDEs. An important issue to be handled is the inclusion of external subroutines for each specific problem. The first subroutine will permit one to decouple the conserved variables into physical or measurable variables of the problem being solved. An additional subroutine is required for non-homogeneous PDEs in order to calculate the forcing functions in terms of the conserved variables or the decoupled variables. León (2004) developed and validated a generalized solver for 1-D hyperbolic PDEs.

Among all the energy sources, including oil, coal, electricity and others, natural gas demand is expected to increase at the highest rate of about 2% per annum over the next 20 years. In recent times, the use of natural gas has become increasingly important year after year due to its non-

polluting properties, which makes natural gas more attractive to the customer, hence the increasing demand. Moreover, the amount of resources available and the inclusion of new applications such as power stations and low emission vehicles are also factors for the rise in consumption.

In 2004, the consumption of natural gas in the United States was about 22 trillion cubic feet. It is important to point out that overall, 24% of the primary energy usage of the United States comes from natural gas (40% from oil, and 23% from coal).

According to the data compiled by Energy Information Administration and Department of Energy (EIA-DOE), in 2004 there were 226 active gas pipeline systems which accounted for more than 306,000 miles of pipelines with a capacity of 178 billion cubic feet.

Pipelines are of paramount importance in the natural gas business. They are a vital infrastructure as essential as roads, electric and telephone wires, which are necessary to maintain the standard of living. Pipelines are used to transport fuel for cars, trucks, planes and ships, along with the traditional use in domestic utilities among which the most important one is heating.

Natural gas is transported to delivery points for various customers at the same time through the pipeline system. Additionally, measurements of gas purchases are made on the flowing stream. The variables usually monitored are volume at standard condition, pressure, temperature, compressibility factor, specific gravity and the energy content per unit volume.

There are various measurement devices to estimate the flow rate of gas. Among those there are orifice-meters, positive displacement meters, turbine meters, Venturi meters, flow nozzles, ultrasonic meters, etc. The measurement obtained from different devices is based on different principles, such as volumetric measurement, displacing metering and differential pressure methods.

To date, the orifice meter is the most widely used differential meter in the natural gas industry. Basically, it consists of a sturdy thin flat plate with a circular hole in the center that is located between two flanges in a horizontal section of the pipe. The flow through the bore in the plate creates a differential pressure across the orifice, and this pressure drop along with the absolute pressure are recorded continuously and translated into flow rate using a formula recommended in

the AGA Committee Report No. 3 (AGA-3). The formula is derived from the Bernoulli's energy equation under the assumptions of one-dimensional, steady, incompressible, frictionless flow. The final expression used to determine the flow rate is a semi-empirical equation that includes up to 9 correction factors (AGA, 1992a). It is widely known that the estimated volumetric gas flow rate using this equation generates some error. Lowering this measurement error is of great importance.

The empirical nature of this expression, along with the importance of the measurements when calculating payments of regular everyday sales is the justification for the present study. The purpose of this work is to develop a fundamental model using the conservation laws of mass, momentum and energy. Ultimately, one of the main objectives of this study is to gain a major understanding of the flow field that takes place in an orifice meter. The model, that uses the compressible Navier-Stokes equations, allows us to have a better perspective of what is occurring at the orifice meter, and to verify how accurate the measurements obtained in the actuality are. The steps followed during this study are summarized below.

Initially, a review of the previous studies performed on orifice metering including experimental work and numerical modeling is done. Additionally, the pertinent literature required for the understanding of this topic is compiled. The highlights include the Boundary-Layer Theory, due to Prandtl (1904), and the consideration of frictional effects, which lay down the principles for the choice of the viscous Navier-Stokes equations over the inviscid Euler's equations. In addition, the advantages of the Essentially Non-Oscillatory (ENO) numerical schemes over Total Variation Diminishing (TVD) methods are presented. In addition, a complete description of the principles used to determine the flow rate using the measurements recorded from a orifice-meter is included.

The ENO method used to discretize the PDEs and the Runge-Kutta Method used to solve the system of ordinary differential equations (ODEs) are described. Such a system arises when using the splitting approach to solve the non-homogeneous system of PDEs. The set of equations for one-dimensional steady-state flow is also a system of ODEs.

For benchmarking purposes, description and solution of several numerical examples, whose exact solutions are known, are presented. This part of the work is essential for the validation of the solver; since no analytical solution exists for the Navier-Stokes equations we have to rely on

these test problems to assess the performance of the numerical methods prior their actual application.

The description of the two-dimensional model in cylindrical coordinates is then presented, including the filtered equations that considered the large scale flow following the Large-Eddy Simulation (LES) approach. Moreover, when describing the eigenstructure of the system, which is the key for the solution of hyperbolic systems of PDEs, an in-house technique is proposed to calculate the Jacobian matrices. This new approach allows us to solve the governing equations using any equation of state (EOS), thus removing the traditional assumption of an ideal gas and the use of the caloric EOS when determining the eigenvalues and corresponding eigenvectors of the system. Later, a simplified one-dimensional model is described and is used for comparison purposes and its steady-state version is utilized to generate the initial conditions of the two-dimensional model. The description of the system to model flow through the orifice plate is later presented. Then, a new approach for the solution of the steady-state case, that includes the pressure-derivative into the fluxes of the momentum and energy equation in order to avoid an ill-posed problem, is proposed.

Solutions of three case studies for a single pipeline are presented. First, the sudden valve closure problem is solved using the one-dimensional model in order to assess the performance of the solver when handling the inviscid Euler's equations which neglects the dissipative effect of viscous fluid flow. In the second case study, the two-dimensional model is run until steady-state conditions are achieved and a fully developed flow can be appreciated after some distance from the inlet of the pipe, as expected. Finally, the sudden valve closure problem is solved but this time using the two-dimensional model, and a comparison between averaged properties and the results from the one-dimensional model allow us to see the effects caused when considering viscous flow.

An assessment of the capability of the model in capturing the many features of orifice meter flow is done through comparison with experimental data. Using a 3 color, 3D laser Doppler anemometer system, the department of mechanical engineering at Texas A&M University measured data for air flowing through a 2-inch diameter pipeline at different cross sections upstream and downstream the orifice plate. The model is able to replicate the data with a maximum relative error of 3.5% for flow conditions at which the Reynolds numbers are 18,400, 54,700 and 91,100.

After matching the experimental data, the model is used to make predictions for a natural gas mixture for a range of Reynolds numbers in the turbulent region. The main features of the flow such as the recirculation zone downstream the orifice plate, the location of the minimum centerline pressure, the maximum centerline velocity, and the vena contracta can be observed. A comprehensive analysis of these results is presented. The error between the predicted flow rates and the values imposed at the inlet of the pipe are included, as well as a comparison of the flow rate predicted by the AGA-3 equation and the actual value specified at the inlet

Appendix A presents a full description of the Equations of State that can be used by the model. These include the Peng Robinson (1976) EOS and the AGA Report No. 8 Equation (AGA, 1992b). A step-by-step explanation of how to apply the complex ENO algorithm is included in Appendix B for the interested readers. Finally, for the sake of brevity only the relevant graphs required to analyze the match achieved by the model of the experimental data are presented in Chapter 7, and the remaining plots are included in Appendix C.

Chapter 2

REVIEW OF PERTINENT LITERAURE

2.1. Background

The preferred means of oil and natural gas transport is through pipelines. As a result, a great deal of studies has been performed in the area of pipeline transport, using both experimental and numerical approaches. In the earlier studies, focus was on empirical approach (see Brill and Arirachakaran, 1992) and several correlations were designed using data from laboratory and field conditions. The main limitation of this approach is the inapplicability of these correlations to a wide range of field conditions. Personal computing has allowed investigators to handle more complex design problems using fundamental approaches in the calculations.

Many studies have been conducted at Penn State, dating back to the work of Vincent (1988) who modeled two-phase steady-state flow in a horizontal pipe assuming mist flow conditions. The inclusion of transient flow and inclined pipes was done by Mucharam (1990). Another improvement was included by Boriyantoro (1994) who considered stratified flow conditions. Dukhovnaya (1996) was the first one to include an energy equation into the model. The work of Ayala (2001) also considered an energy equation and modeled four different flow patterns and their corresponding transitions. Eltohami (2003) used a TVD scheme to solve an eight-equation formulation to model PCB removal from transmission lines. Then León (2004) presented a generalized solver based on a TVD scheme for system of hyperbolic partial differential equations, and showed the application to transients in pipelines.

Up to this point, the transient equations used in all the work done have been solved using TVD schemes developed by Harten (1983). This method has proven to work effectively, but it has the disadvantage of degenerating to first order accuracy near smooth extrema. To overcome this problem, a new series of ENO schemes were proposed by Harten *et al* (1987) which produces better resolution of discontinuities, but so far it has not been used to solve transient flow in pipelines.

One of the most important things during the transportation of natural gas is the accurate measurement of flow rate. The orifice meter is perhaps the oldest known device for measuring the flow of fluids. The original concept of speeding up the fluid by reducing the cross sectional area of the flow stream and then cause a pressure drop date to Bernoulli, Torricelli and Venturi. Fling (1988) highlighted that since the beginning of the 19th century, the orifice plate has been developed to be used as custody transfer device. Then, the American Gas Association (AGA) established a committee to undertake research programs. So far, all the research performed in this area within the natural gas industry has been mainly experimental. Among the main results of this project are:

The determination of absolute values of orifice discharge coefficients by a joint program of the American Society of Mechanical Engineers (ASME) and the AGA was done between 1928 and 1932 (Fling , 1988).

In 1955, the AGA Report Number 3 was published including the data published in the Report Number 2, incorporating different pipe configurations and the gas deviation factor (Fling , 1988).

A joint committee of the American Petroleum Institute (API) and the AGA revised the basic orifice coefficients, and correlate data for gaps and extensions in 1975.

In 1978, the AGA and the API submitted to the American National Standards Institute (ANSI) the AGA Report No. 3 for designation as a national standard, which was published as the standard document ANSI/API 2530.

The standard ANSI/API 2530 was submitted to ISO for consideration as international standard, but it was rejected and in 1980 the ISO 5267 was published but with great differences from the ANSI/API 2530.

These standards include the data that have been generated over the last century by numerous research groups using the experimental approach. Additionally, all the studies described above for modeling of natural gas flow in pipelines, used one-dimensional equations which are good for the case of single pipelines, where the variation of the properties within a cross section of the pipe is negligible, with the exception of the axial velocity, and therefore average values are used.

In order to model flow through an orifice plate, we need at least a two-dimensional model. Moreover, in order to consider the viscous effects, a model that uses the Navier-Stokes equations is required.

Even though, since the beginning of the 20th century, the use of computational fluid dynamics (CFD) had solved many fluid flow problems, not many studies had been carried out to model flow through orifice meters. Mills (1968) was among the first ones to obtain numerical solutions of viscous, incompressible flow through a square-edge orifice for very low Reynolds numbers (0-50). Then, Greenspan (1973) presented a technique that produced converging solution for Reynolds numbers in the range 10 – 500 using the stream function and vorticity equations discretized with the standard five-point Laplace difference operator. These studies focused in an orifice plate with a diameter ratio of $\beta = d/D = 0.5$, therefore in 1977, Mattingly and Davis extended the previous works to various orifice meter configurations solving the momentum and continuity equations using the SOLA finite difference routine described by Hirt *et al.* (1975). Their solutions were generated for diameter ratios in the range $0.3 \leq \beta \leq 0.7$ for the laminar flow region. Davis and Mattingly (1977), continued their work including turbulent flow by means of the two-equation turbulence model developed at Imperial College, London to model high Reynolds numbers in the range $10^4 - 10^6$. The solutions were obtained in terms of the velocities, pressure and turbulence intensity for a fully-developed inlet profile specified by the 1/9th power law.

In 1983, a Workshop on fundamental research issues in orifice metering was held at the National Bureau of Standards (NBS), [Mattingly *et al.*, 1984]. There, the need for improved accuracy was acknowledged due to the rise in the value of fluids being metered, such as natural gas and oil. The description of the testing facilities at NBS-Boulder, National Engineering Lab at Scotland, and NBS-Gaithersburg were also presented. Among other topics, the potential role of computer modeling in orifice research was discussed and it was emphasized that the success of fluid flow analysis had a strong dependence on the mathematical formulation of the problem. It was concluded that validated computer programs were necessary to perform parametric studies in order to evaluate effects such as upstream flow conditions, upstream flow disturbances, length of straight pipe required to eliminate disturbances, etc.

In 1992, Barry *et al.* conducted a study for the Gas Research Institute in which numerical simulations of compressible flows (nitrogen at 600 psia) in orifice meters were performed using

the general purpose computer programs Fluent and Fluent/BFC. This work extended the previous studies by considering a wider range of Reynolds numbers and diameter ratios. Additionally, the effects of roughness, and the presence of upstream and downstream valves, reducers, expansions and bends were also modeled. For turbulent flow, the 1/8th power law was used to specify the inlet profile. They predicted values of discharge coefficients within 4% compared to the experimental data collected by Mattingly and Yeh (1989).

Most of the experimental research in orifice meters has been concentrated in analyzing the influence of non-ideal conditions on flow metering. "Non-ideal" installations imply that the upstream piping conditions produce pipeflow distributions that differ from those associated with "ideal" installations, in which the meter location is preceded by sufficiently long, straight lengths of constant diameter pipeline that the meter performance is not affected by the meter installation position. This experimental work is following summarized.

Mattingly and Yeh (1991) performed experiments that included single and double elbow configurations for Reynolds numbers between 10^4 to 10^5 using water in a pipe with 50 mm (2 inches) of diameter at the National Institute of Standards and Technology (NIST, former NBS) facilities. It was concluded that without flow conditioning, the specifications of upstream pipe lengths in the current flowmetering standards (ISO-5167, 1980 and ANSI/API-2530, 1985) may not be sufficient to achieve the desired flow metering accuracy, among other things because they did not account for any dependence on the Reynolds number and the pipe roughness.

Morrison *et al*. (1993) studied the flow field inside an orifice flowmeter with a diameter radio of 0.5 for Reynolds number of 91,000 using a three-color, there-dimensional laser Doppler anemometer system at Texas A&M University. The fluid used was air mixed with atomized "Rosco Fog/Smoked Fluid" and they observed a velocity profile upstream that is very close to the one predicted by the 1/7th power law. They stated that it is not economically feasible to study all possible installations experimentally, and hence a validated computer program would be very useful for predictions.

Yeh and Mattingly (1994a and 1994b) studied the influence on orifice coefficients downstream of a reducer and downstream of a 45° elbow in a pipe of diameter 5.25 cm and measured relative roughness of 0.006% (based on interior diameter) using water at 21°C for Reynolds numbers between 10^4 to 10^5. The mean and turbulence velocities were obtained by a Laser Doppler

velocimetry (LDV). It was observed that the reducer produced a velocity profile that is flatter than the fully-developed distribution characteristic of this turbulent flow.

Reader-Harris *et al.* (1995) improved the orifice plate discharge coefficient equation using the EEC/API database for pipe diameters between 5 and 60 cm using water and oil. This study was performed in the National Engineering Laboratory (NEL, in U.K.) with the aim of resolving the discrepancies between the Slotz equation presented in ISO 5167 (1991) used in Europe; and the Reader-Harris-Gallager equation presented by the API (1990) and utilized in United States. The revised equation improved tapping terms for low Reynolds number and included an additional term for orifice edge roundness.

Morrison *et al.* (1995) measured the response of the orifice meter to disturbances caused upstream by a concentric tube flow conditioner and a vane-type swirl generator. Axial and tangential velocity profiles were measured for two Reynolds numbers, namely 91,100 and 120,000 in a pipe with 50.8 mm of diameter and for beta ratios in the range 0.43 – 0.726. Air was used at 43°C and 830 kPa.

2.2. Friction Effects and Boundary-Layer Theory

By the end of the 19th century, there were two main opposing views within the fluid dynamics community. The first one, known as theoretical hydrodynamics, evolved from Euler's equations of motion for frictionless, non-viscous fluid. However, the results obtained from this theoretical approach were in a great deal of contradiction with experimental results, specifically in regard with the problem of pressure losses in pipes and the drag of a body moving through a mass of fluid. On the other hand, practical engineers with the need to solve important problems developed a different science called hydraulics, which was based on experimental data and empirical methods in a very different perspective from those proposed by theoretical hydrodynamics.

According to Schlichting (1968), it was known for a long time that the discrepancy between the results provided by both sciences was due to the fact that the theory neglected fluid friction. Moreover, the set of equations that account for friction were known, namely the Navier-Stokes equations. Unfortunately, due to mathematical difficulties in solving these equations, and because in the case of the two most common fluids, water and air, the viscosity is very small, the force

due to viscous friction was considered very small compared with the remaining forces (gravity and pressure forces), and therefore it was neglected.

It was not until the beginning of the 20th century, that Prandtl (1904) took the first step towards unifying the two divergent branches of fluid dynamics, showing that it was possible to analyze viscous flow in cases were it had practical importance. Considering theoretical principles, and performing very simple experiments, he proved that the flow about a solid body can be divided into two regions: a very thin layer in the neighborhood of the body where friction plays a very important role, and the remaining region outside this layer, were friction may be neglected. This is the so called boundary-layer theory.

2.2.1. Real vs. Perfect Fluids

The concept of a perfect fluid is based on the frictionless and incompressible properties. When this perfect fluid is in motion, two contacting layers experience no tangential forces (shearing stresses) but they act on each other with normal forces only (i.e. pressure). This is why the theory of perfect fluids fails to account for the drag of a body, leading to the wrong statement that a body which moves uniformly through a fluid experiences no drag.

This result is called the d'Alembert's paradox, and is due to the fact that the inner layers of a real fluid transmit tangential as well as normal stresses. The tangential or friction forces are strongly interrelated with the viscosity of the fluid and the existence of these stresses along with the condition of no-slip near solid walls is the essential difference between a perfect and a real fluid. It is important to point out, that even in the study of fluids with very small viscosities; the condition of no-slip near a solid boundary prevails.

The no-slip condition, and the nature of viscosity can be best visualized considering the motion of a fluid between two very long parallel plates, one of which is at rest, and the other moving with a constant velocity parallel to itself (Figure 2.1). In this experiment the fluids adheres to both walls, so that its velocity at the lower plate is zero, and that at the upper plate is equal to the velocity of the plate.
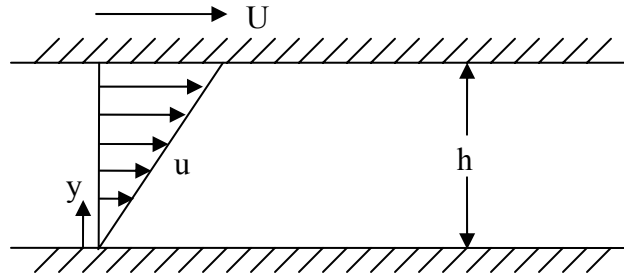
Figure 2.1. Velocity distribution in a viscous fluid between two parallel plates

In order to maintain this dynamic equilibrium it is necessary to apply a tangential force to the upper plate that is equal to the frictional forces in the fluid. The frictional force per unit area, τ, is proportional to U/h, and since the velocity distribution in the fluid between the plates is linear, τ is also proportional to du/dy. The proportionality factor depends of the nature of the fluid, specifically its viscosity, μ, and yield to the fluid friction relationship:

$$\tau = \mu \frac{du}{dy} \qquad (2.1)$$

2.2.2. The Hagen-Poiseuille Equations

The law of friction for a simple flow described before can be applied to the case of flow through a horizontal pipe of circular cross-section with constant diameter, $D = 2R$. As shown in Figure 2.2, the velocity at the wall is zero, because of adhesion, and reaches a maximum on the axis of the pipe. The radial component of the velocity is zero, implying a laminar type of flow (Schlichting, 1968).
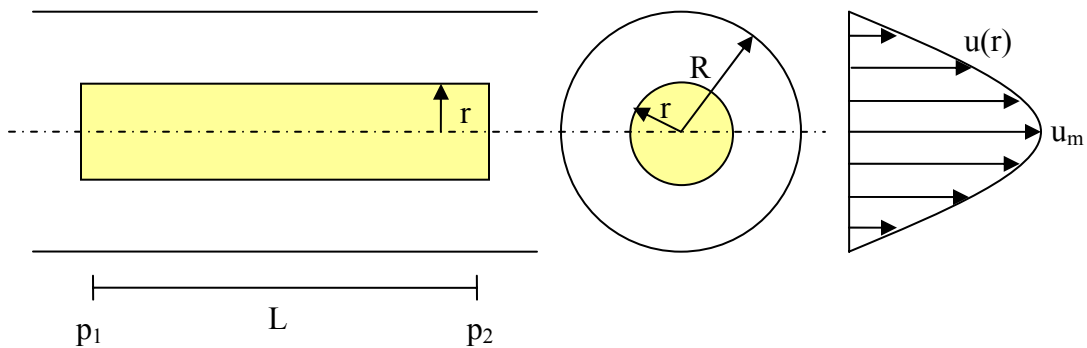
Figure 2.2. Laminar flow through a pipe

Starting with the condition of equilibrium that the pressure force acting on the faces of the cylinder is equal to the shear acting on the circumferential area, then including the law of friction (2.1) and integrating leads to:

$$u(r) = \frac{p_1 - p_2}{4\mu L}(R^2 - r^2) \qquad (2.2)$$

This is a parabolic velocity profile over the radius, and the maximum at the axis is given by:

$$u_m = \frac{p_1 - p_2}{4\mu L}R^2 \qquad (2.3)$$

The flow rate is obtained as the volume of the paraboloid of revolution which is equal to $\frac{1}{2} \times base\ area \times height$:

$$Q = \frac{\pi.R^2}{2}u_m = \frac{\pi.R^4}{8\mu L}(p_1 - p_2) \qquad (2.4)$$

This equation was first deducted by Hagen (1839) and independently after that, Poiseuille (1841) arrived to the same expression.

2.2.3. The Boundary-Layer Concept

In some cases, the pressure distribution nearly agrees with the perfect-fluid theory where the influence of viscosity at high Reynolds number is confined to a very thin layer in the immediate neighborhood of the solid wall. The fact that at the wall the fluid adheres to it means that frictional forces retard the motion of the fluid in a thin layer near the wall. In that thin layer the velocity of the fluid increases from zero (no-slip) to its maximum value, which corresponds to external frictionless flow. The layer in consideration is called boundary layer, and the theory behind it is due to Prandtl (1904).

The thickness of this boundary layer increases along the plate in a downstream direction as shown in Figure 2.3. Before reaching the plate, the velocity distribution is uniform. Then, as the distance is increased, the thickness, δ, of the retarded layer increases continuously as more fluid become

affected. The thickness of the boundary layer is directly proportional to the viscosity of the fluid. But even for very small viscosities (large Reynolds numbers) the frictional shearing stresses (Equation 2.1) are considerable due to the large velocity gradient across the flow.
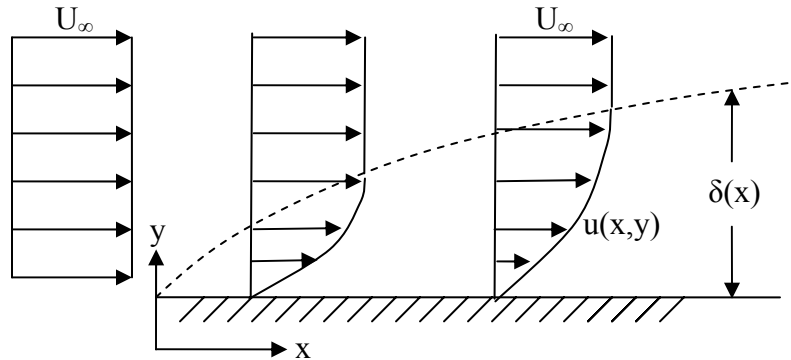
Figure 2.3. Sketch of boundary-layer on a flat plate

2.2.4. Turbulent flow in a pipe

Experiments performed by Reynolds (1883) show that the parabolic velocity distribution presented in Section 2.2.2 exists only at low and moderate Reynolds numbers. The fact that fluid laminae slide over each other, and that there are no radial velocity components, constitutes an essential characteristic of laminar flow. But, when the flow velocity increases it is possible to reach a stage when the fluid particles cease to move along straight lines and the regularity of the motion breaks down. This originates superimposed irregular radial fluctuations on the axial motion. Such a flow pattern is called turbulent. Reynolds concluded that the transition from the laminar to turbulent flow takes place at a fixed value of the Reynolds number, named critical. For the majority of experimental arrangements the critical Reynolds number is approximately:

$$Re_{crit} \approx 2300 \tag{2.5}$$

In the turbulent region, the pressure drop becomes approximately proportional to the square of the mean flow velocity, therefore a considerably larger pressure difference is needed in order to move a fixed quantity of fluid through the pipe, as compared to the laminar flow were the pressure drop is proportional to the first power of the mean flow velocity (see Equation 2.4). This effect is produced because the turbulent mixing dissipates a large amount of energy increasing the resistance of the flow.

2.3 Turbulence

It is very well known [(Lesieur, 1990), (John, 2004) and (Metais and Ferziger, 1997)] that today, turbulence in fluids is considered one of the most difficult problems of modern physics. We are very far from the complexity of microscopic molecular physics for application problems, since we are only dealing with Newtonian mechanics laws applied to a continuum.

A turbulent flow can be defined as a flow which is disordered in time and space, and may possess fairly different dynamics, may be three dimensional or sometimes quasi-two-dimensional and may exhibit well organized structures or otherwise. Lesieur (1990) presented three points to define a turbulent flow and unify different criteria: a) the flow must be unpredictable, in a sense that a small fluctuation at a given time will amplify to a point of impossible deterministic precision, b) it has to be able to mix transported quantities much more rapidly than if only molecular diffusion processes were involved, and c) it must involve a wide range of spatial wave lengths, which allow the application of the term "turbulent" to two-dimensional flows.

Turbulence is a topic where the scientific community is divided in their understanding but agree in the inability to solve the problem (Lesieur, 1990). Two main opposing points are the "statistical" that tries to model the evolution of averaged quantities of flow and believes in the phenomenon of cascades rejecting the possibility of any coherence or order associated to turbulence; in contrast with the "coherence among chaos" people, who consider turbulence from a purely deterministic point of view, by studying either the behavior of dynamical systems, or the stability of flows in various situations.

We can solve the equations of motion in a deterministic manner from an initial state and with the corresponding boundary conditions using numerical schemes. Such equations are based on momentum and energy balances. As described by Voke, Kleiser and Chollet (1994), genuine direct numerical simulations (DNS) resolve all the fluid motions and require the highest practical accuracy in their numerical and temporal discretization. These simulations have the virtue of great fidelity when carried out carefully, and represent a powerful tool for investigating the process of transition to turbulence. DNS may involve calculating interaction of several millions interacting sites (Sagaut, 2002) because it calculates explicitly all the scales of motion (from the large energetic scales to the small dissipative scales).

Unfortunately, the configuration of practical problems such as the atmosphere, the ocean, or industrial applications involves Reynolds numbers that are too large to allow DNS. Numerous other examples of real turbulent flows arise in aeronautics, hydraulics, nuclear and chemical engineering, oceanography, meteorology, astrophysics and internal geophysics.

Solving the unsteady Navier-Stokes equations implies that we must take into account all the space-time scales of the solution if we want to have a result of maximum quality. The discretization has to be fine enough to represent all these scales numerically. That is, the simulation is discretized in steps Δx in space and Δt in time that must be smaller, respectively, than the characteristic length and the characteristic time associated with the smallest dynamically active scale of the exact solution. This is equivalent to saying that the space-time resolution scale of the numerical result must be at least as fine as that of the continuous problem.

There are several ways of reducing the number of degrees of freedom in the numerical solution. In the first approach we calculate the statistical average of the solution directly and it is called Reynolds Averaged Numerical Simulation (RANS) where the exact solution is splits into the sum of its statistical average and a fluctuation. The second approach calculates directly only certain low-frequency modes in time and the average field through three contributing terms, one for the time average of the exact solution, another one is the conditional statistical average, and the last one accounts for the turbulent fluctuation. This method goes by the names of Unsteady Reynolds Averaged Numerical Simulation (URANS), Semi-Deterministic Simulation (SDS), Very Large-Eddy Simulation (VLES) or Coherent Structure Capturing (CSC). The final approach calculates only the low-frequency modes in the space directly and it is called Large-Eddy Simulation (LES).

2.4. Large-Eddy Simulation

For quantitative understanding, we emphasize that a DNS of a turbulent flow considers all scales of motion. The total number of mesh cells in a uniform mesh in a hexahedron is then $N = h^{-3} = N_{\text{Re}}^{9/4}$ (John, 2004), which means that the performance of a DNS on present day computers can only handle about $N = 10^7$ mesh cells which gives the restriction $N_{\text{Re}} \approx 10^{28/9} \approx 1292$. However, reasonable Reynolds numbers for practical applications are of

the order of 10^6. Two-dimensional flow is less restrictive, since for a mesh size of $h = N_{\mathrm{Re}}^{-1/2}$ leads to $N = h^{-2} = N_{\mathrm{Re}}$ mesh cells in a square.

LES is currently a very popular approach for turbulent flow simulation. The basic idea starts by decomposing the quantities which describe the flow into two parts: one part containing the large flow structures (large-scale) and the remainder containing the small scales. This approach makes sense in practical applications, considering a hurricane for example, we are primarily interested in predicting the behavior of the large eddies, which are the most dangerous ones and it is important to predict their way and their velocity in order to protect lives and properties. The actual behavior of the millions of small eddies is not of interest, but these small eddies of course influence the behavior of the large eddies, therefore a prediction of the behavior of the large eddies is not possible without taking into account the interactions coming from the small eddies.

LES is a technique intermediate between the direct simulation of turbulent flows and the solution of the Reynolds-averaged equations (Piomelli, 2000). In LES the contribution of the large, energy-carrying structures to momentum and energy transfer is computed exactly, and only the effect of the smallest scales of turbulence is modeled. Since the small scales tend to be more homogeneous and universal, and less affected by the boundary conditions than the large ones, there is hope that their models can be simpler and require fewer adjustment when applied to different flows than similar models for the RANS equation.

The scale selection in the LES technique for the separation of the large and small scales is determined by a cutoff length (Sagaut, 2002). The scales that are of characteristic size greater than the cutoff length are the large or "resolved scales", and the others are called small or sub-grid scales (SGS).

The problem of the SGS modeling is a particular case of the passage from "micro" to "macro", where the laws governing a medium are known at a certain microscopic level, and one seeks evolution laws at a macroscopic level (Comte and Lesieur, 1998). The Navier-Stokes equations are already a result of such a passage: the micro corresponds here to Boltzmann equations for the molecules, and the macro to the continuous medium approximation, where the molecular viscous and conductive coefficients model the momentum and heat exchanges across the surface of the

fluid parcels, due to molecular fluctuations. In LES of turbulence, the micro corresponds to the individual fluid parcel obeying Navier-Stokes equations, and the macro is the filtered field.

A great deal of research has been done in the development of sub-grid models for incompressible flows. Most of them follow the Smagorinsky model (Germano, 1992) and use an eddy-viscosity model. A different idea is to supplement a similarity idea to the Smagorinsky model (Bardina *et al*, 1984). According to Piomelli (1998), scale-similar models are based on the assumption that the most active SGS are those closer to the cutoff, and that the scales with which they mostly interact are those right above the cutoff.

Since the work of Yoshizawa (1986), who generalized the Smagorinsky model (Smagorinsky, 1963), some work have been conducted on LES of compressible flow. Erlebacher *et al* (1992) extended the standard mixed model to compressible isotropic turbulence, while Moin *et al* (1991) formulated the dynamic model for compressible LES.

2.5. Euler's Equations vs. Navier-Stokes Equations

Both sets of equations included the three fundamental principles on which fluid dynamics is based, namely conservation of mass, momentum and energy. In the most basic, ideal gas, three-dimensional flow problem there are six dependent variables, namely three velocity components and any three thermodynamic properties. In the case of compressible flow we must solve the five coupled partial differential equations.

The inviscid Euler's equations are hyperbolic. The main feature and a very difficult problem unique to this kind of flow is the presence of shock waves, which are represented as discontinuities in the flow solution.

The Navier-Stokes equations model a viscous flow, which as we explained earlier accounts for the transport phenomena of friction and thermal conduction.

On the contrary, the Euler's equations govern the inviscid flow, which by definition is a flow where the dissipative, transport phenomena of viscosity and thermal conductivity are neglected. By simply dropping all the terms involving friction and thermal conduction from the viscous

Navier-Stokes equations one would obtain the inviscid Euler's equations. Both sets of equations are coupled systems of partial differential equations, and hence are very difficult to solve analytically.

For both sets of equations, we have five equations in terms of six unknown flow variables, namely density, pressure, three components of velocity, and internal energy (ρ, p, u, v, w, e). For the simple case of a ideal gas the equation of state (2.6) is the sixth equation, but introduces a seventh unknown, namely temperature, T. Therefore a caloric equation of state (2.7) that relates two state variables is taken as the seventh equation (See Toro, 1999 for description).

$$p = \rho RT \tag{2.6}$$

$$e = \frac{p}{(\gamma - 1)\rho} \tag{2.7}$$

with $\gamma = c_p / c_v$ denoting the ratio of specific heats.

For most general cases, where the Ideal Gas law does not apply, such as the flow of natural gas, the set of flow equations is completed with the appropriate equation of state proposed by Peng and Robison (1976) and the equation for the enthalpy of the departure of a mixture also due to Peng and Robinson (1976).

2.5.1. Associated Boundary Conditions

The viscous and inviscid equations govern the flow of any fluid. They are the same equations whether the flow is air over a Boeing 747, or natural gas through a pipeline. However, although the governing equations are the same, the flow fields are very different from each other. Such a difference is introduced through the boundary conditions, which are quite different for each example. The boundary conditions dictate the particular solutions to be obtained from the governing equations. Hence, once we have the governing flow equations, the real driver for any particular solution is the boundary conditions. For the purpose of this study, one of the most difficult boundaries is a simple wall and therefore is following described.

No-Slip Walls

For a viscous flow, the fluid located immediately at the surface have zero velocity relative to the wall. This is because the friction effects make the fluid to adheres to the wall. In the case of a stationary wall with the flow moving past it, at the wall both velocity components are zero, $v_w = 0$ and $v_n = 0$. The value of density is extrapolated from the interior points.

2.6. Numerical Methods

A large number of techniques have been developed in order to solve non-linear hyperbolic systems of PDEs. Starting with simple algebraic methods used on water hammer problems by Allievi (1903, 1913 and 1925), numerical techniques for non-linear hyperbolic equations appeared with the first-order method of Courant *et al* (1952) and Lax (1954).

After that, one of the earliest successful finite difference schemes for conservation laws is the first-order-accurate Godunov-type (Godunov, 1959) scheme. This is an upwind scheme whose main ingredient is the solution of local Riemann problems at the intercells that have a discontinuity in the primary variables.

2.6.1. Conservation Laws and Conservative Schemes

Expressing the conservation laws in the integral form allows us to derive the governing equations based on physical conservation principles (Equation 2.8). Additionally, the integral formulation requires less smoothness of the solution, which permits the extension of the solutions to include discontinuous solutions (Toro, 1999).

$$\frac{\partial \vec{U}}{\partial t} + \sum_{i=1}^{d} \frac{\partial \vec{F}_i(\vec{U})}{\partial x_i} = 0 \qquad (2.8)$$

In equation (2.8) $\vec{U}$ is the vector of conservative variables, $\vec{F}_i(U)$ is the vector of physical fluxes in the x_i-direction, and d stands for the number of dimensions. For the case of a system of one-dimensional homogeneous hyperbolic conservation laws ($d = 1$) and a control volume $V = [x_L, x_R] \times [t_1, t_2]$ on the x-t plane, the integral form is given by:

$$\int\limits_{x_L}^{x_R} U(x,t_2)dx = \int\limits_{x_L}^{x_R} U(x,t_1)dx + \int\limits_{t_1}^{t_2} F(U(x_L,t))dt - \int\limits_{t_1}^{t_2} F(U(x_R,t))dt \qquad (2.9)$$

And a conservative scheme is defined as a numerical method of the form:

$$U_i^{n+1} = U_i^n - \frac{\Delta t}{\Delta x}(F_{i+\frac{1}{2}}^n - F_{i-\frac{1}{2}}^n)$$

(2.10)

Note that this is an explicit scheme. In order to obtain an implicit scheme the numerical fluxes are defined at time level n+1.

A major problem when solving conservative equations in the vicinity of discontinuities using first-order-accurate schemes comes from the ignored second-order terms in the Taylor series expansion, which generate the appearance of numerical diffusion at the discontinuities. Therefore, the sharp fronts, that are a main feature of the hyperbolic equations, suffer smearing due to the non-viscous assumption. This smearing reflects the effect of the viscosity which is a second-order derivative. In order to correct this problem, the concept of artificial viscosity was introduced as an anti-diffusive term. This type of numerical methods adds second-order derivatives multiplied by a constant value that represents the viscosity.

A different approach came with the second-order accurate Lax-Wendroff (1960) scheme. The first method of the family uses a forward-difference approximation in time and an arithmetic average of the upwind and downwind approximations in space. A complete class of Lax-Wendroff schemes is derived by just changing the fractions of upwind and downwind approximations. However, a disadvantage of these methods arises from to the inclusion of second-order terms, making the scheme non-monotonic and thus generating spurious oscillations in the vicinity of discontinuities. Hence, due to the neglected third-order terms, the solution suffers of numerical dispersion at the discontinuities, which is a feature of many second-order accurate schemes.

2.6.2. TVD vs. ENO Schemes

The problem of spurious oscillations at the discontinuities is solved by ensuring monotonicity of the numerical scheme while keeping the high-order of accuracy. These schemes, proposed by

Harten (1983), are based on non-linear functions and are called Total Variation Diminishing (TVD) schemes. The restriction that characterizes these schemes is the definition of bounded total variation, which says that the total variation in the conserved variables is bounded (Equation 2.11), and therefore no new maxima or minima are created as the solution evolves with time.

$$TV(u(t_2)) \leq TV(u(t_1)), \quad \forall\, t_2 \geq t_1 \tag{2.11}$$

In more practical terms, what TVD schemes guarantee is the second law of the thermodynamics and the conservation of mass. The conservation laws are nothing else but balance equations of mass, momentum and energy. When a perturbation of these primary variables is introduced to the system, as the time evolves, the discontinuity shocks are propagated in the spatial domain, and if no additional perturbation is introduced to the system, there is no reason for the bounds of the solution to increase. If that happens it means that a violation of the conservative laws is taking place in the system, which is not possible. Hence, the TVD schemes are designed in a way that they assure the conservation of the physical principles that govern the hydrodynamic model. Therefore, the appearance of spurious oscillations is only a numerical phenomenon and does not reflect the real behavior of the system.

According to Shu (1997), the original Essentially Non-Oscillatory (ENO) idea presented in Harten *et al*. (1987) was the first successful attempt to obtain a uniformly high-order accurate interpolation for piecewise smooth functions, that is actually essentially non-oscillatory. Due to the importance that Harten's work has had on several investigations in numerical solutions of hyperbolic conservation laws, the original paper was republished in 1997 by the Journal of Computational Physics in commemoration of its 30th anniversary.

The main contribution of the original work is a uniformly high-order interpolation recipe with an adaptive stencil, named ENO reconstruction. Traditional finite-difference methods use fixed stencil interpolations. It is known that in order to increase the order of accuracy we need to take information of more cells. For example, to obtain an interpolation for cell i to third-order accuracy, the information of the four cells i-2, i-1, i and i+1 can be chosen, but also the four cells i-1, i, i+1 and i+2 can be used. However, fixed stencil of second- or higher-order accuracy produces oscillations near discontinuities, which is called Gibbs phenomenon.

Before the ENO idea, there were two ways to eliminate or reduce such oscillations. The first one is the addition of artificial viscosity, which could be tuned so it was large enough near discontinuities to suppress or reduce the oscillations, and also small elsewhere to maintain high-order accuracy. The disadvantage of this approach is that fine tuning of the parameter controlling the size of the artificial viscosity is problem-dependent, which make this method unsuitable for generalization. The other way was to apply limiters to eliminate the oscillations, which implies using a linear rather than a quadratic interpolant near the shock, obtaining in this way the TVD (total variation diminishing) property. Again, the disadvantage of this method is that accuracy necessarily degenerate to first order near smooth extrema.

The reconstruction protocol proposed by Harten *et al*. (1987) is an improvement of a second-order version by Harten and Osher (1987). The new version is a hierarchy that begins with one or two cells, and then adds one cell at the time to the stencil from the two candidates on the left and the right; based on the size of the two relevant Newton divided differences, which are used as a measure of local smoothness. This concept is shown in Figure 2.4.
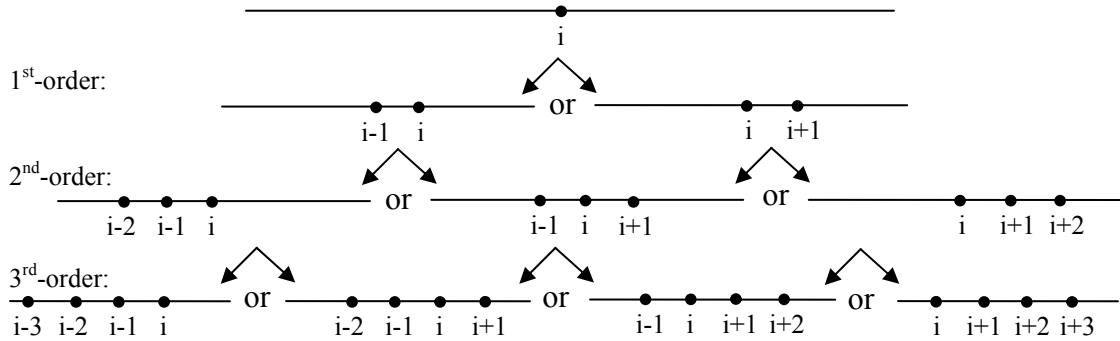
Figure 2.4. Schematic of the ENO hierarchy concept.

Since the original publication of this work, the method has been improved and expanded by many researchers. As an example, Shu and Osher (1988 and 1989) proposed ENO schemes based on point values and TVD Runge-Kutta time discretizations, which save computational costs significantly for multi-space dimensions, and therefore is the approach adopted by the present study.

2.6.3. Justification for ENO Schemes

TVD schemes have at most first-order accuracy, in the sense of truncation error, at extrema of the solution. Therefore a uniformly second-order approximation was constructed (Harten and Osher, 1987), which is non-oscillatory in the sense that the number of extreme of the discrete solution is not increasing in time.

In the new class of non-oscillatory schemes the solution operator is only required to diminish the number of local extremes in the numerical solution. Unlike TVD schemes, non-oscillatory schemes are not required to damp the values of each local extreme at every single time-step, but are allowed to occasionally accentuate a local extreme.

Also, non-oscillatory schemes, like TVD schemes, are monotonicity preserving. In particular, when applied to a step-function, they do not generate spurious oscillations.

2.7. One-Dimensional vs. Multidimensional Flow in a Pipeline

In a one-dimensional system, based on the fact that the length of the pipeline is many orders of magnitude larger than the diameter of the pipe, the radial and angular flows are neglected with respect to the axial flow. Unfortunately, this approach can not be used to account for radial fluctuations of the flow or when the geometry of the system is different from a single pipeline. Therefore, this model can only be used for single pipes where the flow in the axial direction is dominant.

For one-dimensional systems, there is only a single value of each of the flow variables at each cross section of the pipe. These are average values of such variables (Figure 2.5).

A more realistic approach is a three-dimensional flow where for the case of laminar flow, a paraboloid of revolution represents the velocity distribution. Multidimensional models are used when due to the geometry of the system, flow in the radial direction and sometimes even in the angular direction are significant, and therefore need to be considered. In those cases, such as constrictions in pipes, leaks, orifice-meters, flow nozzles, turbine-meters, vortex-meters, splitting

branches, the assessment of one-dimensional models does not generate the actual solution of the problem.

For the specific case of two-dimensional flow, which is solved in this study, a cylindrical domain is chosen, and we assume flow in the angular direction to be negligible. In this kind of systems, a parabolic velocity distribution exists in the case of laminar flow as shown in Figure 2.5.

For the case of a horizontal pipeline, the gravity component in the z-direction is non-existent. The radial component of the gravity is considered negligible due to the low density of the gas and the diameter of the pipe in comparison with its length.
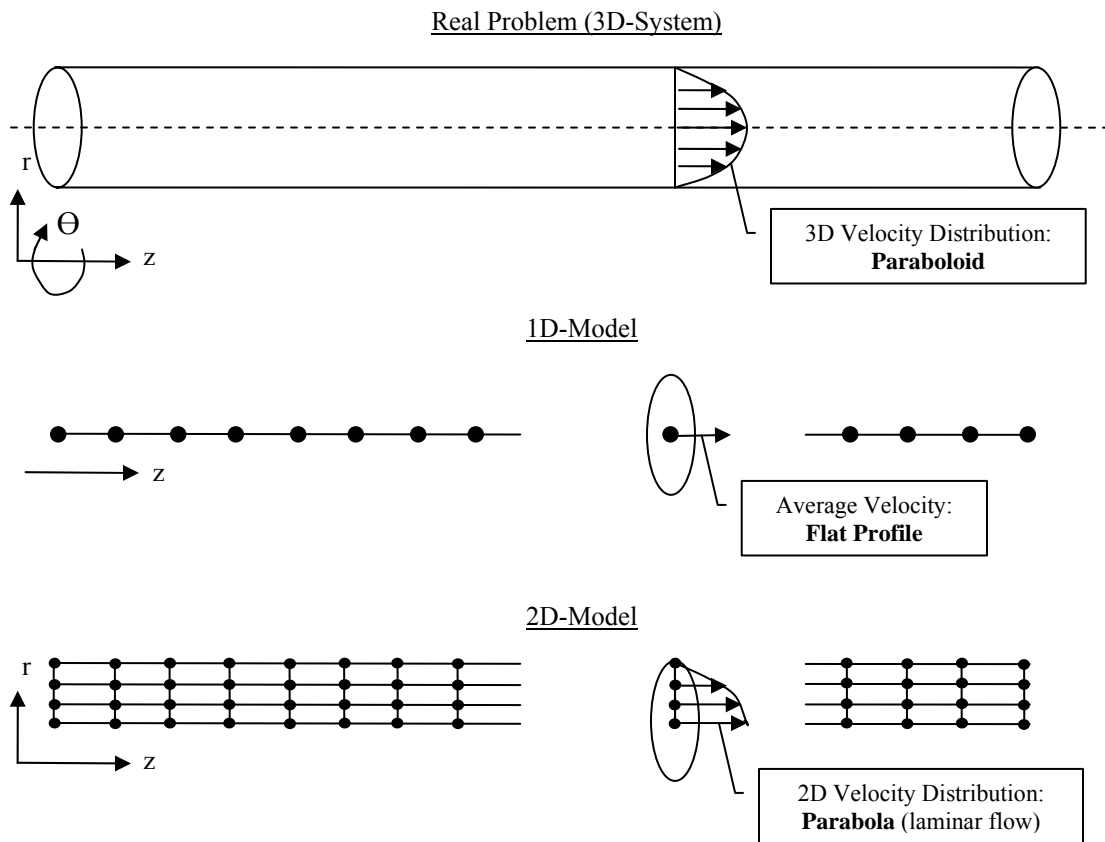
Figure 2.5. Velocity profiles for different grid-systems.

2.8. Transient vs. Steady-State Flow

In real systems the distribution of the flow variables along the pipeline are time dependent. However, for practical purposes if no perturbations are introduced to the system (a closing valve, increase of flow rate, reduction of demand at delivery points, etc) there will be a point in time were no changes in the distribution of the variables will occur. At this point the system has achieved steady-state flow and the time derivatives in the flow equations are equal to zero.

Now, let us assume the system is in steady-state. Any perturbation will create transients in the flow for a prolonged period of time. Such perturbations are introduced numerically by changing the boundary conditions, leading to what is known as transient or unsteady flow. Again, in the absence of any other perturbation, the system will achieve steady-state conditions after a finite period of time.

For the particular case of one-dimensional models, when steady-state conditions prevail, the area averaged model is obtained, which is a much simpler system of Ordinary Differential Equations (ODEs).

2.9. Natural Gas Metering

Natural gas is continuously transported through pipelines. Measurements of gas purchases and deliveries are of paramount importance to calculate the payments, and therefore accurate measurements of the amount of gas that has passed through a section of pipe over a period of time are required. In order to illustrate such importance, an updated version of an example presented by Ikoku (1984) is reproduced here: an error of 1.0% in the measurement of natural gas in a pipeline delivering 300 MMscf/d of gas priced at $10.00 per thousand standard cubic feet (Mscf) will amount to a loss of approximately $11.0 million/year to either the seller or the purchaser.

As a standard of the American Petroleum Institute (API) and the American Gas Association (AGA), the gas is measured by volume at a base pressure and temperature of 14.7 psia and 520 ºR respectively.

There are several measurement techniques to determine the flow rate of gas. Among those there are orifice meters, positive displacement meters, turbine meters, Venturi meters, flow nozzles, etc. The choice of measurement device is made based on factors such as desired accuracy, expected lifetime of the device, maintenance requirements, power availability, operational cost, agreement between involved parties, and others.

The different measurement techniques are based on different principles. These being volumetric measurement, displacement metering, and differential pressure methods. The later one consists of creating a differential pressure by a restriction placed along of the pipe, and then calculating the flow rate as a function of the recorded pressure drop using physical principles. We are interested in this kind of measurement technique, specifically the orifice-meter.

2.9.1. Orifice-Meter

To date, orifice meter is the most widely used differential meter in the gas industry. The device consists of a thin flat plate with an accurately made circular hole in the center. The plate is centered positioned between two flanges in a horizontal section of the pipeline. Two pressure taps are located on the upstream and downstream sides of the plate in order to measure the pressure drop. The typical orifice meter has a stainless steel plate about 3/16 inches thick to create the differential pressure across the orifice. This pressure difference and the absolute pressure at one of the taps are recorded continuously to be translated later into flow rate. Figure 2.6 shows a sketch of the orifice meter, and the flow pattern along the pipe and through the orifice.
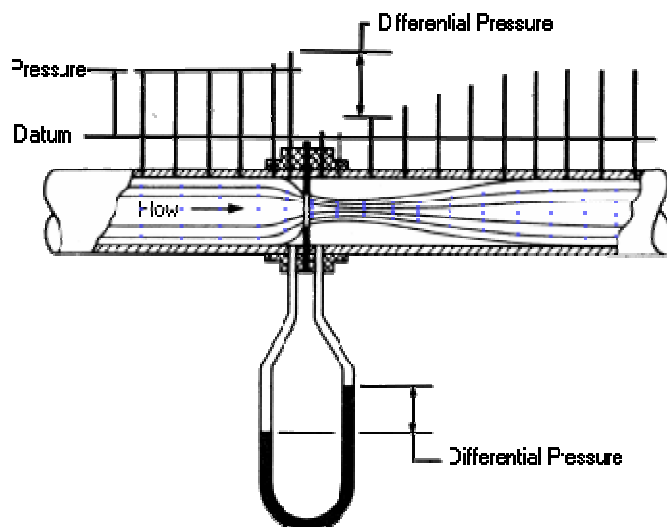
Figure 2.6. Sketch of the orifice meter, and flow pattern along the pipe.

Figure 2.6 shows a point of lowest pressure downstream. Theoretically, at this same point the highest velocity is reached in the fluid flow, and it is called vena contracta.

The formula for the calculation of the flow rate recommended by the AGA Committee Report No. 3 is derived from the Bernoulli's Energy equation (2.12) between the two flanges. The complete derivation can be reviewed in Ikoku (1984) and here we summarize some of the assumptions made to obtain the orifice-meter equation.

$$\int_1^2 \upsilon.dp + \int_1^2 \frac{u.du}{g_c} + \int_1^2 \frac{g.dZ}{g_c} = -w - lw \tag{2.12}$$

where:

υ : specific volume, [ft^3/lbm]

p : pressure, [psia]

u : average linear-flow velocity [ft/s]

g_c : conversion factor, 32.17 [(lbm.ft/s^2) / lbf]

g : gravity acceleration, [ft/s^2]

Z : vertical distance above datum, [ft]

w : work done by flowing fluid, [ft.lbf/lbm]

lw : work energy lost due to frictional effects, [ft.lbf/lbm]

Orifice-meters are generally located in a horizontal section of the pipe, therefore dZ is zero. Additionally, no work is done by the flowing fluid, so $w = 0$. Now, one of the strongest assumptions is the lumping of the frictional losses due to viscosity and turbulence into an empirical constant and using it as a factor of the first integral in Equation (2.12). This empirical constant accounts for friction and other irreversibilities (Equation 2.13).

$$C^2 \int_1^2 v.dp + \int_1^2 \frac{u.du}{g_c} = 0 \tag{2.13}$$

Another important assumption is the use of an average value of specific volume or density ($\bar{v}$ or $\bar{\rho}$) to simplify the integration, instead of obtaining a relationship of the specific volume, v and the pressure, p, between points 1 and 2. The equation becomes:

$$\frac{C^2(144)(p_1 - p_2)}{\bar{\rho}} = \frac{u_2^2 - u_1^2}{2g_c}$$

(2.14)

After some other mathematical manipulations, and expressing the flow rate in cubic feet per hour, the general expression for the flow rate of gas is:

$$q_h = C'\sqrt{h_w p_f}$$

(2.15)

where:

q_h = flow rate at base conditions, $[ft^3/hr]$

C' = orifice flow constant

h_w = differential pressure, in inches of water at 60 ºF

p_f = static pressure, $[psia]$

It is clear that this empirical equation looks very simple; making one wonder where all the physical laws became involved in the measurement calculations. The orifice flow constant C' may be defined as a rate of flow in cubic feet per hour, at base conditions. The factor C' is obtained by multiplying a basic orifice factor, by various correcting factors that are determined by parameters such as the contract requirements, operational conditions, and installation design. This is expressed in the following equation:

$$C' = (F_n)(F_c + F_{sl})(Y_1)(F_{pb})(F_{tb})(F_{tf})(F_{gr})(F_{pv})$$

(2.16)

where:

F_n : numeric conversion factor.

F_c : basic orifice factor, $[ft^3/hr]$

F_{sl} : orifice slope factor.

Y_1 : expansion factor based on upstream static pressure

F_{pb} : pressure base factor (contract)

F_{tb} : temperature base factor (contract)

F_{tf} : flowing temperature factor

F_{gr} : real gas relative density factor

F_{pv} : supercompressibility factor

Deriving of some of these factors may be complex. Moreover, some of them are determined only through experimentation, from which tables of data have been generated in order to obtain them.

Chapter 3

GENERALIZED SOLVER FOR 2-D HYPERBOLIC PDEs

In real application systems, the distribution of the flow variables is time dependent. For example, cost-effective design and operation of gas transmission systems require taking into consideration the responses under non-steady conditions. Transients are present in all pipeline systems, but for practical purposes assuming that no perturbations are introduced to the system there will be a point in time where no changes in the distribution of the variables will occur. At this point the system has achieved steady-state flow and the time derivatives in the flow equations are equal to zero. However, it is important to emphasize that the real problem is unsteady, and therefore a transient solver is developed in this study.

As mentioned before, the solver developed in this work targets the solution of problems that can be modeled using a system of two-dimensional hyperbolic partial differential equations (PDEs) as described by Equation 2.8. Hyperbolic systems arise in many practical problems that can be solved by the developed generalized solver, but the numerical methods available to solve hyperbolic PDEs are designed mainly for one-dimensional and homogeneous cases. Therefore in order to solve our problem, we need first to apply the splitting approach to include the second spatial dimension, and then use an ordinary differential equation (ODE) solver to include the source terms. All these methods are described below.

3.1. Essentially Non-Oscillatory Homogeneous PDEs Solver

The scheme presented here is an approximation to systems of hyperbolic conservation laws of the type:

$$\frac{\partial \vec{U}}{\partial t} + \sum_{i=1}^{d} \frac{\partial \vec{F}_i(\vec{U})}{\partial x_i} = 0, \quad d = 1 \tag{2.8}$$

Where $\vec{U}$ is the vector of conservative variables, and $\vec{F}$ is the vector of physical fluxes in the x - direction. As presented in Section 2.2.1, a conservative scheme to solve this system is a numerical method of the form:

$$U_{i,j}^{n+1} = U_{i,j}^{n} - \frac{\Delta t}{\Delta x}\left(\hat{F}_{i+\frac{1}{2}}^{n} - \hat{F}_{i-\frac{1}{2}}^{n}\right) \tag{2.10}$$

where $\hat{F}_{i+\frac{1}{2}}^{n}$ is the numerical flux, which is an approximation to the physical flux.

3.1.1. Solver for Scalar Problems

The main contribution of the original work by Harten (1987) is a uniformly high-order interpolation recipe with an adaptive stencil, named ENO reconstruction. Traditional finite-difference methods use fixed stencil interpolations. It is known that in order to increase the order of accuracy we need to take information of more cells. Initially, the first point of the stencil is chosen according to the local sign of $F'(U)$ at $x_{i+\frac{1}{2}}$. For the scalar case, the Roe speed may be used:

$$\overline{a}_{i+\frac{1}{2}} = \frac{F(U_{i+1}) - F(U_{i})}{U_{i+1} - U_{i}} \tag{3.1}$$

Now a repetitive protocol to obtain divided differences of the flux, and ultimately the numerical flux to the desired order of accuracy follows. Due to the complexity of the procedure, only the algorithm is presented here, but a step-by-step explanation is included in Appendix B.

a) ENO-Roe Algorithm

1. Compute the Newton divided difference table of F as:

$$F[U(x_0)] = F\big(U(x_0)\big), \text{ and} \tag{3.2}$$

$$F[U(x_0),U(x_1),...,U(x_n)] = \frac{F[U(x_0),U(x_1),...,U(x_{n-1})] - F[U(x_1),U(x_2),...,U(x_n)]}{U(x_0) - U(x_n)},$$

(3.3)

for n>1.

The first few divided differences are:

$$F[U(x_0),U(x_1)] = \frac{F[U(x_0)] - F[U(x_1)]}{U(x_0) - U(x_1)},$$ (3.4)

$$F[U(x_0),U(x_1),U(x_2)] = \frac{F[U(x_0),U(x_1)] - F[U(x_1),U(x_2)]}{U(x_0) - U(x_2)}, \text{ etc.}$$ (3.5)

2. Now let l be the grid-point of interest, and calculate:

$$H[x_{l-\frac{1}{2}}, x_{l+\frac{1}{2}}] = F[U(x_l)], \text{ and}$$ (3.6)

$$H[x_{l-\frac{1}{2}}, x_{l+\frac{1}{2}}, ..., x_{l+k+\frac{1}{2}}] = \frac{1}{k+1} F[U(x_l),...,U(x_{l+k})], \text{ where } k = 1,2,...,r.$$ (3.7)

Note that this scheme will be $(r+1)^{th}$-order-accurate except at isolated points where the derivative is zero, degenerating the scheme to r^{th}-order-accurate.

3. If $\bar{a}_{i+\frac{1}{2}} \geq 0$, then

$$k_{min}^{(1)} = i$$

else

$$k_{min}^{(1)} = i + 1$$

4. Compute:

$$Q^{(1)}(x) = H[x_{k_{min}^{(1)} - \frac{1}{2}}, x_{k_{min}^{(1)} + \frac{1}{2}}](x - x_{k_{min}^{(1)} - \frac{1}{2}})$$ (3.8)

5. Now, inductively having $k_{min}^{(l-1)}$ and $Q^{(l-1)}(x)$ both defined, then let:

$$a^{(l)} = H[x_{k_{min}^{(l-1)} - \frac{1}{2}}, ..., x_{k_{min}^{(l-1)} + l - \frac{1}{2}}]$$ (3.9)

$$b^{(l)} = H[x_{k_{\min}^{(l-1)}-1-\frac{1}{2}},...,x_{k_{\min}^{(l-1)}+l-1-\frac{1}{2}}] \tag{3.10}$$

i. If $\left|a^{(l)}\right| \geq \left|b^{(l)}\right|$, then

$$c^{(l)} = b^{(l)}, \quad k_{\min}^{(l)} = k_{\min}^{(l-1)} - 1 \tag{3.11}$$

otherwise

$$c^{(l)} = a^{(l)}, \quad k_{\min}^{(l)} = k_{\min}^{(l-1)} \tag{3.12}$$

ii. Form:

$$Q^{(l)}(x) = Q^{(l-1)}(x) + c^{(l)} \prod_{k=k_{\min}^{(l-1)}}^{k_{\min}^{(l-1)}+l-1} (x - x_{k-\frac{1}{2}}) \tag{3.13}$$

6. At this point, we have:

$$Q_{i+\frac{1}{2}}(x) = Q^{(r+1)}(x) \tag{3.14}$$

7. And finally, we take:

$$\hat{F}_{i+\frac{1}{2}} = \frac{d}{dx} Q_{i+\frac{1}{2}}(x) \bigg|_{x=x_{i+\frac{1}{2}}} = \frac{Q_{i+\frac{1}{2}}(x_{i+\frac{1}{2}} + \varepsilon_x) - Q_{i+\frac{1}{2}}(x_{i+\frac{1}{2}})}{\varepsilon_x}, \tag{3.15}$$

$$\text{where } dx/8 \leq \varepsilon_x \leq dx$$

According to Shu and Osher (1989), the ENO-Roe Algorithm could yield to a scheme admitting entropy-violating expansion shock; therefore they proposed the following algorithm to fix this problem.

b) ENO-LLF Algorithm

The acronym LLF stands for local Lax-Friedrichs. This algorithm is twice as expensive as ENO-Roe because it requires evaluating two divided difference tables. Again a detailed explanation is included in Appendix B, and the steps are as follows:

1. Computed the divided differences table of F and a table of U using the previous algorithm.

2. Now compute:

$$H^{\pm}[x_{l-\frac{1}{2}}, x_{l+\frac{1}{2}}] = \frac{1}{2}\left(F[U(x_l)] \pm \alpha_{i+\frac{1}{2}} U[x_l]\right), \tag{3.16}$$

$$l = i - r, \ldots, j + r \text{ for } H^+, \quad l = i - r + 1, \ldots, j + r + 1 \text{ for } H^-$$

$$H^{\pm}[x_{l-\frac{1}{2}}, x_{l+\frac{1}{2}}, \ldots, x_{l+k+\frac{1}{2}}] = \frac{1}{k+1} \cdot \frac{1}{2}\left(F[U(x_l), \ldots U(x_{l+k})] \pm \alpha_{i+\frac{1}{2}} U[x_l, \ldots, x_{l+k}]\right), \tag{3.17}$$

$$l = i - r, \ldots, j + r - k \text{ for } H^+, \quad l = i - r + 1, \ldots, j + r - k + 1 \text{ for } H^-, \quad k = 1, 2, \ldots, r$$

where:

$$\alpha_{i+\frac{1}{2}} = \max_{u_i \leq u \leq u_{i+1}} |F'(U)| \tag{3.18}$$

3. For H^+, $k_{min}^{(1)} = i$, then repeat steps (4)-(5) of ENO-Roe Algorithm to get $Q_+^{(r+1)}(x)$. And let:

$$Q_{i+\frac{1}{2}}^+(x) = Q_+^{(r+1)}(x) \tag{3.19}$$

4. For H^-, $k_{min}^{(1)} = i + 1$, then repeat steps (4)-(5) of ENO-Roe Algorithm to get $Q_-^{(r+1)}(x)$. And let:

$$Q_{i+\frac{1}{2}}^-(x) = Q_-^{(r+1)}(x) \tag{3.20}$$

5. Finally, we then take:

$$\hat{F}_{i+\frac{1}{2}} = \frac{d}{dx}Q_{i+\frac{1}{2}}^+(x)\Big|_{x=x_{i+\frac{1}{2}}} + \frac{d}{dx}Q_{i+\frac{1}{2}}^-(x)\Big|_{x=x_{i+\frac{1}{2}}}$$

$$= \frac{Q_{i+\frac{1}{2}}^+(x_{i+\frac{1}{2}} + \varepsilon_x) - Q_{i+\frac{1}{2}}^+(x_{i+\frac{1}{2}})}{\varepsilon_x} + \frac{Q_{i+\frac{1}{2}}^-(x_{i+\frac{1}{2}} + \varepsilon_x) - Q_{i+\frac{1}{2}}^-(x_{i+\frac{1}{2}})}{\varepsilon_x}, \tag{3.21}$$

$$\text{where } \frac{dx}{8} \leq \varepsilon_x \leq dx$$

3.1.2. Application to Systems

For nonlinear systems, the previous algorithms are applied in each characteristic field. First compute the average Jacobian at $x_{i+\frac{1}{2}}$, which for a systems of four equations is:

$$J_{x_{i+\frac{1}{2}}} = \frac{\partial \vec{F}(\vec{U})}{\partial \vec{U}}\bigg|_{U=\frac{1}{2}(U_i+U_{i+1})} = \begin{bmatrix} \dfrac{\partial F_1}{\partial U_1} & \dfrac{\partial F_1}{\partial U_2} & \dfrac{\partial F_1}{\partial U_3} & \dfrac{\partial F_1}{\partial U_4} \\[2mm] \dfrac{\partial F_2}{\partial U_1} & \dfrac{\partial F_2}{\partial U_2} & \dfrac{\partial F_2}{\partial U_3} & \dfrac{\partial F_2}{\partial U_4} \\[2mm] \dfrac{\partial F_3}{\partial U_1} & \dfrac{\partial F_3}{\partial U_2} & \dfrac{\partial F_3}{\partial U_3} & \dfrac{\partial F_3}{\partial U_4} \\[2mm] \dfrac{\partial F_4}{\partial U_1} & \dfrac{\partial F_4}{\partial U_2} & \dfrac{\partial F_4}{\partial U_3} & \dfrac{\partial F_4}{\partial U_4} \end{bmatrix} \tag{3.22}$$

Then the eigenvalues of $J_{x_{i+\frac{1}{2}}}$ are denoted as:

$$\lambda^{(1)}_{i+\frac{1}{2}}, \lambda^{(2)}_{i+\frac{1}{2}}, \lambda^{(3)}_{i+\frac{1}{2}} \text{ and } \lambda^{(4)}_{i+\frac{1}{2}} \tag{3.23}$$

And the corresponding right and left eigenvaectors are given by:

$$\begin{bmatrix} R^{(1)}_{1_{i+\frac{1}{2}}} \\ R^{(1)}_{2_{i+\frac{1}{2}}} \\ R^{(1)}_{3_{i+\frac{1}{2}}} \\ R^{(1)}_{4_{i+\frac{1}{2}}} \end{bmatrix}, \begin{bmatrix} R^{(2)}_{1_{i+\frac{1}{2}}} \\ R^{(2)}_{2_{i+\frac{1}{2}}} \\ R^{(2)}_{3_{i+\frac{1}{2}}} \\ R^{(2)}_{4_{i+\frac{1}{2}}} \end{bmatrix}, \begin{bmatrix} R^{(3)}_{1_{i+\frac{1}{2}}} \\ R^{(3)}_{2_{i+\frac{1}{2}}} \\ R^{(3)}_{3_{i+\frac{1}{2}}} \\ R^{(3)}_{4_{i+\frac{1}{2}}} \end{bmatrix}, \begin{bmatrix} R^{(4)}_{1_{i+\frac{1}{2}}} \\ R^{(4)}_{2_{i+\frac{1}{2}}} \\ R^{(4)}_{3_{i+\frac{1}{2}}} \\ R^{(4)}_{4_{i+\frac{1}{2}}} \end{bmatrix} \tag{3.24}$$

$$
\begin{bmatrix} L_{1_{i+\frac{1}{2}}}^{(1)} & L_{2_{i+\frac{1}{2}}}^{(1)} & L_{3_{i+\frac{1}{2}}}^{(1)} & L_{4_{i+\frac{1}{2}}}^{(1)} \end{bmatrix}
$$

$$
\begin{bmatrix} L_{1_{i+\frac{1}{2}}}^{(2)} & L_{2_{i+\frac{1}{2}}}^{(2)} & L_{3_{i+\frac{1}{2}}}^{(2)} & L_{4_{i+\frac{1}{2}}}^{(2)} \end{bmatrix}
$$

$$
\begin{bmatrix} L_{1_{i+\frac{1}{2}}}^{(3)} & L_{2_{i+\frac{1}{2}}}^{(3)} & L_{3_{i+\frac{1}{2}}}^{(3)} & L_{4_{i+\frac{1}{2}}}^{(3)} \end{bmatrix}
$$

$$
\begin{bmatrix} L_{1_{i+\frac{1}{2}}}^{(4)} & L_{2_{i+\frac{1}{2}}}^{(4)} & L_{3_{i+\frac{1}{2}}}^{(4)} & L_{4_{i+\frac{1}{2}}}^{(4)} \end{bmatrix}
$$

(3.25)

The eigenvectors are normalized, so that:

$$
L_{i+\frac{1}{2}}^{(p)} \cdot R_{i+\frac{1}{2}}^{(q)} = \delta_{pq} = \begin{cases} 1, & \text{if } p = q \\ 0, & \text{if } p \neq q \end{cases}
$$

(3.26)

At this point note that, for any vector $\vec{V}$:

$$
V^{(p)} = L_{i+\frac{1}{2}}^{(p)} \cdot \vec{V}
$$

(3.27)

is the component of $\vec{V}$ in the p$^{\text{th}}$ local characteristic field, because:

$$
\vec{V} = \sum_{p=1}^{m} V^{(p)} \vec{R}_{i+\frac{1}{2}}^{(p)}
$$

(3.28)

The ENO-Roe algorithm can be expanded for systems as follows:

1. Compute the divided difference tables of $\vec{F}$ and $\vec{U}$, and identify:

$$
\vec{H} = \begin{bmatrix} H_1[x_{l-\frac{1}{2}}, x_{l+\frac{1}{2}}] = F_1[U(x_l)] \\ H_2[x_{l-\frac{1}{2}}, x_{l+\frac{1}{2}}] = F_2[U(x_l)] \\ H_3[x_{l-\frac{1}{2}}, x_{l+\frac{1}{2}}] = F_3[U(x_l)] \\ H_4[x_{l-\frac{1}{2}}, x_{l+\frac{1}{2}}] = F_4[U(x_l)] \end{bmatrix}
$$

(3.29)

and

$$\vec{H} = \begin{bmatrix} H_1[x_{l-\frac{1}{2}}, x_{l+\frac{1}{2}}, ..., x_{l+k+\frac{1}{2}}] = \dfrac{1}{k+1} F_1[U(x_l), ...U(x_{l+k})] \\ H_2[x_{l-\frac{1}{2}}, x_{l+\frac{1}{2}}, ..., x_{l+k+\frac{1}{2}}] = \dfrac{1}{k+1} F_2[U(x_l), ...U(x_{l+k})] \\ H_3[x_{l-\frac{1}{2}}, x_{l+\frac{1}{2}}, ..., x_{l+k+\frac{1}{2}}] = \dfrac{1}{k+1} F_3[U(x_l), ...U(x_{l+k})] \\ H_4[x_{l-\frac{1}{2}}, x_{l+\frac{1}{2}}, ..., x_{l+k+\frac{1}{2}}] = \dfrac{1}{k+1} F_4[U(x_l), ...U(x_{l+k})] \end{bmatrix}, \qquad (4.30)$$

2. For each grid-point i compute $H^{(p)}[x_{l-\frac{1}{2}}, ..., x_{l+k+\frac{1}{2}}]$ for $l = j - k, ..., j+1$ and $k = 1, 2, ..., r$,

    by using the divided difference tables of $\vec{H}$ and expression 3.27. This is:

$$H^{(p)} = \begin{bmatrix} L^{(p)}_{1_{i+\frac{1}{2}}} & L^{(p)}_{2_{i+\frac{1}{2}}} & L^{(p)}_{3_{i+\frac{1}{2}}} & L^{(p)}_{4_{i+\frac{1}{2}}} \end{bmatrix} \cdot \begin{bmatrix} H_1 \\ H_2 \\ H_3 \\ H_4 \end{bmatrix} \qquad (3.31)$$

3. Apply steps (3)-(7) of ENO-Roe algorithm to $H^{(p)}$, using $\overline{a}_{i+\frac{1}{2}} = \lambda^{(p)}_{i+\frac{1}{2}}$ to get $\hat{F}^{(p)}_{i+\frac{1}{2}}$. At this

    point we will have: $\hat{F}^{(1)}_{i+\frac{1}{2}}, \hat{F}^{(2)}_{i+\frac{1}{2}}, \hat{F}^{(3)}_{i+\frac{1}{2}}$ and $\hat{F}^{(4)}_{i+\frac{1}{2}}$.

4. Now using Expression 3.28 we obtain the vector of numerical fluxes as:

$$\vec{F} = \sum_{p=1}^{m=4} \hat{F}^{(p)}_{i+\frac{1}{2}} \vec{R}^{(p)}_{i+\frac{1}{2}}$$

$$\begin{bmatrix} \hat{F}_1 \\ \hat{F}_2 \\ \hat{F}_3 \\ \hat{F}_4 \end{bmatrix} = \hat{F}^{(1)}_{i+\frac{1}{2}} \begin{bmatrix} R^{(1)}_{1_{i+\frac{1}{2}}} \\ R^{(1)}_{2_{i+\frac{1}{2}}} \\ R^{(1)}_{3_{i+\frac{1}{2}}} \\ R^{(1)}_{4_{i+\frac{1}{2}}} \end{bmatrix} + \hat{F}^{(2)}_{i+\frac{1}{2}} \begin{bmatrix} R^{(2)}_{1_{i+\frac{1}{2}}} \\ R^{(2)}_{2_{i+\frac{1}{2}}} \\ R^{(2)}_{3_{i+\frac{1}{2}}} \\ R^{(2)}_{4_{i+\frac{1}{2}}} \end{bmatrix} + \hat{F}^{(3)}_{i+\frac{1}{2}} \begin{bmatrix} R^{(3)}_{1_{i+\frac{1}{2}}} \\ R^{(3)}_{2_{i+\frac{1}{2}}} \\ R^{(3)}_{3_{i+\frac{1}{2}}} \\ R^{(3)}_{4_{i+\frac{1}{2}}} \end{bmatrix} + \hat{F}^{(4)}_{i+\frac{1}{2}} \begin{bmatrix} R^{(4)}_{1_{i+\frac{1}{2}}} \\ R^{(4)}_{2_{i+\frac{1}{2}}} \\ R^{(4)}_{3_{i+\frac{1}{2}}} \\ R^{(4)}_{4_{i+\frac{1}{2}}} \end{bmatrix} \qquad (3.32)$$

3.2. Splitting Approach for Multi-Dimensional Problems

In some way, the one-dimensional methods and theory, previously presented, can be applied to problems in more than one dimension (LeVeque, 1992). Here we present the two-dimensional case which in the same way can be expanded to three dimensions. A system of conservation laws in two space dimensions has the form:

$$\frac{\partial \vec{U}}{\partial t} + \frac{\partial \vec{F}(\vec{U})}{\partial x} + \frac{\partial \vec{G}(\vec{U})}{\partial y} = 0 \qquad (2.8)$$

Typically the problem geometry could be complicated, but here we will only discuss the case in which a Cartesian grid is used, meaning that the grid points are of the form (x_i, y_j) as i, j range through the integers, with:

$$x_i = i\Delta x, \quad y_j = j\Delta y \qquad (3.33)$$

The splitting approach uses fully discrete one-dimensional methods, and applies them alternately on one-dimensional problems in the x and y directions. This approach is exact when considering the two-dimensional scalar advection equation:

$$\frac{\partial u}{\partial t} + a\frac{\partial u}{\partial x} + b\frac{\partial u}{\partial y} = 0 \qquad (3.34)$$

with initial data:

$$u(x, y, 0) = u_0(x, y) \qquad (3.35)$$

The exact solution of this problem is:

$$u(x, y, t) = u_0(x - at, y - bt) \qquad (3.36)$$

Alternatively, this problem can be solved by solving a pair of one-dimensional problems. We first solve:

$$\frac{\partial v}{\partial t} + a\frac{\partial v}{\partial x} = 0 \qquad\qquad (3.37)$$

with initial data:

$$v(x, y, 0) = u_0(x, y) \qquad\qquad (3.38)$$

to obtain $v(x, y, t) = u_0(x - at, y)$. We then use this function of x and y as initial data and solve the second one-dimensional problem:

$$\frac{\partial w}{\partial t} + b\frac{\partial w}{\partial y} = 0 \qquad\qquad (3.39)$$

with initial data:

$$w(x, y, 0) = v(x, y, t) = u_0(x - at, y) \qquad\qquad (3.40)$$

to obtain:

$$w(x, y, t) = v(x, y - bt, 0) = u_0(x - at, y - bt) \qquad\qquad (3.41)$$

which is in fact the exact solution to the problem.

3.3. Splitting Approach for Non-Homogeneous Problems

The previous approach can be expanded to solve the most general case, where multi spatial dimensions exist and also a vector of source terms or forcing functions. The simplest non-homogeneous two-dimensional hyperbolic equation is given by the IVP (3.42), where a and b are the two velocity components of a constant velocity vector $V = (a, b)$, and η is another constant parameter.

$$PDE: \frac{\partial u}{\partial t} + a\frac{\partial u}{\partial x} + b\frac{\partial u}{\partial y} = \eta u \left. \right\}$$
$$IC: u(x, y, 0) = u_0(x, y) \qquad$$

(3.42)

The exact solution of (3.42) is:

$$u(x, y, t) = u_0(x - at, y - bt)e^{\eta t} \qquad (3.43)$$

It is also important to note that when $\eta = 0$, the exact solution collapses to the one for the homogeneous equation (3.34). By splitting the problem into three IVPs one obtains Equations (3.44) to (3.46):

$$\left. \begin{array}{l} PDE: \frac{\partial v}{\partial t} + a\frac{\partial v}{\partial x} = 0 \\ IC: v(x, y, 0) = u_0(x, y) \end{array} \right\} \Rightarrow v(x, y, t) = u_0(x - at, y) \qquad (3.44)$$

$$\left. \begin{array}{l} PDE: \frac{\partial w}{\partial t} + b\frac{\partial w}{\partial y} = 0 \\ IC: w(x, y, 0) = v(x, y, t) = u_0(x - at, y) \end{array} \right\}$$
$$\Rightarrow w(x, y, t) = v(x, y - bt, t) = u_0(x - at, y - bt) \qquad (3.45)$$

$$\left. \begin{array}{l} ODE: \frac{dq}{dt} = \eta q \\ IC: q(0) = w(x, y, t) = u_0(x - at, y - bt) \end{array} \right\}$$
$$\Rightarrow q(t) = q(0)e^{\eta t} = u_0(x - at, y - bt)e^{\eta t} \qquad (3.46)$$

Note that the solution of the source problem described by equation (3.46) is the solution of the original problem described by Equation (3.42). Moreover, this is the exact solution described by Equation (3.43) given before. In terms of solution operators the approach can be expressed as:

$$u(x, y, t) = O^{(t)} \left[P_y^{(t)} \left[P_x^{(t)} \left[u_0(x, y, z) \right] \right] \right] \qquad (3.47)$$

where $P_x^{(t)}$ and $P_y^{(t)}$ are the homogeneous hyperbolic PDE operators applied over a time t, in the x and y spatial directions respectively, and $O^{(t)}$ is the ODE operator also applied on the timeframe t.

3.4. Numerical Methods based on Splitting Technique

An exact solution, like the one generated for the linear advection equation (3.42), can no longer be obtained when applying the scheme to non-linear systems. However, good approximate numerical solutions can be obtained when using the method for discrete data. The solution is computed by evolving the initial value U^n, by one time step of size Δt, to a value U^{n+1} in a spatial domain $[0, L]$, which has been discretized into a finite number N of grid-points. Having a system as described by Equation (3.48), the steps of Equations (3.44)-(3.46) can be generalized as Equations (3.49)-(3.51):

$$\left. \begin{array}{l} PDEs: \quad \dfrac{\partial \vec{U}}{\partial t} + \dfrac{\partial \vec{F}(U)}{\partial x} + \dfrac{\partial \vec{G}(U)}{\partial y} + \dfrac{\partial \vec{H}(U)}{\partial z} = \vec{Q}(U) \quad ,0 \leq x \leq L \\ \\ ICs: \quad U(x, y, z, t^n) = U^n \end{array} \right\} \tag{3.48}$$

$$\left. \begin{array}{l} PDEs: \quad \dfrac{\partial \vec{U}}{\partial t} + \dfrac{\partial \vec{F}(U)}{\partial x} = 0 \\ \\ ICs: \quad U^n \end{array} \right\} \overset{\Delta t}{\Rightarrow} U^{n+\frac{1}{3}} \tag{4.49}$$

$$\left. \begin{array}{l} PDEs: \quad \dfrac{\partial \vec{U}}{\partial t} + \dfrac{\partial \vec{G}(U)}{\partial y} = 0 \\ \\ ICs: \quad U^{n+\frac{1}{3}} \end{array} \right\} \overset{\Delta t}{\Rightarrow} U^{n+\frac{2}{3}} \tag{3.50}$$

$$\left. \begin{array}{l} ODEs: \quad \dfrac{d}{dt}\vec{U} = \vec{Q}(U) \\ \\ ICs: \quad U^{n+\frac{2}{3}} \end{array} \right\} \overset{\Delta t}{\Rightarrow} U^{n+1} \tag{3.51}$$

For numerical methods, analogous to Equation (3.47), a first-order accurate version of the splitting approach can be described as:

$$U^{n+1} = O^{(\Delta t)}\left[P_y^{(\Delta t)}\left[P_x^{(\Delta t)}\left[U^n\right]\right]\right] \tag{3.52}$$

3.5. Ordinary Differential Equation Solver

The generic problem in ordinary differential equations can be reduced to the study of a set of M coupled first-order differential equations for the functions y_i, $i = 1,2,...,M$, having the general form:

$$\frac{dy_i(x)}{dx} = f_i(x, y_1,..., y_M)$$ (3.53)

Where the functions f_i on the RHS are known. For a system of ODEs the nature of the problem's boundary conditions is crucial. Boundary conditions are algebraic conditions of the functions y_i as shown in Equation (3.53). Usually, it is the nature of the boundary conditions what determines which numerical methods can be used. Boundary conditions are divided into initial value problems (IVP) and two-point boundary value problems. Typically, one is interested in IVP, in which all the y_i are given at some starting value x_o, and it is desired to find the y_i values at some final point x_f.

The underlying idea of any routine for solving the IVP is rewriting the derivatives (*dx, dy*) in Equation (4.53) as finite steps ($\Delta x, \Delta y$), and then multiplying the equations by Δx. In the limit of making the stepsize very small, a good approximation to the underlying differential equation is achieved. Literal implementation of this procedure results in Euler's method, which is however not recommended for any practical use.

Among the major types of practical numerical methods for solving IVP of ODEs are the Runge-Kutta methods. These methods propagate the solution over an interval by combining the information from several Euler-style steps (each involving one evaluation of the RHS), and then using the information obtained to match a Taylor series expansion up to some higher order. Runge-Kutta succeeds virtually always; but is not usually the fastest method, except when evaluating f_i is not expensive and the required accuracy is not that demanding (i.e. $\leq 10^{-5}$).

3.5.1. Runge-Kutta Method

The Euler's method is stated as:

$$y_{i+1} = y_i + \Delta x . f(x_i, y_i) \tag{3.54}$$

However, there are several reasons why the Euler's method is not recommended for practical use, which include that the method is neither very accurate nor very stable when compared with others. But, let us consider the use of a step like the one described by Equation (3.54) to take a trial step to the midpoint of the interval, and then use the values at that midpoint to compute the real step across the whole interval, what results is the so called second-order Runge-Kutta method or midpoint method.

Moreover, there are many ways to evaluate the RHS using different coefficients of higher-order error terms. Adding the right combination of these, the error terms can be eliminated order by order, and this is the basic idea of the Runge-Kutta method. In this sense, one of the most used is the classical fourth-order Runge-Kutta method.

3.5.2. Fifth-Order Cash & Karp Embedded Runge-Kutta Method

Felhberg (1968) presented one of the earliest attempts in embedded Runge-Kutta methods. A fifth-order accurate estimate of the solution is obtained by the Runge-Kutta-Fehlberg method:

$$U(s + \Delta s)\big|_{5^{th}} = U_0 + \sum_{i=1}^{6} a_i^F F_i^F \tag{3.55}$$

where a_i^F are constant coefficients proposed by Fehlberg (1968), and the quantities F_i^F are computed by evaluating the RHS vector with formulas of the type:

$$F_i^F = \Delta s . RHS\left(U_0 + \sum_{j=1}^{i-1} d_{ij}^F F_j^F \right) \quad , \quad 1 \le i \le 6 \tag{3.56}$$

The constant coefficients d_{ij}^F are also given by Fehlberg (1968). Note that to get all the F_i^F quantities, six evaluations of the RHS vector are required. Once all these quantities are known, the final solution is calculated from (3.55).

The original values of the constants (a_i^F, d_{ij}^F) are given by Fehlberg (1968), but according to Press *et al* (1994), Cash and Karp (1990) proposed ones that produce a more efficient method, with better error properties (see Table 3.1) and those are the ones chosen to be used in this study.

Table 3.1. Cash-Karp parameters for Embedded Runge-Kutta method.

i	a_i	d_{ij}					e_i
1	$\frac{37}{378}$						$-\frac{277}{64512}$
2	0	$\frac{1}{5}$					0
3	$\frac{250}{621}$	$\frac{3}{40}$	$\frac{9}{40}$				$\frac{6925}{370944}$
4	$\frac{125}{594}$	$\frac{3}{10}$	$-\frac{9}{10}$	$\frac{6}{5}$			$-\frac{6925}{202752}$
5	0	$-\frac{11}{54}$	$\frac{5}{2}$	$-\frac{70}{27}$	$\frac{35}{27}$		$-\frac{277}{14336}$
6	$\frac{512}{1771}$	$\frac{1631}{55296}$	$\frac{175}{512}$	$\frac{575}{13824}$	$\frac{44275}{110592}$	$\frac{253}{4096}$	$\frac{277}{7084}$
j		1	2	3	4	5	

In order to test the capabilities and robustness of the numerical methods presented here, a series of benchmark problems were solved, and very accurate solutions were obtained compared with the exact values. The description and solution of these problems are presented in Chapter 4.

Chapter 4

APPLICATION TO BENCHMARK PROBLEMS

The assessment of the reliability of numerical methods to be used in practical computations, prior their actual application, is of considerable importance. Some classes of test problems that can be used are tests with exact solution, and tests with reliable numerical solution to equivalent one-dimensional equations obtained under the assumption of symmetry. When solving these test problems one solves the same or equivalent governing PDEs and thus one seeks complete agreement in the comparisons.

In this chapter, a number of benchmarking problems, whose analytical solutions are available, is used to validate the solver. These problems have the essential characteristics of shocks, including homogenous and non-homogeneous, linear and non-linear systems.

4.1. Application to 1-D Problems

4.1.1. Linear Advection Equation

This is the simplest hyperbolic PDE. It describes a wave propagating in the x-direction with a constant velocity a. The initial value problems (IVPs) (4.1)-(4.2) are solved in the spatial domain [0,4], using 400 gridpoints, and for a CFL number of 0.5. In the first test we take a positive velocity $a = 1$, while for the second problem a negative velocity $a = -1$ is used.

$$\frac{\partial U}{\partial t} + a\frac{\partial U}{\partial x} = 0 \qquad (4.1)$$

$$IC_1 : U(x,0) = U_0(x) = \begin{cases} 1 & if\ 0.5 < x < 1.5 \\ 0 & otherwise \end{cases} \qquad IC_2 : U(x,0) = U_0(x) = \begin{cases} 1 & if\ 2.5 < x < 3.5 \\ 0 & otherwise \end{cases}$$

$$(4.2)$$

The exact solution of this problem is such that given an initial distribution of the data $U_o(x)$, the PDE translate it with a speed a. This is:

$$U(x,t) = U_o(x - at) \tag{4.3}$$

The results, for an output time 2.0, are shown in Figures 4.1 and 4.2, where the exact solutions are represented by the solid line, and they are compare very favorably with their numerical counterparts.
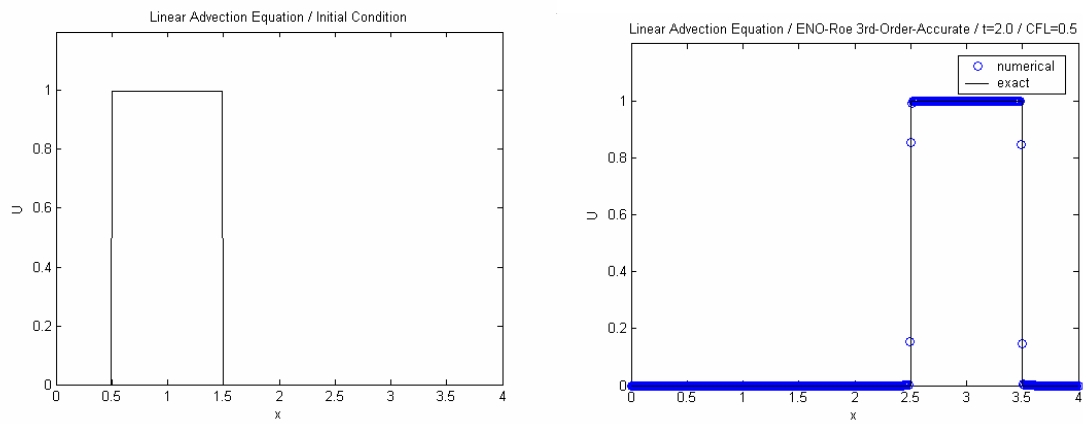
Figure 4.1. Test 1A, Initial Condition and Solution at t=2.0 for a=1.
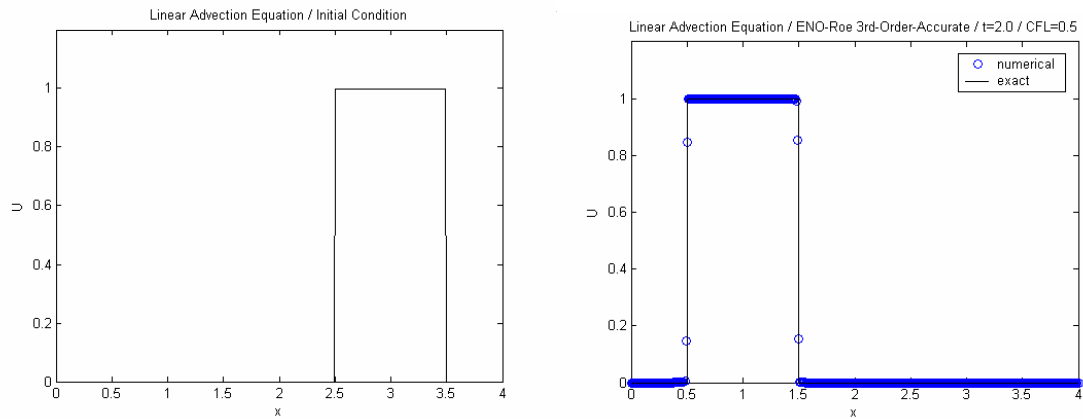
Figure 4.2. Test 1B, Initial Condition and Solution at t=2.0 for a=-1.

Two test problems were proposed by Zalesak (1987) in order to assess the performance of the numerical scheme for non-sharp contact discontinuities. The IVPs (4.1)-(4.4) and (4.1)-(4.5) were solved using 300 gridpoints in the domain [0,3] for a CFL number of 1/6 and an output time 1.0.

Figures 4.3 and 4.4 show the initial data and a comparison between the numerical and exact solutions.

$$IC : U(x,0) = U_0(x) = e^{-300(x-1)^2} \tag{4.4}$$

$$IC : U(x+1.0) = U_0(x+1.0) = \begin{cases} \sqrt{1 - \left(\dfrac{10x}{3}\right)^2}\,1 & if \; -0.3 < x < 0.3 \\ 0 & otherwise \end{cases} \tag{4.5}$$
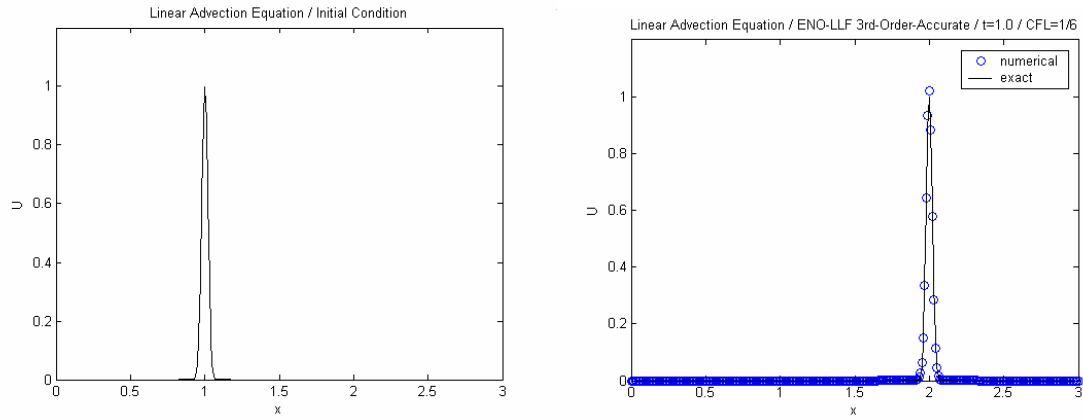
Figure 4.3. Test 2, Initial Condition and Solution at t=1.0.
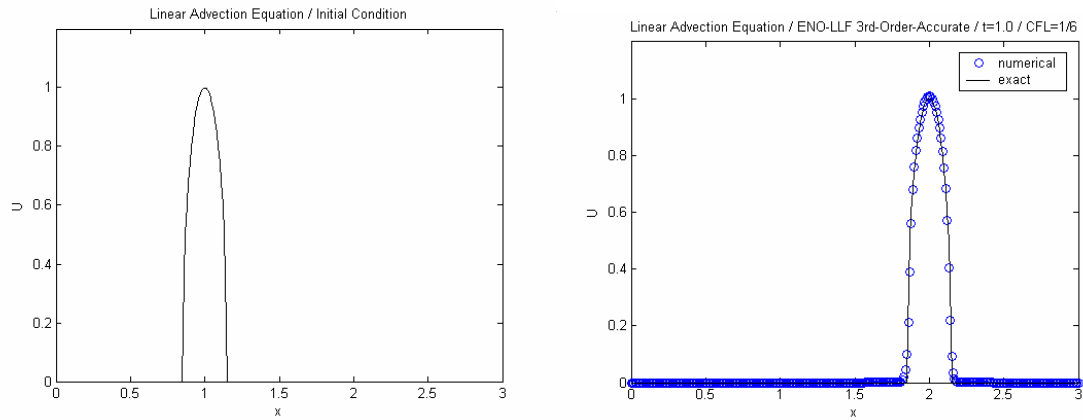
Figure 4.4. Test 3, Initial Condition and Solution at t=1.0.

A test similar to the one proposed by Harten *et al* (1987) is represented by the IVP (4.1)-(4.6). The problem is solved in the spatial domain [0, 2.5] using 250 gridpoints and for a CFL number equal to 1/6. The numerical results at $t = 1.0$ are comparable to those obtained by Shu and Osher (1988), and they are presented in Figure 4.5 were they are compared to the exact solution.

$$IC: U(x+1.0) = U_0(x+1.0) = \begin{cases} 2x-1-\dfrac{\sin(3\pi(x+1.5))}{6} & if \ x < -0.5 \\[3mm] -x\sin\left(\dfrac{3\pi(x-0.5)^2}{2}\right) & if \ -0.5 \le x < 0.2 \\[3mm] \left|\sin(2\pi(x-0.5))\right| & if \ 0.2 \le x \le 0.8 \\[3mm] 2x-1-\dfrac{\sin(3\pi(x-0.5))}{6} & if \ 0.8 < x \le 1.0 \end{cases}$$

$$(4.6)$$
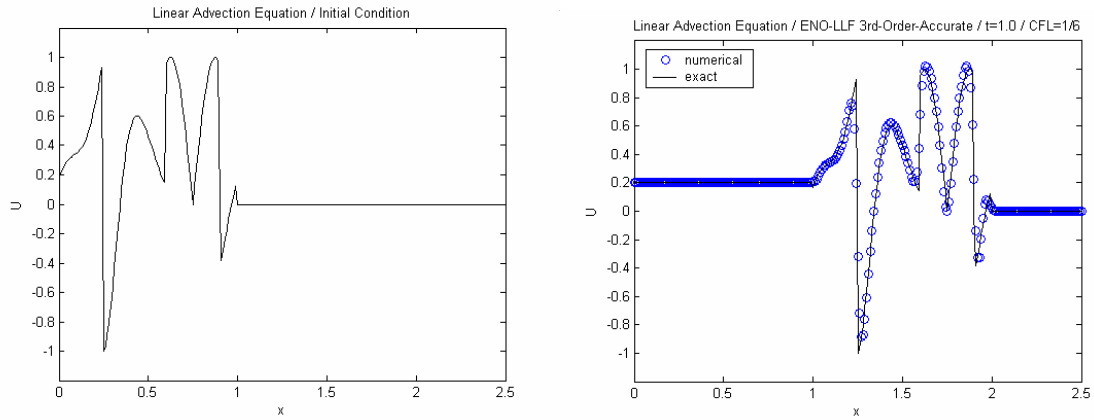
Figure 4.5. Test 4, Initial Condition and Solution at t=1.0.

4.1.2. One-Dimensional Burger's Equation

The usual fluid mechanics problems are highly non-linear and the simplest non-linear equation is the so called inviscid Burger's equation (4.7). In order to asses the performance of the numerical scheme with negative signs, two symmetrical problems are solved here using 400 cells in the domain [0, 4], and for a CFL number of 1/5. The initial conditions of the two IVPs are given by expression (4.8). The comparisons between the numerical and the analytical solutions are presented in Figures 4.6 and 4.7 respectively.

$$\text{PDE:} \ \frac{\partial U}{\partial t} + \frac{\partial F(U)}{\partial x} = 0, \qquad F(U) = \frac{U^2}{2} \qquad (4.7)$$

$$IC_1 : U(x,0) = U_0(x) = \begin{cases} \frac{1}{2} & \textit{if } x \le \frac{1}{4} \\ 2 & \textit{if } \frac{1}{4} < x < 1 \\ 1 & \textit{if } x \ge 1 \end{cases} \qquad IC_2 : U(x,0) = U_0(x) = \begin{cases} -1 & \textit{if } x \le 3 \\ -2 & \textit{if } 3 < x < 3.75 \\ -\frac{1}{2} & \textit{if } x \ge 3.75 \end{cases}$$

$$(4.8)$$
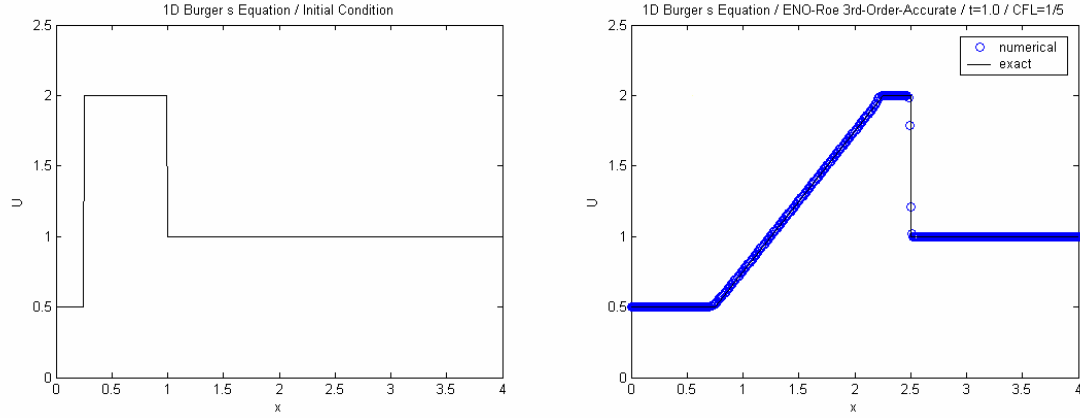
Figure 4.6. Test 5A, Initial Condition and Solution at t=1.0.
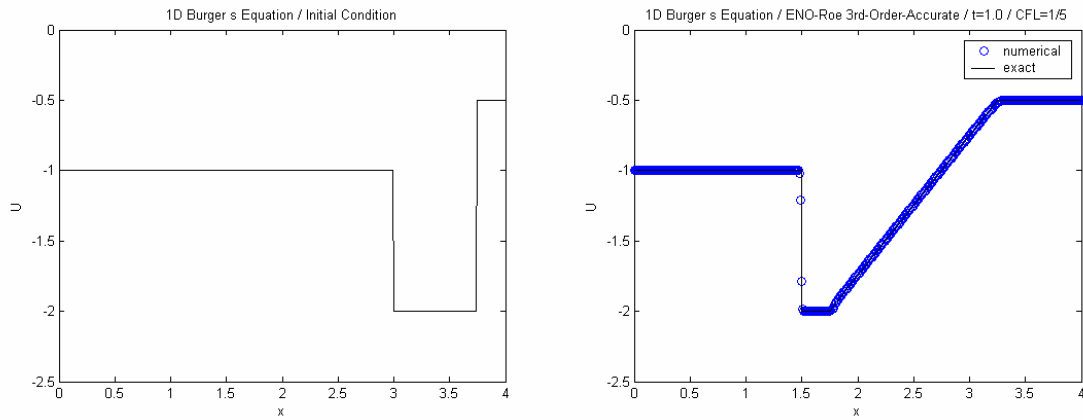
Figure 4.7. Test 5B, Initial Condition and Solution at t=1.0.

4.1.3. One-Dimensional Euler's Equations

The non-linear hyperbolic laws that govern the motion of an inviscid non-heat conducting gas are the time-dependent Euler equations [Equation (4.9)]. The Euler equations are of interest because many of the major elements of fluid dynamics, such as shock waves and contact surfaces are incorporated in them (Tannehill, 1997). The system of gas dynamics equations includes balances

of mass, momentum and energy, and it has been used by several investigators as a Benchmark problem, specifically the shock tube problem first proposed by Sod (1978).

$$\left.\begin{array}{l} \dfrac{\partial \rho}{\partial t} + \dfrac{\partial (\rho u)}{\partial x} = 0 \\[2mm] \dfrac{\partial (\rho u)}{\partial t} + \dfrac{\partial (\rho u^2 + p)}{\partial x} = 0 \\[2mm] \dfrac{\partial E}{\partial t} + \dfrac{\partial [u(E+p)]}{\partial x} = 0 \end{array}\right\} \qquad (4.9)$$

The system (4.9) can be expressed in the conservative form (2.8), where U and $F(U)$ are given respectively by:

$$\frac{\partial \vec{U}}{\partial t} + \frac{\partial \vec{F}(U)}{\partial x} = 0 \qquad (2.8)$$

$$\vec{U} = \begin{bmatrix} U_1 \\ U_2 \\ U_3 \end{bmatrix} = \begin{bmatrix} \rho \\ \rho u \\ E \end{bmatrix}, \qquad \vec{F}(\vec{U}) = \begin{bmatrix} F_1 \\ F_2 \\ F_3 \end{bmatrix} = \begin{bmatrix} \rho u \\ \rho u^2 + p \\ u(E+p) \end{bmatrix}$$

where ρ is density, p is pressure, u is particle velocity and E is total energy per unit volume defined as:

$$E = \frac{\rho u^2}{2} + \rho e \qquad (4.10)$$

Here e is the specific internal energy given by a caloric equation of state as: $e = e(T, p) = e(\rho, p)$. For ideal gases one has the following expression:

$$e = \frac{p}{(\gamma - 1)\rho} \qquad (4.11)$$

where $\gamma = c_p / c_v$ denote the ratio of specific heats.

The so called shock tube problem is a closed tube initially divided into a high-pressure section and a low-pressure section by a fixed diaphragm; making both sections to be initially at velocity zero (Anderson, 1995). Then the diaphragm is removed, allowing the discontinuity to propagate. This problem was solved numerically for two different initial conditions (Table 4.1), in the spatial domain [0,1], using 200 cells, a CFL number of 0.1 and $\gamma = 1.4$.

Table 4.1. Specifications for different tests. Euler's equations.

Test	x_0	Time	U_{1L}	U_{2L}	U_{3L}	U_{1R}	U_{2R}	U_{3R}
1	0.5	0.25	1.000	0.000	2.500	0.125	0.00	0.250
2	0.6	0.10	0.445	0.298	8.919	0.500	0.00	1.427

The numerical results are presented in Figures 4.8 and 4.9, where they are compared against the exact solutions obtained from the exact solver described by Toro (1999), and presented in Leon (2004).
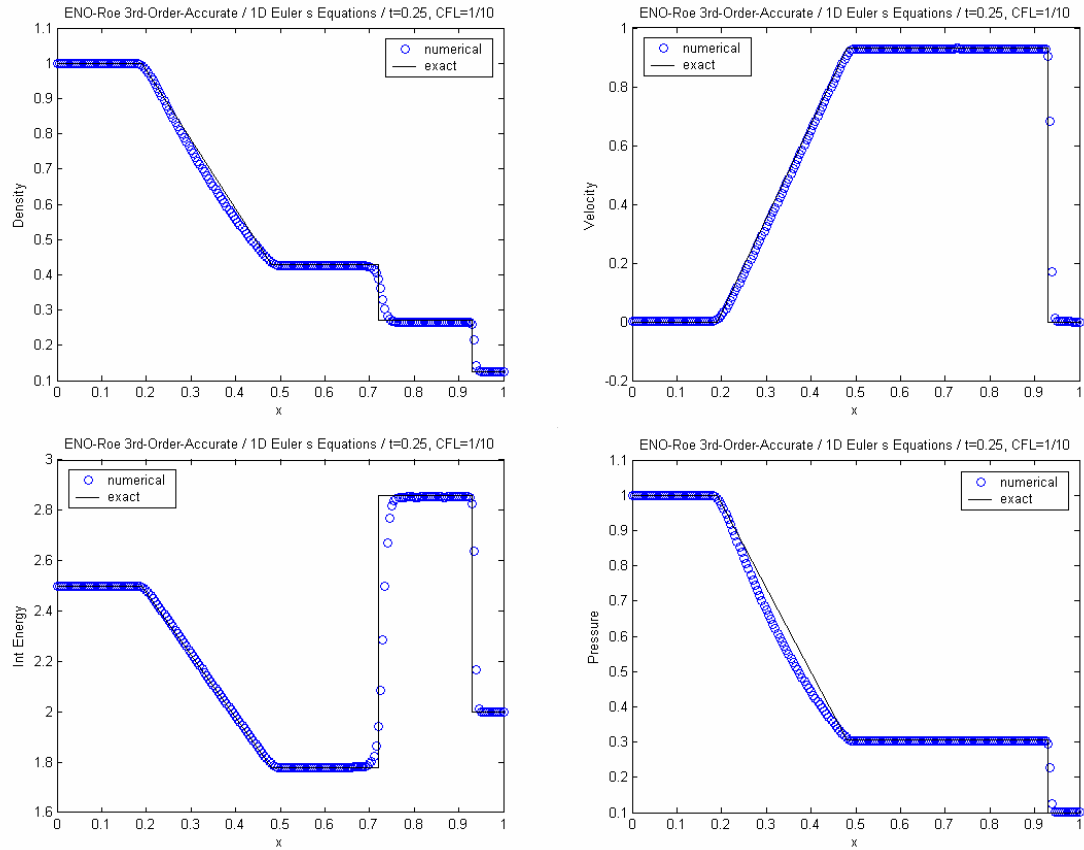
Figure 4.8. Test 6A, Comparison between numerical and exact solutions at t=0.25.
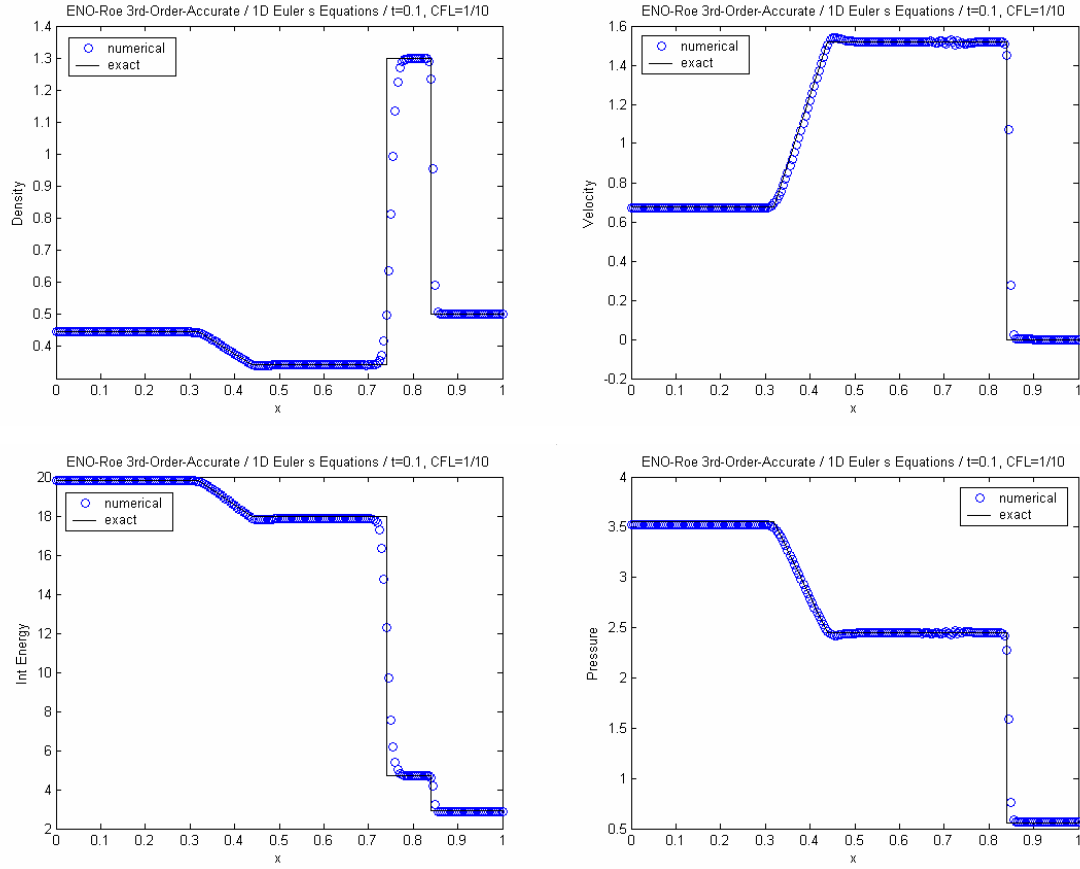
Figure 4.9. Test 6B, Comparison between numerical and exact solutions at t=0.1.

4.1.4. System of Two Coupled Equations

Here we solved the non-homogeneous system of equations proposed by León (2004). These two coupled equations can be written in conservative vector form as:

$$\frac{\partial \vec{U}}{\partial x} + \frac{\partial \vec{F}(U)}{\partial x} = \vec{Q}(U) \tag{4.12}$$

where:

$$\vec{U} = \begin{bmatrix} U_1 \\ U_2 \end{bmatrix}; \quad \vec{F} = \begin{bmatrix} F_1 \\ F_2 \end{bmatrix} = \begin{bmatrix} \left(\dfrac{a_1 + a_2}{2}\right)U_1 + \left(\dfrac{a_1 - a_2}{2}\right)U_2 \\ \left(\dfrac{a_1 - a_2}{2}\right)U_1 + \left(\dfrac{a_1 + a_2}{2}\right)U_2 \end{bmatrix}; \quad \vec{Q} = \begin{bmatrix} Q_1 \\ Q_2 \end{bmatrix} = \begin{bmatrix} \left(\dfrac{\eta_1 + \eta_2}{2}\right)U_1 + \left(\dfrac{\eta_1 - \eta_2}{2}\right)U_2 \\ \left(\dfrac{\eta_1 - \eta_2}{2}\right)U_1 + \left(\dfrac{\eta_1 + \eta_2}{2}\right)U_2 \end{bmatrix}$$

$$\tag{4.13}$$

The initial conditions of the system are determined by:

$$
\left.\begin{array}{l}
U_1(x,0) = U_{1_o}(x) = u_o^*(x) + v_o^*(x) \\
U_2(x,0) = U_{2_o}(x) = u_o^*(x) - v_o^*(x)
\end{array}\right\} \tag{4.14}
$$

And the exact solution can be written as:

$$
\left.\begin{array}{l}
U_1(x,t) = u^*(x,t) + v^*(x,t) = u_o^*(x-a_1 t)e^{\eta_1 t} + v_o^*(x-a_2 t)e^{\eta_2 t} \\
U_2(x,t) = u^*(x,t) - v^*(x,t) = u_o^*(x-a_1 t)e^{\eta_1 t} - v_o^*(x-a_2 t)e^{\eta_2 t}
\end{array}\right\} \tag{4.15}
$$

In terms of the auxiliary variables presented by Leon (2004), the initial conditions are:

$$
ICs: \quad
\begin{array}{l}
u^*(x,0) = u_o^*(x) = \begin{cases} 2 & if\ x \le 0.5 \\ 0 & if\ x > 0.5 \end{cases} \\[2mm]
v^*(x,0) = v_o^*(x) = \begin{cases} 1 & if\ x \le 0.5 \\ 0 & if\ x > 0.5 \end{cases}
\end{array} \tag{4.16}
$$

And using expression (4.14), allow us to write them explicitly as follow.

$$
ICs: \quad
\begin{array}{l}
U_1(x,0) = U_{1_o}(x) = \begin{cases} 3 & if\ x \le 0.5 \\ 0 & if\ x > 0.5 \end{cases} \\[2mm]
U_2(x,0) = U_{2_o}(x) = \begin{cases} 1 & if\ x \le 0.5 \\ 0 & if\ x > 0.5 \end{cases}
\end{array} \tag{4.17}
$$

The system represented by Equations (4.12)-(4.13), with ICs given by (4.17), was solved in the spatial domain [0, 5.0] using 500 cells, and a CFL number 0.2. The constants used are: $a_1 = 1.0$, $a_2 = 2.0$, $\eta_1 = 2.0$, $\eta_2 = 1.0$. The numerical solutions are computed for an output time of 1.5 using the splitting scheme, and they are compared against the exact profiles in Figure 4.10.
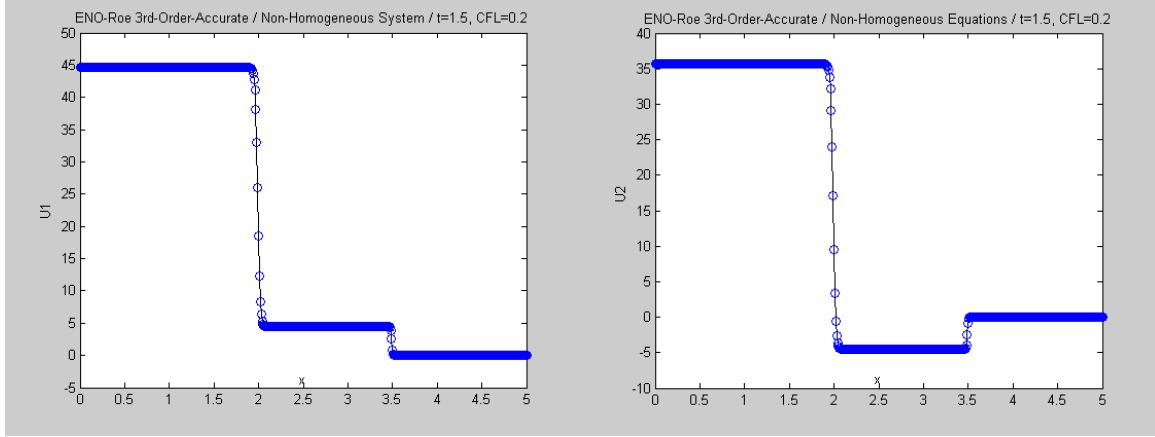
Figure 4.10. Test 7, Comparison between numerical and exact solutions at t=1.5.

4.1.5. Cylindrical One-Dimensional Euler's Equations

Toro (1999) proposed test problems for two-dimensional Euler equations for ideal gases with $\gamma = 1.4$. The geometry and initial conditions for the problem allow simplifying it to a one-dimensional cylindrical problem due to its symmetry, yielding to the following non-homogeneous system of equations (2.8)-(4.18).

$$\vec{U} = \begin{bmatrix} U_1 \\ U_2 \\ U_3 \end{bmatrix} = \begin{bmatrix} \rho \\ \rho u \\ E \end{bmatrix}, \quad \vec{F} = \begin{bmatrix} F_1 \\ F_2 \\ F_3 \end{bmatrix} = \begin{bmatrix} \rho u \\ \rho u^2 + p \\ u(E + p) \end{bmatrix}, \quad \vec{Q} = \begin{bmatrix} Q_1 \\ Q_2 \\ Q_3 \end{bmatrix} = -\frac{1}{r} \begin{bmatrix} \rho u \\ \rho u^2 \\ u(E + p) \end{bmatrix} \quad (4.18)$$

Where r is the radial direction. At this point, the one-dimensional system is solved numerically for two purposes, (1) to asses the performance of the solver when solving non-homogeneous systems, and (2) to provide an accurate numerical solution to compare with the numerical solution of the two-dimensional Euler's equations.

The test, presented in Toro (1999), simulates an explosion in two dimensions. The spatial domain is a 2.0 x 2.0 square in the Cartesian plane. The initial conditions are represented by two areas (Figure 4.11). An inner circular area of radius 0.4 and centered at (1.0,1.0) and the area outside the circle. Two constants states are defined in those areas by Equation 4.19.
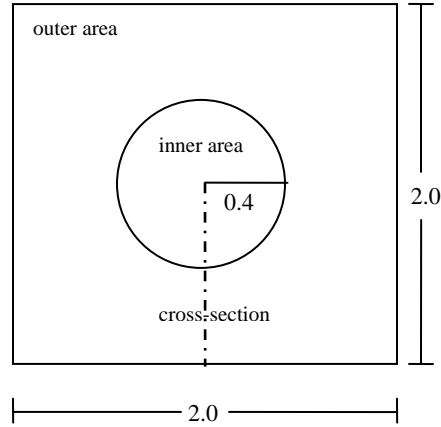
Figure 4.11. Sketch of the initial domain for Test 8.

Figure 4.12 shows the numerical results when solving the problem using the one-dimensional cylindrical equations (4.18) along a cross section that bisect the area. 100 gridpoints were used, and the output time is 0.25. Later, these results will be compared with the ones generated when using the two-dimensional equations in the full domain.
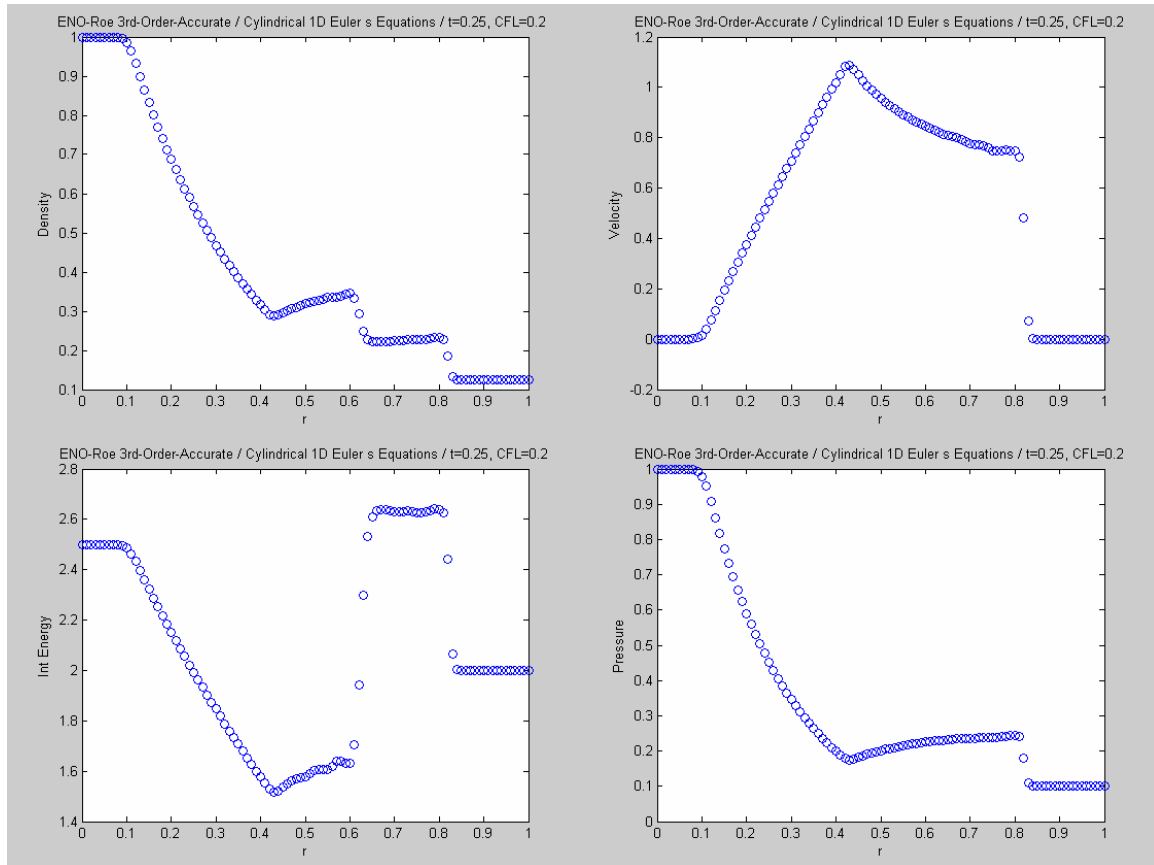
Figure 4.12. Test 8, Numerical Solution at t=0.25.

$$\left.\begin{array}{ll}\rho_{inside}=1.0 & , \quad \rho_{outside}=0.125 \\ v_{x\,inside}=0.0 & , \quad v_{x\,outside}=0.0 \\ v_{y\,inside}=0.0 & , \quad v_{y\,outside}=0.0 \\ p_{inside}=1.0 & , \quad p_{outside}=0.1\end{array}\right\} \tag{4.19}$$

4.2. Application to2-D Problems

4.2.1. Two-Dimensional Burger's Equation

Here the Riemann problem for two space dimensions proposed by Wagner (1983) and used by Shu and Osher (1989) is solved. This generalizes the Riemann problem in one space variable, the study of which has been a key to the understanding of solutions to systems of non-linear hyperbolic conservation laws. The two-dimensional Burger's equation are written as:

$$\frac{\partial U}{\partial t}+\frac{\partial}{\partial x}\left(\frac{U^2}{2}\right)+\frac{\partial}{\partial y}\left(\frac{U^2}{2}\right)=0 \tag{4.20}$$

The problem is solved in a 2.0 x 2.0 square domain divided in four areas. The initial data for the IVP is as follows:

$$U(x,y,0)=\begin{cases}U_1, & x>1, \ y>1 \\ U_2, & x<1, \ y>1 \\ U_3, & x<1, \ y<1 \\ U_4, & x>1, \ y<1\end{cases} \tag{4.21}$$

And, depending on the orders of the $U_i's$, there are eight different solution types. The initial data for the eight tests are presented in table 4.2.

The numerical results were obtained for an output time of 1.0, using 200 gridpoints in each direction, and for a CFL number 0.2. The results for all test are shown in Figures 4.13 to 4.20, and they are comparable with the ones obtained by Shu and Osher (1989).

Table 4.2: Specifications for different tests. 2D Burger's Equation.

Test	U₁	U₂	U₃	U₄
9A	-1.0	-0.2	0.5	0.8
9B	-0.2	-1.0	0.5	0.8
9C	-1.0	0.5	-0.2	0.8
9D	-1.0	-0.2	0.5	0.8
9E	-1.0	-0.2	0.8	0.5
9F	0.8	-1.0	0.2	-0.5
9G	0.8	-1.0	0.5	-0.2
9H	0.8	-0.2	-1.0	0.5
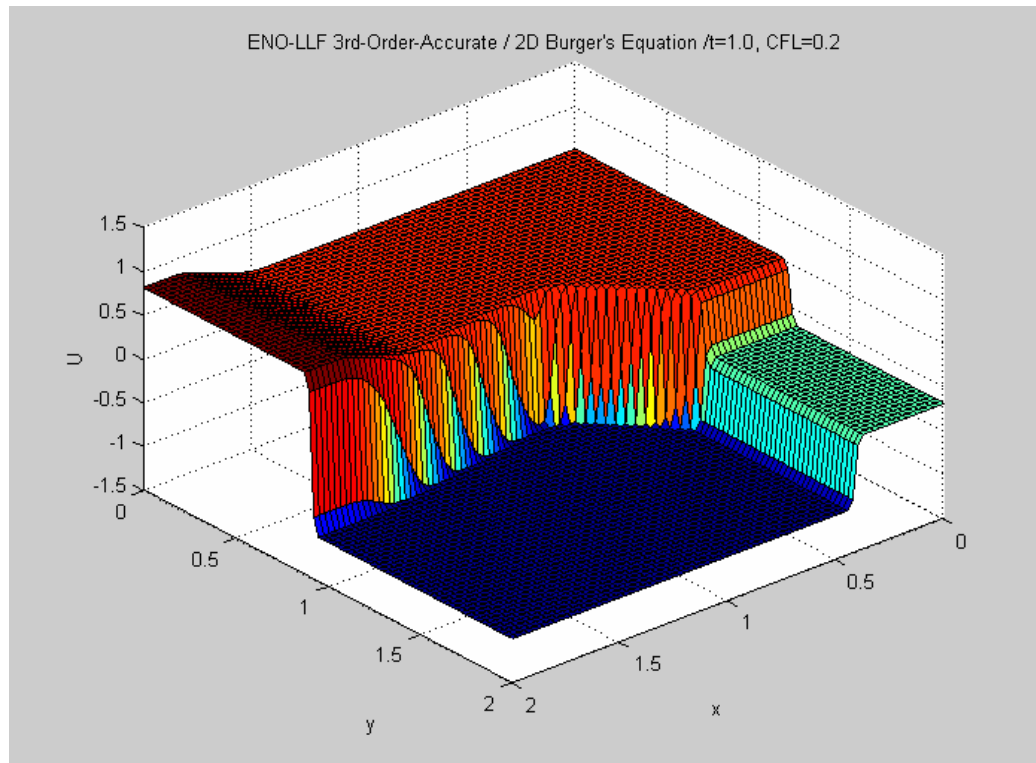
Figure 4.13. Test 9A, Numerical Solution at t=1.0.
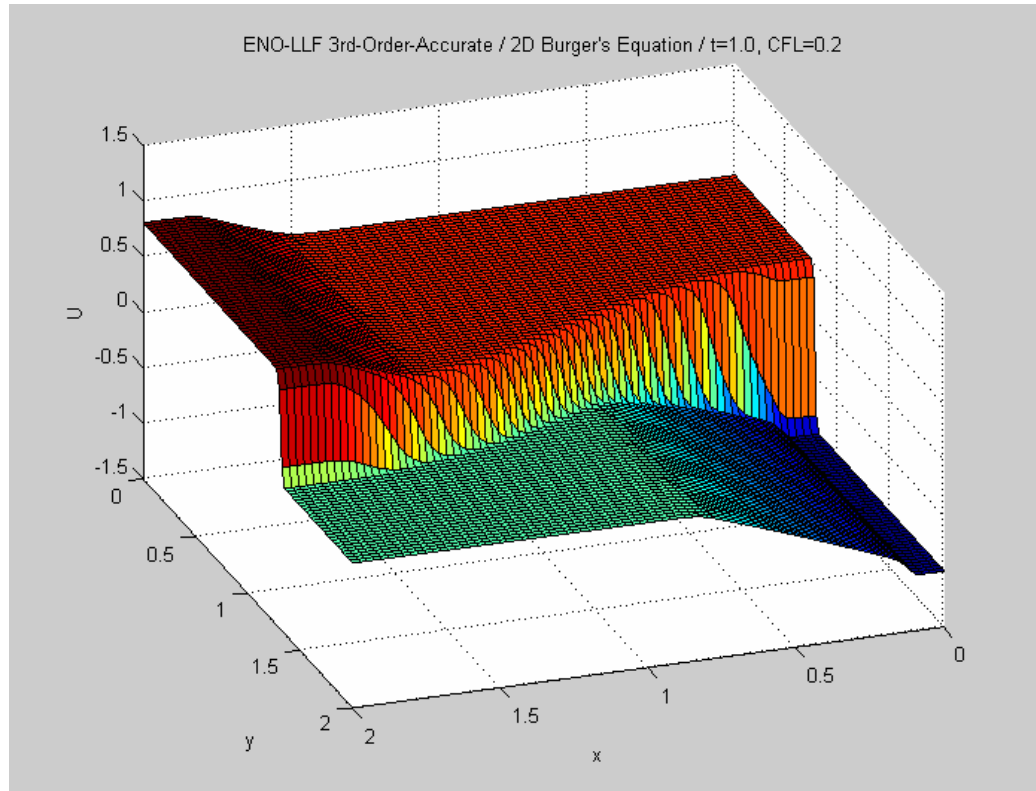
Figure 4.14. Test 9B, Numerical Solution at t=1.0.
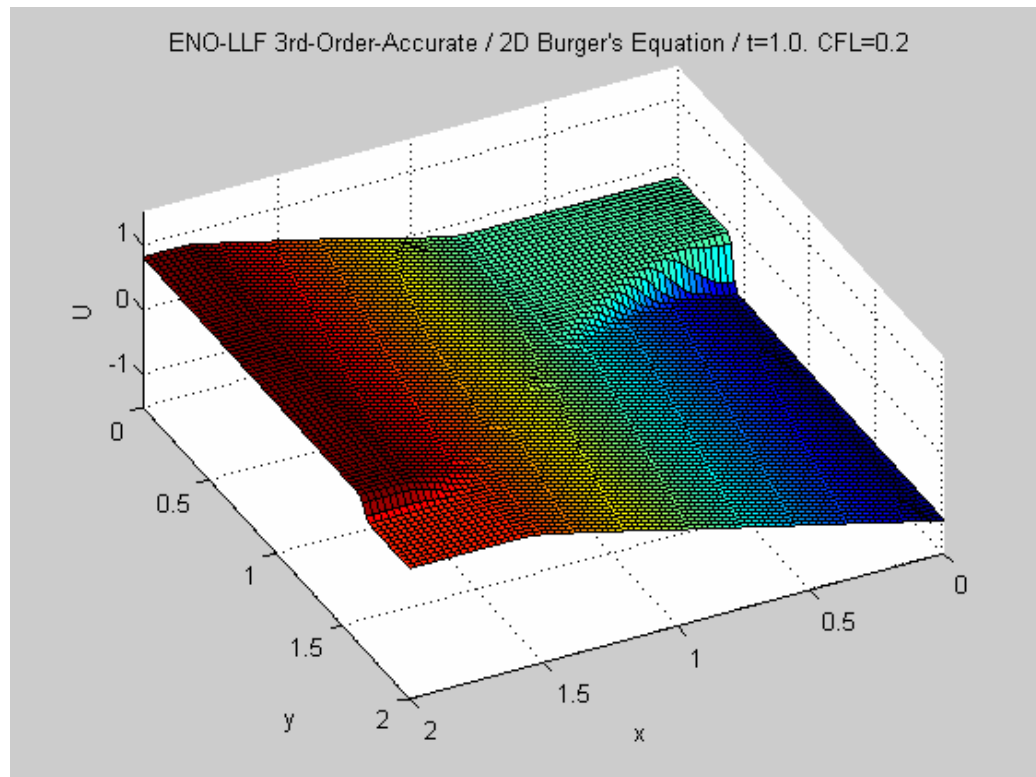
Figure 4.15. Test 9C, Numerical Solution at t=1.0.
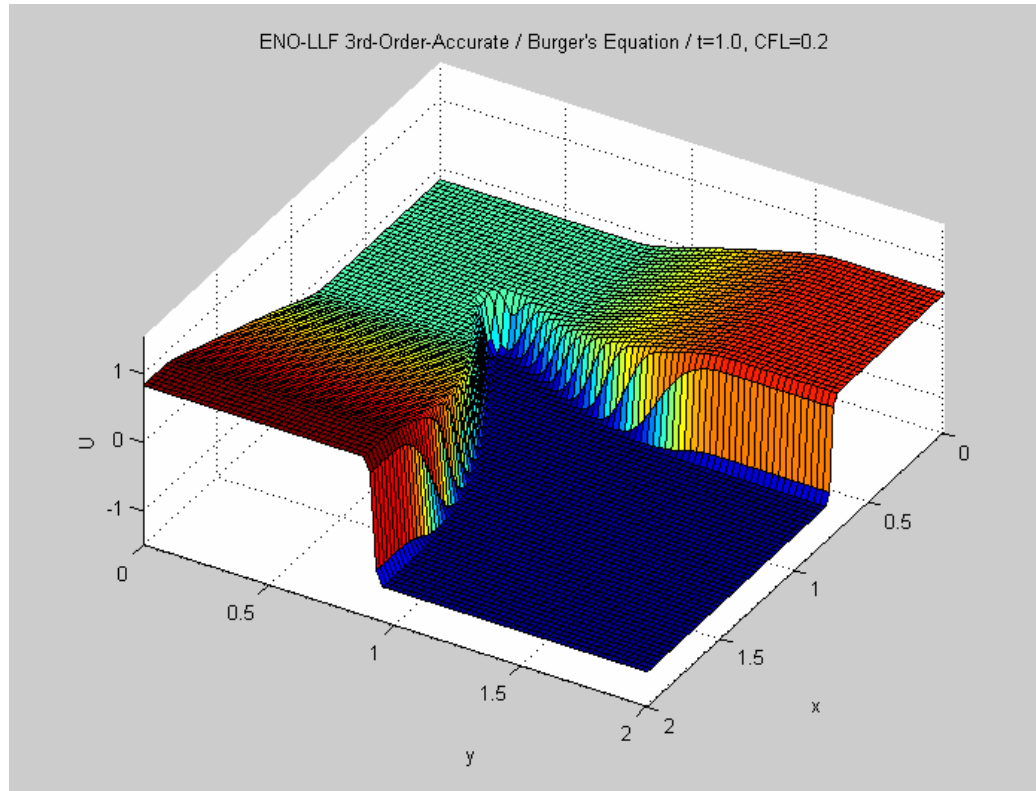
Figure 4.16. Test 9D, Numerical Solution at t=1.0.
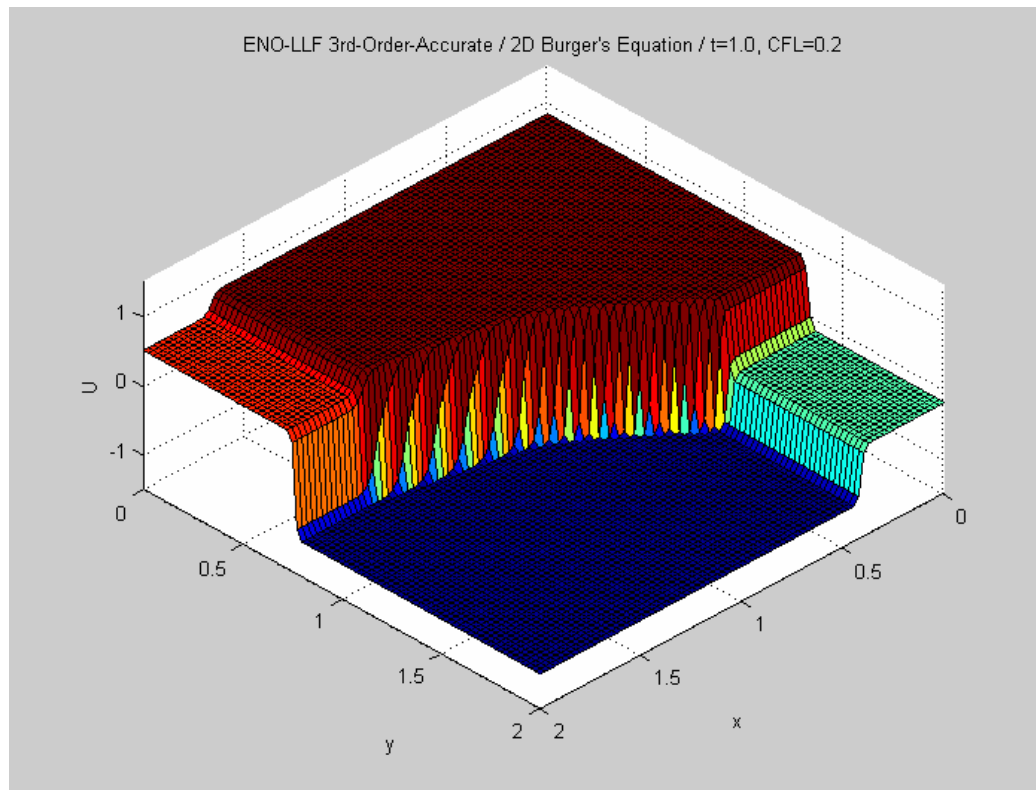
Figure 4.17. Test 9E, Numerical Solution at t=1.0.
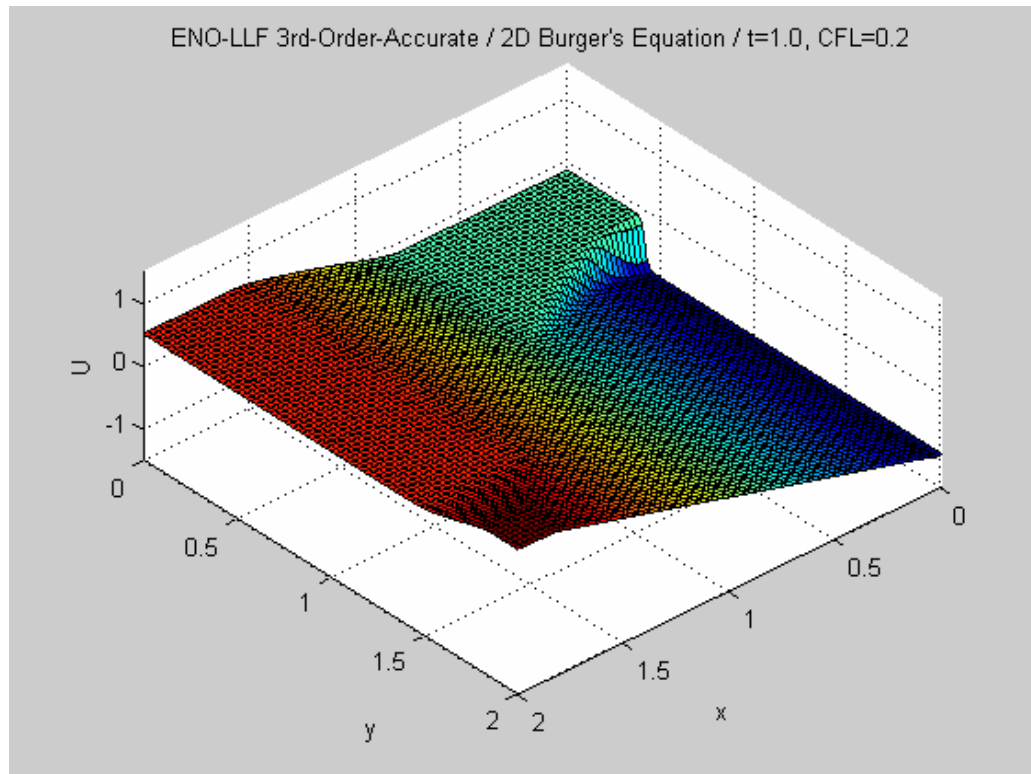
Figure 4.18. Test 9F, Numerical Solution at t=1.0.
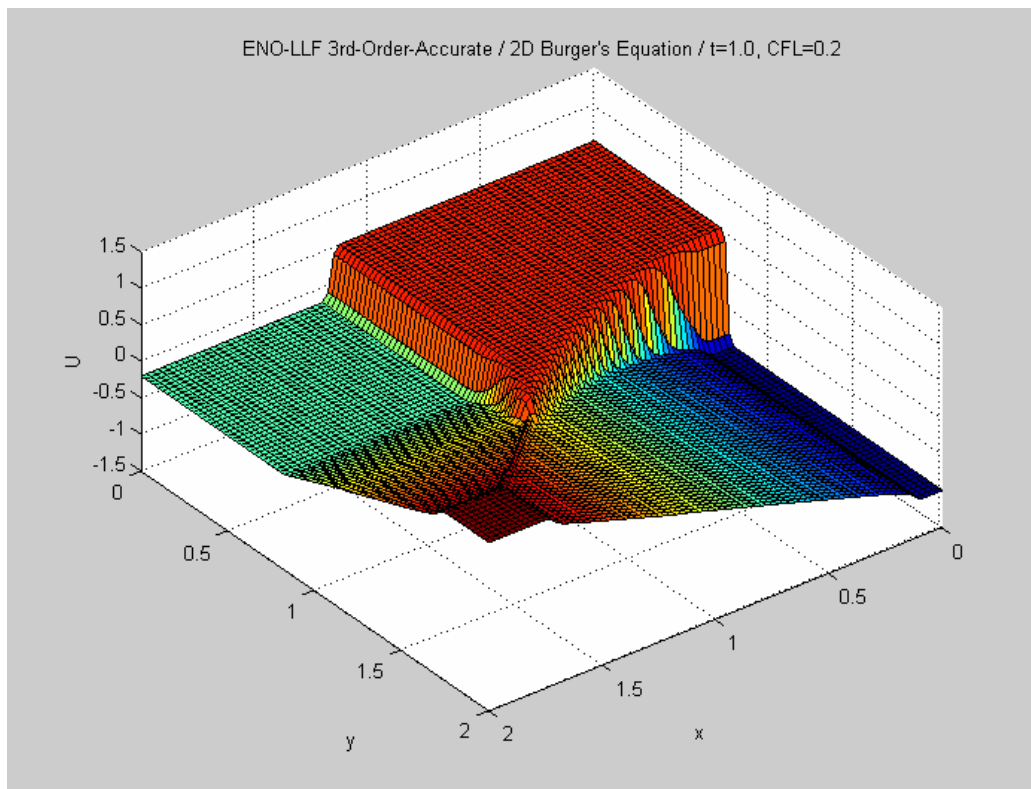
Figure 4.19. Test 9G, Numerical Solution at t=1.0.
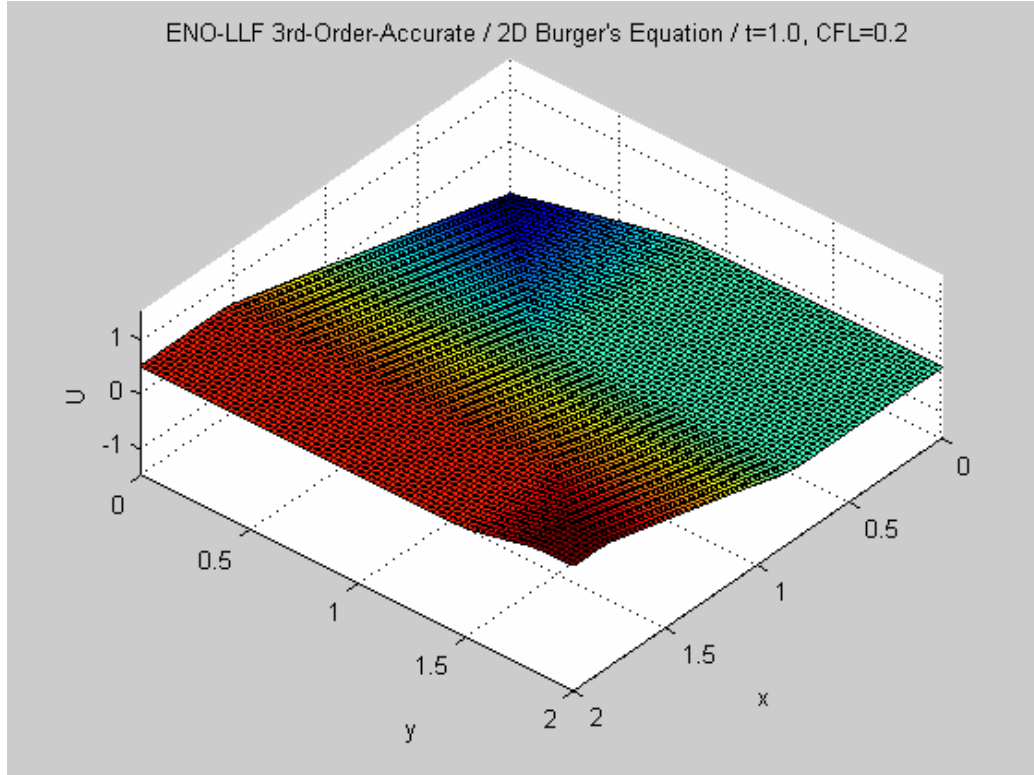
Figure 4.20. Test 9H, Numerical Solution at t=1.0.

4.2.2. Two-Dimensional Euler's Equations

In section 4.3 the one-dimensional Euler's equations were explained. Here we present the two-dimensional case along with some basic properties.

$$\frac{\partial \vec{U}}{\partial x} + \frac{\partial \vec{F}(U)}{\partial x} + \frac{\partial \vec{G}(U)}{\partial y} = 0 \qquad (2.8)$$

where:

$$\vec{U} = \begin{bmatrix} \rho \\ \rho.v_x \\ \rho.v_y \\ E \end{bmatrix}, \quad \vec{F}(\vec{U}) = \begin{bmatrix} \rho.v_x \\ \rho.v_x^2 + p \\ \rho.v_x.v_y \\ (E+p).v_x \end{bmatrix}, \quad \vec{G}(\vec{U}) = \begin{bmatrix} \rho.v_y \\ \rho.v_x.v_y \\ \rho.v_y^2 + p \\ (E+p).v_y \end{bmatrix} \qquad (4.22)$$

All the variables were defined in section 4.3. And the total energy per unit volume is defined as:

$$E = \frac{\rho V^2}{2} + \rho e \qquad (4.23)$$

$$V^2 = (v_x^2 + v_y^2) \qquad (4.24)$$

The two-dimensional version of the explosion problem, presented by Toro (1999), is solved here. Recall that the solution was obtained using the simplified one-dimensional radial equations in Section 4.5. The initial conditions are given by Equation (4.18). Figures 4.21 to 4.25 show the three dimensional view of the numerical results, and they are comparable with the ones obtained by Toro (1999).
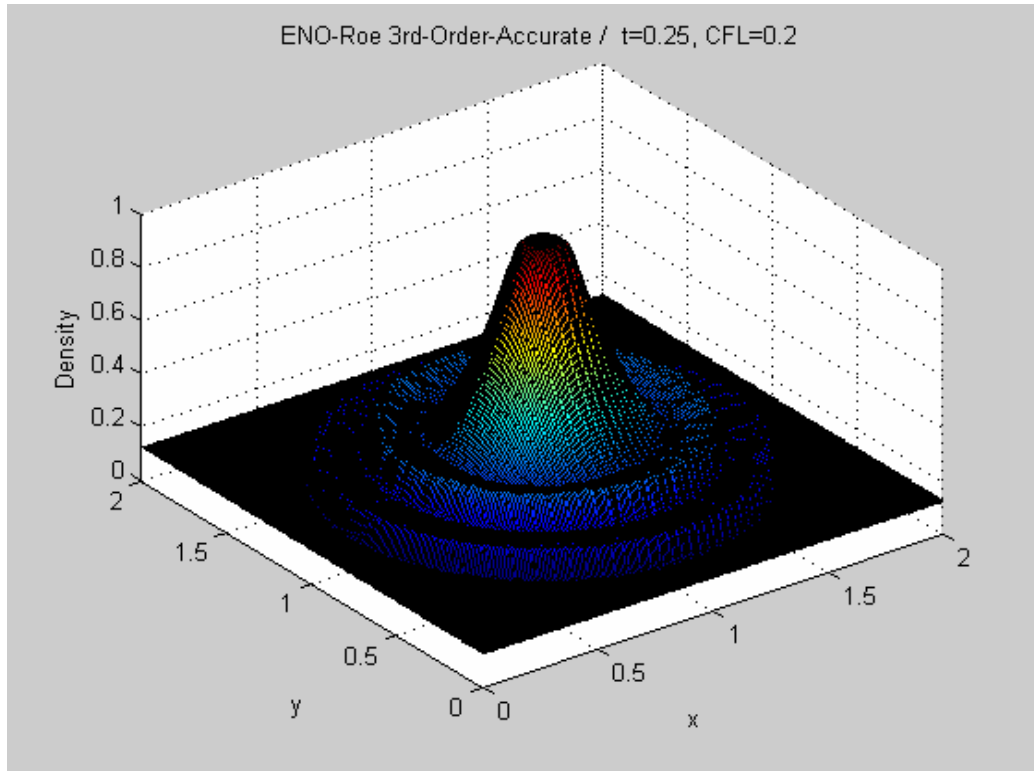
Figure 4.21. Test 10, 3D view of density distribution at t=0.25.
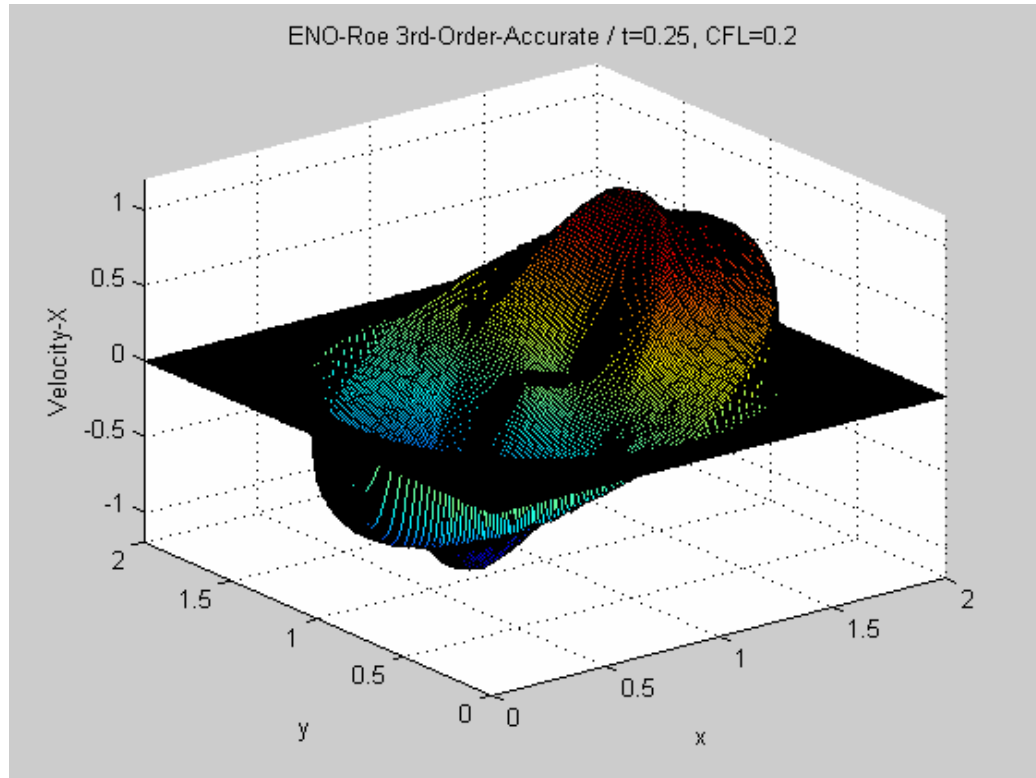
Figure 4.22. Test 10, 3D view of x-velocity distribution at t=0.25.
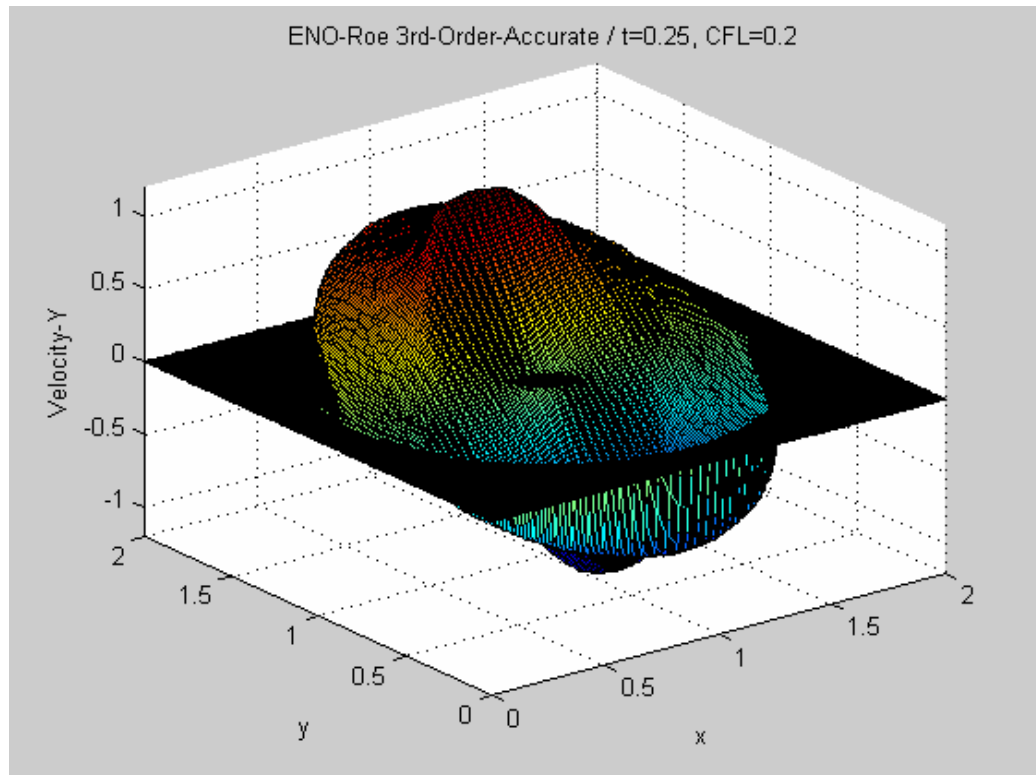
Figure 4.23. Test 10, 3D view of y-velocity distribution at t=0.25.
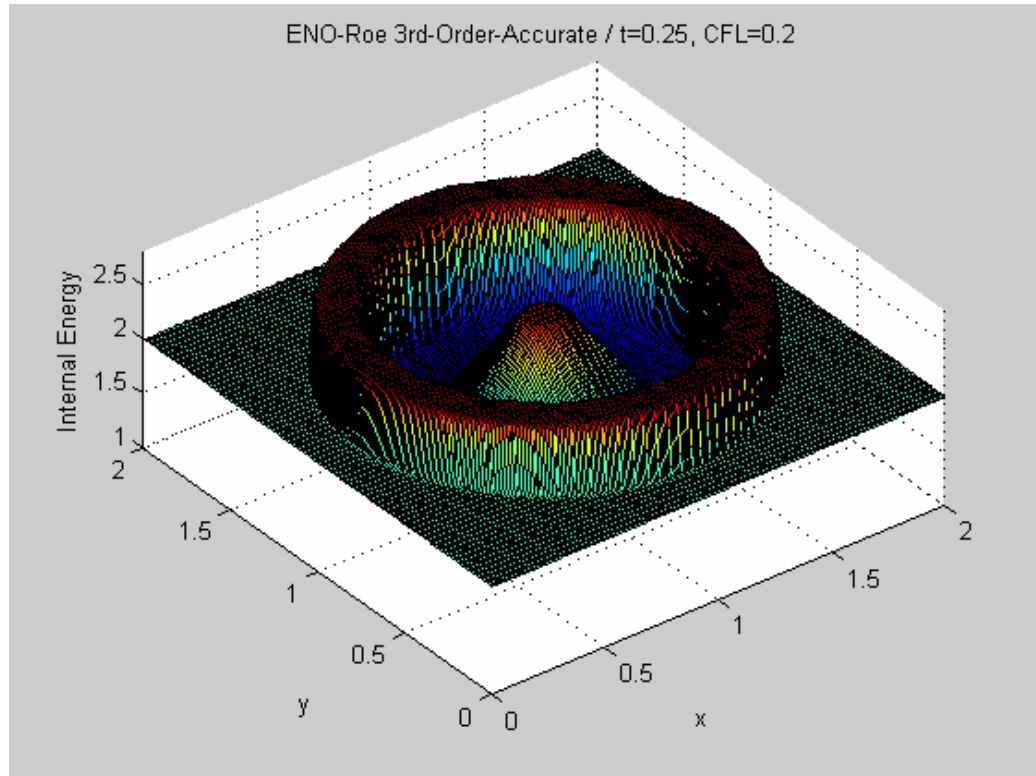
Figure 4.24. Test 10, 3D view of internal energy distribution at t=0.25.
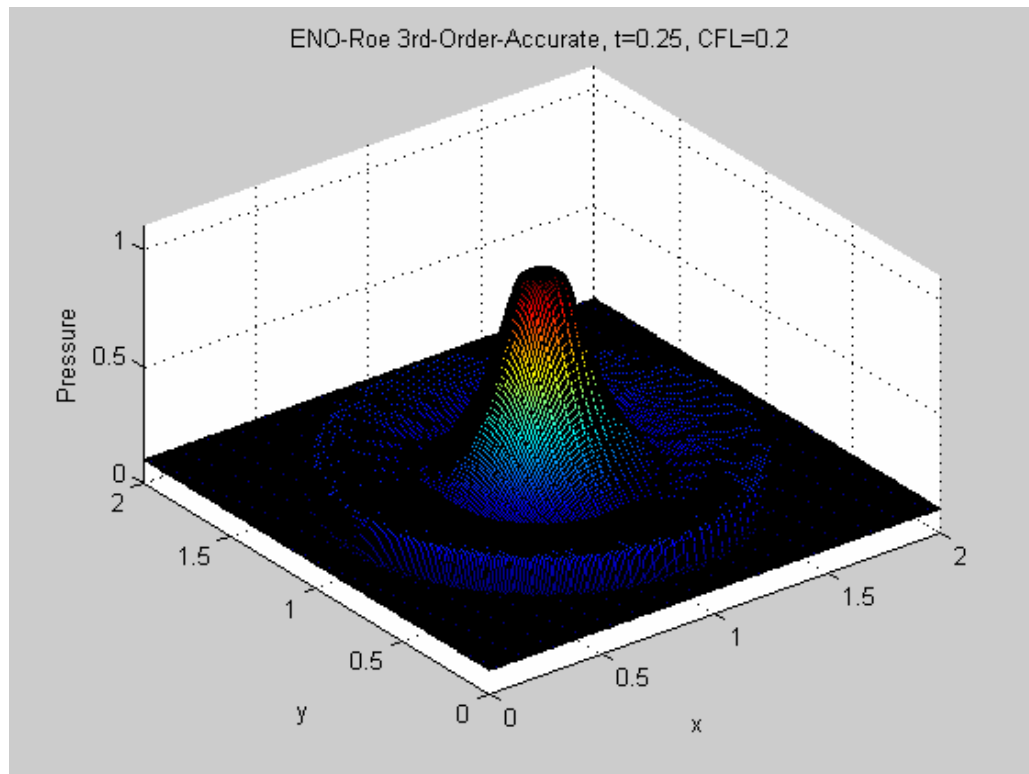
Figure 4.25. Test 10, 3D view of pressure distribution at t=0.25.

For comparison purposes, the solution along a cross section that bisects the area is presented in Figure 4.26. They are in very good agreement with the ones obtained by the one-dimensional cylindrical equations (4.12)-(4.18).
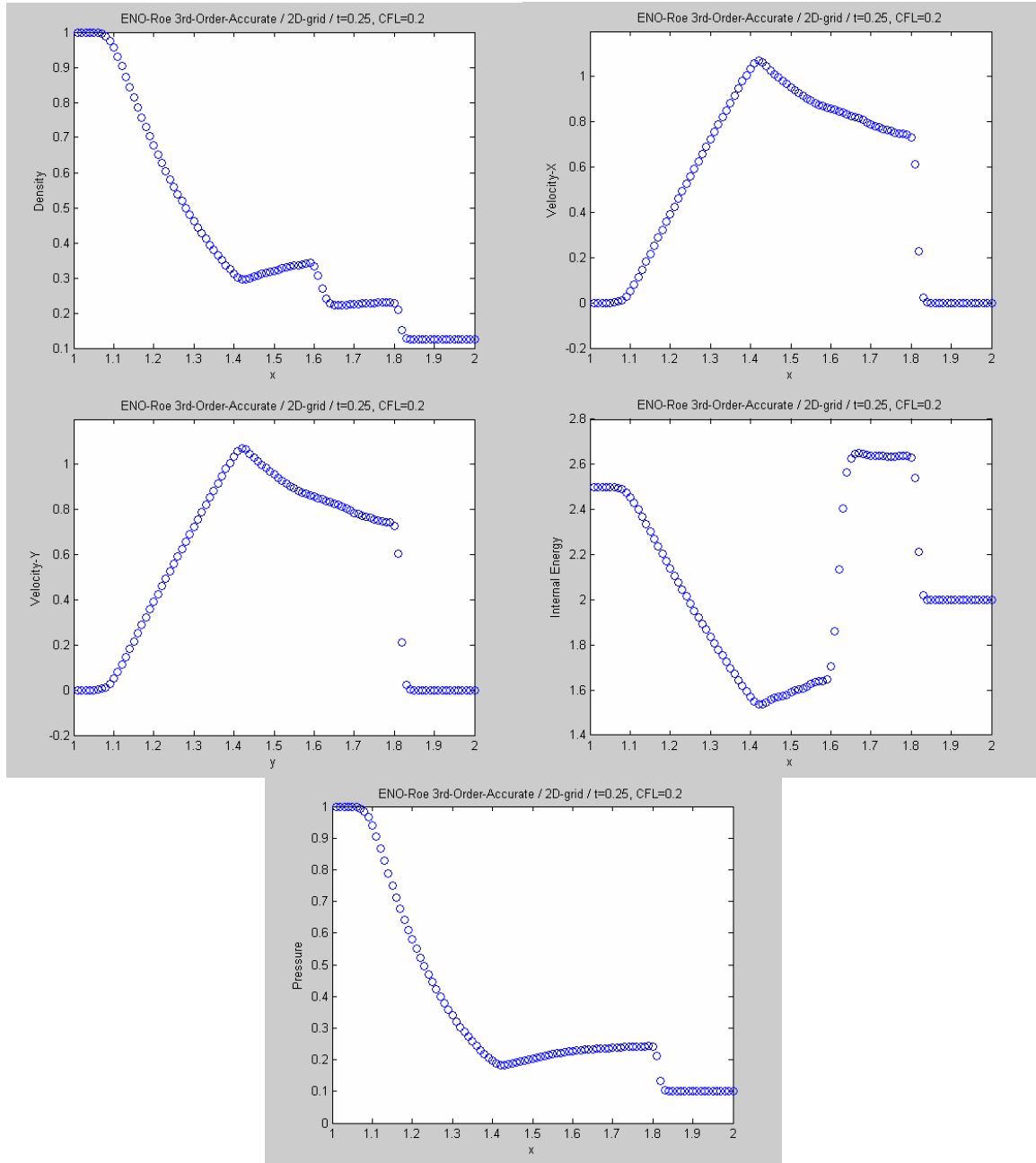
Figure 4.26. Test 10, 2D view of numerical solution at t=0.25.

Chapter 5

DESCRIPTION OF THE CYLINDRICAL MODEL

The complete representation of transient flow through any pipeline can be derived from the general transport equation. The model comprises the laws of conservation of mass, momentum and energy. These equations are written in their conserved form in order to ensure global conservation of the flux variables.

5.1. Conservation Laws in 2D Cylindrical Coordinates

In formulating the fluid flow equations, a cylindrical domain is chosen. Due to symmetry we assume flow in the angular direction to be negligible, and therefore flow is assumed to occur in the radial and axial directions only. Figure 5.1 shows the computational point-distributed grid imposed over the physical domain.
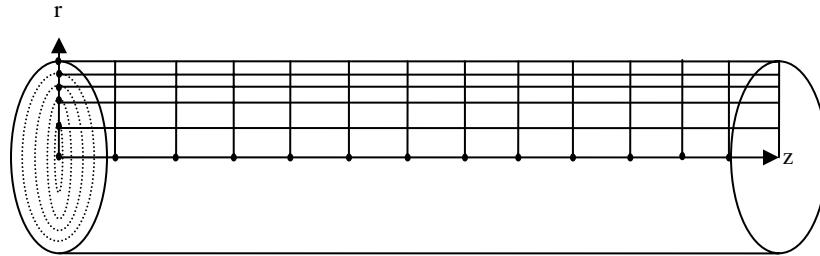
Figure 5.1 Schematic of a 2D Cylindrical Coordinates.

In the case of flow through a pipeline, no slip occurs at the wall of the pipe, and the larger value of velocity is encountered in the axis of the pipe, but since the domain is confined it can not be treated as an external flow, but rather as an internal flow. Moreover, internal flows even with very small viscosities (large Reynolds numbers) have frictional shear stresses of considerable magnitude because of the large velocity gradient across the flow. Therefore we are faced with the reliability of the inviscid Euler equations in appropriately modeling this problem, and hence viscous Navier-Stokes equations are used.

5.1.1. Continuity Equation

The continuity equation is a mathematical description of conservation of mass. In radial coordinates, the continuity equation is given by:

$$\frac{\partial(\rho)}{\partial t} + \frac{1}{r}\frac{\partial(r.\rho.v_r)}{\partial r} + \frac{\partial(\rho.v_z)}{\partial z} = 0 \qquad (5.1)$$

In order to remove the coefficient in the radial spatial derivative, we expand it as:

$$\frac{1}{r}\frac{\partial(r.\rho.v_r)}{\partial r} = \frac{\partial(\rho.v_r)}{\partial r} + \frac{\rho.v_r}{r} \qquad (5.2)$$

to yield:

$$\frac{\partial(\rho)}{\partial t} + \frac{\partial(\rho.v_r)}{\partial r} + \frac{\partial(\rho.v_z)}{\partial z} = -\frac{\rho.v_r}{r} \qquad (5.3)$$

where:

ρ : density, $[\,lbm\,/\,ft^3\,]$

v_r : radial velocity, $[\,ft\,/\,s\,]$

v_z : axial velocity, $[\,ft\,/\,s\,]$

r : radial distance from the pipe axis, $[\,ft\,]$

z : axial distance, $[\,ft\,]$

t : time, $[\,sec\,]$

5.1.2. Momentum Equations

The Newton's second law of motion states that the acceleration of an element is proportional to the net force acting on that element, where the constant of proportionality is the mass of the element. For the two-dimensional system, we have separate mathematical expressions for the momentum in the radial and axial direction:

$$\frac{\partial(\rho.v_r)}{\partial t} + \frac{\partial(\rho.v_r^2 + p)}{\partial r} + \frac{\partial(\rho.v_r.v_z)}{\partial z} = \frac{2\mu}{r}\left[\frac{\partial v_r}{\partial r} - \frac{1}{3}\left(\frac{v_r}{r} + \frac{\partial v_r}{\partial r} + \frac{\partial v_z}{\partial z}\right)\right]$$

$$+ \frac{4}{3}\frac{\partial}{\partial r}\left(\mu\frac{\partial v_r}{\partial r}\right) - \frac{2}{3}\left[\left(\frac{\mu}{r}\frac{\partial v_r}{\partial r} + \frac{\mu v_r}{r^2} + \frac{v_r}{r}\frac{\partial \mu}{\partial r}\right) + \frac{\partial}{\partial r}\left(\mu\frac{\partial v_z}{\partial z}\right)\right] + \frac{\partial \tau_{zr}}{\partial z} - F_{gr}$$

(5.4)

$$\frac{\partial(\rho.v_z)}{\partial t} + \frac{\partial(\rho.v_r.v_z)}{\partial r} + \frac{\partial(\rho.v_z^2 + p)}{\partial z} =$$

$$\left\{\frac{\tau_{rz}}{r} + \frac{\partial \tau_{rz}}{\partial r} + \frac{4}{3}\frac{\partial}{\partial z}\left(\mu\frac{\partial v_z}{\partial z}\right) - \frac{2}{3}\left[\left(\frac{\mu}{r}\frac{\partial v_r}{\partial z} + \frac{v_r}{r}\frac{\partial \mu}{\partial z}\right) + \frac{\partial}{\partial z}\left(\mu\frac{\partial v_r}{\partial r}\right)\right]\right\} - F_{gz}$$

(5.5)

where:

p : pressure, $[lbm/ft.s^2]$

μ : viscosity, $[lbm/ft.s]$

F_{gr} : gravitational force in the r-direction per unit volume, $[lbm/ft^2.s]$

F_{gz} : gravitational force in the z-direction per unit volume, $[lbm/ft^2.s]$

The above are the so called Navier-Stokes equations. They differ from the Euler's equations of motion by the viscous term enclosed in the brackets on the RHS.

5.1.3. Energy Equation

The law of conservation of energy is an extension of the first law of classical thermodynamics, which for open systems allows the exchange of heat, work and mass with its surroundings. Mass carries energy in the form of kinetic and potential energy, as well as energy stored at the molecular level. This molecular energy carried by the mass includes the internal energy and enthalpy due to the work associated with a flow stream which increases the energy content of the flowing mass. The conservation of energy is obtained by taking energy balance in the control volume such as the rate of energy change in it, is equivalent to the sum of the net energy flux into the control volume and the rate of work done on the fluid by the body and surface forces.

For a two-dimensional cylindrical system, the energy balance equation is written as follows:

$$\frac{\partial(E)}{\partial t} + \frac{1}{r}\frac{\partial(r.(E+p)v_r)}{\partial r} + \frac{\partial((E+p)v_z)}{\partial z} = \left[\frac{\partial}{\partial r}\left(k\frac{\partial T}{\partial r}\right) + \frac{k}{r}\frac{\partial T}{\partial r} + \frac{\partial}{\partial z}\left(k\frac{\partial T}{\partial z}\right)\right]$$
$$+ \mu \cdot \left(2\cdot\left[\left(\frac{\partial v_r}{\partial r}\right)^2 + \left(\frac{v_r}{r}\right)^2 + \left(\frac{\partial v_z}{\partial z}\right)^2\right] + \left(\frac{\partial v_r}{\partial z} + \frac{\partial v_z}{\partial r}\right)^2 - \frac{2}{3}\left(\frac{v_r}{r} + \frac{\partial v_r}{\partial r} + \frac{\partial v_z}{\partial z}\right)^2\right)$$

$$(5.6)$$

In order to remove the coefficient of the radial derivative, we expand the spatial derivative in the r-direction as:

$$\frac{1}{r}\frac{\partial(r.(E+p)v_r)}{\partial r} = \frac{1}{r}\left[(E+p)v_r + r\frac{\partial((E+p)v_r)}{\partial r}\right] = \frac{(E+p)v_r}{r} + \frac{\partial((E+p)v_r)}{\partial r}$$

$$(5.7)$$

to yield:

$$\frac{\partial(E)}{\partial t} + \frac{\partial((E+p)v_r)}{\partial r} + \frac{\partial((E+p)v_z)}{\partial z} = -\frac{(E+p)v_r}{r} + \left[\frac{\partial}{\partial r}\left(k\frac{\partial T}{\partial r}\right) + \frac{k}{r}\frac{\partial T}{\partial r} + \frac{\partial}{\partial z}\left(k\frac{\partial T}{\partial z}\right)\right] + \cdots$$
$$\mu \cdot \left(2\cdot\left[\left(\frac{\partial v_r}{\partial r}\right)^2 + \left(\frac{v_r}{r}\right)^2 + \left(\frac{\partial v_z}{\partial z}\right)^2\right] + \left(\frac{\partial v_r}{\partial z} + \frac{\partial v_z}{\partial r}\right)^2 - \frac{2}{3}\left(\frac{v_r}{r} + \frac{\partial v_r}{\partial r} + \frac{\partial v_z}{\partial z}\right)^2\right)$$

$$(5.8)$$

where:

E : total energy per unit volume, $[\,lbm/ft.s^2\,]$

k : thermal conductivity, $[\,lbm.ft/s^3.°C\,]$

T : temperature, $[\,°C\,]$

At this point it is important to point out, that E is defined as the sum of kinetic energy and internal energy. This is:

$$E = \rho\left[\frac{1}{2}\left(v_r^2 + v_z^2\right) + e\right] \qquad (5.9)$$

where:

e : internal energy, $[\,ft^2/s^2\,]$

Note that axial gravity force, F_{gz}, is zero because we consider a horizontal piepeline. The radial component of the gravity force (F_{gr}) is assumed negligible because of the low density of the gas and the small distance represented by the diameter of the pipe compared with the length of the pipe.

5.1.4. Vector Form of the Equations

The conservation laws expressed by Equations (5.3), (5.4), (5.5) and (5.8) can be written in vector form as:

$$\frac{\partial \vec{U}}{\partial t} + \frac{\partial \left(\vec{F}(\vec{U}) \right)}{\partial r} + \frac{\partial \left(\vec{G}(\vec{U}) \right)}{\partial z} = \vec{Q} \tag{5.10}$$

where the conservative variables are:

$$\vec{U} = \begin{bmatrix} U_1 \\ U_2 \\ U_3 \\ U_4 \end{bmatrix} = \begin{bmatrix} \rho \\ \rho.v_r \\ \rho.v_z \\ E \end{bmatrix} \tag{5.11}$$

The physical fluxes are written in terms of the conservative variables:

$$\vec{F} = \begin{bmatrix} F_1 \\ F_2 \\ F_3 \\ F_4 \end{bmatrix} = \begin{bmatrix} \rho.v_r \\ \rho.v_r^2 + p \\ \rho.v_r.v_z \\ (E+p)v_r \end{bmatrix} = \begin{bmatrix} U_2 \\ \frac{U_2^2}{U_1} + p \\ \frac{U_2 U_3}{U_1} \\ (U_4 + p)\frac{U_2}{U_1} \end{bmatrix}, \tag{5.12}$$

$$\vec{G} = \begin{bmatrix} G_1 \\ G_2 \\ G_3 \\ G_4 \end{bmatrix} = \begin{bmatrix} \rho.v_z \\ \rho.v_r.v_z \\ \rho.v_z^2 + p \\ (E+p)v_z \end{bmatrix} = \begin{bmatrix} U_3 \\ \frac{U_2 U_3}{U_1} \\ \frac{U_3^2}{U_1} + p \\ (U_4 + p)\frac{U_3}{U_1} \end{bmatrix} \tag{5.13}$$

And the vector of source terms is:

$$\vec{Q} = \begin{bmatrix} Q_1 \\ Q_2 \\ Q_3 \\ Q_4 \end{bmatrix}$$

$$Q_1 = -\frac{\rho.v_r}{r} \tag{5.14}$$

$$Q_2 = \frac{2\mu}{r}\left[\frac{\partial v_r}{\partial r} - \frac{1}{3}\left(\frac{v_r}{r} + \frac{\partial v_r}{\partial r} + \frac{\partial v_z}{\partial z}\right)\right]$$
$$+ \left\{\frac{4}{3}\frac{\partial}{\partial r}\left(\mu\frac{\partial v_r}{\partial r}\right) - \frac{2}{3}\left[\left(\frac{\mu}{r}\frac{\partial v_r}{\partial r} + \frac{\mu v_r}{r^2} + \frac{v_r}{r}\frac{\partial \mu}{\partial r}\right) + \frac{\partial}{\partial r}\left(\mu\frac{\partial v_z}{\partial z}\right)\right] + \frac{\partial \tau_{zr}}{\partial z}\right\} \tag{5.15}$$

$$Q_3 = \left\{\frac{\tau_{rz}}{r} + \frac{\partial \tau_{rz}}{\partial r} + \frac{4}{3}\frac{\partial}{\partial z}\left(\mu\frac{\partial v_z}{\partial z}\right) - \frac{2}{3}\left[\left(\frac{\mu}{r}\frac{\partial v_r}{\partial z} + \frac{v_r}{r}\frac{\partial \mu}{\partial z}\right) + \frac{\partial}{\partial z}\left(\mu\frac{\partial v_r}{\partial r}\right)\right]\right\} \tag{5.16}$$

$$Q_4 = -\frac{(E+p)v_r}{r} + \left[\frac{\partial}{\partial r}\left(k\frac{\partial T}{\partial r}\right) + \frac{k}{r}\frac{\partial T}{\partial r} + \frac{\partial}{\partial z}\left(k\frac{\partial T}{\partial z}\right)\right] + \cdots$$
$$+ \mu \cdot \left(2\cdot\left[\left(\frac{\partial v_r}{\partial r}\right)^2 + \left(\frac{v_r}{r}\right)^2 + \left(\frac{\partial v_z}{\partial z}\right)^2\right] + \left(\frac{\partial v_r}{\partial z} + \frac{\partial v_z}{\partial r}\right)^2 - \frac{2}{3}\left(\frac{v_r}{r} + \frac{\partial v_r}{\partial r} + \frac{\partial v_z}{\partial z}\right)^2\right) \tag{5.17}$$

5.2. Compressible Filtered Navier-Stokes Equations

For turbulent flows, assuming the continuum hypothesis, the governing equations are the so-called Navier-Stokes equations written as 5.10 to 5.17.

Note that:

$$\sigma_r = \left\{\frac{2\mu}{r}\left[\frac{\partial v_r}{\partial r} - \frac{1}{3}\left(\frac{v_r}{r} + \frac{\partial v_r}{\partial r} + \frac{\partial v_z}{\partial z}\right)\right] + \frac{4}{3}\frac{\partial}{\partial r}\left(\mu\frac{\partial v_r}{\partial r}\right) - \frac{2}{3}\left[\left(\frac{\mu}{r}\frac{\partial v_r}{\partial r} + \frac{\mu v_r}{r^2} + \frac{v_r}{r}\frac{\partial \mu}{\partial r}\right) + \frac{\partial}{\partial r}\left(\mu\frac{\partial v_z}{\partial z}\right)\right] + \frac{\partial \tau_{zr}}{\partial z}\right\} \tag{5.18}$$

$$\sigma_z = \left\{\frac{\tau_{rz}}{r} + \frac{\partial \tau_{rz}}{\partial r} + \frac{4}{3}\frac{\partial}{\partial z}\left(\mu\frac{\partial v_z}{\partial z}\right) - \frac{2}{3}\left[\left(\frac{\mu}{r}\frac{\partial v_r}{\partial z} + \frac{v_r}{r}\frac{\partial \mu}{\partial z}\right) + \frac{\partial}{\partial z}\left(\mu\frac{\partial v_r}{\partial r}\right)\right]\right\} \tag{5.19}$$

$$\tau_{zr} = \tau_{rz} = \mu\left[\frac{\partial v_z}{\partial r} + \frac{\partial v_r}{\partial z}\right] \tag{5.20}$$

$$q = \mu \cdot \left(2 \cdot \left[\left(\frac{\partial v_r}{\partial r}\right)^2 + \left(\frac{v_r}{r}\right)^2 + \left(\frac{\partial v_z}{\partial z}\right)^2\right] + \left(\frac{\partial v_r}{\partial z} + \frac{\partial v_z}{\partial r}\right)^2 - \frac{2}{3}\left(\frac{v_r}{r} + \frac{\partial v_r}{\partial r} + \frac{\partial v_z}{\partial z}\right)^2\right) \tag{5.21}$$

In large-eddy simulation (LES) scales are separated by applying a scale high-pass filter, i.e. low-pass frequency, to the exact solution. This filtering is represented mathematically in physical space as a convolution product (Sagaut, 2002). Any flow variable ϕ is decomposed into a mean and fluctuating part respectively as follows:

$$\phi = \bar{\phi} + \phi' \tag{5.22}$$

where:

$$\bar{\phi} = \int_D G(x - x', \Delta)\phi(x')d^3x' \tag{5.23}$$

G is a filter function which depends on the relative position vector $x - x'$ in the flow domain D and on the computational mesh size Δ. G is usually taken to be a Gaussian distribution in an infinite flow domain or a piecewise continuous distribution of bounded support otherwise. In the limit as Δ approaches zero, Equation (5.23) becomes a Dirac delta sequence.

$$\underset{\Delta \to 0}{Lim} \int_D G(x - x', \Delta)\phi(x')d^3x' = \int_D \delta(x - x')\phi(x')d^3x' = \phi \tag{5.24}$$

where $\delta(x - x')$ is the Dirac delta function (Speziale, 1985). The application of the filter to equations is expressed as:

$$\frac{\partial(\bar{\rho})}{\partial t} + \frac{\partial\left(\overline{\rho.v_r}\right)}{\partial r} + \frac{\partial\left(\overline{\rho.v_z}\right)}{\partial z} = -\frac{\overline{\rho.v_r}}{r} \tag{5.25}$$

$$\frac{\partial\left(\overline{\rho.v_r}\right)}{\partial t} + \frac{\partial\left(\overline{\rho.v_r^2 + \bar{p}}\right)}{\partial r} + \frac{\partial\left(\overline{\rho.v_r.v_z}\right)}{\partial z} = \overline{\sigma_r} \tag{5.26}$$

$$\frac{\partial\left(\overline{\rho.v_z}\right)}{\partial t} + \frac{\partial\left(\overline{\rho.v_r.v_z}\right)}{\partial r} + \frac{\partial\left(\overline{\rho.v_z^2 + \overline{p}}\right)}{\partial z} = \overline{\sigma_z} \tag{5.27}$$

$$\frac{\partial\left(\overline{E}\right)}{\partial t} + \frac{\partial\left(\overline{(E+p)v_r}\right)}{\partial r} + \frac{\partial\left(\overline{(E+p)v_z}\right)}{\partial z} = -\frac{\overline{(E+p)v_r}}{r} + \overline{q} + \left[\frac{\partial}{\partial r}\left(\overline{k\frac{\partial T}{\partial r}}\right) + \frac{k}{r}\overline{\frac{\partial T}{\partial r}} + \frac{\partial}{\partial z}\left(\overline{k\frac{\partial T}{\partial z}}\right)\right] \tag{5.28}$$

In compressible flow, it is convenient to use Favre-filtering to avoid the introduction of subgrid scale (SGS) terms in the equation of conservation of mass. As shown in Piomelli (1998) a Favre-filtered (or density-weighted) variable is defined as:

$$\overline{\overline{f}} = \frac{\overline{\rho f}}{\overline{\rho}} \tag{5.29}$$

Note that:

$$\overline{\rho v_r} = \overline{\rho}\,\overline{\overline{v_r}}, \quad \overline{\rho v_r v_z} = \overline{\rho}\,\overline{\overline{v_r v_z}}, \quad \overline{E} = \overline{\overline{E}}, \quad \overline{(E+p)v_r} = \overline{\overline{v_r E}} + \overline{v_r p} \tag{5.30}$$

The Favre-filtered equations of motion can be written in the form:

$$\frac{\partial\left(\overline{\rho}\right)}{\partial t} + \frac{\partial\left(\overline{\rho}.\overline{\overline{v_r}}\right)}{\partial r} + \frac{\partial\left(\overline{\rho}.\overline{\overline{v_z}}\right)}{\partial z} = -\frac{\overline{\rho}.\overline{\overline{v_r}}}{r} \tag{5.31}$$

$$\frac{\partial\left(\overline{\rho}.\overline{\overline{v_r}}\right)}{\partial t} + \frac{\partial\left(\overline{\rho}.\overline{\overline{v_r.v_r}} + \overline{p}\right)}{\partial r} + \frac{\partial\left(\overline{\rho}.\overline{\overline{v_r.v_z}}\right)}{\partial z} = \overline{\overline{\sigma_r}} - F_{gr} \tag{5.32}$$

$$\frac{\partial\left(\overline{\rho}.\overline{\overline{v_z}}\right)}{\partial t} + \frac{\partial\left(\overline{\rho}.\overline{\overline{v_r.v_z}}\right)}{\partial r} + \frac{\partial\left(\overline{\rho}.\overline{\overline{v_z.v_z}} + \overline{p}\right)}{\partial z} = \overline{\overline{\sigma_z}} - F_{gz} \tag{5.33}$$

$$\frac{\partial\left(\overline{\overline{E}}\right)}{\partial t} + \frac{\partial\left(\overline{\overline{v_r E}} + \overline{v_r p}\right)}{\partial r} + \frac{\partial\left(\overline{\overline{v_z E}} + \overline{v_z p}\right)}{\partial z} = -\frac{\overline{\overline{v_r E}} + \overline{v_r p}}{r} + \overline{q} + \left[\frac{\partial}{\partial r}\left(\overline{k\frac{\partial T}{\partial r}}\right) + \frac{k}{r}\overline{\frac{\partial T}{\partial r}} + \frac{\partial}{\partial z}\left(\overline{k\frac{\partial T}{\partial z}}\right)\right] \tag{5.34}$$

Now, expressing the non-linear terms in the summation form (Erlebacher et al., 1992) and considering Equation (5.30) we have:

$$\overline{\overline{\rho v_r v_z}} = \overline{\rho} \left(\overline{\overline{\overline{v_r + v_r{'}}}} \right) \left(\overline{\overline{\overline{v_z + v_z{'}}}} \right) \tag{5.35}$$

$$\overline{\overline{\rho v_r v_z}} = \overline{\overline{\overline{\rho v_r v_z}}} + \overline{\overline{\overline{\rho v_r v_z{'}}}} + \overline{\overline{\overline{\rho v_r{'} v_z}}} + \overline{\overline{\rho v_r{'} v_z{'}}} \tag{5.36}$$

The non-linear terms can now be written entirely as a function of the filtered quantity and the fluctuation. Now, the triple or Leonard decomposition consists of considering that it is possible to evaluate the terms directly from the filtered variables, Leonard (1974) defined a subgrid tensor that represents interactions among the large scales:

$$L_{rz} = \overline{\overline{\overline{\rho v_r v_z}}} - \overline{\overline{\rho v_r v_z}} \tag{5.37}$$

The cross-stress tensor, which represents the interactions between large and small scales, and the Reynolds subgrid tensor, which reflects the interactions between subgrid scales are respectively defined as:

$$C_{rz} = \overline{\overline{\overline{\rho v_r v_z{'}}}} + \overline{\overline{\overline{\rho v_r{'} v_z}}} \tag{5.38}$$

$$R_{rz} = \overline{\overline{\rho v_r{'} v_z{'}}} \tag{5.39}$$

And now we have the total subgrid tensor defined as:

$$\Psi_{rz} = L_{rz} + C_{rz} + R_{rz} = \overline{\overline{\rho v_r v_z}} - \overline{\overline{\rho v_r v_z}} \tag{5.40}$$

The same decomposition is applied to the terms in the energy equations, and after the triple decomposition the filtered Navier-Stokes equations become:

$$\frac{\partial (\overline{\rho})}{\partial t} + \frac{\partial \left(\overline{\rho . \overline{v_r}} \right)}{\partial r} + \frac{\partial \left(\overline{\rho . \overline{v_z}} \right)}{\partial z} = -\frac{\overline{\rho . \overline{v_r}}}{r} \tag{5.41}$$

$$\frac{\partial \left(\overline{\rho . \overline{v_r}} \right)}{\partial t} + \frac{\partial \left(\overline{\rho . \overline{v_r} . \overline{v_r}} + \overline{p} \right)}{\partial r} + \frac{\partial \left(\overline{\rho . \overline{v_r} . \overline{v_z}} \right)}{\partial z} = \overline{\overline{\sigma}}_r - \frac{\partial \Psi_{rr}}{\partial r} - \frac{\partial \Psi_{rz}}{\partial z} - F_{gr} \tag{5.42}$$

$$\frac{\partial \left(\overline{\rho . \overline{v_z}} \right)}{\partial t} + \frac{\partial \left(\overline{\rho . \overline{v_r} . \overline{v_z}} \right)}{\partial r} + \frac{\partial \left(\overline{\rho . \overline{v_z} . \overline{v_z}} + \overline{p} \right)}{\partial z} = \overline{\overline{\sigma}}_z - \frac{\partial \Psi_{rz}}{\partial r} - \frac{\partial \Psi_{zz}}{\partial z} - F_{gz} \tag{5.43}$$

$$\frac{\partial\left(\overline{\overline{E}}\right)}{\partial t} + \frac{\partial\left(\overline{\overline{v_r.\overline{\overline{E}} + \overline{\overline{v}}_r\overline{\overline{p}}}}\right)}{\partial r} + \frac{\partial\left(\overline{\overline{v_z.\overline{\overline{E}} + \overline{\overline{v}}_z\overline{\overline{p}}}}\right)}{\partial z} = -\frac{\overline{\overline{v_r.\overline{\overline{E}} + \overline{\overline{v}}_r\overline{\overline{p}}}}}{r} + \overline{\overline{q}} + \left[\frac{\partial}{\partial r}\left(\overline{\overline{k}}\frac{\partial\overline{\overline{T}}}{\partial r}\right) + \frac{\overline{\overline{k}}}{r}\frac{\partial\overline{\overline{T}}}{\partial r} + \frac{\partial}{\partial z}\left(\overline{\overline{k}}\frac{\partial\overline{\overline{T}}}{\partial z}\right)\right] + \cdots$$

$$-\frac{\overline{\overline{v_r.\overline{E}}} - \overline{\overline{v}}_r.\overline{\overline{E}}}{r} - \frac{\overline{\overline{v_r p}} - \overline{\overline{v}}_r\overline{\overline{p}}}{r} - \underbrace{\frac{\partial\left(\overline{\overline{v_r.\overline{E}}} - \overline{\overline{v}}_r.\overline{\overline{E}}\right)}{\partial r} - \frac{\partial\left(\overline{\overline{v_z.\overline{E}}} - \overline{\overline{v}}_z.\overline{\overline{E}}\right)}{\partial z}}_{\text{SGS convective terms}} - \underbrace{\frac{\partial\left(\overline{\overline{v_r p}} - \overline{\overline{v}}_r\overline{\overline{p}}\right)}{\partial r} - \frac{\partial\left(\overline{\overline{v_z p}} - \overline{\overline{v}}_z\overline{\overline{p}}\right)}{\partial z}}_{\text{SGS pressure−dilatation term}} + \cdots$$

$$\underbrace{\left(\overline{q} - \overline{\overline{q}}\right)}_{\text{SGS viscous term}} + \underbrace{\left(\left[\frac{\partial}{\partial r}\left(\overline{k\frac{\partial T}{\partial r}}\right) - \frac{\partial}{\partial r}\left(\overline{\overline{k}}\frac{\partial\overline{\overline{T}}}{\partial r}\right)\right] + \left(\frac{\overline{k\frac{\partial T}{r\,\partial r}}} - \frac{\overline{\overline{k}}}{r}\frac{\partial\overline{\overline{T}}}{\partial r}\right) + \left[\frac{\partial}{\partial z}\left(\overline{k\frac{\partial T}{\partial z}}\right) - \frac{\partial}{\partial z}\left(\overline{\overline{k}}\frac{\partial\overline{\overline{T}}}{\partial z}\right)\right]\right)}_{\text{SGS heat−flux term}}$$

$$(5.44)$$

Note that $\overline{\overline{\sigma}}_r$, $\overline{\overline{\sigma}}_z$ and $\overline{\overline{q}}$ are defined as Equations 5.18 to 5.21, except that all constituent variables are replaced with their Favre-filtered counterparts.

5.2.1. Closure of the Momentum Equations

To apply the dynamic model concept (Liu, Meneveau and Katz, 1994) we use the spectral data contained in the resolved field by introducing a "test filter" (Moin et al., 1991). The width of the test filter is denoted by $\hat{\Delta}$ and the test filter stresses ψ_{rz} is defined by analogy to SGS stresses Ψ_{rz} as:

$$\psi_{rz} = \overline{\hat{\rho v_r v_z}} - \frac{\overline{\hat{\rho v_r}}\,\overline{\hat{\rho v_z}}}{\hat{\rho}} \qquad (5.45)$$

The test filter is applied to the resolved field, thus quantities with the hat, $\hat{}$, are the filtered flow variables obtained from the computed field. Using Germano's identity (Germano, 1992), the Leonard stresses can be expressed in terms of ψ_{rz} and Ψ_{rz} as:

$$\ell m_{rz} = \psi_{rz} - \Psi_{rz} \qquad (5.46)$$

Applying the definitions given by Equation (5.40) we have:

$$\ell m_{rz} = \left(\overline{\widehat{\rho v_r v_z}} - \frac{\overline{\widehat{\rho v_r}}\,\overline{\widehat{\rho v_z}}}{\overline{\widehat{\rho}}} \right) - \left(\overline{\widehat{\rho \overline{v_r v_z}}} - \overline{\widehat{\rho}}\,\overline{\widehat{\overline{v_r}\,\overline{v_z}}} \right) = \overline{\widehat{\rho}}\,\overline{\widehat{\overline{v_r}\,\overline{v_z}}} - \frac{\overline{\widehat{\rho v_r}}\,\overline{\widehat{\rho v_z}}}{\overline{\widehat{\rho}}} \tag{5.47}$$

which is completely computable from the resolved variables.

5.2.2. Closure of the Energy Equation

With respect to the SGS pressure-dilatation terms in the energy equation, this study follows the approach of Erlebacher *et al* (1992) in a way that when writing them as a function of temperature by means of an EOS, they represent the contribution of the dilatation of the small scales to the internal energy variation of the fluid and this effect is expected to be small as shown by direct numerical simulations performed by Sarkar *et al* (1991), so the terms are neglected. Comte and Lesieur (1998) also neglected these terms for high Reynolds numbers.

Previous studies (Vreman, 1994 and Piomelli, 1998) neglected the effect of the SGS heat-flux terms because compared to the other SGS terms, this contribution is negligible as has been verified with priori tests. The same conclusion was made by Vreman (1994) when considering the SGS viscous terms, while Comte and Lesieur (1998) did the same for high Reynolds numbers. The filtered energy equation is simplified to:

$$\frac{\partial \left(\overline{\overline{E}} \right)}{\partial t} + \frac{\partial \left(\overline{\overline{v_r}}.\overline{\overline{E}} + \overline{\overline{v_r}}\,\overline{p} \right)}{\partial r} + \frac{\partial \left(\overline{\overline{v_z}}.\overline{\overline{E}} + \overline{\overline{v_z}}\,\overline{p} \right)}{\partial z} = - \frac{\overline{\overline{v_r}}.\overline{\overline{E}} + \overline{\overline{v_r}}\,\overline{p}}{r} + \overline{\overline{q}} + \left[\frac{\partial}{\partial r} \left(\overline{\overline{k}} \frac{\partial \overline{\overline{T}}}{\partial r} \right) + \frac{\overline{\overline{k}}}{r} \frac{\partial \overline{\overline{T}}}{\partial r} + \frac{\partial}{\partial z} \left(\overline{\overline{k}} \frac{\partial \overline{\overline{T}}}{\partial z} \right) \right] - \cdots$$

$$\underbrace{\frac{\partial \left(\overline{\overline{v_r.E}} - \overline{\overline{v_r}}.\overline{\overline{E}} \right)}{\partial r} - \frac{\partial \left(\overline{\overline{v_z.E}} - \overline{\overline{v_z}}.\overline{\overline{E}} \right)}{\partial z}}_{SGS\ convective\ terms} - \frac{\overline{\overline{v_r.E}} - \overline{\overline{v_r}}.\overline{\overline{E}}}{r}$$

$$\tag{5.48}$$

Therefore, for closure we need to model the convective terms. Applying the dynamic similarity model proposed by Liu, Meneveau and Katz (1994) and presented in Sagaut (2002), which introduces a test filter and following the same approach used to close the momentum equations, we obtain:

$$\ell e_r = \overline{\overline{\widehat{v_r.E}}} - \overline{\overline{\widehat{v_r}}}.\overline{\overline{\widehat{E}}} \tag{5.49}$$

$$\ell e_z = \overline{\overline{v}}_z . \overline{\overline{\hat{E}}} - \overline{\overline{v}}_z . \overline{\hat{E}}$$

(5.50)

Note that these terms are completely computable from the resolved variables. The final set of filtered equations can be expressed as:

$$\frac{\partial(\bar{\rho})}{\partial t} + \frac{\partial\left(\bar{\rho}.\overline{\overline{v}}_r\right)}{\partial r} + \frac{\partial\left(\bar{\rho}.\overline{\overline{v}}_z\right)}{\partial z} = -\frac{\bar{\rho}.\overline{\overline{v}}_r}{r}$$

(5.51)

$$\frac{\partial\left(\bar{\rho}.\overline{\overline{v}}_r\right)}{\partial t} + \frac{\partial\left(\bar{\rho}.\overline{\overline{v}}_r.\overline{\overline{v}}_r + \bar{p}\right)}{\partial r} + \frac{\partial\left(\bar{\rho}.\overline{\overline{v}}_r.\overline{\overline{v}}_z\right)}{\partial z} = \overline{\overline{\sigma}}_r - \frac{\partial(\ell m_{rr})}{\partial r} - \frac{\partial(\ell m_{rz})}{\partial z} - F_{gr}$$

(5.52)

$$\frac{\partial\left(\bar{\rho}.\overline{\overline{v}}_z\right)}{\partial t} + \frac{\partial\left(\bar{\rho}.\overline{\overline{v}}_r.\overline{\overline{v}}_z\right)}{\partial r} + \frac{\partial\left(\bar{\rho}.\overline{\overline{v}}_z.\overline{\overline{v}}_z + \bar{p}\right)}{\partial z} = \overline{\overline{\sigma}}_z - \frac{\partial(\ell m_{rz})}{\partial r} - \frac{\partial(\ell m_{zz})}{\partial z} - F_{gz}$$

(5.53)

$$\frac{\partial\left(\overline{\overline{E}}\right)}{\partial t} + \frac{\partial\left(\overline{\overline{v}}_r.\overline{\overline{E}} + \overline{\overline{v}}_r\bar{p}\right)}{\partial r} + \frac{\partial\left(\overline{\overline{v}}_z.\overline{\overline{E}} + \overline{\overline{v}}_z\bar{p}\right)}{\partial z} = -\frac{\overline{\overline{v}}_r.\overline{\overline{E}} + \overline{\overline{v}}_r\bar{p}}{r} + \overline{\overline{q}} + \left[\frac{\partial}{\partial r}\left(\overline{\overline{k}}\frac{\partial\overline{\overline{T}}}{\partial r}\right) + \frac{\overline{\overline{k}}}{r}\frac{\partial\overline{\overline{T}}}{\partial r} + \frac{\partial}{\partial z}\left(\overline{\overline{k}}\frac{\partial\overline{\overline{T}}}{\partial z}\right)\right] - \cdots$$

$$\frac{\partial(\ell e_r)}{\partial r} - \frac{\partial(\ell e_z)}{\partial z} - \frac{\ell e_r}{r}$$

(5.54)

Note that the system of equations (5.54) can be written in the conservative form (2.8) and is solved using the generalized solver presented in Chapter 3.

5.3. Eigenstructure of the System

For classical problems, the eigenstructure of the system is well known. However, for most general problems, no analytical expressions can be devised to obtain the eigenvalues and corresponding eigenvectors. In such cases one option is to generate them numerically.

The Jacobian matrices are obtained numerically. The key ingredient of this approach is the calculation of the pressure partial derivatives which is done in such a way that allow us to use any EOS. This procedure removes the traditional assumption of an ideal gas and the use of the caloric EOS. Therefore, any fluid can now be modeled by the governing equations by just selecting the adequate EOS. The description of the approach follows.

5.3.1. Jacobian Matrix in the r-direction

Having the flux functions written in terms of the conserved variables, the Jacobian matrix is defined as:

$$J_r = \frac{\partial \vec{F}(\vec{U})}{\partial \vec{U}} = \begin{bmatrix} \dfrac{\partial F_1}{\partial U_1} & \dfrac{\partial F_1}{\partial U_2} & \dfrac{\partial F_1}{\partial U_3} & \dfrac{\partial F_1}{\partial U_4} \\[2mm] \dfrac{\partial F_2}{\partial U_1} & \dfrac{\partial F_2}{\partial U_2} & \dfrac{\partial F_2}{\partial U_3} & \dfrac{\partial F_2}{\partial U_4} \\[2mm] \dfrac{\partial F_3}{\partial U_1} & \dfrac{\partial F_3}{\partial U_2} & \dfrac{\partial F_3}{\partial U_3} & \dfrac{\partial F_3}{\partial U_4} \\[2mm] \dfrac{\partial F_4}{\partial U_1} & \dfrac{\partial F_4}{\partial U_2} & \dfrac{\partial F_4}{\partial U_3} & \dfrac{\partial F_4}{\partial U_4} \end{bmatrix} \tag{5.55}$$

The entries of the Jacobian are:

$$\frac{\partial F_1}{\partial U_1} = 0, \quad \frac{\partial F_1}{\partial U_2} = 1, \quad \frac{\partial F_1}{\partial U_3} = 0, \quad \frac{\partial F_1}{\partial U_4} = 0$$

$$\frac{\partial F_2}{\partial U_1} = -\frac{U_2^2}{U_1^2} + \frac{\partial p}{\partial U_1}, \quad \frac{\partial F_2}{\partial U_2} = \frac{2U_2}{U_1} + \frac{\partial p}{\partial U_2}, \quad \frac{\partial F_2}{\partial U_3} = \frac{\partial p}{\partial U_3}, \quad \frac{\partial F_2}{\partial U_4} = \frac{\partial p}{\partial U_4}$$

$$\frac{\partial F_3}{\partial U_1} = -\frac{U_2 U_3}{U_1^2}, \quad \frac{\partial F_3}{\partial U_2} = \frac{U_3}{U_1}, \quad \frac{\partial F_3}{\partial U_3} = \frac{U_2}{U_1}, \quad \frac{\partial F_3}{\partial U_4} = 0$$

$$\frac{\partial F_4}{\partial U_1} = -\frac{U_4 U_2}{U_1^2} + U_2 \left(\frac{U_1 \dfrac{\partial p}{\partial U_1} + p}{U_1^2} \right), \quad \frac{\partial F_4}{\partial U_2} = \frac{U_4}{U_1} + \frac{1}{U_1}\left(U_2 \frac{\partial p}{\partial U_2} + p \right)$$

$$\frac{\partial F_4}{\partial U_3} = \frac{U_2}{U_1} \frac{\partial p}{\partial U_3}, \quad \frac{\partial F_4}{\partial U_4} = \frac{U_2}{U_1} + \frac{U_2}{U_1} \frac{\partial p}{\partial U_4}$$

5.3.2. Jacobian Matrix in the z-direction

For the flux functions in the z-direction, the Jacobian matrix is defined as:

$$J_z = \frac{\partial \vec{G}(\vec{U})}{\partial \vec{U}} = \begin{bmatrix} \dfrac{\partial G_1}{\partial U_1} & \dfrac{\partial G_1}{\partial U_2} & \dfrac{\partial G_1}{\partial U_3} & \dfrac{\partial G_1}{\partial U_4} \\[2mm] \dfrac{\partial G_2}{\partial U_1} & \dfrac{\partial G_2}{\partial U_2} & \dfrac{\partial G_2}{\partial U_3} & \dfrac{\partial G_2}{\partial U_4} \\[2mm] \dfrac{\partial G_3}{\partial U_1} & \dfrac{\partial G_3}{\partial U_2} & \dfrac{\partial G_3}{\partial U_3} & \dfrac{\partial G_3}{\partial U_4} \\[2mm] \dfrac{\partial G_4}{\partial U_1} & \dfrac{\partial G_4}{\partial U_2} & \dfrac{\partial G_4}{\partial U_3} & \dfrac{\partial G_4}{\partial U_4} \end{bmatrix} \tag{5.56}$$

Whose entries are:

$$\frac{\partial G_1}{\partial U_1} = 0, \quad \frac{\partial G_1}{\partial U_2} = 0, \quad \frac{\partial G_1}{\partial U_3} = 1, \quad \frac{\partial G_1}{\partial U_4} = 0$$

$$\frac{\partial G_2}{\partial U_1} = -\frac{U_2 U_3}{U_1^2}, \quad \frac{\partial G_2}{\partial U_2} = \frac{U_3}{U_1}, \quad \frac{\partial G_2}{\partial U_3} = \frac{U_2}{U_1}, \quad \frac{\partial G_2}{\partial U_4} = 0$$

$$\frac{\partial G_3}{\partial U_1} = -\frac{U_3^2}{U_1^2} + \frac{\partial p}{\partial U_1}, \quad \frac{\partial G_3}{\partial U_2} = \frac{\partial p}{\partial U_2}, \quad \frac{\partial G_3}{\partial U_3} = \frac{2U_3}{U_1} + \frac{\partial p}{\partial U_3}, \quad \frac{\partial G_3}{\partial U_4} = \frac{\partial p}{\partial U_4}$$

$$\frac{\partial G_4}{\partial U_1} = -\frac{U_4 U_3}{U_1^2} + U_3 \left(\frac{U_1 \dfrac{\partial p}{\partial U_1} + p}{U_1^2} \right), \quad \frac{\partial G_4}{\partial U_2} = \frac{U_3}{U_1} \frac{\partial p}{\partial U_2}$$

$$\frac{\partial G_4}{\partial U_3} = \frac{U_4}{U_1} + \frac{1}{U_1} \left(U_3 \frac{\partial p}{\partial U_3} + p \right), \quad \frac{\partial G_4}{\partial U_4} = \frac{U_3}{U_1} + \frac{U_3}{U_1} \frac{\partial p}{\partial U_4}$$

5.3.3. Pressure Partial Derivatives Calculation

Here a prediction tool that generates properties of the gas mixtures as a function of pressure and temperature using the equations of state (EOS) is used. EOS are functions interrelating pressure, temperature and volume of the system. For the problem under consideration, due to the continuous change in pressure and temperature along the pipeline, the state of the system always varies. In this sense, an EOS monitors these thermodynamic changes, and thus, it describes the volumetric behavior of the system. The model used in this study can choose between the Peng-Robinson (1976) EOS and the AGA 8 EOS (both described in Appendix A). For the case of a

single piepeline, the Peng Robinson EOS was used, while for the specific problem of flow through the orifice meter, where accuracy is of utmost importance, the AGA 8 was utilized.

.

The phase behavior model is a tool such that given the pressure, temperature and overall composition of the mixture, all the other properties of the system can be obtain, such as density and internal energy. This is:

$$[\rho, e] = EOS_1(p, T) \tag{5.57}$$

The search algorithm proposed by León (2004), which uses the Newton-Raphson protocol, allows us to obtain the pressure and temperature of the system for given values of density and internal energy. This is:

$$[p, T] = EOS_2(\rho, e) \tag{5.58}$$

Let us solve the internal energy from Equation (5.9).

$$e = \frac{E}{\rho} - \frac{1}{2}\left(v_r^2 + v_z^2\right) \tag{5.59}$$

Writing this expression in terms of the conservative variables one gets:

$$e = \frac{U_4}{U_1} - \frac{1}{2}\left[\left(\frac{U_2}{U_1}\right)^2 + \left(\frac{U_3}{U_1}\right)^2\right] \tag{5.60}$$

At this point, a new approach to determine the partial derivatives of pressure as a function of the conservative variables is proposed. Let us define the epsilons for each conservative variable as $\varepsilon_{U_1}, \varepsilon_{U_2}, \varepsilon_{U_3}$, and ε_{U_4}. For each calculation, the values of the epsilons are determined as:

$$\varepsilon_{U_1} = \frac{U_1}{10000}, \quad \varepsilon_{U_2} = \frac{U_2}{10000}, \quad \varepsilon_{U_3} = \frac{U_3}{10000}, \quad \varepsilon_{U_4} = \frac{U_4}{10000}$$

Then the pressure partial derivatives are calculated as follows:

$$\frac{\partial p}{\partial U_1} = \frac{p'-p}{\varepsilon_{U_1}}$$ (5.61)

where:
$$p' = EOS_2(\rho_1', e_1')$$

$$\rho_1' = \rho + \varepsilon_{U_1}$$

$$e_1' = \frac{U_4}{U_1 + \varepsilon_{U_1}} - \frac{1}{2}\left[\left(\frac{U_2}{U_1 + \varepsilon_{U_1}}\right)^2 + \left(\frac{U_3}{U_1 + \varepsilon_{U_1}}\right)^2\right]$$

$$\frac{\partial p}{\partial U_2} = \frac{p'-p}{\varepsilon_{U_2}}$$ (5.62)

where:
$$p' = EOS_2(\rho, e_2')$$

$$e_2' = \frac{U_4}{U_1} - \frac{1}{2}\left[\left(\frac{U_2 + \varepsilon_{U_2}}{U_1}\right)^2 + \left(\frac{U_3}{U_1}\right)^2\right]$$

$$\frac{\partial p}{\partial U_3} = \frac{p'-p}{\varepsilon_{U_3}}$$ (5.63)

where:
$$p' = EOS_2(\rho, e_3')$$

$$e_3' = \frac{U_4}{U_1} - \frac{1}{2}\left[\left(\frac{U_2}{U_1}\right)^2 + \left(\frac{U_3 + \varepsilon_{U_3}}{U_1}\right)^2\right]$$

$$\frac{\partial p}{\partial U_4} = \frac{p'-p}{\varepsilon_{U_4}}$$ (5.64)

where:
$$p' = EOS_2(\rho, e_4')$$

$$e_4' = \frac{U_4 + \varepsilon_{U_4}}{U_1} - \frac{1}{2}\left[\left(\frac{U_2}{U_1}\right)^2 + \left(\frac{U_3}{U_1}\right)^2\right]$$

It is clear that this new procedure that calculates the pressure derivatives given by equations (5.61) to (5.64) allows us to generalize the solution of governing equations for any kind of fluid by implementing the appropriate EOS.

The entries of the Jacobian matrices (5.55) and (5.56) can now be calculated using any equation of state removing the considerations of an ideal gas and the use of the caloric equation of state (2.7) utilized in previous works.

5.3.4. Eigenvalues

Having the Jacobian matrices (5.55) and (5.56), the eigenvalues are the ones that solve the characteristic polynomial defined as:

$$\det(J_r - I\lambda) = \left| J_r - I\lambda \right| = \left\| \begin{bmatrix} \frac{\partial F_1}{\partial U_1} - \lambda & \frac{\partial F_1}{\partial U_2} & \frac{\partial F_1}{\partial U_3} & \frac{\partial F_1}{\partial U_4} \\ \frac{\partial F_2}{\partial U_1} & \frac{\partial F_2}{\partial U_2} - \lambda & \frac{\partial F_2}{\partial U_3} & \frac{\partial F_2}{\partial U_4} \\ \frac{\partial F_3}{\partial U_1} & \frac{\partial F_3}{\partial U_2} & \frac{\partial F_3}{\partial U_3} - \lambda & \frac{\partial F_3}{\partial U_4} \\ \frac{\partial F_4}{\partial U_1} & \frac{\partial F_4}{\partial U_2} & \frac{\partial F_4}{\partial U_3} & \frac{\partial F_4}{\partial U_4} - \lambda \end{bmatrix} \right\| = 0 \qquad (5.65)$$

5.3.5. Right Eigenvectors

Any matrix has an associated polynomial whose roots are the eigenvalues of the matrix. The reverse is also true: for any polynomial, there is an associated matrix whose eigenvalues are the same as the roots of the polynomial. However, "the correspondence between polynomial and matrices cannot be one-to-one" (Heath, 2002). This is because a general matrix of order m, depends on m^2 parameters (its entries), whereas a polynomial of degree m depends on only $m+1$ parameters (its coefficients). Thus, distinct matrices can have the same characteristic polynomial. The right eigenvectors of a system are defined as column vectors, $R^{(p)}$, satisfying the relation:

$$J_r.R^{(p)} = \lambda_p.R^{(p)} \qquad (5.66)$$

5.3.6. Left Eigenvectors

The left eigenvectors are defined as row vectors satisfying the relationship:

$$L^{(p)}.Jr = \lambda_p.L^{(p)} \qquad (5.67)$$

5.4. Discretization of Viscous Terms in the Source Terms

Here we consider the treatment of the physical viscous terms and heat conduction terms in the compressible Navier-Stokes equations. All these terms are of the form $\dfrac{\partial}{\partial r}\left(\mu\dfrac{\partial v_z}{\partial r}\right)$ and $\dfrac{\partial}{\partial z}\left(k\dfrac{\partial T}{\partial z}\right)$.

According to Roache (1998), using a single-time-level differencing, the second-order partial derivative can be expressed by the following form:

$$\frac{\partial}{\partial r}\left(\mu\frac{\partial v_z}{\partial r}\right)\bigg|_{i,j} = \frac{\left(\mu\dfrac{\partial v_z}{\partial r}\right)\bigg|_{i+\frac{1}{2},j} - \left(\mu\dfrac{\partial v_z}{\partial r}\right)\bigg|_{i-\frac{1}{2},j}}{\Delta r} = \frac{\mu_{i+\frac{1}{2},j}\left(\dfrac{v_{z(i+1,j)} - v_{z(i,j)}}{\Delta r}\right) - \mu_{i-\frac{1}{2},j}\left(\dfrac{v_{z(i,j)} - v_{z(i-1,j)}}{\Delta r}\right)}{\Delta r}$$

$$\frac{\partial}{\partial r}\left(\mu\frac{\partial v_z}{\partial r}\right)\bigg|_{i,j} = \frac{\mu_{i+\frac{1}{2},j}\left(v_{z(i+1,j)} - v_{z(i,j)}\right) - \mu_{i-\frac{1}{2},j}\left(v_{z(i,j)} - v_{z(i-1,j)}\right)}{\Delta r^2} + O(\Delta r^2) \qquad (5.68)$$

The same applies for the temperature derivatives yielding to:

$$\frac{\partial}{\partial z}\left(k\frac{\partial T}{\partial z}\right)\bigg|_{i,j} = \frac{k_{i,j+\frac{1}{2}}\left(T_{(i,j+1)} - T_{(i,j)}\right) - k_{i,j-\frac{1}{2}}\left(T_{(i,j)} - T_{(i,j-1)}\right)}{\Delta z^2} + O(\Delta z^2) \qquad (5.69)$$

The terms $\mu_{i+\frac{1}{2},j}$ and $k_{i,j+\frac{1}{2}}$ are pressure and temperature dependent, therefore they are evaluated as:

$$\mu_{i+\frac{1}{2},j} = \frac{1}{2}\left[\mu\ of\ (p_{i,j},T_{i,j}) + \mu\ of\ (p_{i+1,j},T_{i+1,j})\right] \qquad (5.70)$$

$$k_{i,j+\frac{1}{2}} = \frac{1}{2}\left[k\ of\ (p_{i,j},T_{i,j}) + k\ of\ (p_{i,j+1},T_{i,j+1})\right] \qquad (5.71)$$

The first-order derivatives in the RHS, such as $\dfrac{\partial v_r}{\partial r}$, are discretized using a central difference approximation. This is:

$$\left.\frac{\partial v_r}{\partial r}\right|_{i,j} = \frac{v_{r(i+1,j)} - v_{r(i-1,j)}}{2\Delta r} \qquad (5.72)$$

5.5. Description of the System

For the purpose of this work, an orifice-plate with a forward edge is studied. The thickness of the plate is 1/8" and the edge is inclined 45 degrees as shown in Figure 5.2. Note that the orifice plate thickness was chosen according to the standard given by the AGA Report Number 3, Part 2 for a pipe of nominal size equal to 2 inches, which is the diameter used in this study. The minimum and maximum accepted thicknesses are 0.115" and 0.319", while the recommended thickness is equal to 0.125" as the one used for the forward plate.
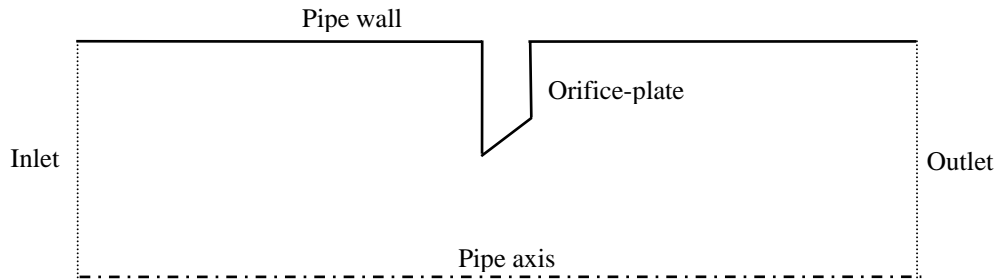
Figure 5.2. Schematic of an orifice-plate with a) flat edge and b) forward edge.

The length of the pipe section upstream the plate is 3 pipe diameters, while the length downstream the plate is 6 pipe diameters. Davis and Mattingly (1977) predicted that these specifications guarantee that a fully developed turbulent flow occurs at the inlet and at the outlet of the section when a flow conditioner is used. Moreover, Morrison *et al* (1993) confirmed these dimensions experimentally.

5.5.1. Grid Discretization

For all cases we are using a structured point-distributed grid. The system is discretized in the r-direction using 16 gridblocks, which correspond to a value of dr equal to 1/16". In the z-direction the size of the gridblocks is also 1/16". A schematic of the discretized grid is shown in Figure 5.3.

a)   dr = dz = 1/16"

no-flow boundary

pipe wall

pipe axis
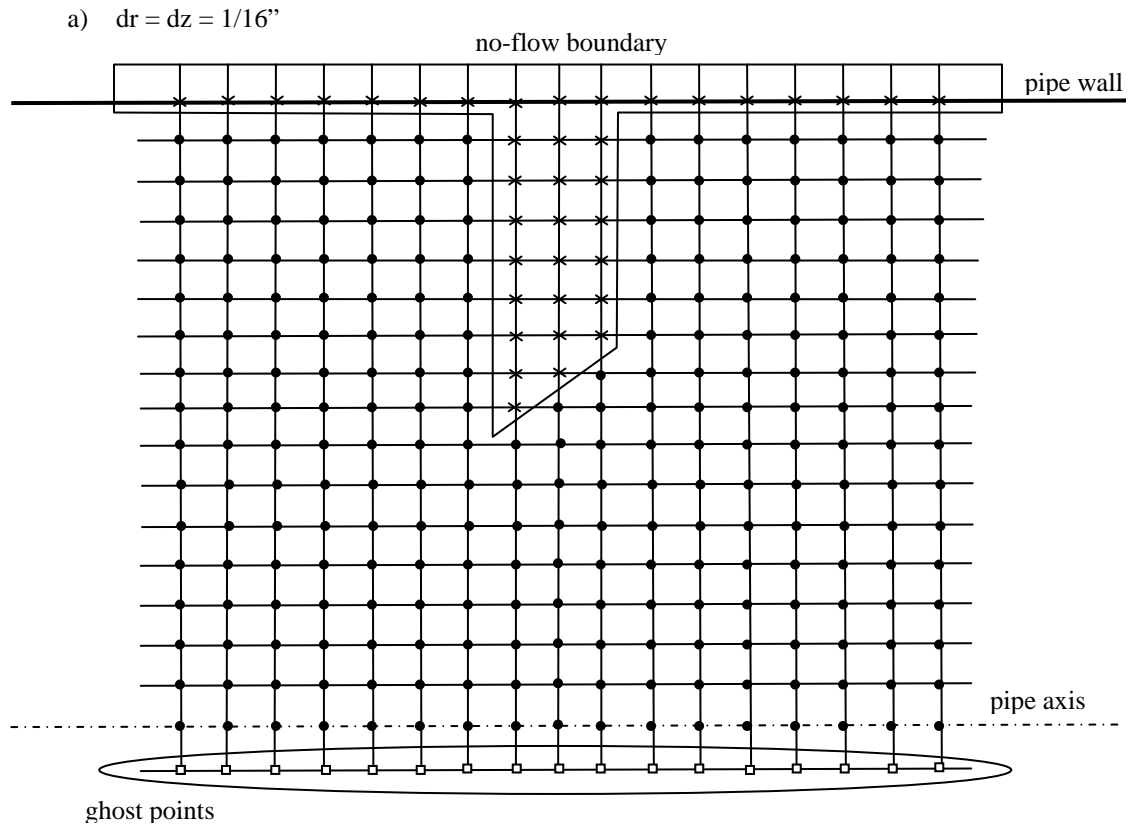
ghost points

Figure 5.3. Forward plate discretized using dr = dz = 1/16".

A no-flow boundary represents the wall of the pipe and the plate. Moreover, ghost points are used next to the axis of the pipe to represent the symmetry boundary condition.

5.5.2. Pressure Tap Location

Figure 5.4 represents a Weld Neck Flange Orifice Meter as specified by the ANSI/ASME B16.5 standard. This belongs to the Class 300 Forged Flanges. In the figure, we can see that the flange has 1.63 inches of thickness and it is connected to the meter run. Then a packer of 1/8" of

thickness is located between the flange and the orifice plate. Note also that the pressure tap is located in the center of the flange.
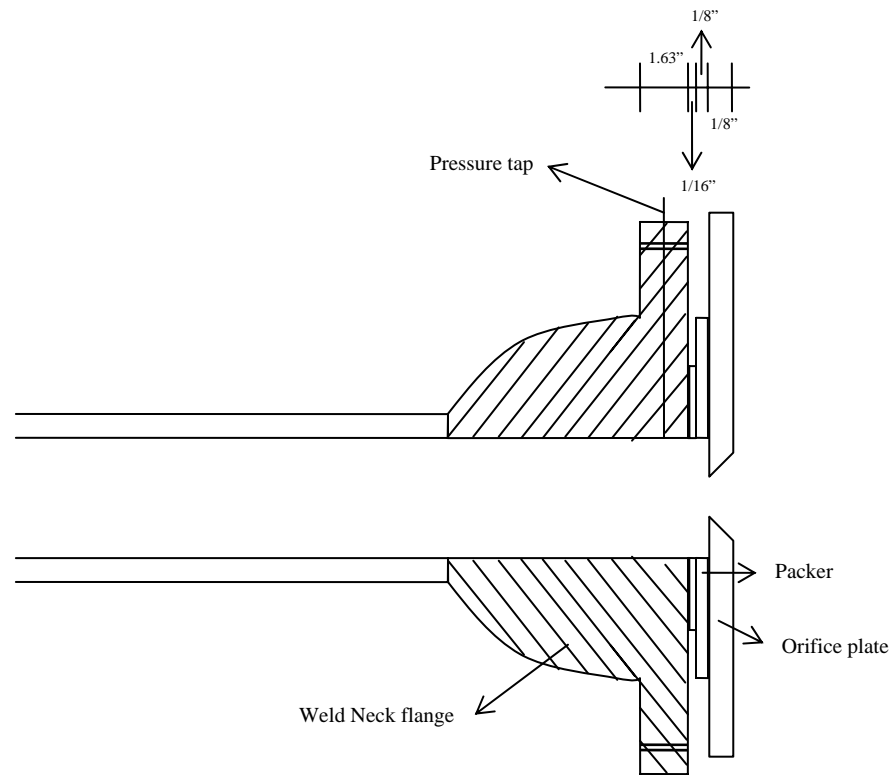
Figure 5.4. Schematic of the Well Neck Flange.

In order to calculate the pressure drop that occurs due to the constriction imposed by the orifice plate, the distance from the center of the plate and the pressure tap must me determined. From the Figure 5.4 we add half of the thickness of the flange, the 1/16" section next to the packer, the packer and half of the plate thickness. The calculation is as follows:

$$\frac{1.63"}{2} + \frac{1}{16}" + \frac{1}{8}" + \frac{1/8}{2}" = 1.065"$$

The distance between the center of the plate and the pressure tap is 1.065 inches.

5.6. Boundary Conditions

The discretization of the system was shown in Figure 5.3. There are five types of boundaries in the system, namely the inlet of the pipe, the axis of the pipe, the pipe outlet, the pipe wall, and the plate wall.
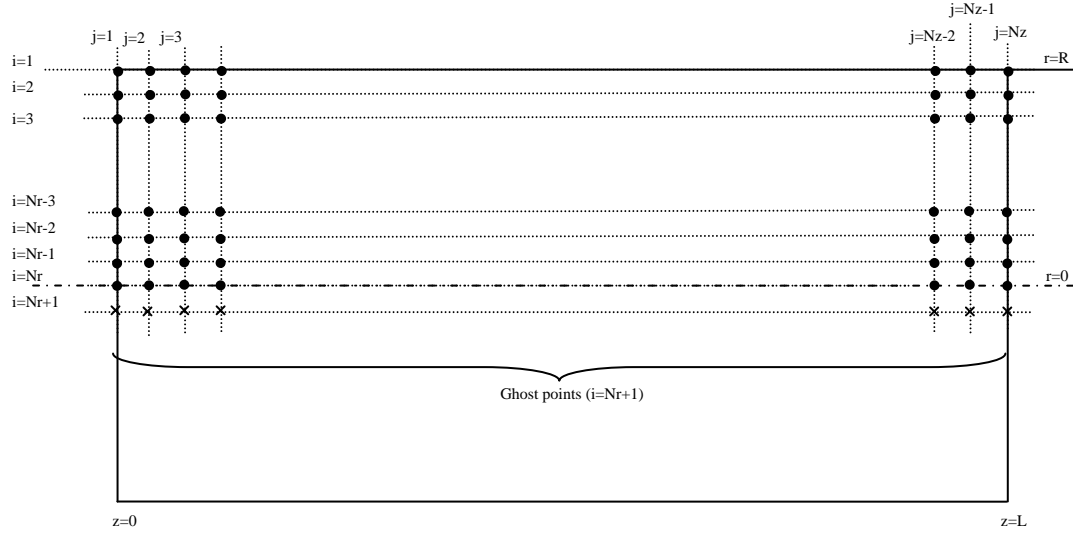
Figure 5.5. Schematic of the grid discretization.

5.6.1. Inlet of the Pipe

At the inlet of the pipe (z=0, i.e. j=1) the primitive variables, pressure, temperature and flow rate are specified as the inlet conditions. Based on flow rate, the velocity profile can be determined for both laminar and turbulent flow. The inlet conditions are:

$$v_r = 0 \quad \rightarrow \quad U_{2_{(i,1)}} = 0 \tag{5.73}$$

$$p = p_{inlet} \quad and \quad T = T_{inlet} \tag{5.74}$$

$$q_t = q_{inlet} \tag{5.75}$$

The density of the fluid is obtained using the real gas equation of state:

$$U_{1_{(i,1)}} = \rho = \frac{p_{inlet} M}{z R T_{inlet}} \tag{5.76}$$

where the compressibility factor is calculated by means of the Peng-Robinson (1976) EOS, the AGA 8 EOS (both described in Appendix A) or the correlation for dry air proposed by Adebiyi (2005). For the case of a single piepeline, the Peng Robinson EOS was used, while for the specific problem of natural gas flow through the orifice meter, where accuracy is of utmost importance, the AGA 8 was utilized.

$$z = z(p_{pr}, T_{pr}), \quad p_{pr} = \frac{p_{inlet}}{p_{pc}}, \quad T_{pr} = \frac{T_{inlet}}{T_{pc}} \tag{5.77}$$

where:

p_{pr} : pseudo reduced pressure, [$psia$]

p_{pc} : pseudo critical pressure, [$psia$]

T_{pr} : pseudo reduced temperature, [$^{\circ}R$]

T_{pc} : pseudo critical temperature, [$^{\circ}R$]

The velocity distribution at the inlet of the pipe is calculated using the 1/9th power law, as recommended by Davis and Mattingly (1977).

$$U_{3_{(i,1)}} = \rho.v_z = \rho.v_{z\max}\left(1 - \frac{r}{R}\right)^{1/n}, \quad n=9 \tag{5.78}$$

For different inlet conditions, the solution of the flow field is definitely different as the boundary conditions are the main drive of the partial differential equations. Several authors have suggested the use of the 1/7th and 1/8th power law (Morison et al, 1993 and Mattingly and Yeh, 1989) for turbulent flow. For laminar flow, a parabolic profile is suitable (Hagen, 1839 and Poiseuille, 1841), but the accuracy of the solution does no vary depending on the boundary conditions, they simply produce the solution of a different problem. However, one must be aware to impose the appropriate inlet profile based on the features of the flow being modeled.

5.6.2. Axis of the Pipe

Since the Navier-Stokes equations are second-order PDEs in velocity, two boundary conditions are required in the r-direction. The first boundary condition was imposed at the wall of the pipe and now the symmetry boundary condition will be imposed at the axis of the pipe.

Due to the two-dimensional nature of the grid we are using, the solution with respect to the axis of the pipe must be symmetrical. Moreover, no mass or convective flux occurs across the axis of the pipe. Therefore the following conditions shall be satisfied:

$$U_{1_{(Nr+1,j)}} = U_{1_{(Nr-1,j)}} \tag{5.79}$$

$$v_{r_{(Nr+1,j)}} = -v_{r_{(Nr-1,j)}} \quad \rightarrow \quad U_{2_{(Nr+1,j)}} = -U_{2_{(Nr-1,j)}} \tag{5.80}$$

$$U_{3_{(Nr+1,j)}} = U_{3_{(Nr-1,j)}} \tag{5.81}$$

$$U_{4_{(Nr+1,j)}} = U_{4_{(Nr-1,j)}} \tag{5.82}$$

Additionally, when handling the origin in the cylindrical coordinate system we encounter the singularity problem at r=0 where the term goes to infinity. In order to solve this problem we use a Cartesian coordinate at the origin (Equations 5.83 and 5.84).

$$\frac{D(\rho \vec{v})}{Dt} = \left(-\nabla p - [\nabla \cdot \tau] + \rho \vec{g} \right)_{cartesian} \tag{5.83}$$

$$\frac{D(\rho \vec{v})}{Dt} = \left(-\nabla p - [\nabla \cdot \tau] + \rho \vec{g} \right)_{cylindrical} \tag{5.84}$$

Thus obtaining the RHS of the momentum equations to be:

$$\sigma_r = \left[\frac{\partial \tau_{rr}}{\partial r} + \frac{\partial \tau_{zr}}{\partial z} \right]; \quad \sigma_z = \left[\frac{\partial \tau_{rz}}{\partial r} + \frac{\partial \tau_{zz}}{\partial z} \right] \tag{5.85}$$

$$\tau_{rr} = -2\mu \left(\frac{\partial v_r}{\partial r} \right) + \frac{2}{3} \mu \left(\frac{\partial v_r}{\partial r} + \frac{\partial v_z}{\partial z} \right) \tag{5.86}$$

$$\tau_{zz} = -2\mu \left(\frac{\partial v_z}{\partial z} \right) + \frac{2}{3} \mu \left(\frac{\partial v_r}{\partial r} + \frac{\partial v_z}{\partial z} \right) \tag{5.87}$$

$$\tau_{rz} = \tau_{zr} = -\mu\left(\frac{\partial v_z}{\partial r} + \frac{\partial v_r}{\partial z}\right) \tag{5.88}$$

5.6.3. Outlet of the Pipe

As stated by Roache (1998), there are a wide variety of methods for treating downstream boundaries, for compressible flow. One choice is the linear interpolation of the conservative variables,

$$U_{(i,Nz)} = 2U_{(i,Nz-1)} - U_{(i,Nz-2)} \tag{5.89}$$

or the non-conservative variables,

$$f_{(i,Nz)} = 2f_{(i,Nz-1)} - f_{(i,Nz-2)}, \quad \text{where } f = \rho, v_r, v_z, T \tag{5.90}$$

Another choice is the use of the simple condition:

$$U_{(i,Nz)} = U_{(i,Nz-1)} \tag{5.91}$$

or equivalently

$$f_{(i,Nz)} = f_{(i,Nz-1)} \tag{5.92}$$

According to Roache (1998), Allen (1968) found that this simple boundary condition caused the solution to diverge monotonically, but other authors such as Ruo (1967), Eaton and Zumwalt (1967) and Kessler (1968) found that the method gave good results and in some cases even accelerated the convergence compared with other methods. For the purposes of this study the following combination of outflow boundary conditions is used.

The density and the radial velocity are extrapolated from the inner points as:

$$U_{1_{(i,Nz)}} = 2U_{1_{(i,Nz-1)}} - U_{1_{(i,Nz-2)}} \tag{5.93}$$

$$v_{r_{(i,Nz)}} = 2v_{r_{(i,Nz-1)}} - v_{r_{(i,Nz-2)}}, \quad U_{2_{(i,Nz)}} = U_{1_{(i,Nz)}} \cdot v_{r_{(i,Nz)}} \tag{5.94}$$

The mass flux in the z-direction is set equal to the previous node:

$$U_{3_{(i,Nz)}} = U_{3_{(i,Nz-1)}} \qquad (5.95)$$

Finally, the internal energy is also extrapolated from the inner points, and then the total energy is calculated as:

$$e_{(i,Nz)} = 2e_{(i,Nz-1)} - e_{(i,Nz-2)}$$

$$U_{4_{(i,Nz)}} = U_{1_{(i,Nz)}} \left(\frac{1}{2} \left[\left(\frac{U_{2_{(i,Nz)}}}{U_{1_{(i,Nz)}}} \right)^2 + \left(\frac{U_{3_{(i,Nz)}}}{U_{1_{(i,Nz)}}} \right)^2 \right] + e_{(i,Nz)} \right) \qquad (5.96)$$

5.6.4. Wall of the Pipe

At a solid wall boundary, the normal velocity is zero, since no mass or other convective flux can penetrate the solid body. This is:

$$v_{r_{(1,j)}} = 0 \quad and \quad U_{2_{(1,j)}} = 0 \qquad (5.97)$$

Additionally, since we are dealing with real fluids, the existence of intermolecular attractions cause the fluid to adhere to the solid wall and this gives rise to shear stresses. According to Schlichting (1968), the existence of tangential (shear) stresses does not allow difference in relative tangential velocities between the fluid and the wall. This is called the no-slip boundary condition and is represented as:

$$v_{z_{(1,j)}} = 0 \quad and \quad U_{3_{(1,j)}} = 0 \qquad (5.98)$$

The density/pressure is obtained from the interior flow towards the boundary. It is extrapolated directly from their values at points adjacent to the wall surface. According to Hirsch (1988) first order extrapolation formulas such as (5.99) are generally sufficient for second-order schemes, but quadratic extrapolation (5.100) can be used as well, and therefore they are used in this study.

$$U_{1_{(1,j)}} = 2U_{1_{(2,j)}} - U_{1_{(3,j)}} \qquad (5.99)$$

$$U_{1_{(1,j)}} = 3U_{1_{(2,j)}} - 3U_{1_{(3,j)}} + U_{1_{(4,j)}} \qquad (5.100)$$

Since the velocities in both directions are zero, the total energy per unit volume is given solely by the internal energy of the fluid, this is:

$$U_{4_{(1,j)}} = E_{(1,j)} = \rho.e = U_{1_{(1,j)}} \cdot e_{(1,j)} \qquad (5.101)$$

5.6.4.1. Wall Stress Model

Turbulent models that do not include wall correction terms in the differential equations are called high-Reynolds-number turbulence models. High-Reynolds-turbulence models rely on empirically derived algebraic models of the near-wall region of the boundary layer to provide boundary condition information to the mean flow Navier-Stokes equations at the first point off the wall. These models of the near-wall region are called wall functions. Because the high-gradient region near the wall is modeled with these empirical relationships, the first point off the wall may be placed much farther away than with low-Reynolds-number models. This reduces the number of points required to discretize a flow-field and increases the maximum allowable time step (Nichols and Nelson, 2004).

The high-Reynolds number solution must be patched to a solution field that is valid in the vicinity of the wall. This patching can be done by using a prescribed functional distribution for the mean field and the turbulent field to which the Reynolds number solution can be matched (Gatski, 1997).

Due to the definition of boundary layer flow structure, there is a problem in applying the LES technique to the solid walls. The mechanisms originating the turbulence, i.e. the flow driving mechanisms, are associated with fixed characteristic length scales on the average. This factor makes it such that the subgrid models become inoperative because they no longer permit a reduction of the number of degrees of freedom while ensuring at the same time a fine representation of the flow driving mechanisms (Sagaut, 2002).

One possibility is to resolve the near-wall dynamics directly by increasing the resolution in order to capture small scales. Another possibility is to model the near-wall dynamics by using a special subgrid model called wall model. Since the distance from the first grid point to the wall is greater than the characteristic scales of the modes existing in the modeled region, the no-slip condition will only apply to the values of the velocity components, but a wall stress model will choose a very large first mesh, so that it is not able to represent correctly the dynamics of the inner layer.

The main advantage of this approach is that the number of degrees of freedom in the simulation can be reduced greatly, but since a part of the dynamics is modeled, it constitutes another source of error. The wall model should provide the value of wall stress, which cannot be accurately computed directly on the grid because of its coarseness, and the value of the wall-normal velocity component. Two wall models are presented below.

5.6.4.2. Nichols and Nelson Wall Model

The wall model proposed by Nichols and Nelson (2004) is presented here. The model is applicable to compressible fluid and it has five fundamental assumptions in the lower part of the boundary layer:

a) Analytical expressions are available for the velocity and temperature profiles.
b) There is no pressure gradient normal to the wall.
c) The shear stress is constant.
d) The heat transfer is constant.
e) There are no chemical reactions, that is, the chemistry is frozen.

This approach follows the incompressible law-of-the-wall term of Spalding (1961) and the outer velocity concept of White and Christoph (1971). The present model considers the compressibility and heat transfer effects. It can also consider the surface roughness effect by adjusting two constants.

For adiabatic or constant heat transfer the wall shear stress is determined using the following protocol:

1) Set the velocity at the wall to zero, $v_{r_{(1,j)}} = 0$ and $v_{z_{(1,j)}} = 0$.

2) Given the velocity and temperature at the first point off the wall ($v_{z_{(2,j)}}, T_{(2,j)}$), solve for the wall temperature $T_w = T_{(1,j)}$ from:

$$T_w = T_{(1,j)} = \frac{T_{(2,j)}}{\left(1 + \left[(\gamma - 1)\frac{r}{2}\right]v_{z_{(2,j)}}\right)}$$ (5.102)

3) Extrapolate pressure at the wall ($p_w = p_{(1,j)}$) from the inner domain, and solve for the wall density ($\rho_w = \rho_{(1,j)}$) using the equation of state:

$$\rho_w = \rho_{(1,j)} = EOS(p_{(1,j)}, T_{(1,j)})$$ (5.103)

4) Set an initial guess for the wall shear stress, or take the value of the previous iteration.

5) Define the friction velocity as:

$$v_\tau = \sqrt{\frac{\sigma_z}{\rho_w}}$$ (5.104)

6) Iteratively solve for the wall shear stress using the following expressions:

$$\beta = \frac{q_w \mu_w}{\rho_w T_w k_w v_\tau}$$ (5.105)

$$\Gamma = \frac{r_f v_\tau^2}{2c_{cp}T_w}$$ (5.106)

$$Q = \left(\beta^2 + 4\Gamma\right)^{\frac{1}{2}}$$ (5.107)

$$\phi = \sin^{-1}\left(\frac{-\beta}{Q}\right)$$ (5.108)

$$y_o^+ = e^{-\kappa B_r}$$ (5.109)

$$u^+ = \left(\frac{1}{2\Gamma}\right)\left[\beta + Q\sin\left(\phi + \left(\frac{\sqrt{\Gamma}}{\kappa}\right)\right)\ln\left(\frac{y^+}{y_o^+}\right)\right] \tag{5.110}$$

$$y_{White}^+ = \exp\left[\left(\frac{\kappa}{\sqrt{\Gamma}}\right)\left(\sin^{-1}\left(\frac{2\Gamma u^+ - \beta}{Q}\right) - \phi\right)\right]e^{-\kappa B_r} \tag{5.111}$$

$$y^+ = u^+ + y_{White}^+ - e^{\kappa B_r}\left[1 + \kappa u^+ + \frac{(\kappa u^+)^2}{2} + \frac{(\kappa u^+)^3}{6}\right] \tag{5.112}$$

where:

q_w : Wall heat transfer.

k_w : Molecular kinetic energy.

c_{cp} : Pressure coefficient.

r_f : Recovery factor, $\text{Pr}^{1/3}$.

Pr : Molecular Prandlt number.

Γ : nondimensional parameter for compressibility effects.

κ : constant for tuning roughness at the boundary.

B_r : constant for tuning roughness at the boundary.

u^+ : velocity parallel to the wall (law-of-the-wall)

y^+ : velocity parallel to the wall (law-of-the-wall)

5.6.4.3. Gatski Wall Model

Gatski (1997) also considered a zero pressure gradient in the inner region of the boundary layer. He derived a model starting with the mean momentum and total energy equations and neglecting the mass flux and turbulent transport. The main steps for implementing the wall function are:

1) Set an initial guess for the wall shear stress, σ_z, or take the value from the previous iteration.

2) Compute the temperature at the wall, $T_w = T_{(1,j)}$, from the expression:

$$\tilde{T}_w = \tilde{T}_{(1,j)} = T_{(2,j)} + \frac{\Pr_t}{c_p}\left(\frac{q_w \tilde{v}_z}{\overline{\sigma}_z} + \frac{\tilde{v}_z^2}{2}\right) \tag{5.113}$$

3) Knowing the temperature and velocity profiles from the previous iteration time step, calculate:

$$D = \left(\frac{\overline{q}_w^2}{\overline{\sigma}_z} + \frac{2c_p \tilde{T}_w}{\Pr_t}\right)^{1/2} \tag{5.114}$$

$$\tilde{v}_c \cong \left(\frac{2c_p \tilde{T}_w}{\Pr_t}\right)^{1/2}\left[\arcsin\left(\frac{\tilde{q}_w + \tilde{v}_z \overline{\sigma}_z}{\overline{\sigma}_z D}\right) - \arcsin\left(\frac{\tilde{q}_w}{\overline{\sigma}_z D}\right)\right] \tag{5.115}$$

4) Update the wall shear stress from the equation:

$$\overline{\sigma}_z = \overline{\rho}_w\left(\frac{\tilde{v}_c}{\frac{1}{\kappa}\left[\ln\left(\frac{\overline{\rho}_w y}{\overline{\mu}_w}\right) + \ln\left(\sqrt{\frac{\overline{\sigma}_z}{\overline{\rho}_w}}\right)\right] + B_c}\right)^2 \tag{5.116}$$

where:

$K_c = K_c(M_r, B_q, \Pr_t)$

$B_c = B_c(M_r, B_q, \Pr_t)$

$$B_q = \frac{\overline{q}_w}{\overline{\rho}_w c_p\left(\sqrt{\overline{\sigma}_z/\overline{\rho}_w}\right)\tilde{T}_w} \tag{5.117}$$

5) Repeat steps 1, 2, 3 and 4 until convergence.

5.6.4.4. Effect of Roughness

Note that for smooth pipe, the constants κ and B_c are generally taken as 0.4 and 5.5 respectively (Nichols and Nelson, 2004). These two parameters can be tuned to include the effect of surface roughness. However, Reader-Harris and Keegans (1986) found that a pipe with k/D smaller than 10^{-4} behaves as it was hydraulically smooth; and that the relative error due to the roughness is

negligible when a section of 2.5 pipe diameters of smooth pipe is placed immediately upstream the orifice. Moreover, according to the standards recommended by the American Gas Association (AGA, 2000), the meter-tube roughness must be in the range 34 to 300 μinches (0.000034 – 0.0003 inches). Therefore, for the purposes of this study we are using a smooth pipe in the modeled section.

5.6.5. Walls of the Plate

No-slip boundary conditions represented by Equations (5.97) and (5.98) are imposed at the wall of the plate. The density is extrapolated from the inner domain using Equations (5.99) and (5.100) but applied in the axial direction.

5.6.6. Handling the Penultimate Nodes

Due to the high-order accuracy of the numerical scheme used, information is required to be known in the second and the penultimate block of the grid. Therefore the ENO scheme is only applied in the domain from the third node (j=3) to the node before the penultimate one (j=Nz-2). At the second node, the inflow conditions are calculated first by linear interpolation of the density.

$$U_{1_{(i,2)}} = \frac{U_{1_{(i,1)}} + U_{1_{(i,3)}}}{2} \tag{5.118}$$

The mass fluxes in both r- and z-direction are set equal to the inlet conditions.

$$U_{2_{(i,2)}} = U_{2_{(i,1)}} \tag{5.119}$$

$$U_{3_{(i,2)}} = U_{3_{(i,1)}} \tag{5.120}$$

The internal energy is obtained by linear interpolation, and then the total energy is calculated.

$$e_{(i,1)} = \frac{U_{4_{(i,1)}}}{U_{1_{(i,1)}}} - \frac{1}{2}\left[\left(\frac{U_{2_{(i,1)}}}{U_{1_{(i,1)}}}\right)^2 + \left(\frac{U_{3_{(i,1)}}}{U_{1_{(i,1)}}}\right)^2\right], \quad e_{(i,3)} = \frac{U_{4_{(i,3)}}}{U_{1_{(i,3)}}} - \frac{1}{2}\left[\left(\frac{U_{2_{(i,3)}}}{U_{1_{(i,3)}}}\right)^2 + \left(\frac{U_{3_{(i,13)}}}{U_{1_{(i,3)}}}\right)^2\right]$$

$$e_{(i,2)} = \frac{e_{(i,1)} + e_{(i,3)}}{2}$$

$$U_{4_{(i,2)}} = U_{1_{(i,2)}} \left(\frac{1}{2} \left[\left(\frac{U_{2_{(i,2)}}}{U_{1_{(i,2)}}} \right)^2 + \left(\frac{U_{3_{(i,2)}}}{U_{1_{(i,2)}}} \right)^2 \right] + e_{(i,2)} \right) \tag{5.121}$$

At the outflow boundary, the density and the radial velocity are extrapolated from the inner points as:

$$U_{1_{(i,Nz-1)}} = 2U_{1_{(i,Nz-2)}} - U_{1_{(i,Nz-3)}} \tag{5.122}$$

$$v_{r_{(i,Nz-1)}} = 2v_{r_{(i,Nz-2)}} - v_{r_{(i,Nz-3)}}, \quad U_{2_{(i,Nz-1)}} = U_{1_{(i,Nz-1)}} \cdot v_{r_{(i,Nz-1)}} \tag{5.123}$$

The mass flux in the z-direction is set equal to the previous node:

$$U_{3_{(i,Nz-1)}} = U_{3_{(i,Nz-2)}} \tag{5.124}$$

Finally, the internal energy is also extrapolated from the inner points, and then the total energy is calculated as:

$$e_{(i,Nz-1)} = 2e_{(i,Nz-2)} - e_{(i,Nz-3)}$$

$$U_{4_{(i,Nz-1)}} = U_{1_{(i,Nz-1)}} \left(\frac{1}{2} \left[\left(\frac{U_{2_{(i,Nz-1)}}}{U_{1_{(i,Nz-1)}}} \right)^2 + \left(\frac{U_{3_{(i,Nz-1)}}}{U_{1_{(i,Nz-1)}}} \right)^2 \right] + e_{(i,Nz-1)} \right) \tag{5.125}$$

5.7. One-Dimensional Model and Initial Conditions

In order to obtain a solution using the transient model, an initial distribution of the flow properties is required. Then, the model marches the solution in time until steady-state conditions are achieved. This study uses the criterion suggested by Mattingly and Davis (1977) to determine when steady-state is attained, which occurs when the change in the maximum axial velocity within one timestep is less than 0.05%.

Here we present the description of the one-dimensional, steady-model used to generate the initial conditions for the transient model. For the case of a horizontal pipeline, if no variations are assumed to occur within a given cross-section of the pipe, the spatial derivatives in the r-direction are dropped yielding the averaged equations:

$$\frac{\partial \vec{U}}{\partial t} + \frac{\partial \left(\vec{F}(\vec{U}) \right)}{\partial z} = \vec{Q} \tag{5.126}$$

where the conservative variables are:

$$\vec{U} = \begin{bmatrix} U_1 \\ U_2 \\ U_3 \end{bmatrix} = \begin{bmatrix} \rho \\ \rho.\bar{v} \\ E \end{bmatrix} \tag{5.127}$$

The physical fluxes are written in terms of the conservative variables:

$$\vec{F} = \begin{bmatrix} F_1 \\ F_2 \\ F_3 \end{bmatrix} = \begin{bmatrix} \rho.\bar{v} \\ \rho.\bar{v}^2 + p \\ (E+p)\bar{v} \end{bmatrix} = \begin{bmatrix} U_2 \\ \frac{U_2^2}{U_1} + p \\ (U_3 + p)\frac{U_2}{U_1} \end{bmatrix}, \tag{5.128}$$

And the vector of source terms is:

$$\vec{Q} = \begin{bmatrix} Q_1 \\ Q_2 \\ Q_3 \end{bmatrix} = \begin{bmatrix} 0 \\ -F_{wz} \\ Q_t + (\bar{v}F_{wz}) \end{bmatrix} \tag{5.129}$$

where:

F_{wz} : wall friction force per unit volume, [$lbm / ft^2.s$]

Q_t : total heat transfer between the system and its surroundings per unit volume, [$lbm / ft.s^3$]

When steady state conditions prevail in the system, the previous system of equations collapse to the system of ordinary differential equations (ODEs):

$$\frac{d\left(\vec{F}(\vec{U})\right)}{dz} = \vec{Q} \tag{5.130}$$

5.7.1. Fluxes Decoupling Approach

In the solution of the steady-state problem (5.130), a marching algorithm is used, which moves the solution from the inlet of the pipe to the next gridpoint using the ODE Solver described in Section 3.5.2. Due to the nature of the fluxes, the physical variables such as density, velocity and internal energy are implicitly embedded. One traditional approach to solving this problem is to separate the pressure derivative in both the momentum and energy equations and write them with a negative sign on the RHS of the equation. However, this technique may lead to an ill-posed problem whose solution is not appropriate.

Note that the values of the fluxes (5.128) are known at the inlet of the pipe ($\vec{F}_{j=1}$), then the solution marches to the next gridpoint ($\vec{F}_{j=2}$), and at this point the fluxes need to be decoupled into physical variables. The present work proposes an approach that uses the Newton-Raphson protocol to obtain these primitive variables. The new technique is as follows:

Having the fluxes at the given gridpoint (F_1, F_2 and F_3), the residuals are calculated as:

$$R_1^{(k)} = \rho^{(k)} v_z^{(k)} - F_1 = 0 \tag{5.131}$$

$$R_2^{(k)} = \left(\rho^{(k)}(v_z^{(k)})^2 + p^{(k)}\right) - F_2 = 0 \tag{5.132}$$

$$R_3^{(k)} = v_z^{(k)}\left[\rho^{(k)}\left(\frac{1}{2}v_z^{(k)} + e^{(k)}\right) + p^{(k)}\right] - F_3 = 0 \tag{5.133}$$

where the initial guess values are obtained as:

$$\rho^{(k)} = \rho_{inlet}, \quad v_z^{(k)} = \frac{F_1}{\rho^{(k)}}, \quad e^{(k)} = e_{inlet} \tag{5.134}$$

The Jacobian matrix is defined as:

$$J^{(k)} = \begin{bmatrix} \dfrac{\partial R_1}{\partial \rho} & \dfrac{\partial R_1}{\partial v_z} & \dfrac{\partial R_1}{\partial e} \\[2mm] \dfrac{\partial R_2}{\partial \rho} & \dfrac{\partial R_2}{\partial v_z} & \dfrac{\partial R_2}{\partial e} \\[2mm] \dfrac{\partial R_3}{\partial \rho} & \dfrac{\partial R_3}{\partial v_z} & \dfrac{\partial R_3}{\partial e} \end{bmatrix}^{(k)}$$

(5.135)

where the partial derivatives are:

$$[p*^{(k)}, T*^{(k)}] = EOS_2(\rho^{(k)} + \varepsilon_\rho, e^{(k)})$$

$$\left.\frac{\partial R_1}{\partial \rho}\right|^{(k)} = \frac{\left[(\rho^{(k)} + \varepsilon_\rho)v_z^{(k)} - F_1\right] - R_1^{(k)}}{\varepsilon_\rho}$$

$$\left.\frac{\partial R_2}{\partial \rho}\right|^{(k)} = \frac{\left[\left((\rho^{(k)} + \varepsilon_\rho)(v_z^{(k)})^2 + p*^{(k)}\right) - F_2\right] - R_2^{(k)}}{\varepsilon_\rho}$$

$$\left.\frac{\partial R_3}{\partial \rho}\right|^{(k)} = \frac{\left(v_z^{(k)}\left[(\rho^{(k)} + \varepsilon_\rho)\left(\frac{1}{2}v_z^{(k)} + e^{(k)}\right) + p*^{(k)}\right] - F_3\right) - R_3^{(k)}}{\varepsilon_\rho}$$

$$\left.\frac{\partial R_1}{\partial v_z}\right|^{(k)} = \frac{\left[\rho^{(k)}(v_z^{(k)} + \varepsilon_v) - F_1\right] - R_1^{(k)}}{\varepsilon_v}$$

$$\left.\frac{\partial R_2}{\partial v_z}\right|^{(k)} = \frac{\left[\left(\rho^{(k)}(v_z^{(k)} + \varepsilon_v)^2 + p^{(k)}\right) - F_2\right] - R_2^{(k)}}{\varepsilon_v}$$

$$\left.\frac{\partial R_3}{\partial v_z}\right|^{(k)} = \frac{\left((v_z^{(k)} + \varepsilon_v)\left[\rho^{(k)}\left(\frac{1}{2}(v_z^{(k)} + \varepsilon_v) + e^{(k)}\right) + p^{(k)}\right] - F_3\right) - R_3^{(k)}}{\varepsilon_v}$$

$$[p*^{(k)}, T*^{(k)}] = EOS_2(\rho^{(k)}, e^{(k)} + \varepsilon_e)$$

$$\left.\frac{\partial R_1}{\partial e}\right|^{(k)} = \frac{\left[\rho^{(k)}v_z^{(k)} - F_1\right] - R_1^{(k)}}{\varepsilon_e}$$

$$\left.\frac{\partial R_2}{\partial e}\right|^{(k)} = \frac{\left[\left(\rho^{(k)}(v_z^{(k)})^2 + p*^{(k)}\right) - F_2\right] - R_2^{(k)}}{\varepsilon_e}$$

$$\frac{\partial R_3}{\partial e}\bigg|^{(k)} = \frac{\left(v_z^{(k)}\left[\rho^{(k)}\left(\frac{1}{2}v_z^{(k)} + (e^{(k)} + \varepsilon_e) \right) + p*^{(k)} \right] - F_3 \right) - R_3^{(k)}}{\varepsilon_e}$$

For each calculation, the values of the epsilons are determined as:

$$\varepsilon_\rho = \frac{\rho}{10000}, \quad \varepsilon_v = \frac{v_z}{10000}, \quad \varepsilon_e = \frac{e}{10000}$$

Note that the pressure $(p*^{(k)})$ is obtained using the search algorithm proposed by León (2004). Then, the physical variables are updated by solving the linear system:

$$\begin{bmatrix} & & \\ & J & \\ & & \end{bmatrix}^{(k)} \cdot \begin{bmatrix} \Delta\rho \\ \Delta v_z \\ \Delta e \end{bmatrix}^{(k+1)} = -\begin{bmatrix} R_1 \\ R_2 \\ R_3 \end{bmatrix}^{(k)} \tag{5.136}$$

And:

$$\begin{bmatrix} \rho \\ v_z \\ e \end{bmatrix}^{(k+1)} = \begin{bmatrix} \rho \\ v_z \\ e \end{bmatrix}^{(k)} + \begin{bmatrix} \Delta\rho \\ \Delta v_z \\ \Delta e \end{bmatrix}^{(k+1)} \tag{5.137}$$

The process continues until the differences (5.137) are smaller than a tolerance (0.00001).

5.7.2. Gravitational Force

For non-horizontal sections of the pipeline, the fluids are subject to the force of gravity. The magnitude of this force depends upon the density of the fluid and the angle of inclination of the pipe with respect to a horizontal plane. For both directions they are given as:

$$F_{gr} = \rho \frac{g}{g_c}\cos(\beta) \tag{5.138}$$

$$F_{gz} = \rho \frac{g}{g_c} \sin(\beta) \tag{5.139}$$

where:

g : gravity acceleration, $[\, ft / s^2 \,]$

g_c : conversion factor, $32.174 \, [\, lbm.ft / lbf.s^2 \,]$

5.7.3. Wall Friction Force

The flow of fluid through a pipeline is resisted by the frictional force between the fluid and the pipe wall. The magnitude of the force is a function of the surface area of contact and a friction factor, which depends on the pipe roughness and the Reynolds number.

$$F_{wz} = A_{wz} f_w \frac{\rho |\bar{v}| \bar{v}}{2 g_c} \tag{5.140}$$

where:

$$A_{wz} = \frac{total\ wall\ area}{total\ volume} = \frac{2\pi.r.\Delta z}{\pi.r^2.\Delta z} = \frac{4}{d} \tag{5.141}$$

and:

f_w : friction factor, [dimensionless]

For laminar flow, the friction factor is given by:

$$f_w = \frac{16}{\mathrm{Re}} \tag{5.142}$$

And for turbulent flow, f_w is given by Chen's equation (1979):

$$\frac{1}{\sqrt{f_w}} = -4\log\left[\frac{(\xi/D)}{3.7065} - \frac{5.0452}{\mathrm{Re}}\log\left(\frac{(\xi/D)^{1.1098}}{2.82257} + \frac{5.8506}{\mathrm{Re}^{0.8981}} \right) \right] \tag{5.143}$$

where:

ξ : roughness of the pipe, $[\ ft\ ]$

D : diameter of the pipe, $[\ ft\ \ ]$

The Reynolds number is defined as:

$$N_{\mathrm{Re}} = \frac{\rho.\bar{v}.D}{\mu} \tag{5.144}$$

5.7.4. Heat Transfer Term

The heat transfer between the system and its surroundings depends on the temperature differential between the fluid and the surroundings. It is a function of the overall heat transfer coefficient (U_{ht}), which lumps all the effects of convection, radiation and conduction through the pipe from or to the environment.

$$Q_t = \frac{U_{ht} \times (total\ wall\ area) \times (T_s - T)}{total\ volume} = \frac{U_{ht} \times (2\pi.r.\Delta z) \times (T_s - T)}{\pi.r^2.\Delta z} = \frac{4U_{ht}(T_s - T)}{d}$$

$$\tag{5.145}$$

where:

U_{ht} : Overall heat transfer coefficient, $[\ BTU\ /\ s.ft^2.°R\ ]$

T_s : Surroundings temperature, $[°R\ ]$

Note that Q_t is positive when the system is taking heat from the environment ($T < T_s$).

Chapter 6

APPLICATION TO SINGLE PIPELINES

The system of PDEs expressed by Equations (5.3), (5.4), (5.5) and (5.8) with the set of boundary conditions described in section 5.6 represents the problem of flow through a pipeline. For validation purposes, the proposed model was used to solve this problem. The solution of three case studies is presented in this chapter.

6.1. Gas Mixture Description

The following case studies were solved using the fluid described in Table 6.1. This is a hypothetical gas mixture presented by Vincent (1988), and then used by Ayala (2001). This fluid is a modification of the retrograde gas used by Furukawa *et al* (1986), which represents the mixture fluid of an offshore pipeline in the North Sea.

Table 6.1. Composition of the original gas mixture (Furukawa *et al*, 1986).

Component	z_i
N_2	0.0101
CO_2	0.0032
CH_4	0.7557
C_2H_6	0.1122
C_3H_8	0.0778
$i\text{-}C_4H_{10}$	0.0078
$n\text{-}C_4H_{10}$	0.0171
$i\text{-}C_5H_{12}$	0.0028
$n\text{-}C_5H_{12}$	0.0031
Pseudo-1	0.0041
Pseudo-2	0.0033
Pseudo-3	0.0028

In order to reduce the computation time, Vincent (1988) lumped these components into 3-pseudo components, whose properties are presented in Tables 6.2 and 6.3. The properties of the lumped components were determined by adjusting them to fit the phase envelope of the real mixture.

Table 6.2. Properties of the pure components (Vincent, 1988).

Name	z_i	Pc_i(psia)	Tc_i(°R)	w_i	MW_i	Vc_i(ft^3/lbm)
Lumped-1	0.7658	665.47	341.80	0.01075	16.201	0.09817
Lumped-2	0.2240	659.73	630.80	0.13420	39.368	0.07460
Lumped-3	0.0120	230.00	1300.00	0.19000	130.000	0.06683

Table 6.3. Interaction Coefficients (Vincent, 1988).

	Lumped-1	Lumped-2	Lumped-3
Lumped-1	0.00000	0.01800	0.03900
Lumped-2	0.01800	0.00000	0.00500
Lumped-3	0.03900	0.00500	0.00000

For benchmarking purposes both the one-dimensional, and the two-dimensional models are validated using a horizontal pipeline which data is summarized in Table 6.4.

Table 6.4. Pipeline Data

Case Study	1	2	3
Model	1D	2D	2D
Pipeline Length	1 mile (5280 ft)	200 ft	100 ft
Number of nodes in z-direction	528	21	41
Internal pipe diameter	27.75 inches		
Number of nodes in r-direction	-	8, 15	8
Wall Roughness	0.0008 ft		
Overall Heat Transfer Coefficient	0.33 BTU/hr.ft^2.°R		

The horizontal case studies presented in here are similar to the ones proposed by Vincent (1988) and also used by Ayala (2001). The only difference is the length of the pipeline. Since this study is interested in single phase natural gas and transient flow, only a section where one-phase exists (5280 ft for the one-dimensional case) is utilized. Moreover, due to the computational time required for the two-dimensional model shorter pipelines (200 ft and 100 ft) are used. The inlet conditions for all the cases are provided in Table 6.5.

Table 6.5. Conditions for the case studies

Flow Rate	544 MMSCF/D
Inlet pressure	2050 psia
Inlet temperature	240 ºF
Temperature of the environment	80 ºF

6.2. Case Study 1 – 1D Sudden Valve Closure

To validate the one-dimensional transient model, the valve closure problem is solved. This test simulates a strong pulse generated at the outlet by suddenly closing the valve which makes the mass flux equal to zero. This is:

$$U_{2_{(Nz)}} = (\rho v_z)_{(Nz)} = 0 \tag{6.1}$$

Again, due to the high-order accuracy of the numerical scheme, information is required to be known at the penultimate node (j=Nz-1).

$$U_{2_{(Nz-1)}} = \frac{U_{2_{(Nz-2)}} + U_{2_{(Nz)}}}{2} \tag{6.2}$$

For this single-phase system a shock wave is generated in the system and then propagated back to the inlet of the pipe. The purpose of this test is to track the simulated backward propagation of the shock wave and then compare the location to the exact solution. This experiment will help us to verify the numerical handling of the hyperbolic system of equations.

For the one-dimensional case, the Euler's inviscid equations are solved, which neglect the dissipative effects of viscous fluid flow, therefore the shock waves propagate as a sharp discontinuity. Additionally, the location of the wave can be determined knowing the speed of the backward propagating shock wave ($v_z - c$), where c represent the speed of sound.

Figures 6.1 to 6.6 show the solution profiles for the one-dimensional case. These profiles are given from the steady-state solution (bold straight line), before the outlet valve was closed, to 2.5 seconds where each curve represents times that are 0.5 seconds apart, after the valve closure.

Figure 6.1 shows the mass flux going to zero at the outlet node, but in the previous nodes the mass flux does not go to zero due to the continuous compression experienced by the gas. This is consistent with the increase in pressure at these nodes as shown in Figure 6.2. Due to the same effect, density also suddenly rises after the valve closure as represented in Figure 6.3.

Since the mass flux decreases during the backward propagation while the density increases, the velocity of the fluid must decrease as shown in Figure 6.4. The shock propagation in the system makes the temperature increase (Figure 6.5) as a result of the Joule Thompson effect which is caused by the pressure increment. This process also causes the internal energy to rise as seen on Figure 6.6.

So far, the model has proven to be able to predict the hydrodynamic behavior of the natural gas system. No numerical dispersion at the shock fronts is seen on the results, and they show high resolution by avoiding smearing of the solution.
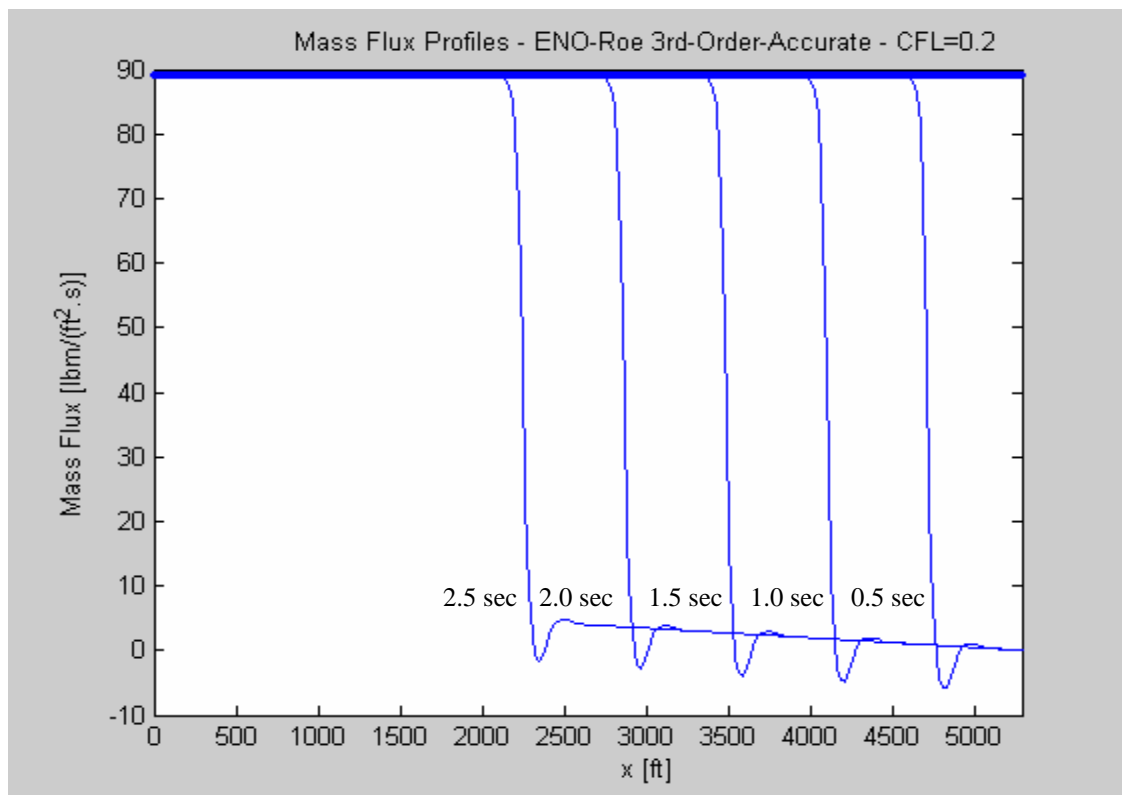
Figure 6.1. Mass Flux 2.5 seconds after valve closure.
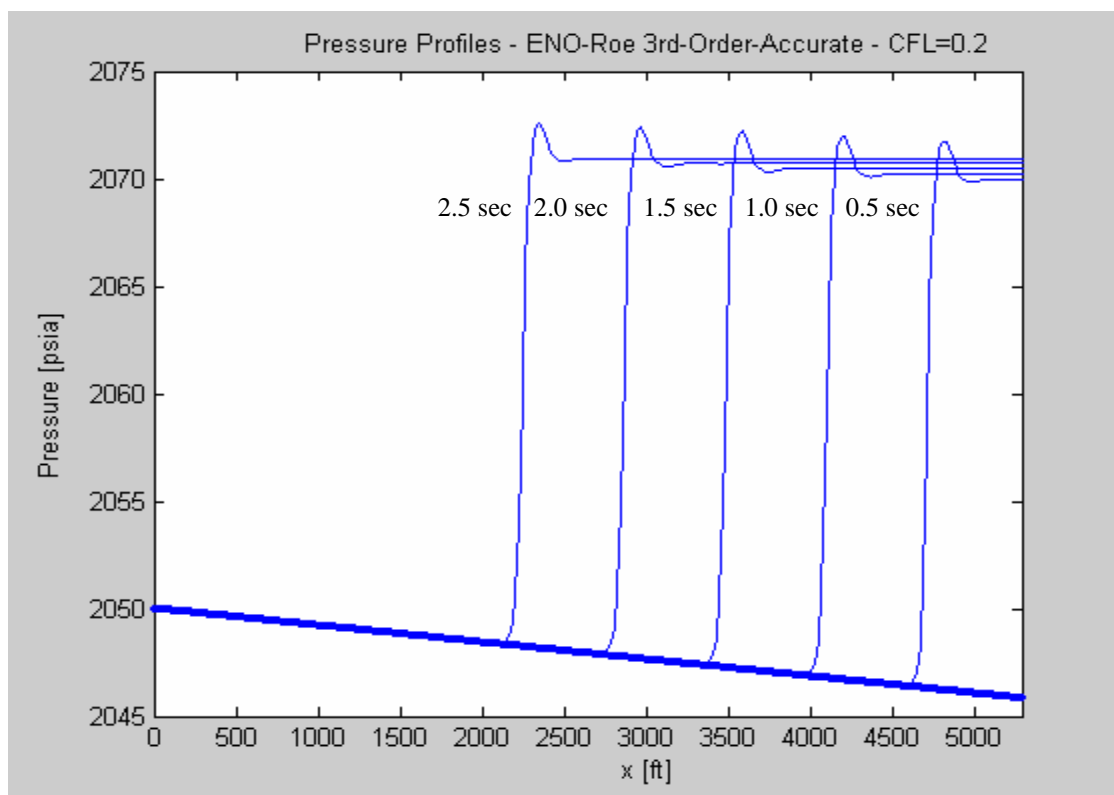
Figure 6.2. Pressure profiles 2.5 seconds after valve closure.
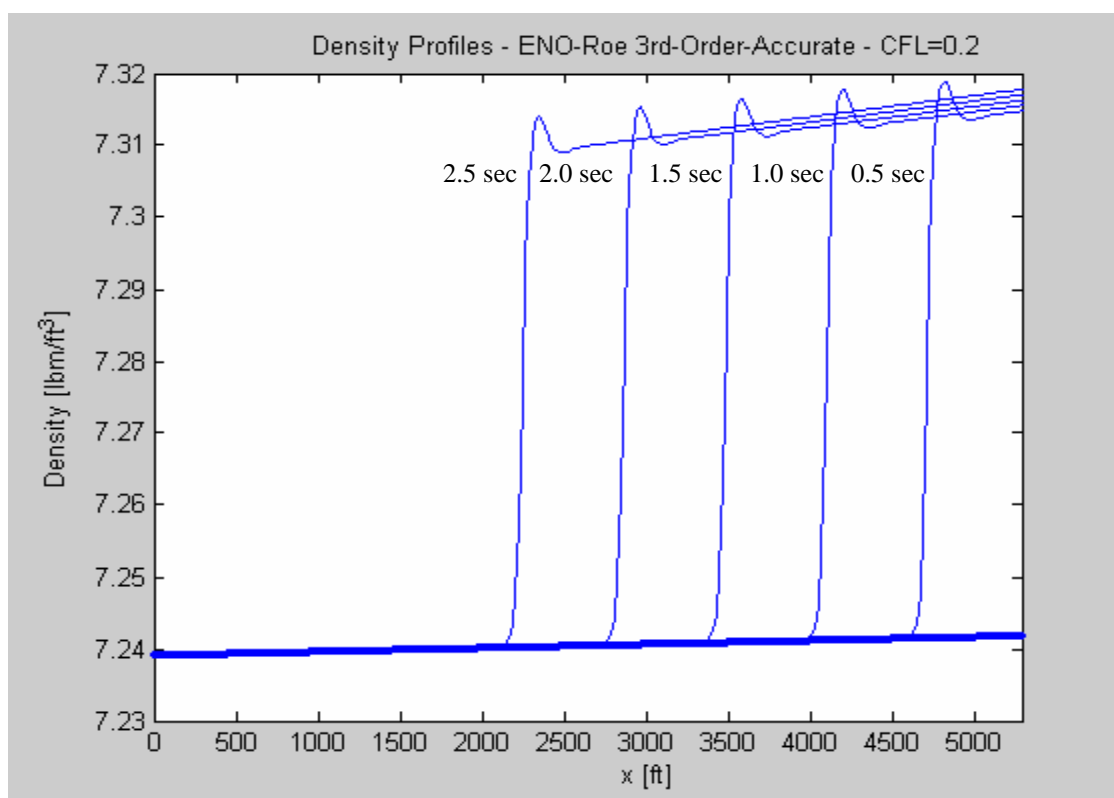
Figure 6.3. Density profiles 2.5 seconds after valve closure.
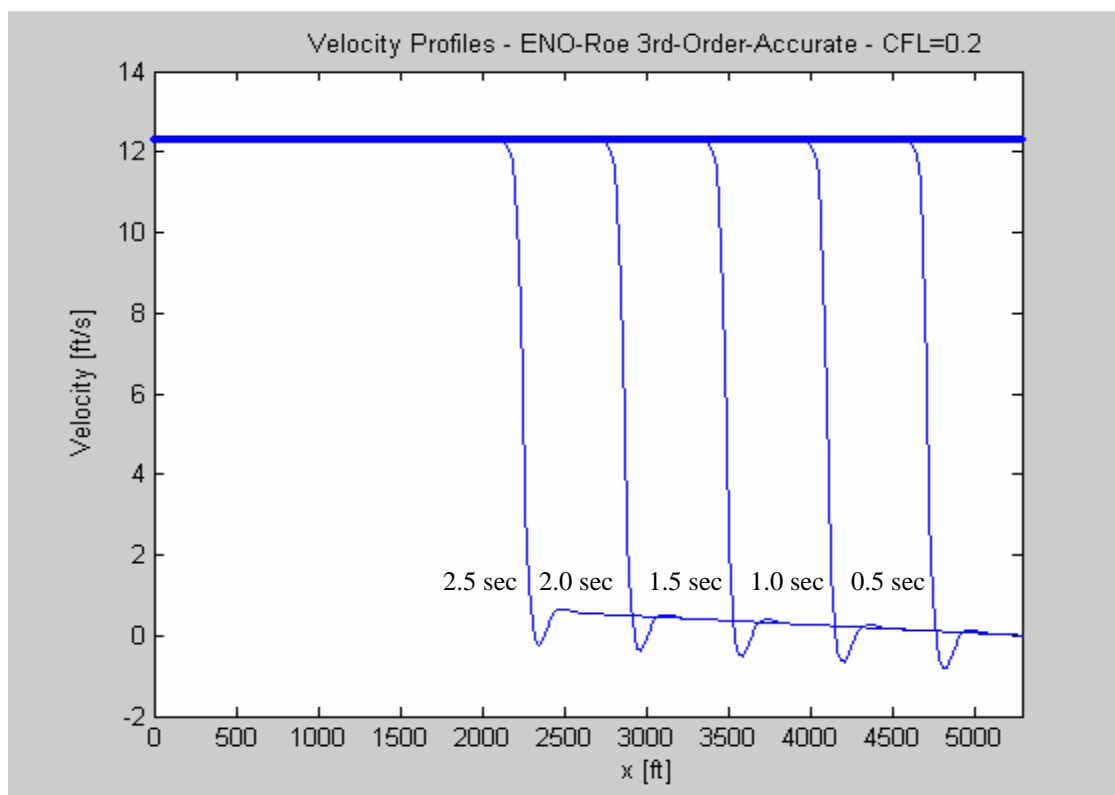
Figure 6.4. Velocity profiles 2.5 seconds after valve closure.
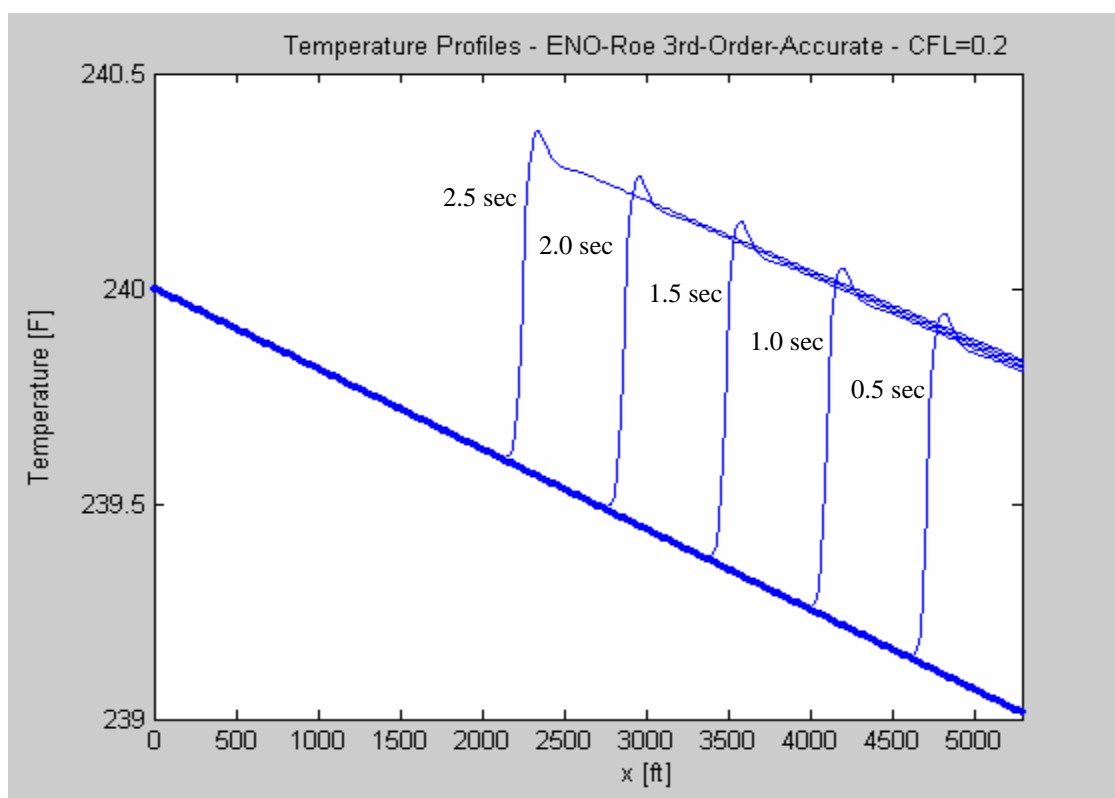
Figure 6.5. Temperature profiles 2.5 seconds after valve closure.
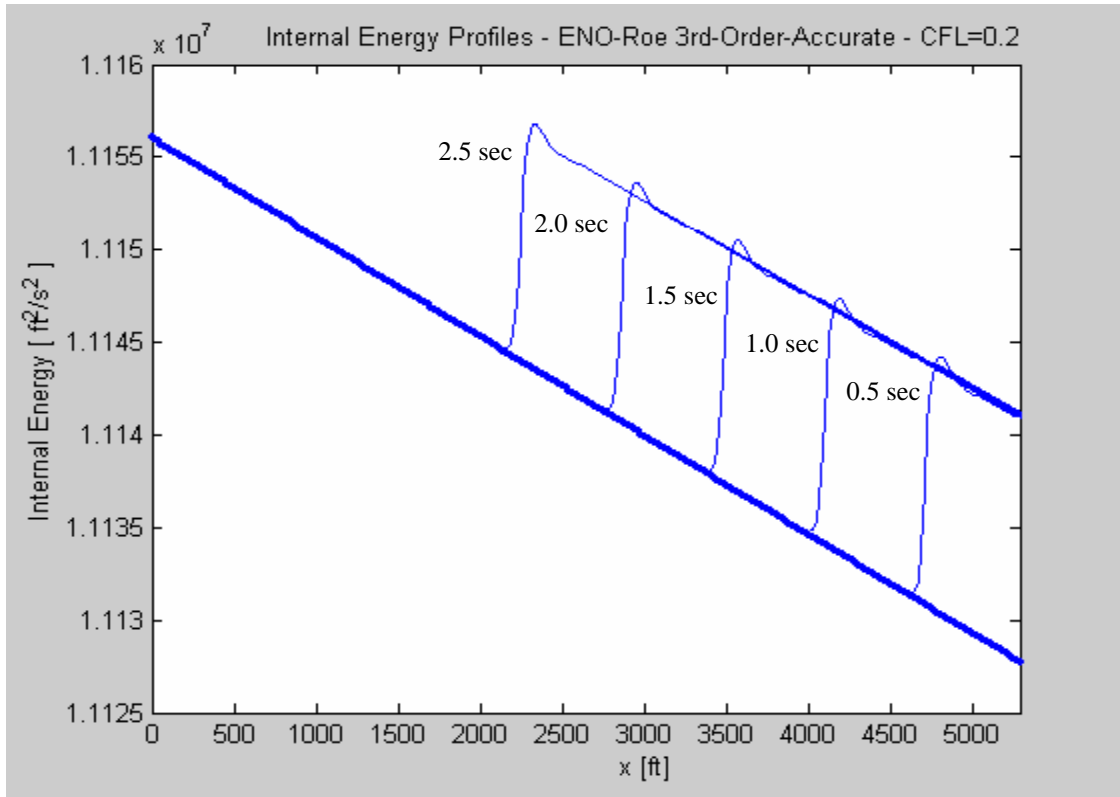
Figure 6.6. Internal Energy profiles 2.5 seconds after valve closure.

6.2.1. Quality of the Solution

Examining the profiles obtained using the one-dimensional model, presented in Figures 6.1 to 6.6 we can observe "bumps" at the fronts, which at first thought might look as oscillations. However, after performing several numerical experiments we have found that these bumps are in fact part of the solution.

For the case of the velocity profiles it is obvious that these bumps represent negative values of velocity on the fronts which are expected since the shock waves are back propagating towards the inlet of the pipe. On the other hand, this phenomenon observed in the density profiles is not as trivial to explain as in the case of the velocity. As explained before, the shocks are back propagating towards the inlet with negative velocity, while the rest unperturbed fluid is still moving downstream in their original direction with positive velocity. At the front, the two flow streams collide and this causes a compression effect that makes the pressure to increase more than in the rest of the domain, and therefore the density rises along with the temperature.
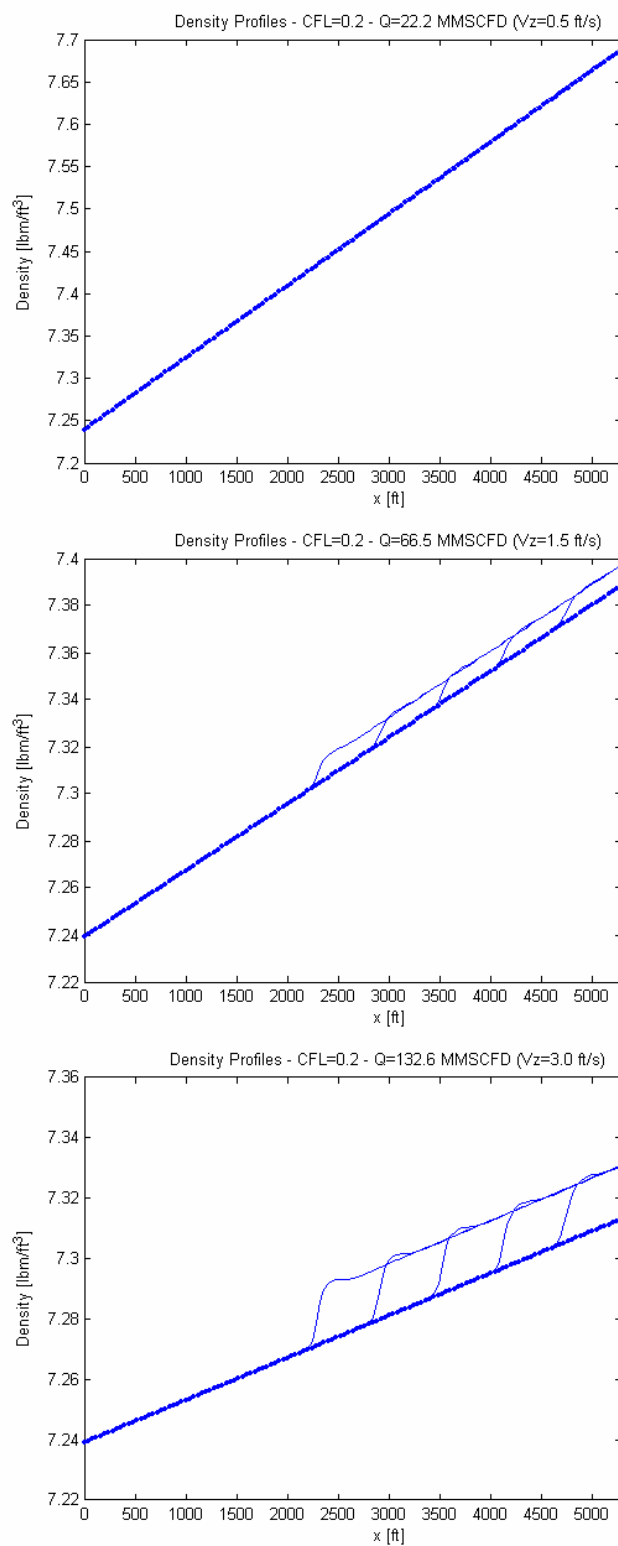
Figure 6.7. Density profiles for a variety of flow rates.
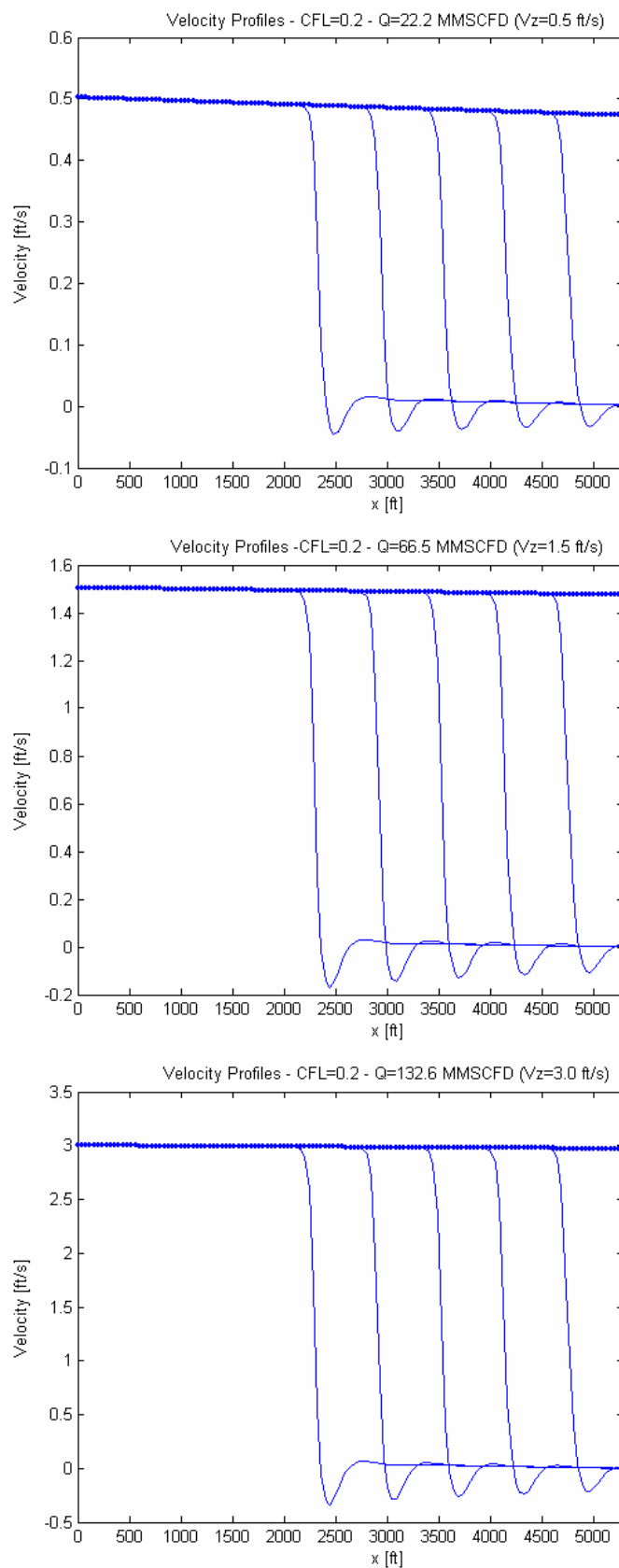
Figure 6.8. Velocity profiles for a variety of flow rates.

In order to prove this, we have run tests similar to the previous one, but varying the flow rate at the inlet. For very small velocities we expect the compression effect to be almost non-existent as it would happen for near zero velocities. Moreover, when increasing the velocity the bumps should start appearing in the solution as a result of the compression phenomenon becoming stronger. However, even for small velocities, negative values (represented by bumps) should always be present at the fronts in order to make the fluid to back propagate. Figure 6.7 shows the density profiles for three different inlet velocities, namely 0.5, 1.5 and 3.0 ft/s, while Figure 6.8 presents the corresponding velocity profiles. We can observe the phenomenon previously explained which make us realize that this bumps at the fronts are in fact part of the solution.

6.3. Case Study 2 – 2D Steady-State Conditions

When a fluid enters a pipeline from a source (tank, reservoir, etc) using or not a propulsion device (pump, turbine, etc) the velocity distribution in the cross-sections of the "inlet length" varies with the distance from the initial cross-section (Schlichting, 1968). For the cross-sections located near the inlet, the distribution is almost uniform, but further downstream due to the effect of friction the velocity distribution changes until a fully developed profile occurs at a given section and remains constant for the remaining length of the pipe.

According to Schlichting (1968), for laminar flow the length where a fully developed flow is attained ranges between 150 to 300 pipe diameters. This distance is called "inlet length". For the case of turbulent flow the range varies from 25 to 100 pipe diameters.

When fully developed turbulent profile prevails, the 1/7-th-power law (Equation 6.3) can approximate the velocity profile, which is no longer parabolic as in the laminar case, but rather flat since the viscous contribution is important only in the vicinity of the wall

$$v_z(r) = v_{z,max} \cdot \left(1 - \frac{r}{R}\right)^{1/7} \tag{6.3}$$

The present case study is designed to show how a pipeline, with uniform velocity profiles as initial condition everywhere, develops a turbulent fully developed profile after the two-

dimensional model is run. Additionally, we can observe the inlet length of the pipeline into consideration.

Figure 6.9 shows the axial velocity profiles at different cross sections in the pipeline. The dotted line represents the inlet velocity profile which is a uniform distribution imposed as the boundary condition. As the distance from the inlet increases, the velocity monotonically decreases due to the friction effects. The solid lines represent the velocity profiles at the cross sections located at 50, 100, 150, and 200 feet from the inlet. The fully developed turbulent profile can be appreciated clearly at those locations.

From Figure 6.10 the inlet length of this case can be seen to be approximately 50 feet. The dotted line represents the velocity distribution along the vicinity of the wall pipe, while the dashed line represents the velocity distribution along the axis of the pipe. It is clear that after 50 feet the difference between both velocity profiles is constant confirming that a fully developed flow has been attained.

Figure 6.9. Axial Velocity profiles at different cross-sections, Nr=8.
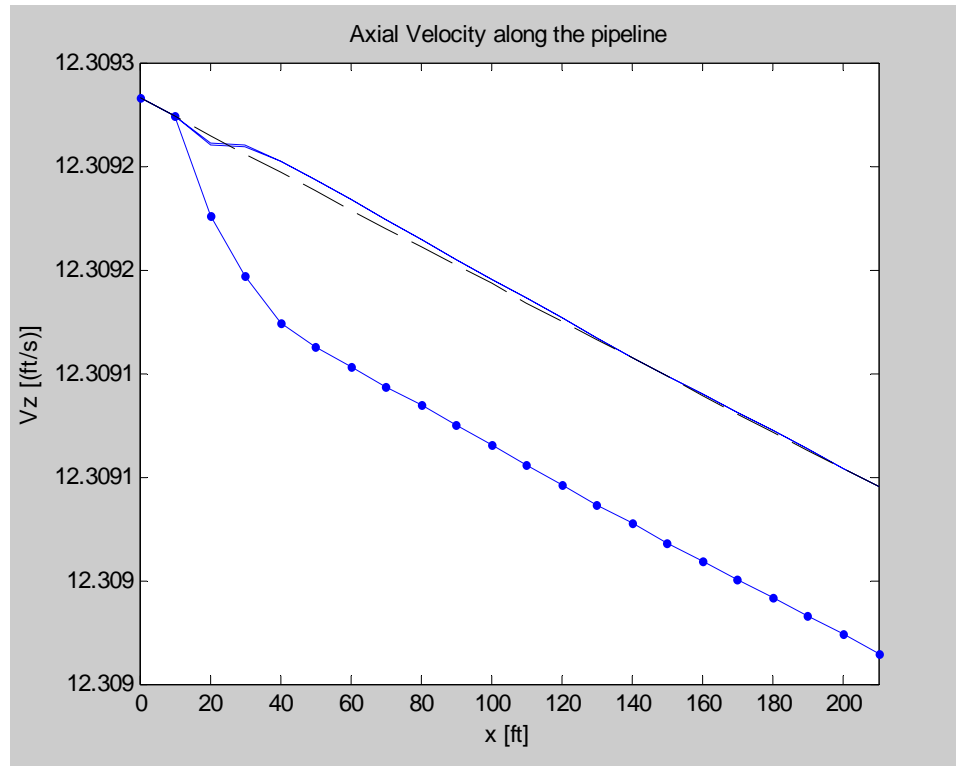
Figure 6.10. Axial Velocity along the pipeline, Nr=8.

Figures 6.11 to 6.13 show profiles at several cross-sections. The dotted lines represent the profiles at the inlet, and the solid lines show the profiles in increments of 50 feet from the inlet of the pipe. Additionally, distributions along the pipeline, at the vicinity of the wall and at the axis of the pipe are also plotted for the thermodynamic properties density, pressure and temperature. Note that there is no appreciable variation of these properties at any given cross section.

Note in Figure 6.11 the radial velocity profiles at different cross-sections and the distribution along the pipeline. Irregular radial fluctuations can be seeing in the axial motion, showing that the fluid does not move along straight lines and there is no regularity in the motion. This is one of the essential differences between one- and two-dimensional flow.
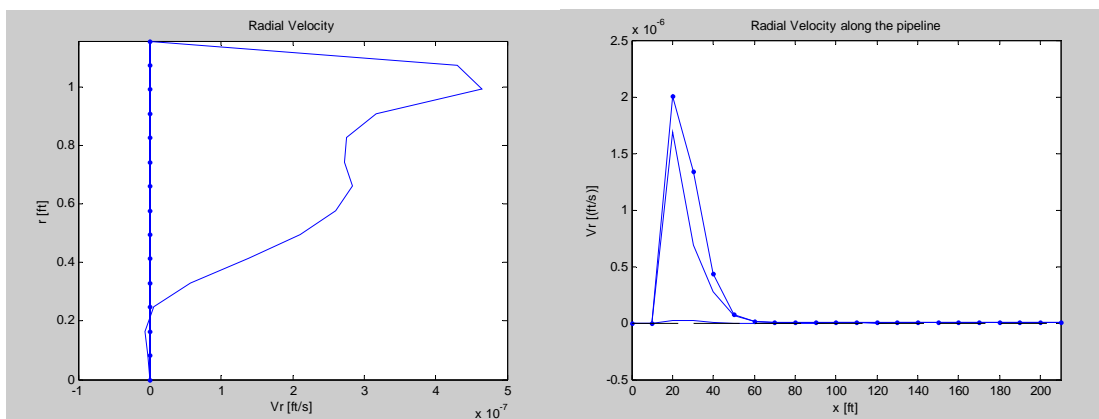
Figure 6.11. Radial Velocity profiles at (a) different cross sections and (b) along the pipe.
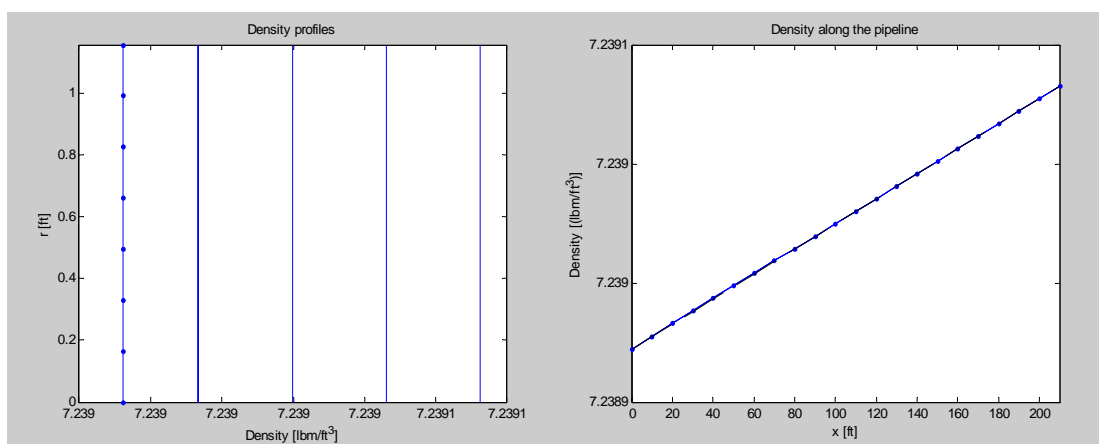
Figure 6.12. Density profiles at (a) different cross sections and (b) along the pipe.
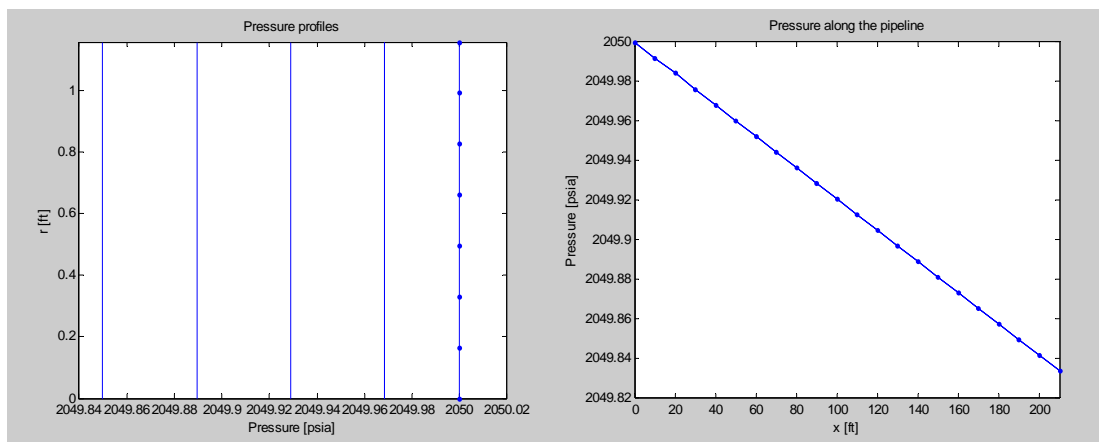
Figure 6.13. Pressure profiles at (a) different cross sections and (b) along the pipe.
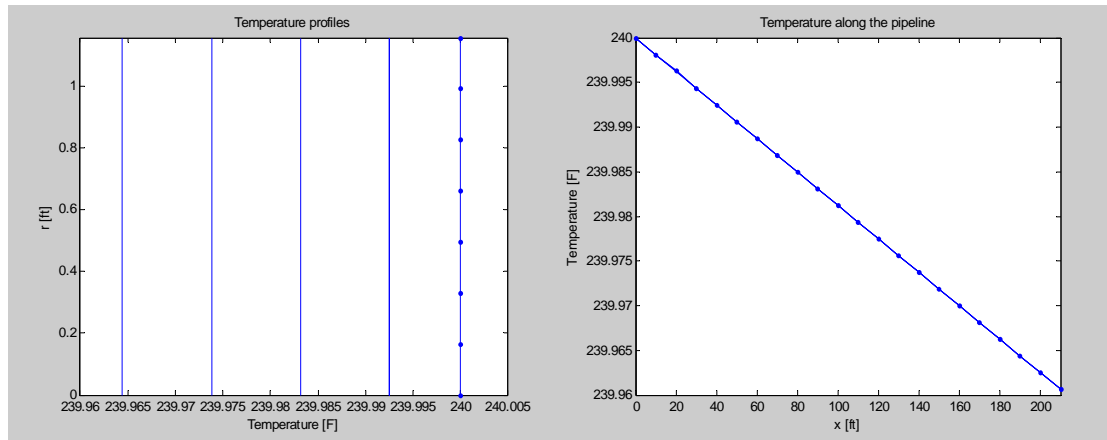
Figure 6.14. Temperature profiles at (a) different cross sections and (b) along the pipe.

For comparison purposes the previous experiment has been repeated but using a finer space discretization in the radial direction. This time 15 nodes instead of 8 are used in the r-direction. Figure 6.15 shows the axial velocity profiles at different cross sections in the pipeline, where again the dotted line represents the inlet velocity profile which is an imposed uniform distribution. The solid lines represent the velocity profiles at the cross sections located at 50, 100, 150, and 200 feet from the inlet, which monotonically decreases with distance due to the friction effects. As in the previous test with coarser grid, a turbulent fully developed flow can be appreciated, and Figure 6.16 shows the inlet length being also about 50 feet, confirming the results obtained previously. The dotted line represents the velocity distribution along the vicinity of the wall pipe, while the dashed line represents the velocity distribution along the axis of the pipe.
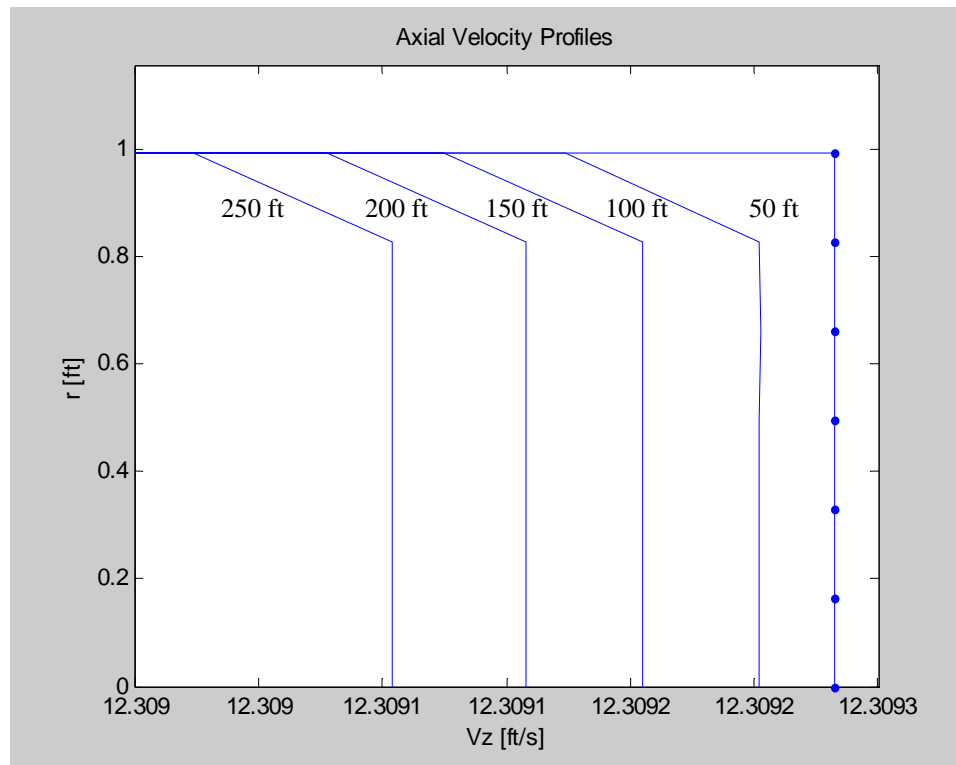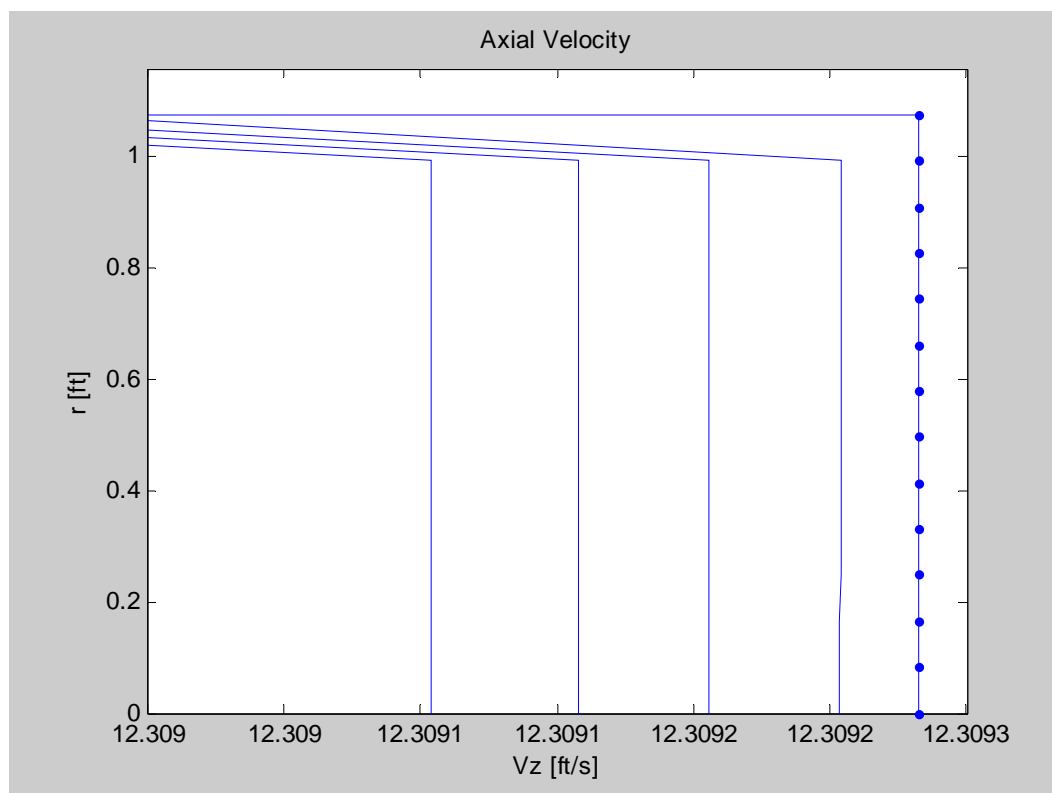
Figure 6.15. Axial Velocity profiles at different cross-sections, Nr=15.
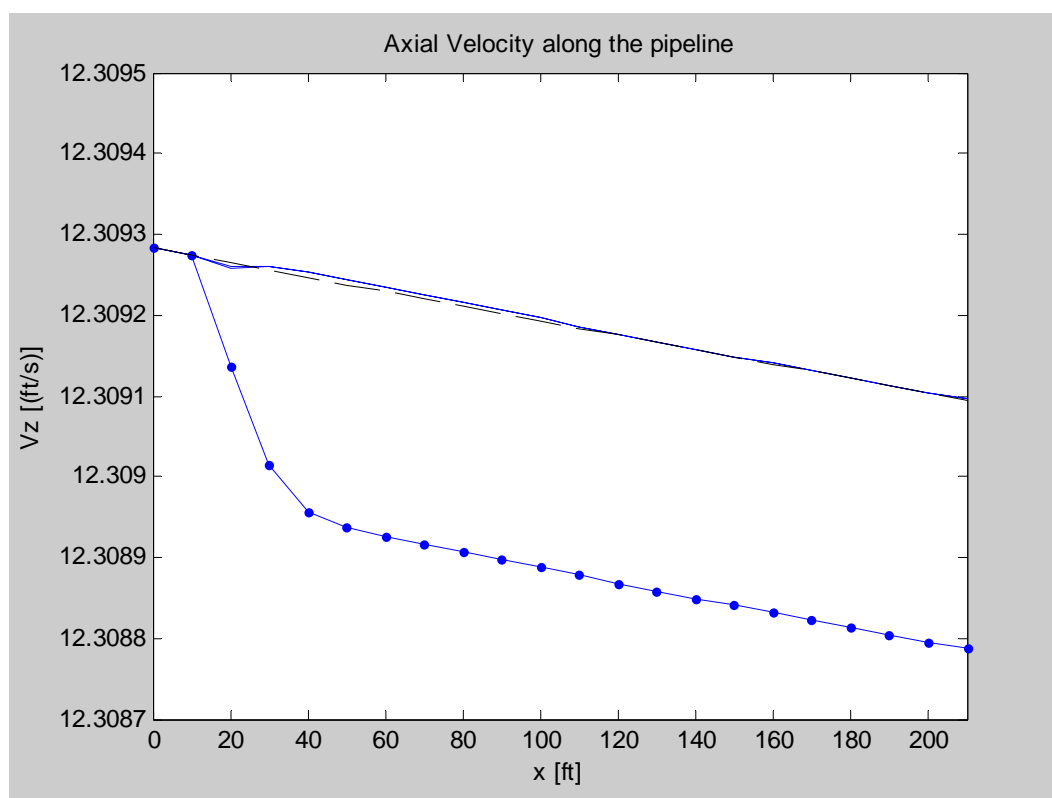
Figure 6.16. Axial Velocity along the pipeline, Nr=15.

6.4. Case Study 3 – 2D Sudden Valve Closure

At this point, the sudden valve closure problem is solved using the two-dimensional model. A strong pulse is generated at the outlet when the valve is suddenly closed, which is imposed by making the mass flux equal to zero. The boundary conditions are:

$$U_{2_{(i,Nz)}} = (\rho v_r)_{(i,Nz)} = 0 \tag{6.4}$$

$$U_{3_{(i,Nz)}} = (\rho v_z)_{(i,Nz)} = 0 \tag{6.5}$$

At the penultimate nodes (j=Nz-1), the following conditions are applied:

$$U_{2_{(i,Nz-1)}} = \frac{U_{2_{(i,Nz-2)}} + U_{2_{(i,Nz)}}}{2} \tag{6.6}$$

$$U_{3_{(i,Nz-1)}} = \frac{U_{3_{(i,Nz-2)}} + U_{3_{(i,Nz)}}}{2} \tag{6.7}$$

As in the first case study, the shock wave generated in the system propagates back to the inlet of the pipe. This shock is tracked during the backward propagation to check its location, allowing us to assess the numerical capabilities of the solver.

In this case, the Navier-Stokes viscous equations are solved, and in contrast with the one-dimensional case, the dissipative effects of viscous fluid flow are taken into consideration, therefore the shock waves does not propagate as sharp as in the first case study.

Additionally, for comparison purposes, average properties for each cross section (constant j) are calculated and compared with the equivalent one-dimensional solution. These are:

$$\overline{(\rho.v_z^2)}_{(j)} = \frac{\int_0^R \rho v_z^2 . 2\pi r dr}{\int_0^R 2\pi r dr} = \frac{\sum_{i=1}^{Nr-1}\left(\left(\rho_{(i,j)}v_{z_{(i,j)}}^2 r_{(i)} + \rho_{(i+1,j)}v_{z_{(i+1,j)}}^2 r_{(i+1)}\right)\cdot \Delta r\right)}{R^2} \tag{6.8}$$

$$\overline{p}_{(j)} = \frac{\int_0^R p.2\pi r dr}{\int_0^R 2\pi r dr} = \frac{\sum_{i=1}^{Nr-1}\left((p_{(i,j)}r_{(i)} + p_{(i+1,j)}r_{(i+1)})\cdot\Delta r\right)}{R^2} \tag{6.9}$$

$$\overline{\rho}_{(j)} = \frac{\int_0^R \rho.2\pi r dr}{\int_0^R 2\pi r dr} = \frac{\sum_{i=1}^{Nr-1}\left((\rho_{(i,j)}r_{(i)} + \rho_{(i+1,j)}r_{(i+1)})\cdot\Delta r\right)}{R^2} \tag{6.10}$$

$$\overline{v}_{z(j)} = \frac{\int_0^R v_z.2\pi r dr}{\int_0^R 2\pi r dr} = \frac{\sum_{i=1}^{Nr-1}\left((v_{z_{(i,j)}}r_{(i)} + v_{z_{(i+1,j)}}r_{(i+1)})\cdot\Delta r\right)}{R^2} \tag{6.11}$$

$$\overline{T}_{(j)} = \frac{\int_0^R T.2\pi r dr}{\int_0^R 2\pi r dr} = \frac{\sum_{i=1}^{Nr-1}\left((T_{(i,j)}r_{(i)} + T_{(i+1,j)}r_{(i+1)})\cdot\Delta r\right)}{R^2} \tag{6.12}$$

$$\overline{e}_{(j)} = \frac{\int_0^R e.2\pi r dr}{\int_0^R 2\pi r dr} = \frac{\sum_{i=1}^{Nr-1}\left((e_{(i,j)}r_{(i)} + e_{(i+1,j)}r_{(i+1)})\cdot\Delta r\right)}{R^2} \tag{6.13}$$

Due to the length of the pipe, the magnitude of the variations in the properties is not very large. However, they can be appreciated in Figure 6.17, where the initial conditions are plotted.

Figures 6.18 to 6.23 represent the solution profiles for the average properties. These solutions are given from the steady-state distribution (bold straight line), before the outlet valve was closed, to 0.05 seconds in intervals of 0.01 seconds, after the valve closure.

Similar to the one-dimensional case, the mass flux goes to zero at the outlet node, but in the previous nodes, as shown in Figure 6.18, the continuous compression experienced by the gas does not allow the mass flux to reach a zero value. Consistently, pressure and density suddenly rise at these nodes as shown in Figures 6.19 and 6.20 respectively. On the other hand, to compensate the effect of density increase in the mass flux, the velocity of the fluid must decrease during the back

propagation (Figure 6.21). Although the magnitude of the radial velocities is small, in Figure 6.22 we can appreciate the irregular fluctuations on the axial motion which are characteristic of turbulent flow.
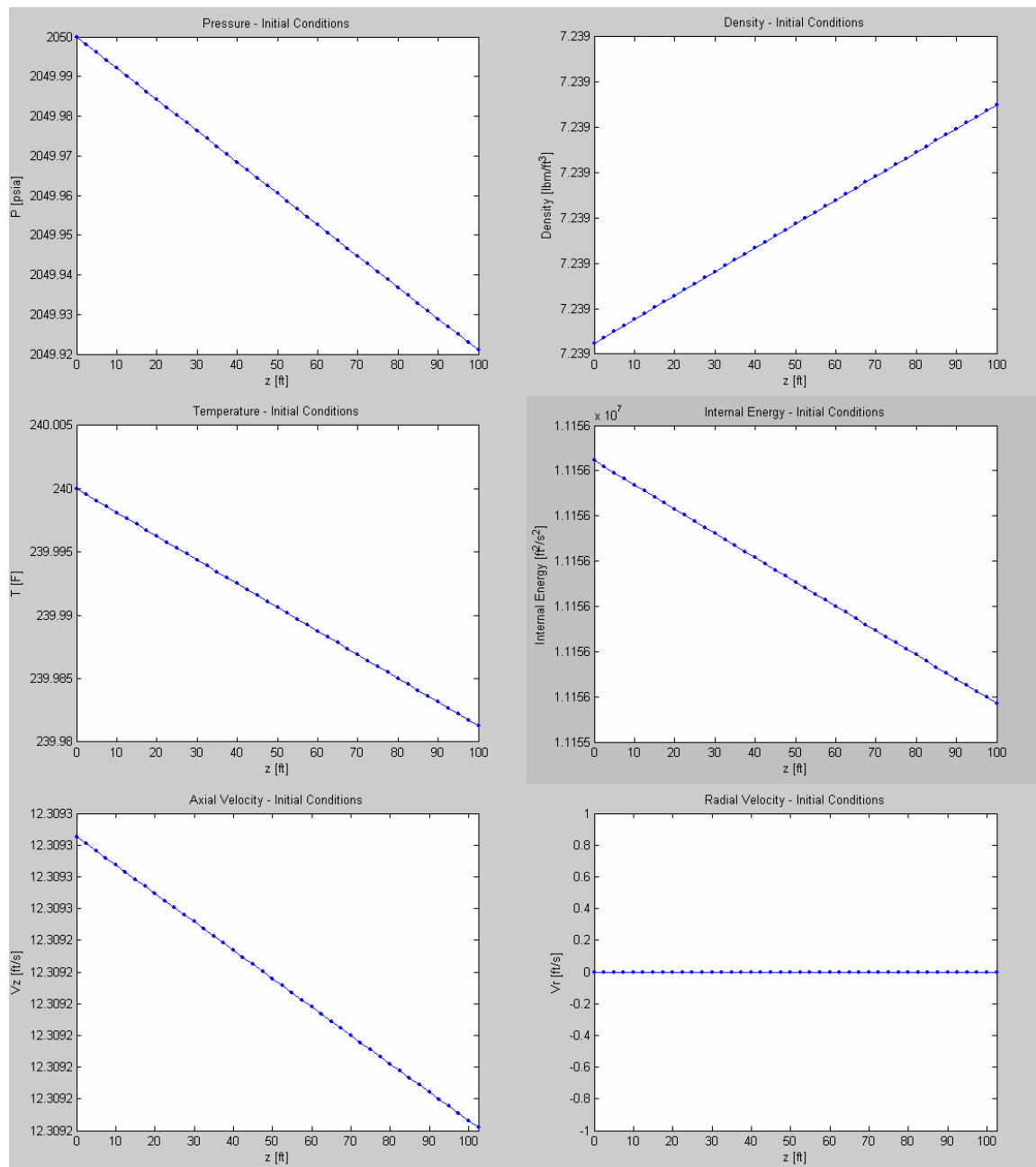
Figure 6.17. Initial Conditions for the case study 2.

Moreover, as a result of the propagation of the shock in the system, the temperature increases due to the Joule Thompson effect caused by the pressure rise (See Figure 6.23). Analogously, the internal energy suddenly rises as seen on Figure 6.24.

Comparing qualitatively all the profiles (Figures 6.18 to 6.24) with the result obtained in the one-dimensional case (Figure 6.1 to 6.6), we can appreciate that the discontinuities representing shock waves are not as sharp in this case study as in the first one. This is because the two-dimensional model uses the Navier-Stokes equations which take into consideration the dissipative effects of viscous fluid flow. This is one of the main differences between this set of equations and the inviscid Euler's equations.
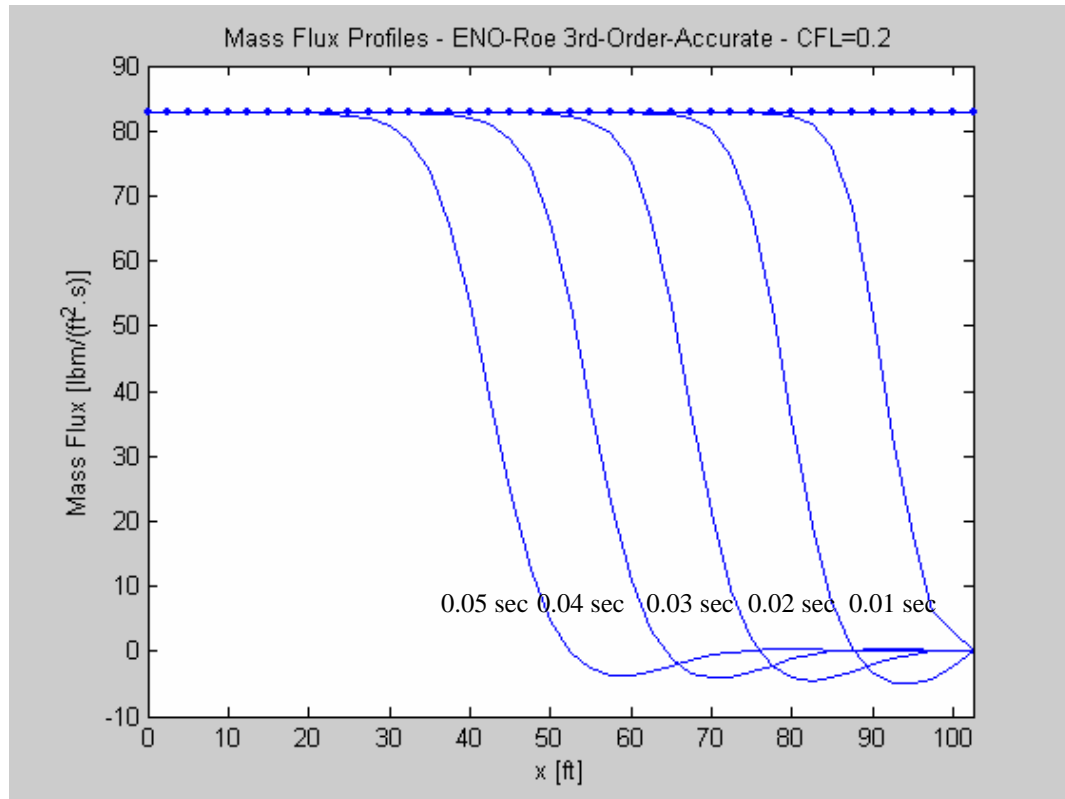
Figure 6.18. Average mass flux profiles 0.05 seconds after valve closure
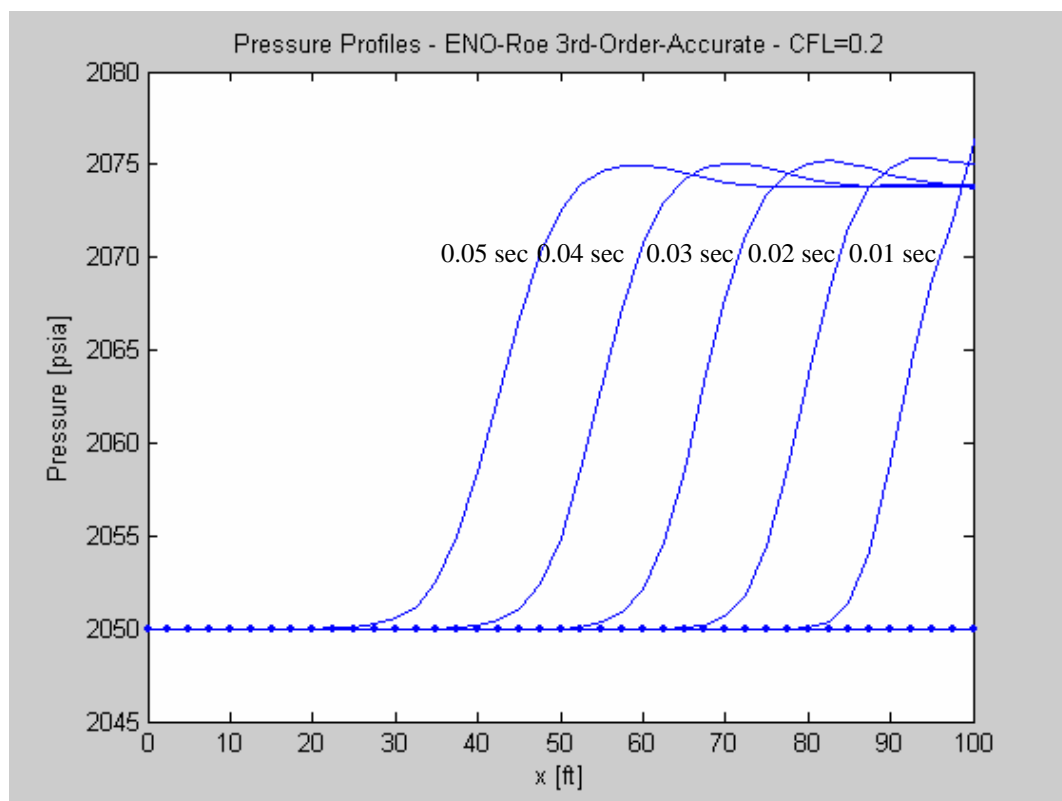
Figure 6.19. Average Pressure profiles 0.05 seconds after valve closure
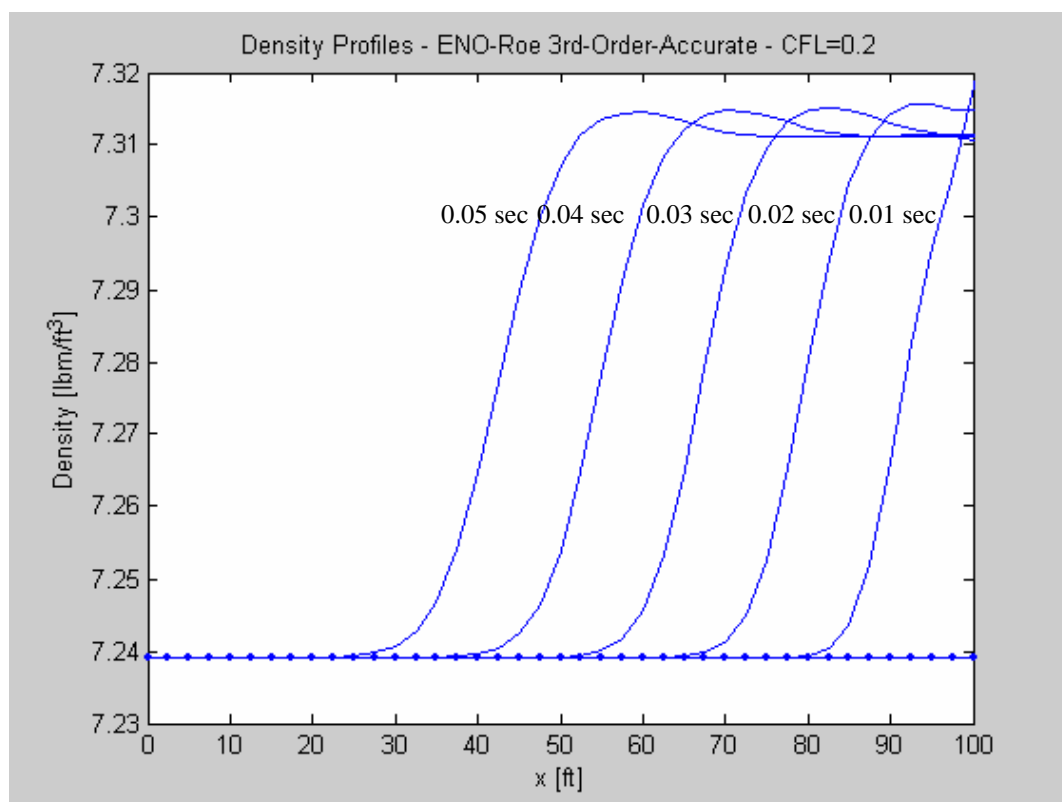
Figure 6.20. Average Density profiles 0.05 seconds after valve closure
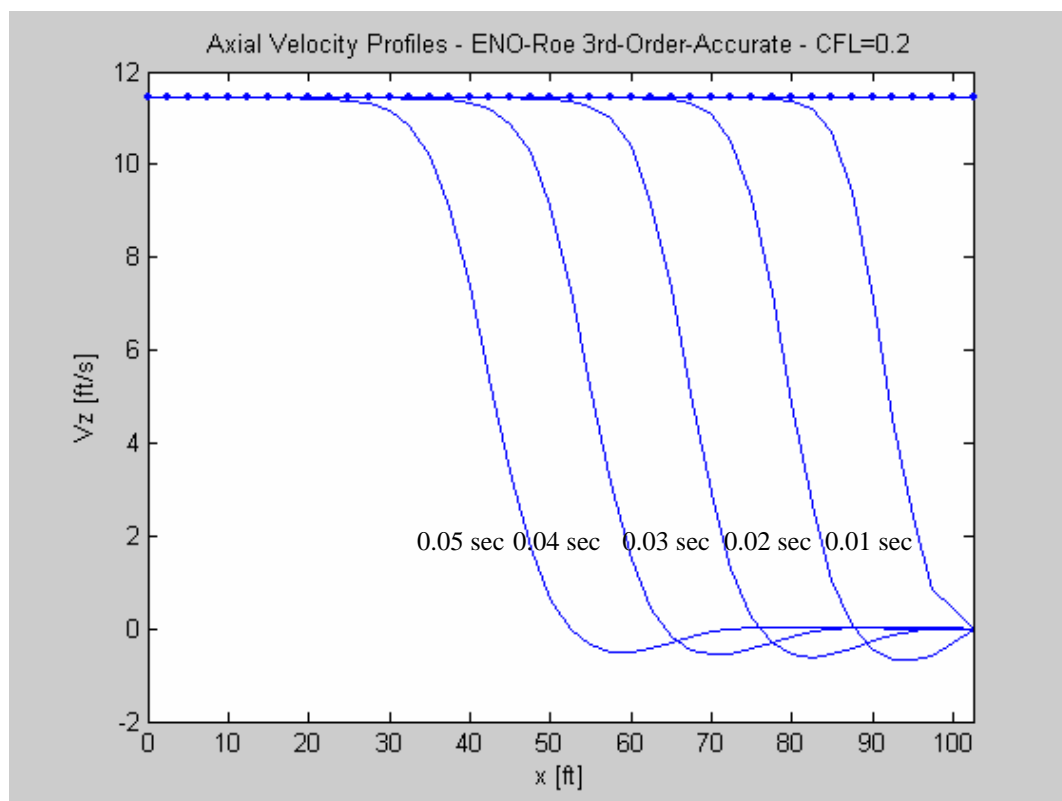
Figure 6.21. Average Axial Velocity profiles 0.05 seconds after valve closure
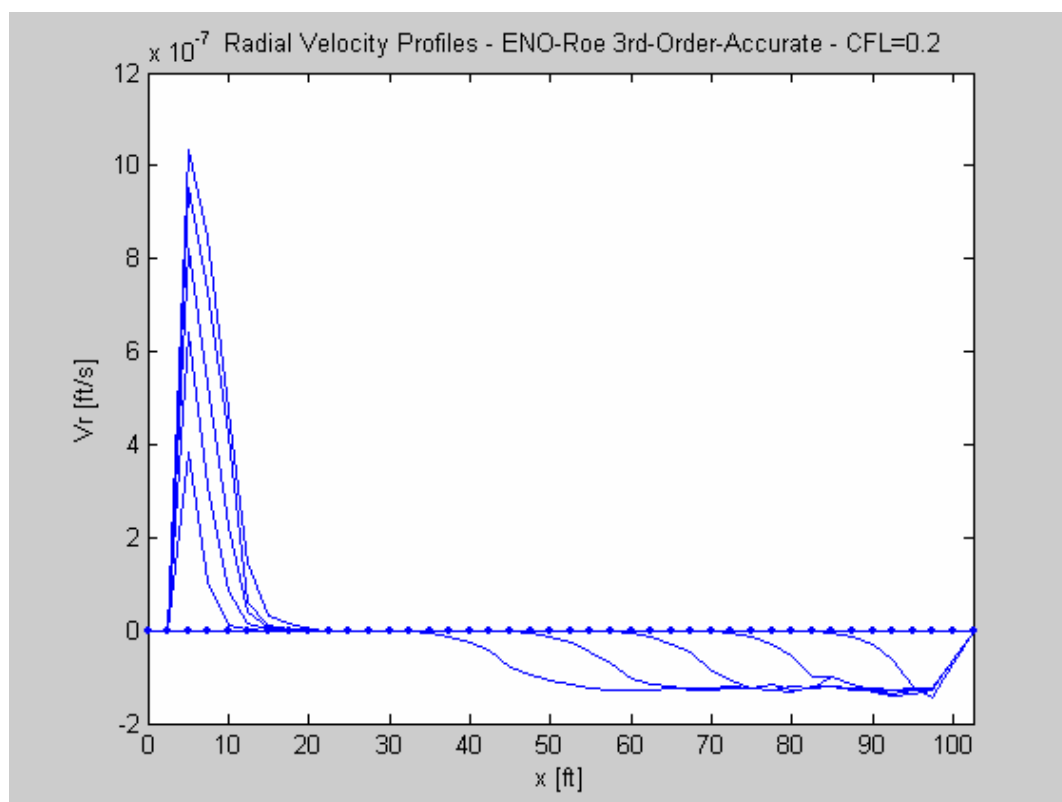
Figure 6.22. Average Radial Velocity profiles 0.05 seconds after valve closure
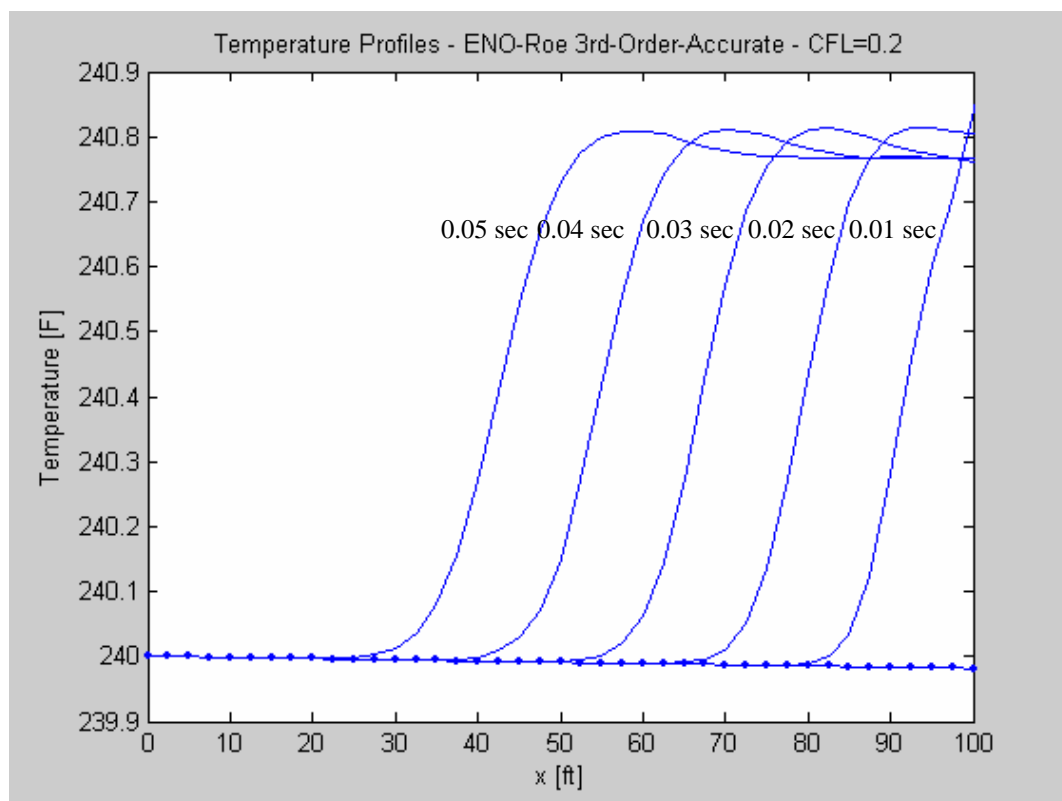
Figure 6.23. Average Temperature profiles 0.05 seconds after valve closure
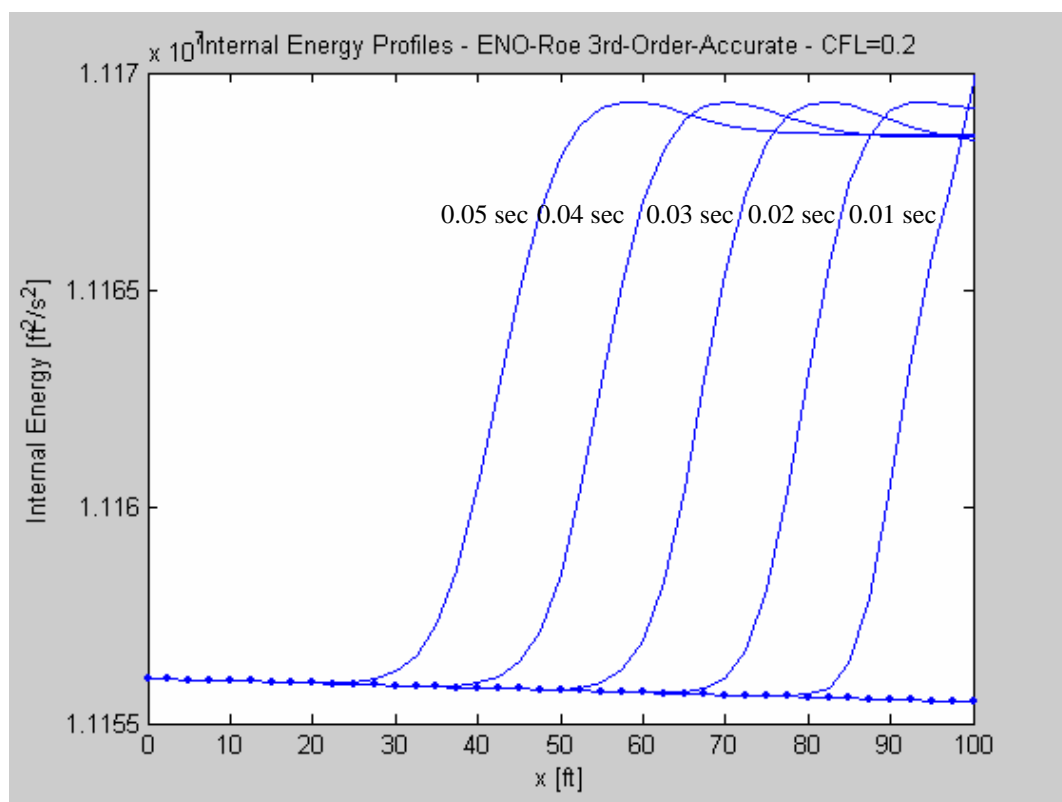
Figure 6.24. Average Internal Energy profiles 0.05 seconds after valve closure

6.5. Variation of CFL Number

The problem solved in the first case study is repeated here for a variety of CFL numbers (due to Courant-Friedrichs-Lewy) to determine the dependency of the solution of this factor. For these numerical experiments 264 gridpoints were used, for a space discretization of 20 feet. In Figure 6.25, density profiles for CFL numbers 0.05, 0.1 and 0.2 are shown. It is clear that for smaller CFL numbers, the shock resolution decreased due to the effect of numerical diffusion, which causes the solution to smear. Moreover, as the CFL increases, the solution is sharper, but the undesirable appearance of spurious oscillations occurs.

6.6. Variation of the Order of Accuracy

The order of accuracy of the solution can be improved by adding more gridpoints when calculating the numerical approximation of the partial derivatives. The order of accuracy tells us how far the numerical solution is from the actual solution in terms of the space discretization ($\Delta r, \Delta z$). We are looking for a solution with enough accuracy to reproduce the actual result, specially the location of the shock waves which are the main feature of the solution of hyperbolic PDEs. For this purpose, we perform some numerical test varying the order of accuracy of the approximation. Figure 6.26 shows the density profiles for approximations of second, third and fourth order of accuracy. It can be seen that, for a fixed CFL number (0.2), as we increase the order of accuracy, the resolution of the fronts is improved. However, spurious oscillations start appearing in the solution.

6.7. Concluding Remarks

After a cost-benefit analysis, it was determined that in order to obtain solutions of fourth and fifth order of accuracy, the CFL numbers must be decreased to the order of 0.01 to 0.05. This will require smaller time steps which increase the CPU time. To achieve a balance of the resolution of the solution and the computational cost, we have selected a scheme of third order of accuracy for the problems solved in this study, and a CFL number of 0.2.

Recalling the importance of the CFL number (Equation 6.14), the resolution of the shock front and discontinuities is strongly related with this number. The CFL number bound the time step size ensuring that a discontinuity does not enter and leave a gridpoint during the same time step, allowing us in this way to account for the location of the front during that time step. This is done using both the size of the grid block (Δr, Δz) and the speed of propagation of the discontinuity which is given by the eigenvalues (λ_{max}^{n}) of the system of the governing equations being solved.

$$CFL = \frac{\Delta t \times \lambda_{max}^{n}}{\Delta x}$$ (6.14)

Note that for a given CFL number, larger grid blocks will require larger time steps but the averaging over that larger block will reduce the accuracy of the representation of the solution. On the contrary, smaller grid blocks will increase the accuracy of the solution but the time steps will be reduced causing longer simulation times and therefore greater CPU times, which sometimes are computationally impossible.

For all the experiments, a CFL number of 0.2 was used. After substantial numerical tests, it was determined that solutions for CFL numbers greater than 0.2 suffer the phenomenon of spurious oscillations. On the other hand, for smaller CFL number the solutions have less resolution, due to smearing caused by smaller time steps.
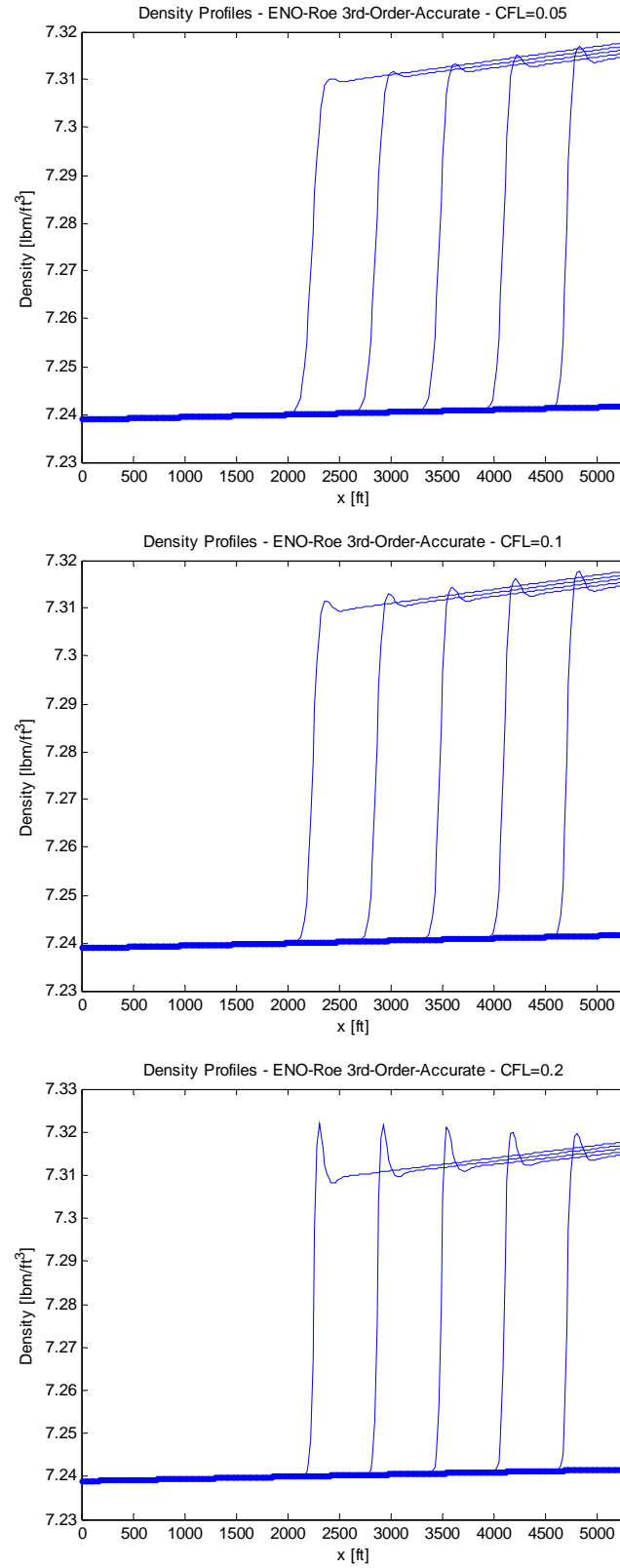
Figure 6.25. Comparison for density profiles using a variety of CFL numbers.
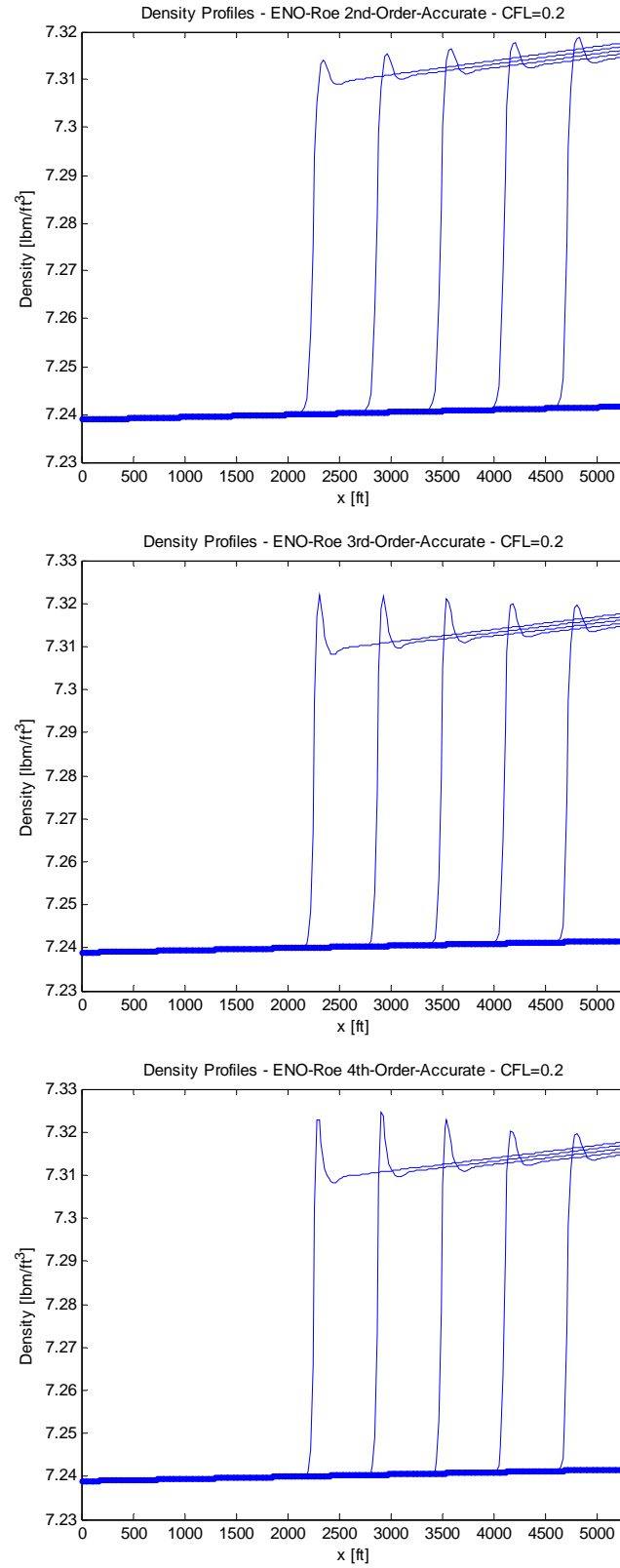
Figure 6.26. Comparison for density profiles using approximations of different order of accuracy.

Chapter 7

COMPARISON WITH EXPERIMENTAL DATA IN ORIFICE-METERS

To the best of the author's knowledge, no experimental data or no numerical predictions are currently available for the case of flow of natural gas through orifices. However experimental data is available for the case of air flow through orifice. It is important to emphasize that the thermodynamic properties of air are very different from those of hydrocarbon mixtures, and therefore different correlations are used to estimate them. Before the actual application of the model to the case of natural gas flow, a further validation process was performed in order to assess the capabilities of the model. For this purpose, measured data kindly supplied by Prof. Gerald Morrison of Texas A&M University (2006) was used. The data were obtained in an experimental facility, where a 3-D Laser Doppler Velocimeter (LDV) was utilized to collect data for axial and radial velocities at different cross-sections and various radial distances measured from the axis of the pipe. Their measurements were obtained for a 2-in diameter pipe and an orifice plate with a Beta ratio of 0.5. Air was supplied to the system at 10 in Hg (4.91 psig) and 300 K. The density at the inlet was determined to be 0.1009 lbm/ft^3 using the real gas law. The data was obtained for three different Reynolds numbers based on the diameter of the pipe and the mean axial velocity at the inlet, namely 18,400, 54,700 and 91,100. They are given in Table 7.1.

Table 7.1. Flow rates and mean velocities for the experimental Reynolds numbers.

Q [MSCF/D]	U_m [ft/s]	N_{Re}
33.500	13.4465	18,400
99.600	39.9783	54,700
165.900	66.5904	91,100

The complete description of the experimental facility as well as the process to acquire and process the data was presented by Panak (1990). He performed experiments for the Reynolds number of 54,700. Morrison (1989) had published results for a larger range of Reynolds number, from 18,400 to 128,000, and he addressed the need to use the experimental data as boundary conditions for predictions using a numerical model. Nail (1991) used the general purpose Fluent

program to get numerical results which he compared with the experimental data for air, obtaining a maximum relative error in the discharge coefficient close to 13%.

The transient model marches the solution in time until steady-state conditions are achieved, which occurs when the change in the maximum axial velocity within one timestep is less than 0.05% as suggested by Mattingly and Davis (1977). For modeling purposes, the present study uses Sutherland's formula (Crane, 1988) to calculate the air viscosity. This is:

$$\mu = \mu_o \left(\frac{a}{b}\right)\left(\frac{T}{T_o}\right)^{3/2} \tag{7.1}$$

$$a = 0.555T_0 + C, \quad b = 0.555T + C$$

where:

μ : viscosity, [cp]

μ_o : reference viscosity at reference temperature, (0.01827 cp for air)

T : temperature, [°R]

T_o : reference temperature (524.07 °R for air)

C : Sutherland's constant (120 for air)

The compressibility factor was determined using the correlation proposed by Adebiyi (2005).

$$z = 1 + \left(\frac{0.093842}{Tr} - \frac{0.422}{T_r^{2.6}} - \frac{0.013416}{T_r^{5.2}}\right)p_r \tag{7.2}$$

where:

T_r : reduced temperature

p_r : reduced pressure

Adebiyi (2005) also proposed the following equation for specific enthalpy of the air:

$$h_r = \left(\sum_{k=0}^{6}\frac{a_k}{k+0.5}T_r^{k+0.5} + h_{r0}\right) + \left(b_1 + \frac{2.6b_2}{T_r^{1.6}} + \frac{1.6b_3}{T_r^{0.6}}\right)P_r \tag{7.3}$$

$$a_0 = 1.685175, \quad a_1 = 2.283617, \quad a_2 = -0.49965, \quad a_3 = 0.108826$$

$$a_4 = -0.012765,\ a_5 = 7.471154 \times 10^{-4},\ a_6 = -1.732085 \times 10^{-5}$$

$$b_1 = 0.1629,\ \ b_2 = -0.338964,\ b_3 = -0.143369$$

where:

h_r : specific enthalpy, [kJ/kg]

h_{r0} : reference specific enthalpy, (-9.098244 kJ/kg)

The simple Equation 7.4 was found to give good results for specific enthalpy. Note that the specific enthalpy is defined to be zero at 0°C.

$$h = 1.007T - 0.026 \quad for\ T > 0°C \tag{7.4}$$

$$h = 1.005T \quad for\ T < 0°C$$

Finally, the thermal conductivity of the air is estimated using the expression:

$$k = -7.0 \times 10^{-9} T^2 + 4.0 \times 10^{-5} T + 0.0226,\ [\text{W/m°C}] \tag{7.5}$$

The main purpose of this chapter is to present a comparison between the experimental data and the numerical results generated by the model. A full description of the flow field and the main features of flow through an orifice meter will be presented in Chapter 8.

7.1. N_{Re} = 91,100 Case

The numerical results for the radial distributions of the normalized axial and radial velocity at various cross sections, upstream the orifice plate, are presented in Figures 7.1 and 7.2 respectively. It can be observed that the axial component of the flow accelerates near the pipe centerline, and decelerates close to the wall of the pipe. Figures 7.1 and 7.2 show that the radial velocities increase in negative value as they approach the orifice; this represents how the flow turns toward the orifice.

Downstream the plate, near the axis of the pipe, the normalized axial velocities start to increase until certain point when it reaches a maximum and then it start to decrease as shown in Figure 7.3. Close to the pipe wall, we can appreciate negative values of velocity indicating the backflow

and the formation of a recirculation zone. Farther from the plate, the profiles become flatter as they approach a fully developed turbulent flow. Figure 7.4 illustrates the random and erratic pattern characteristic of the turbulence flow created by the orifice-plate in the radial velocities. It can also be appreciate how the radial velocities decrease approaching to zero as the distance from the plate increases.
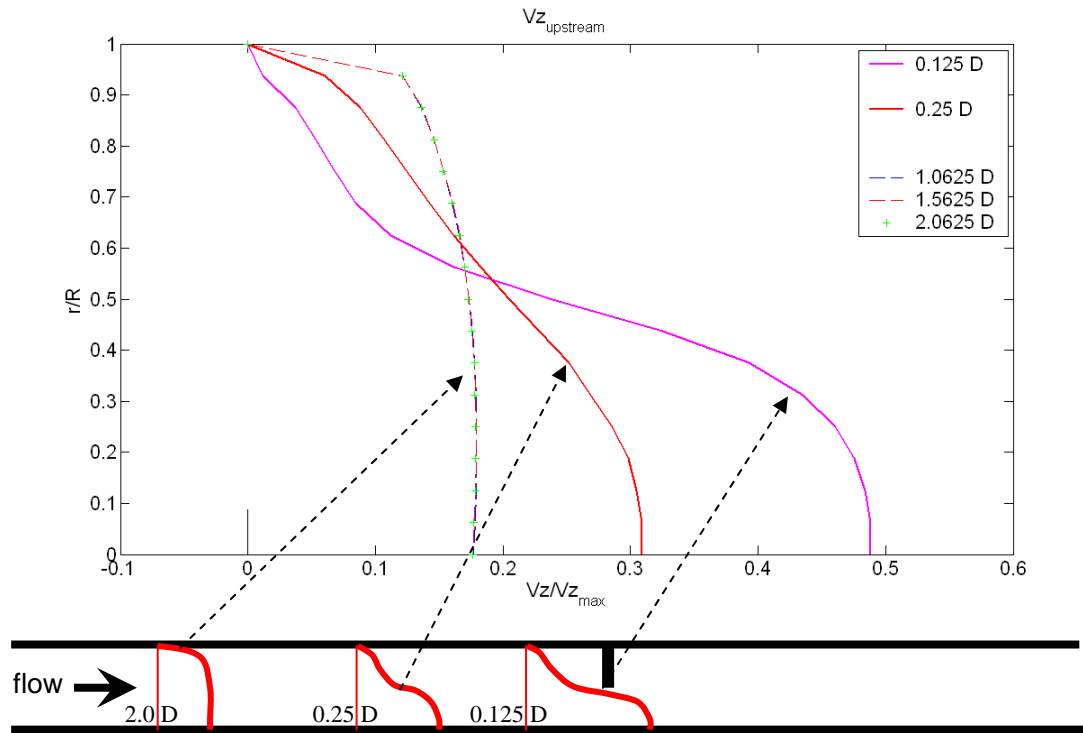
Figure 7.1. Axial Velocity profiles upstream the orifice-plate for N_{Re}=91,100.
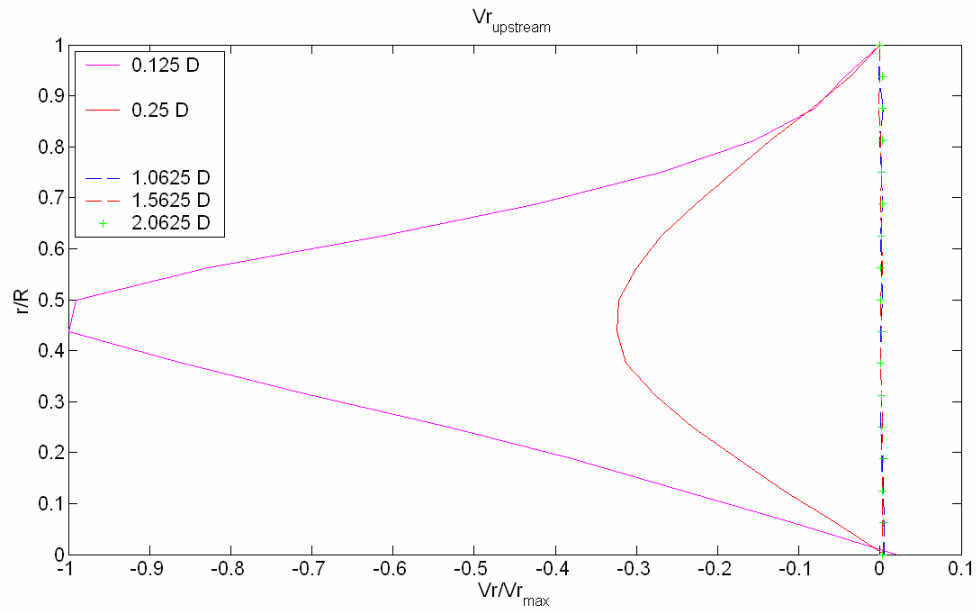
Figure 7.2. Radial Velocity profiles upstream the orifice-plate for N_{Re} =91,100.
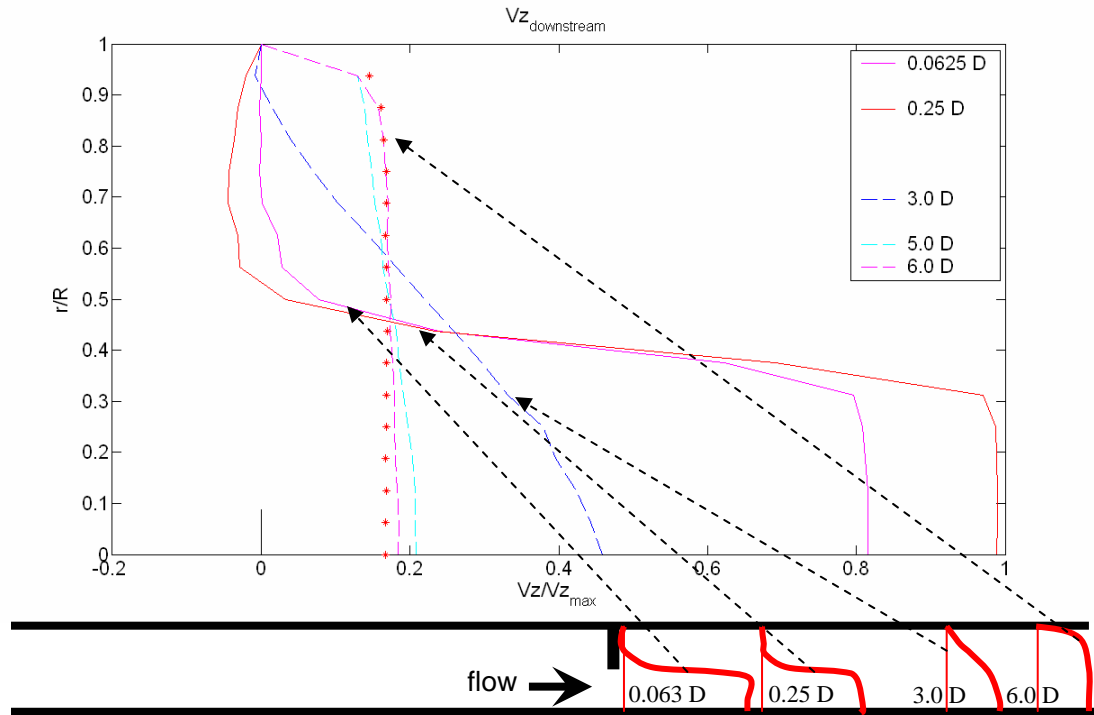
Figure 7.3. Axial Velocity profiles downstream the orifice-plate for N_{Re} =91,100.
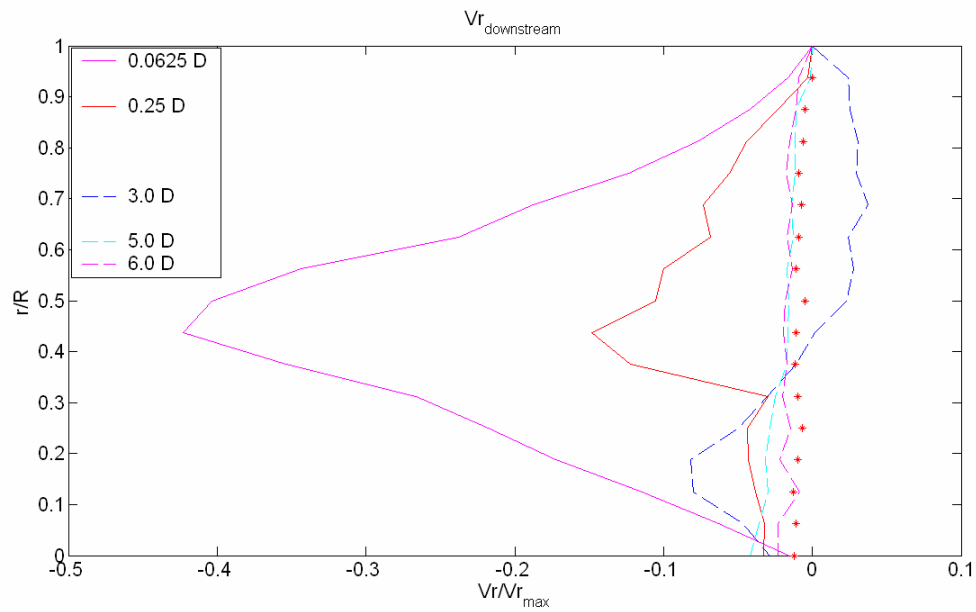
Figure 7.4. Radial Velocity profiles downstream the orifice-plate for N_{Re} =91,100.

Figure 7.5 shows the relative error of the axial velocity upstream the plate for different cross-sections. A maximum of 2.86% difference is observed near the wall as one gets closer to the plate. For the radial velocity, in Figure 7.6 a maximum error of 18.60% can be observed to occur

near the pipe wall, but considering the absolute value of velocity been very close to zero, any small difference will produce a high relative error.

Figure 7.7 is a cross plot comparison between the numerical and experimental values for the axial velocity profiles downstream plate. It is clear that they are all very close to the unity slope line, which confirms the good match achieved by the numerical model. Moreover, it is known that the region downstream of the plate is the one where the turbulent effects are at their maximum and this start the generation of eddies which are characteristic of the recirculation phenomenon that takes place in that area. Again, the behavior of the fluid is very erratic in that region and the direction of the flow is somehow random; therefore the difference in magnitude of the radial velocities increase near the downstream face of the plate as shown in the cross plot presented in Figure 7.8. As the distance from the orifice increases, the points become closer to the unity slope line indicating the reduction of the erratic turbulent effects.

Figure 7.9 shows the velocity field near the orifice plate, where the size of the arrows represents the magnitude of the velocity. The acceleration can be clearly seen when the flow turns toward the orifice and also downstream the plate. Moreover, near the pipe wall the backflow characteristic of the recirculation zone can be appreciated. This effect is observed in Figure 7.10 where that area is magnified. The orifice jet reattachment occurs at the cross section where no more backflow is present. This location can be determined downstream the plate because this is where the value of wall shear stress (Equation 7.6) changes sign. For this case, this occurs at 0.4 ft downstream of the plate (2.4 pipe diameters) as shown in Figure 7.11.

$$\tau_w = \left(\frac{\partial v_z}{\partial r} + \frac{\partial v_r}{\partial z} \right) \tag{7.6}$$

Figure 7.12 shows the axial distribution of the pipe wall pressure (dashed black line) and the centerline pressure (solid blue line). The minimum pressure at the axis of the pipe is 16.31 psia and it occurs 0.026 ft downstream of the plate. Additionally, the location of the maximum axial velocity (472 ft/s) can be located at 0.0521 ft downstream of the plate. Note that the points of maximum centerline velocity and minimum wall pressure do not coincide, as expected for the one-dimensional case. This phenomenon will be explained in detail in the next chapter where the results will be discussed.

Very close to the downstream face of the plate, the velocities are very small due to the friction effects that make the fluid adhere to the wall as specifies by the no-slip boundary condition. Any small absolute difference between the experimental data and the numerical results will generate a large relative error which will not be representative of the quality of the numerical prediction. For this reason, the comparisons against the experimental data for the velocity profiles downstream the plate were made using the absolute errors rather than the relative ones. Finally, Figure 7.13 shows the experimental values of the axial velocity profile closest to the downstream face of the plate compare to the numerical predictions. This plot shows a very good match of the data. The maximum and average relative errors, as well as the standard deviation for the velocities upstream the plate are summarized in Table 7.2. The same quantities but for the absolute errors of the velocities downstream the plate are presented in Table 7.3.

A similar analysis as the one just presented is included for the cases of N_{Re} = 54,700 and 18,400 in the following sections. For the sake of brevity some of the plots are presented in Appendix C. Only the relevant graphs to study the matching procedure are included in this chapter.

Figure 7.5. Relative Error of Vz upstream the orifice-plate for N_{Re} =91,100.

Realtive Error between Numerical and Experimental Data
Upstream Radial Velocities - N$_{Re}$=91,100
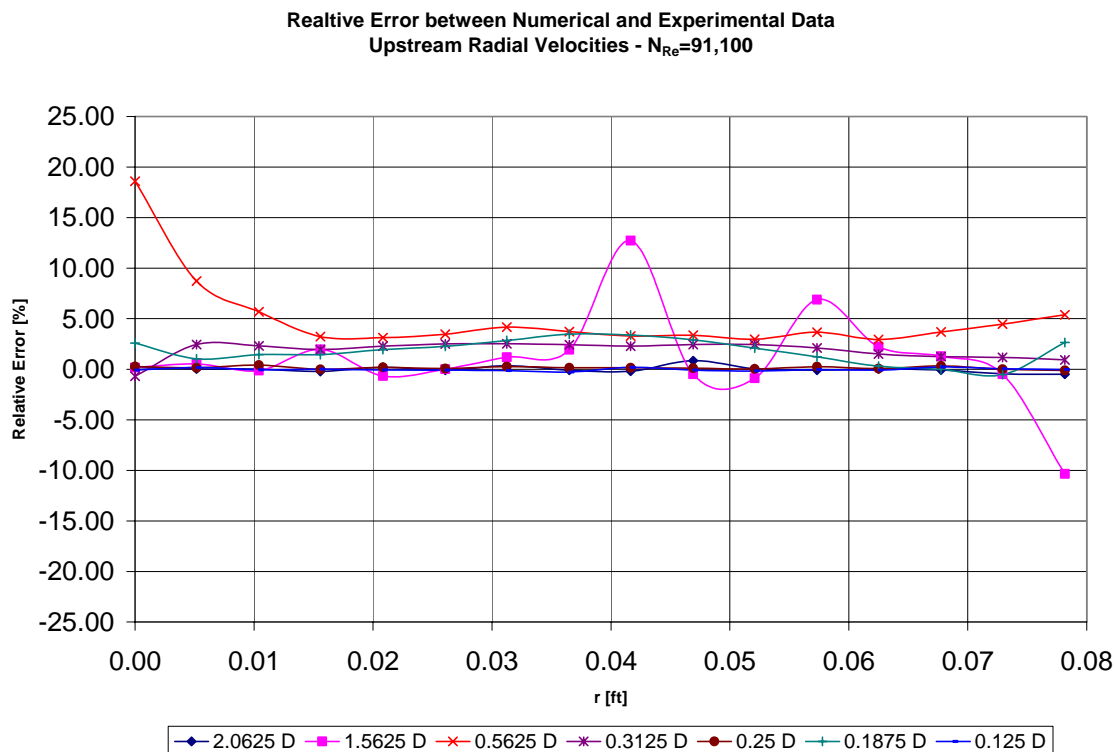
Figure 7.6. Relative Error of Vr upstream the orifice-plate for N$_{Re}$ =91,100.

Comparison of Vz downstream the plate - Re = 91,100
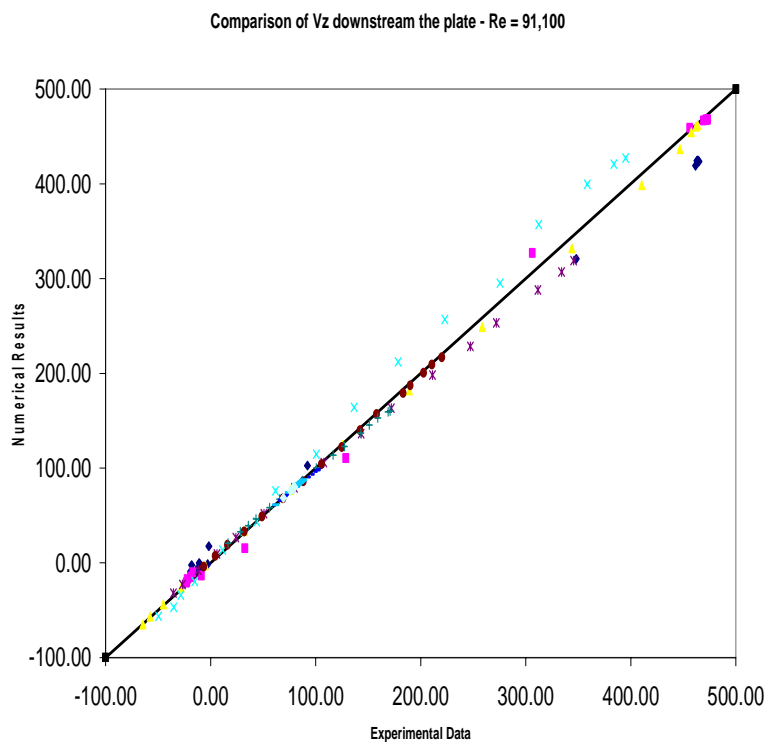
Figure 7.7. Cross plot comparison for Vz at N$_{Re}$ =91,100.
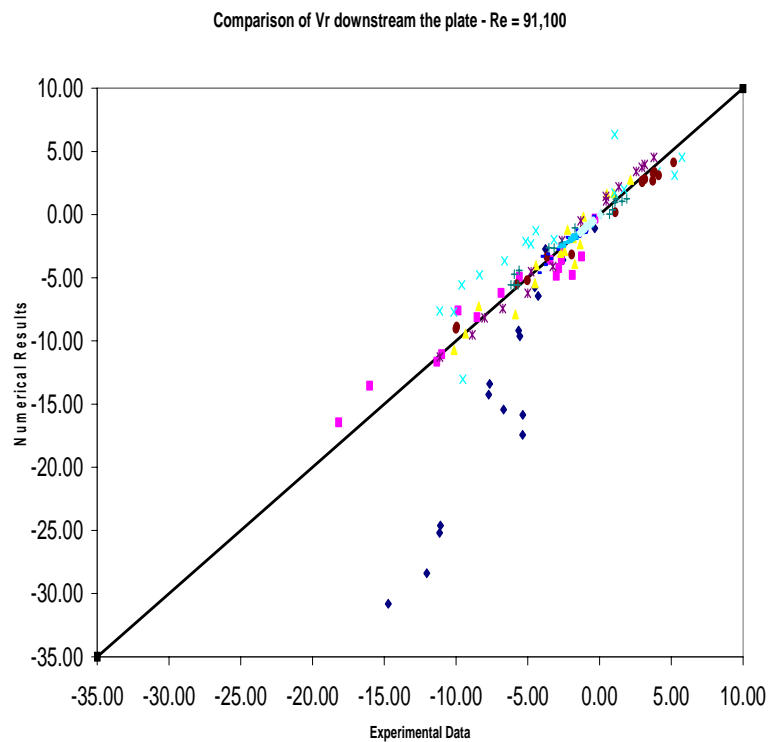
Figure 7.8. Cross plot comparison for Vr at N_{Re} =91,100.
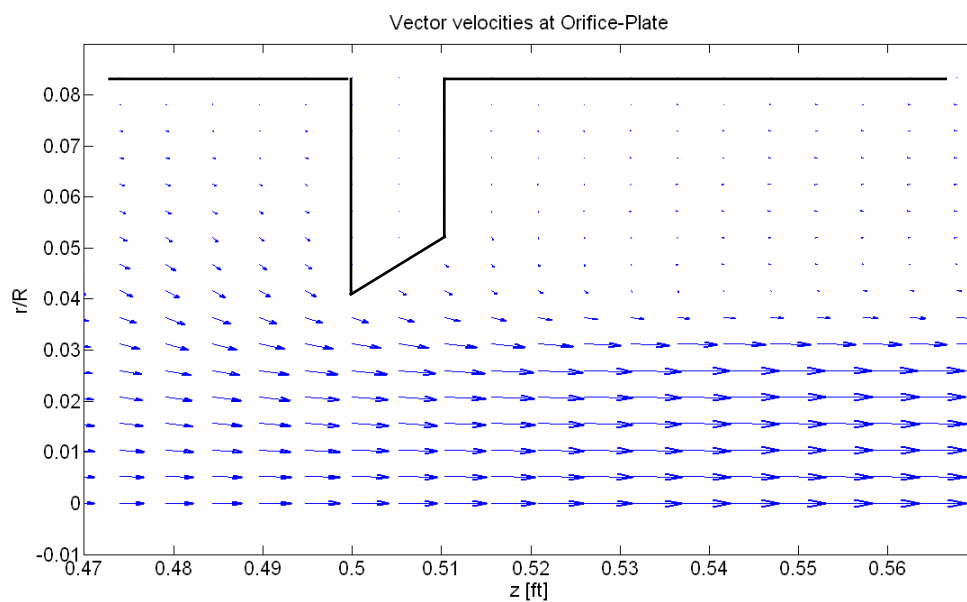
Figure 7.9. Vector velocities near the orifice-plate for N_{Re} =91,100.
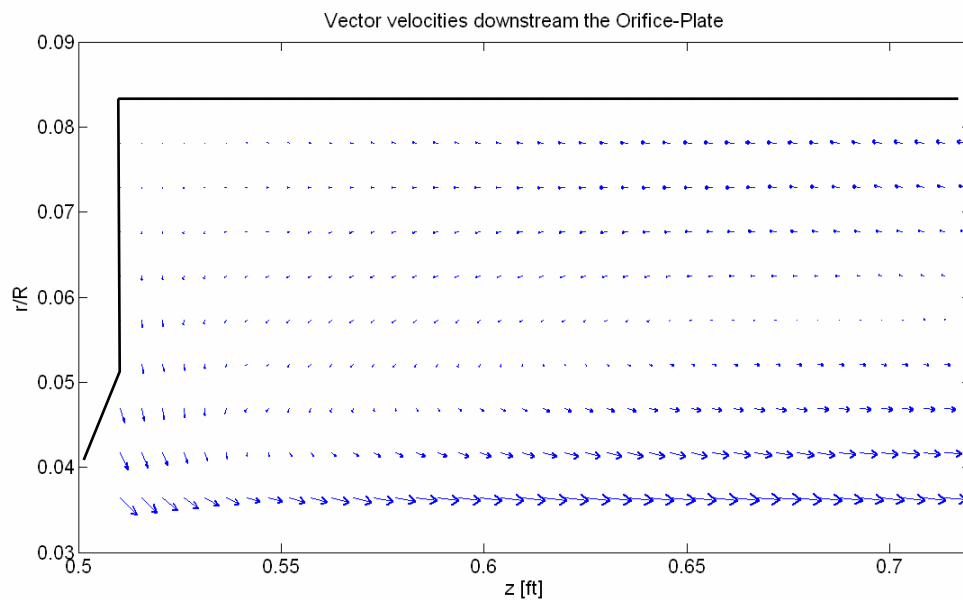
Figure 7.10. Vector velocities downstream the orifice-plate for N_{Re} =91,100.
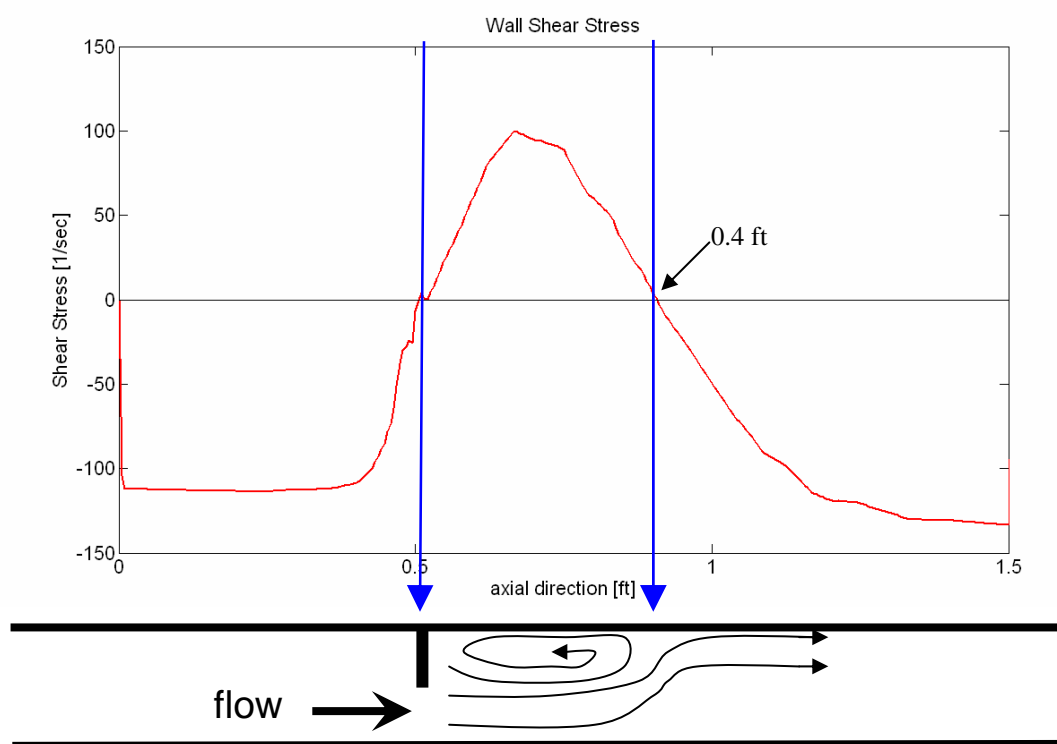
Figure 7.11. Wall Shear Stress for N_{Re} =91,100.
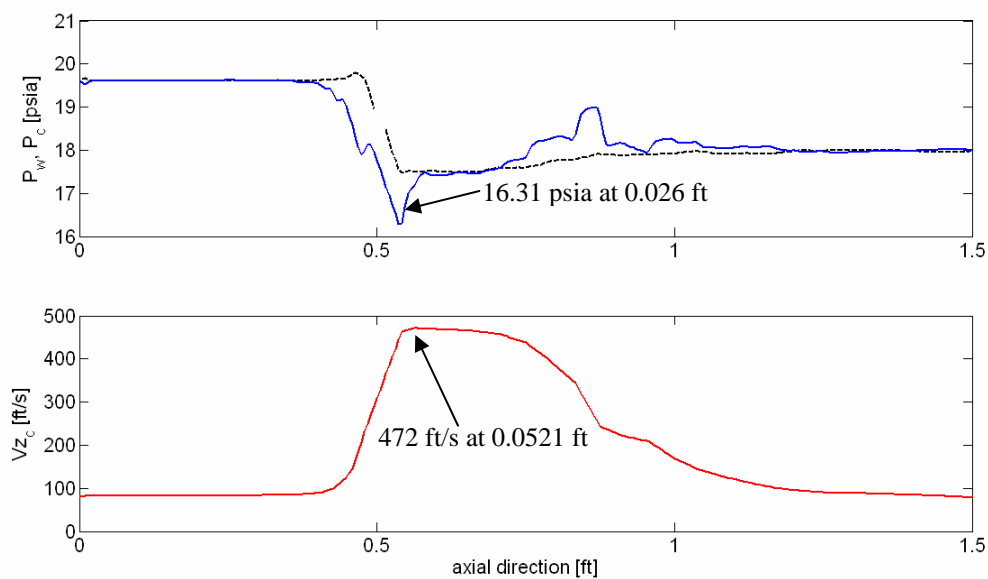
Figure 7.12. Axial distribution of Pressure and Velocity for N_{Re} =91,100.
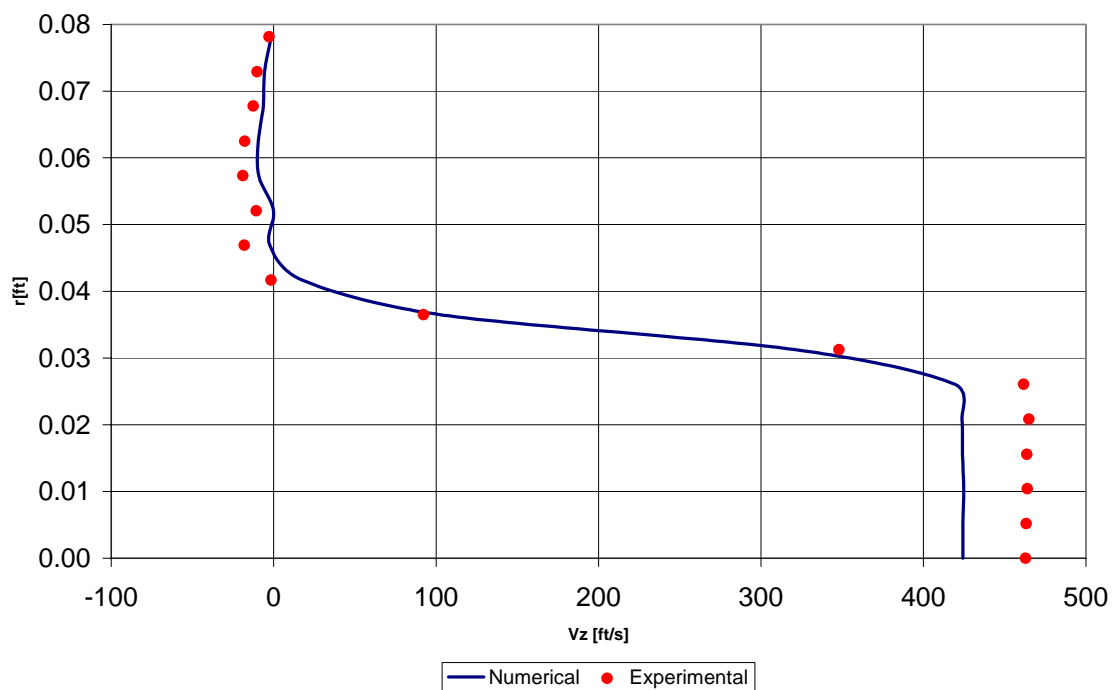
Figure 7.13. Comparison of Vz profiles for N_{Re} = 91,100.

7.2. Re=54,700 Case

As for the previous case, Figures C.1 and C.2 illustrate the normalized axial and radial velocities upstream the plate respectively. The acceleration and turning of the flow towards the orifice is observed. Then, the backflow can be seen in Figure C.3 downstream the plate, by means of the negative values in the axial velocities close to the wall, as well as the acceleration of the fluid near the axis of the pipe. The random behavior of the radial velocities downstream of the plate is presented in Figure C.4. Maximum relative errors of 3.5% and 27.3% in the axial and radial velocities are observed in Figures 7.14 and 7.15 respectively.

Figures 7.16 and 7.17 present cross plots comparing the measured and predicted values, for the axial and radial velocities downstream the plate, respectively. As explained before, these plots show that the quality of the numerical prediction is good even though the relative errors are large, which is caused by the proximity of the values to zero where any small difference generates a very large error. This can be confirmed in Figure 7.18, where a very good match of the axial velocity profiles can be seen.

The velocity field nears the orifice, and located downstream the plate are plotted in Figures C.5 and C.6 respectively. The increase of flow velocity at the orifice and downstream its throat, up to a maximum of 269 ft/s located 0.0729 ft from the plate (Figure E.8), can be seen as well as the recirculation zone which extends 0.3334 ft from the plate as represented by the sign change in the value of wall shear stress (Figure C.7). It is important to address that the minimum centerline pressure (17.19 psia) takes place 0.0052 ft downstream the plate which is not the same location that the maximum axial velocity.

Table 7.2 presents the relative errors for the velocities upstream the plate as well as the standard deviation. The absolute errors and the standard deviation of the velocities downstream the plate are summarized in Table 7.3.
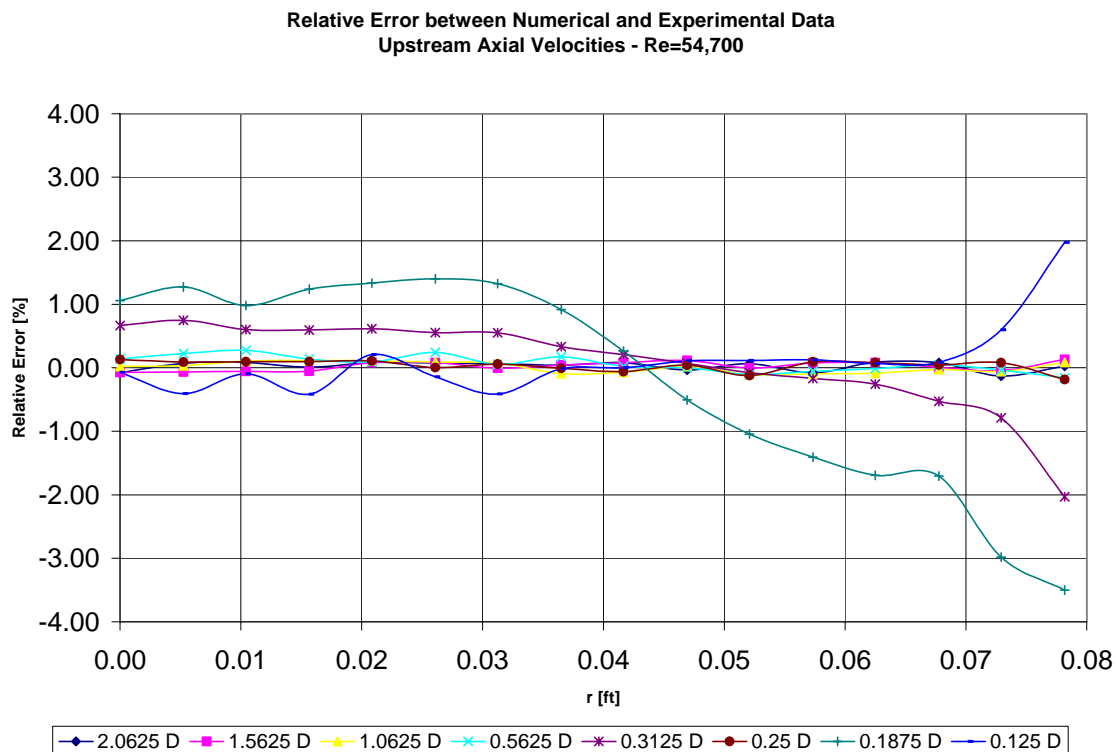
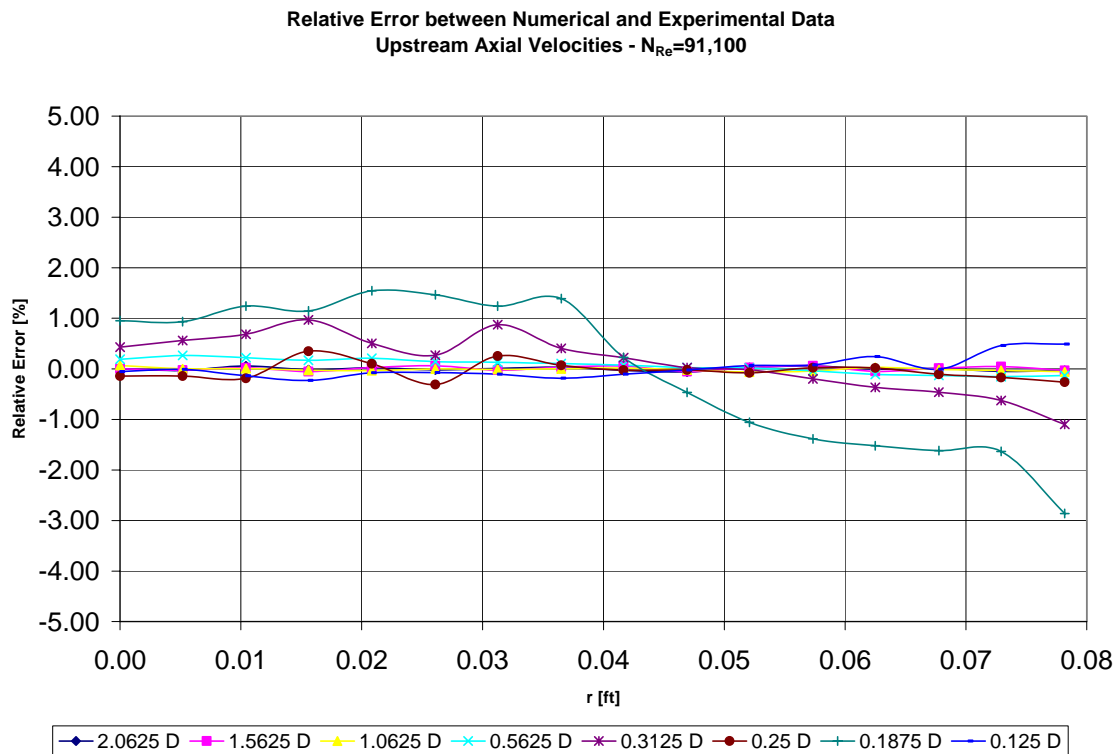Figure 7.14. Relative Error of Vz upstream the orifice-plate for $N_{Re} = 54,700$.

Figure 7.15. Relative Error of Vr upstream the orifice-plate for $N_{Re} = 54,700$.

**Comparison of Vz downstream the plate - Re = 54,700**
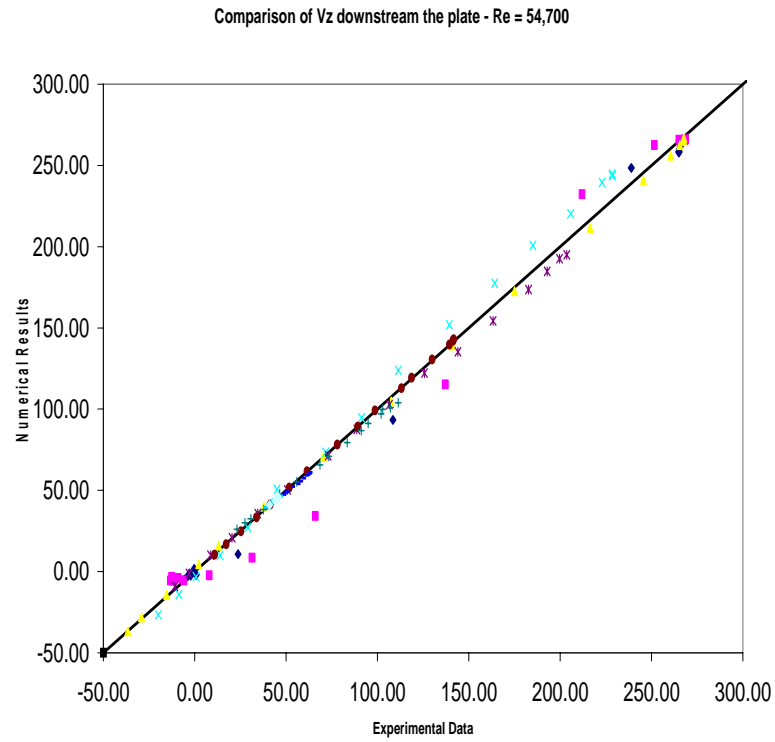
Figure 7.16. Cross plot comparison for Vz at N_{Re} =57,400.

Comparison of Vr downstream the plate - Re = 54,700
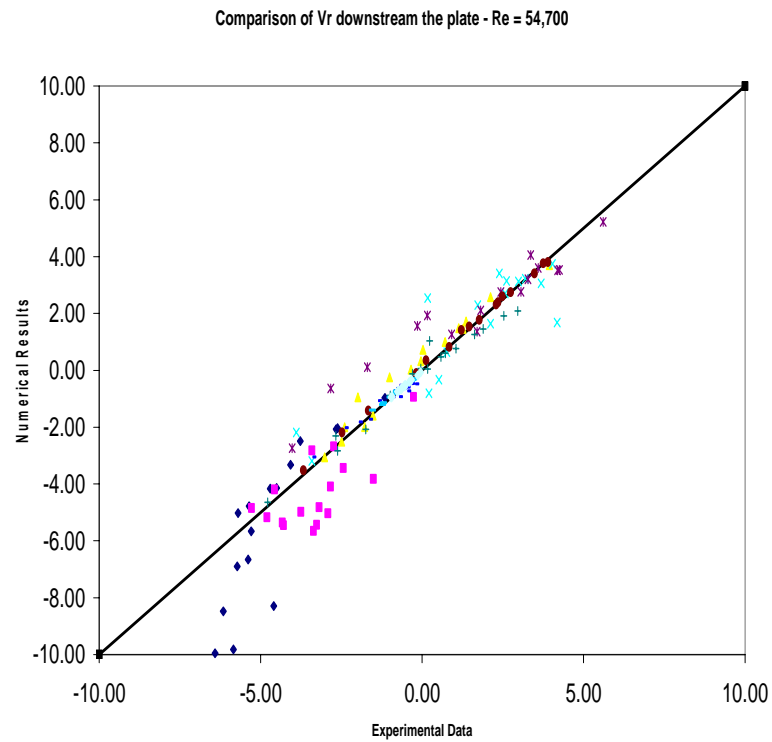
Figure 7.17. Cross plot comparison for Vr at N_{Re} =54,700.

Comparison between Experimental Data and Numerical Result - Re = 54,700
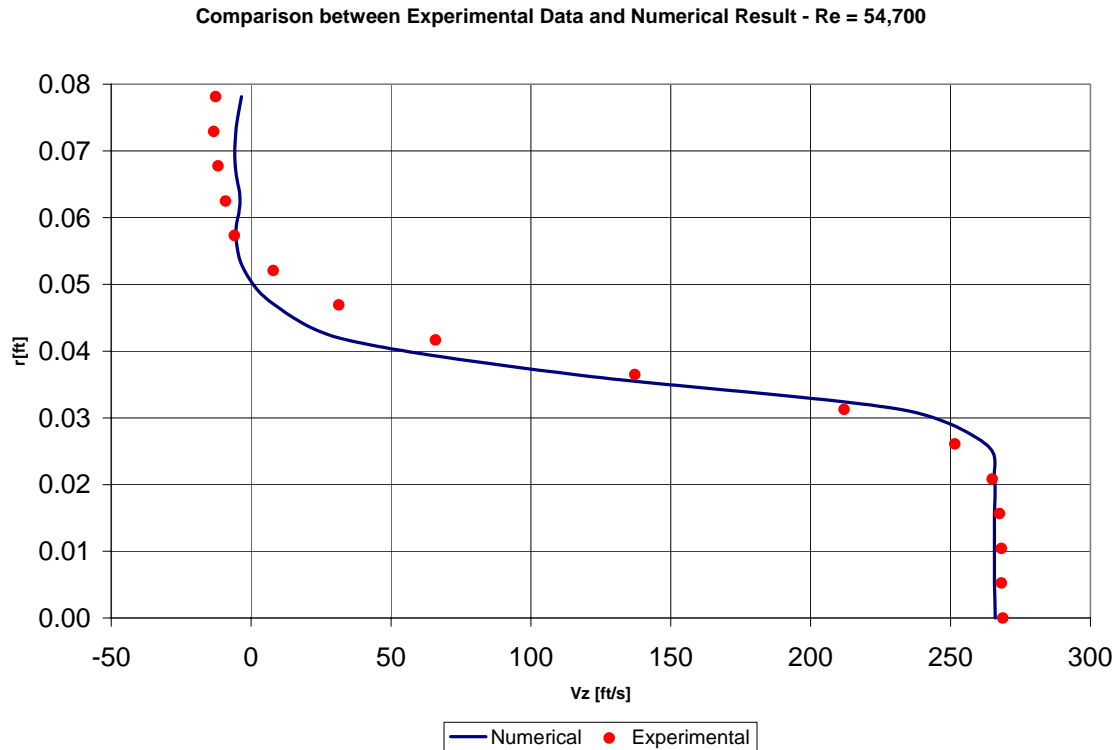
Figure 7.18. Comparison of Vz profiles for N_{Re} =54,700.

7.3. N_{Re}=18,400 Case

The same trend is observed as for the previous two Reynolds numbers. Upstream the plate, the fluid accelerates and turns towards the orifice as shown in Figures C.9 and C.10 in the normalized axial and radial velocity profiles respectively. Then, Figures C.11 and C.12 present the streamwise and radial velocity profiles downstream the plate, which show the erratic behavior of turbulent flow. We can appreciate the continuous acceleration of the fluid near the axis until a maximum is reach and the velocity begins to decrease. Close to the pipe wall, backflow can be seen, which represents the recirculation zone. Figures 7.19 and 7.20 show that upstream the plate, the maximum relative errors compared with the experimental data are 2.29% and 86.90% in the axial and radial velocities respectively.

Comparison cross plots of the experimental data and the numerical results are presented for the axial and radial velocities downstream the orifice in Figures 7.21 and 7.22 respectively. These

plots show how the points lie very close to the unity slope line confirming the very good agreement between the numerical predictions and the measured values seen also in Figure 7.23.

The velocity field near the orifice plate is shown in Figure C.13 where the increase in velocity at the orifice and downstream the plate is observed. Moreover, the negative values of velocity representing the backflow and recirculation phenomenon are presented in Figure C.14 where the area downstream the plate is magnified. The extension of the recirculation zone is determined from Figure C.15 where the wall shear stress changes sign at 0.3281 ft downstream the plate. The maximum centerline velocity (89.3 ft/s) occurs at a distance of 0.0833 ft from the plate, while the minimum centerline pressure of 19.05 psia is located 0.0052 ft downstream the plate as shown in Figure C.16.

The summary of the relative and absolute errors is presented in Tables 7.2 and 7.3 as well as the standard deviation.
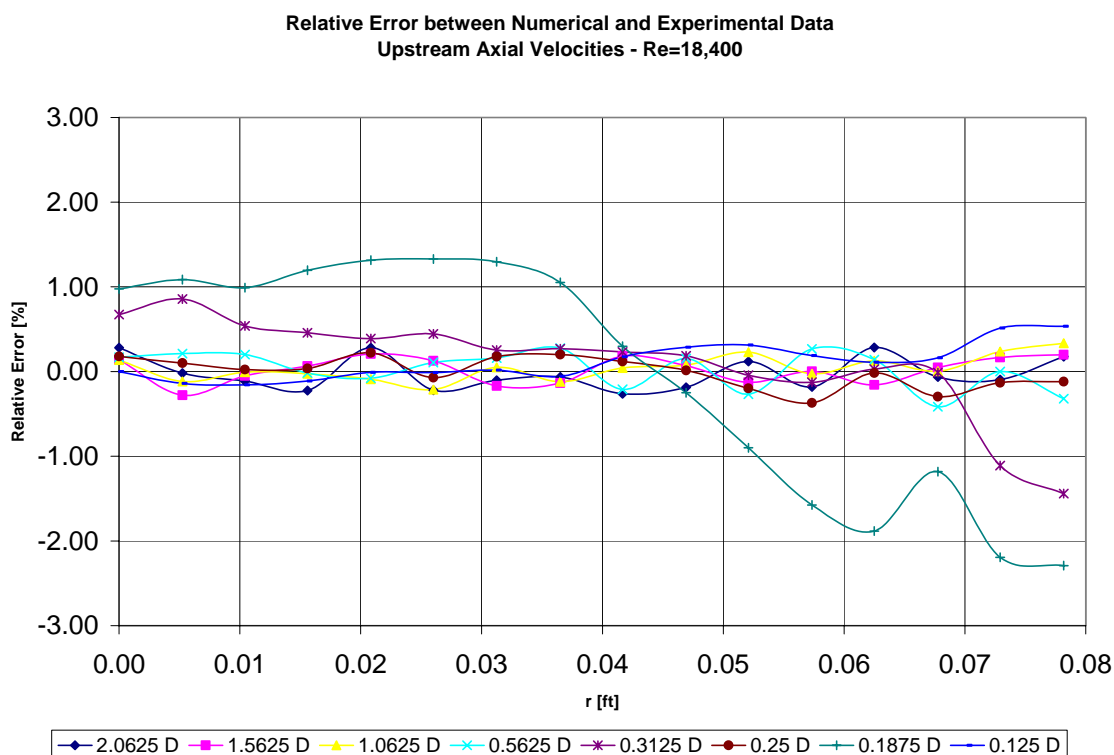
Figure 7.19. Relative Error of Vz upstream the orifice-plate for N_{Re} =18,400.

**Realtive Error between Numerical and Experimental Data
Upstream Radial Velocities - Re=18,400**
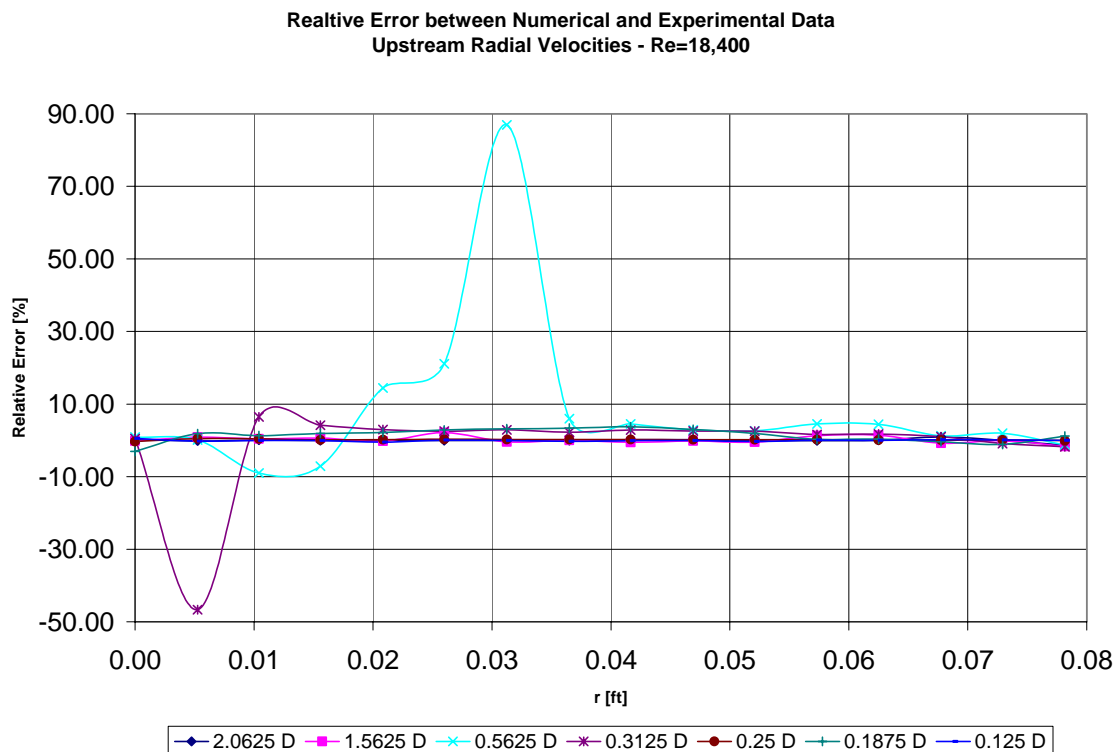
Figure 7.20. Relative Error of Vr upstream the orifice-plate for N_{Re} =18,400.

Comparison of Vz downstream the plate - Re = 18,400
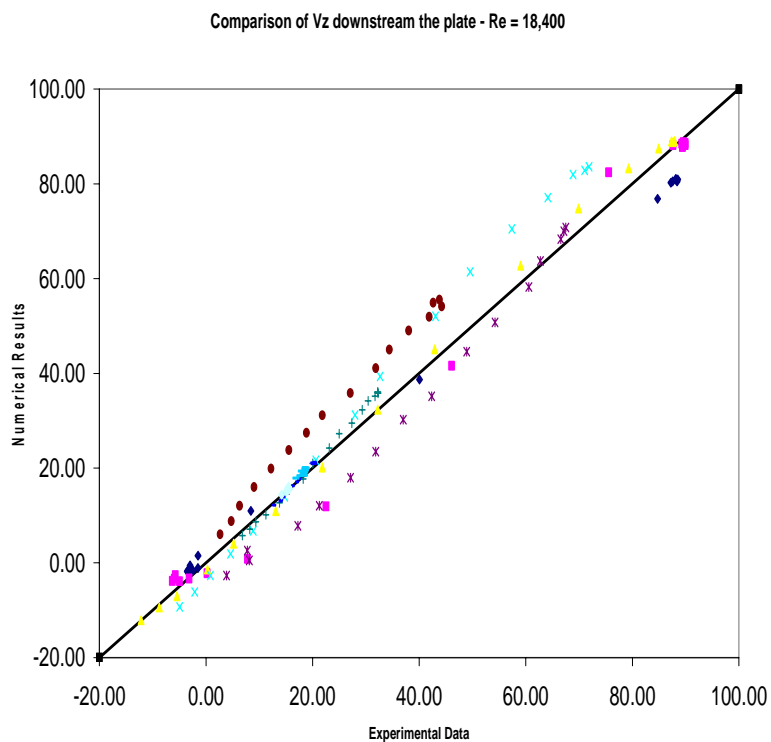
Figure 7.21. Cross plot comparison for Vz at N_{Re} =18,400.

Comparison of Vr downstream the plate - Re = 91,100
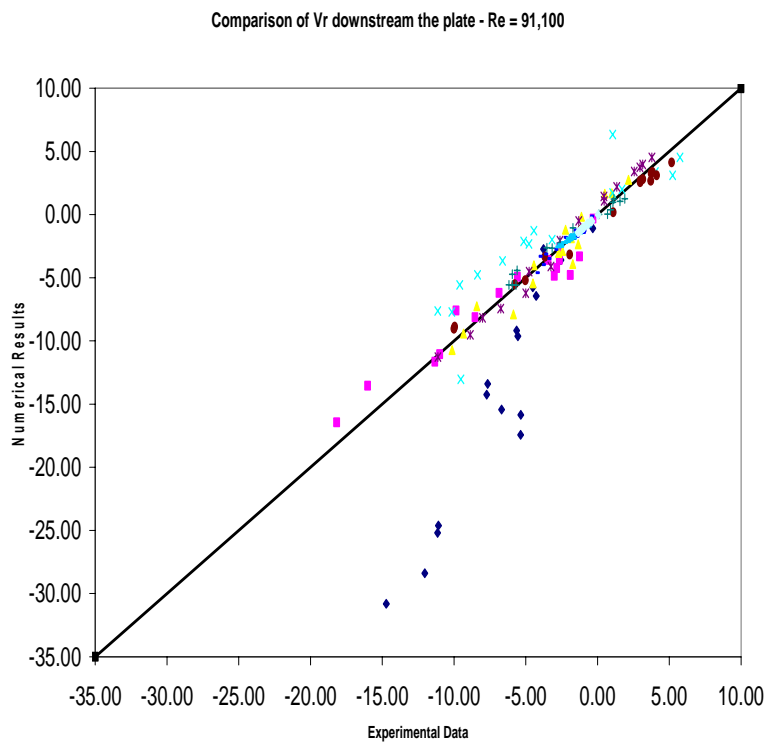
Figure 7.22. Cross plot comparison for Vr at N_{Re} =18,400.

Comparison between Experimental Data and Numerical Result - Re = 18,400

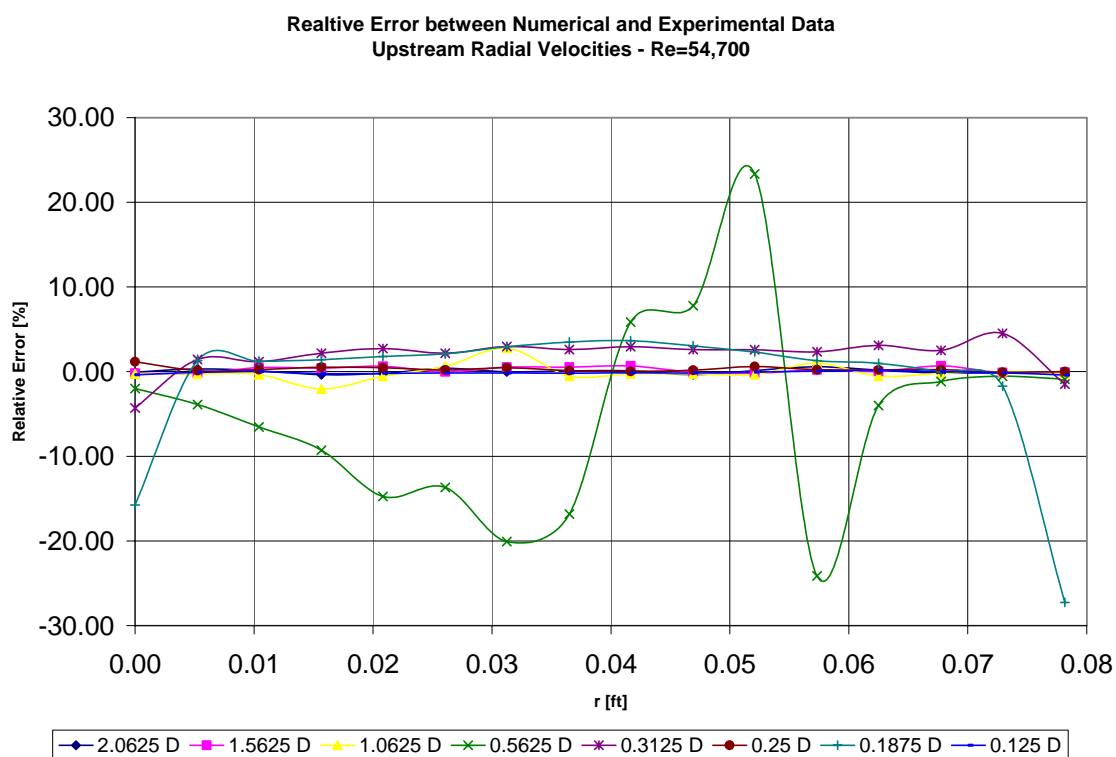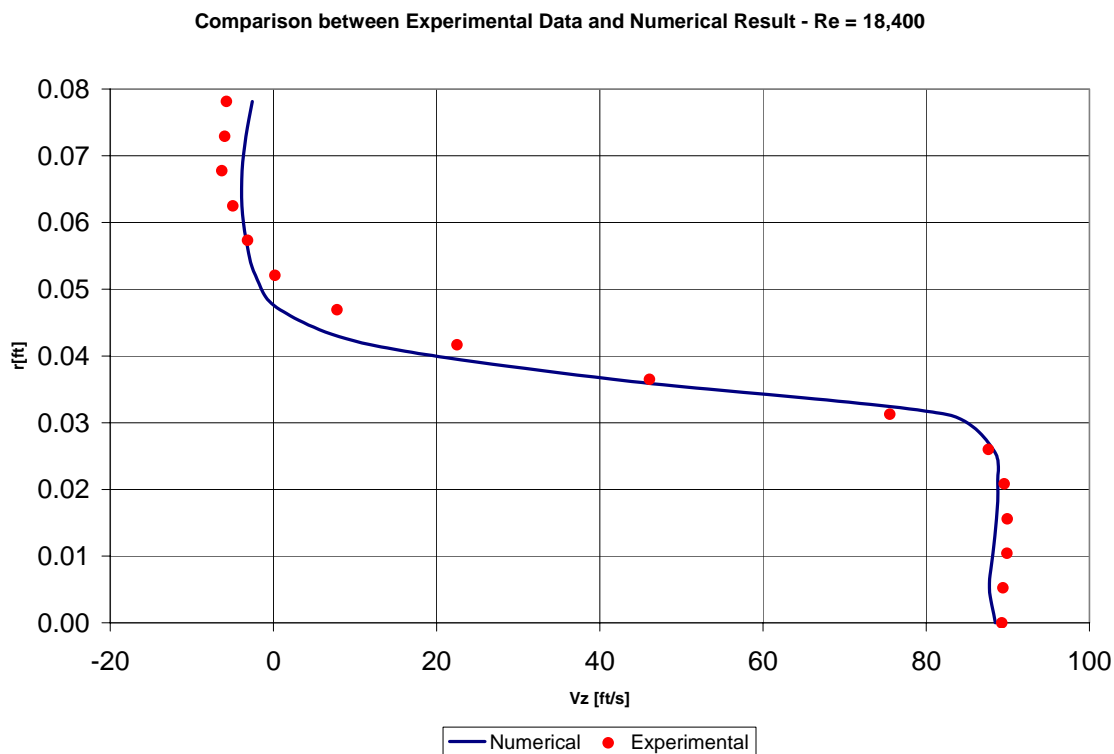Figure 7.23. Comparison of Vz profiles for N_{Re} =18,400.

From Table 7.2 and 7.3 it is clear that for all the cases, the maximum error in the axial velocity upstream the orifice-plate is within 3.5%. Moreover, for the radial velocity profiles the average errors are below 12%, but considering the erratic behavior of the turbulent flow and the small values of velocities we consider these results very reasonable. Additionally, the cross plots for the comparison downstream the plate show excellent agreement between the experimental data and the numerical predictions.

Table 7.2. Relative Errors for the velocities upstream the plate.

Reynolds Number	Upstream the plate					
	Relative Error [%]					
	Vz			Vr		
	Maximum	*average*	*st. dev.*	*maximum*	*average*	*st. dev.*
18,400	2.29	0.35	0.4668	86.90	7.80	11.6415
54,700	3.50	0.37	0.6389	27.30	2.69	5.6527
91,100	2.86	0.31	0.5131	18.60	11.38	3.5580

Table 7.3. Absolute Errors for the velocities downstream the plate.

Reynolds Number	Downstream the plate					
	Absolute Error [ft/s]					
	Vz			Vr		
	Maximum	*average*	*st. dev.*	*maximum*	*average*	*st. dev.*
18,400	13.10	3.50	3.6672	3.13	0.49	0.5938
54,700	31.80	3.96	5.6580	3.98	0.61	0.7830
91,100	44.80	7.70	11.2126	16.40	1.49	2.8908

After this rigorous validation stage, we are confident of the robustness of the model and hence we make predictions for the actual problem of natural gas flow through an orifice meter.

Chapter 8

PREDICTIONS FOR NATURAL GAS FLOW IN ORIFICE-METERS

In this chapter the results for numerical predictions for natural gas flow through the orifice plate are presented for different pipe configurations and flow conditions. The inner diameter of the pipe is 2 inches. Initially, a full description and analysis of all the flow variables for the case of Reynolds number equal to 110,000, Beta ratio = 0.5 and specific gravity of 0.55 is included with all the graphical results. The remaining cases are presented as parametric studies varying the Reynolds number, the specific gravity of the fluid, and the Beta ratio. For all the cases the pressure at the inlet of the pipe section was chosen to be 20 psia, while the temperature both at the inlet and on the surroundings was set to 65 ºF.

As mentioned before, the transient model marches the solution in time until steady-state conditions are achieved, which occurs when the change in the maximum axial velocity within one timestep is less than 0.05% as suggested by Mattingly and Davis (1977).

8.1. N_{Re} = 110,000 Case

In this specific case, the fluid is pure methane. By the means of a flow conditioner a fully developed turbulent flow is set at the inlet of the section of the pipe using the power law. Figure 8.1 presents the radial profiles of the axial velocity at different locations upstream the plate. The values of velocity have been normalized with respect to the maximum velocity in the field while the radial distance was normalized by the radius of the pipe. For illustration purposes, the x-axis of this plot represents the magnitude of the normalized velocity and the y-axis corresponds to the normalized radial distance. Below the plot, a schematic of the pipe is included with the location of the plate and the velocity profiles. Note that only the solution for half of the pipe is obtained assuming symmetry with respect to the axis of the pipe. There is almost no variation between the profiles at z = -2.0625 D (pipe diameters) and -0.5625 D, indicating that the presence of the plate does not influence the fully developed flow in this region. When approaching the plate, from z = -0.3125 D to -0.1875 D the axial velocities increased significantly in the region near the axis of the

pipe while close to the wall it start to decrease since the fluid is turning towards the orifice. Then, very close to the plate at z = -0.125 D the highest velocity is reached at the centerline as the fluid is now entering the bore, which also causes the values of velocity to approach zero near the wall of the pipe.
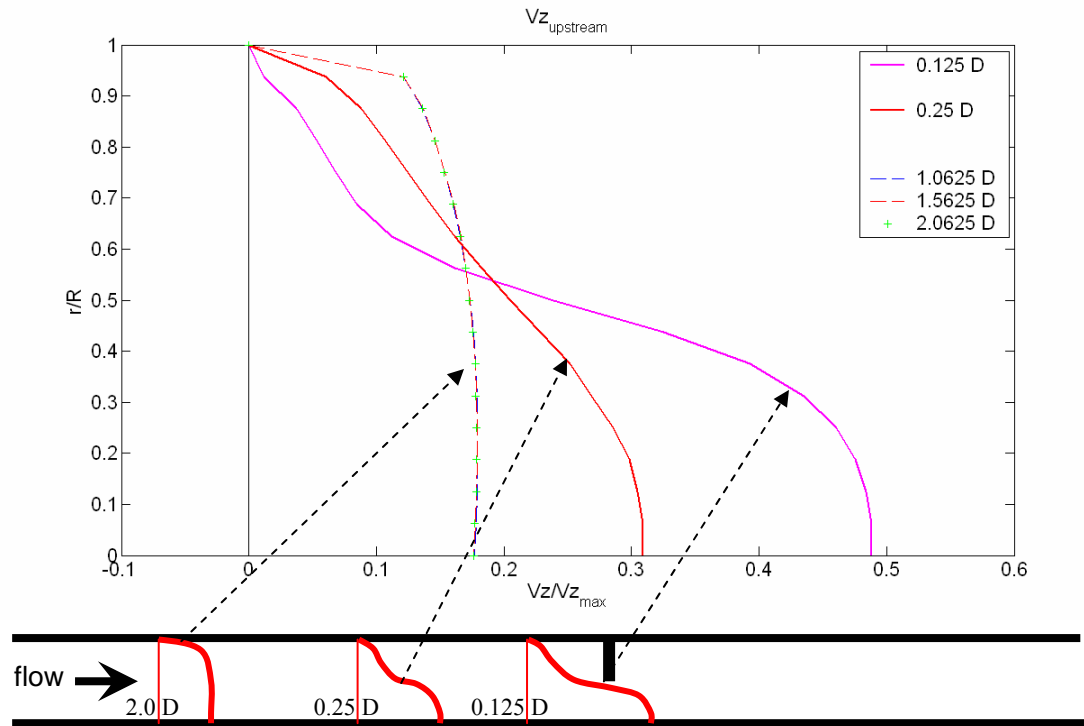
Figure 8.1. Axial Velocity profiles upstream the orifice-plate for N_{Re}=110,000.

Figure 8.2 shows the radial distribution of the normalized axial velocities at different locations downstream the plate. It can be clearly seen how the velocities increased significantly as the fluid exits the orifice (from z=0.065 D to 0.25 D). At some locations the velocity at the centerline even doubles the highest value of velocity upstream the plate (comparing $V_z/V_{z,max}$=0.49 at z=-0.125 D with $V_z/V_{z,max}$=0.98 at z=0.25 D). At these locations, the velocity remains approximately constant from the centerline to r/R = 0.25 showing a nearly flat profile. However, near the wall of the pipe (from r/R = 0.5 to 1.0), negative values of velocities can be observed which characterize the backflow that takes place behind the plate due to the recirculation phenomenon. As the fluid moves downstream, the flow starts spreading as the velocity near the centerline decreases but still negative velocities are observed between z = 1.0 D and 3.0 D. For the profiles located at z > 3.0 D no more negative velocities can be observed which indicates that no more backflow takes place. Additionally, the velocity profiles flatten out as they approach a fully developed flow at z = 5.0 D.
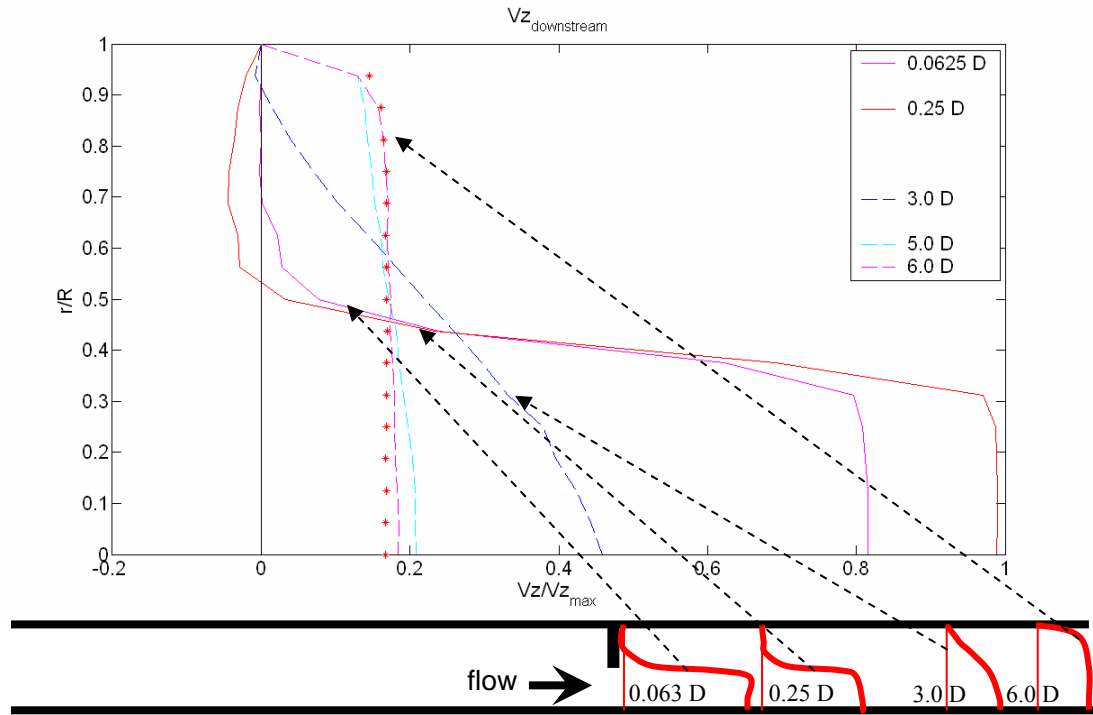
Figure 8.2. Axial Velocity profiles downstream the orifice-plate for N_{Re}=110,000.

The radial distributions of the normalized radial velocity at various locations upstream the plate are plotted in Figure 8.3. Note that the x-axis represents the magnitude of the normalized radial velocity, and negative values indicate flow from the wall towards the centerline. Between the inlet and z = -0.5625 D, the radial velocity component is mainly zero since a fully developed flow takes place which is not influenced by the orifice plate. In the cross sections closer to the plate (z > -0.5625 D) the values of radial velocity become negative across the entire pipe, which indicates how the fluid is turning towards the bore. Note that these are the same locations where the axial velocity increases (Figure 8.1) as the fluid is rapidly converging toward the centerline before entering through the orifice. Very close to the orifice, at z = -0.125 D, the minimum value of radial velocity is obtained near the edge of the plate, which represents how the fluid is actually entering the bore. Note that the radial location of the minimum radial velocity is r/R=0.5 which coincides with the tip of the plate.

Figure 8.4 shows how just downstream from the plate the radial components of the velocity reduce to half of the values observed upstream the orifice (comparing $V_r/V_{r,max}$=-1.0 at z=-0.125 D with $V_r/V_{r,max}$=-0.42 at z=0.0625 D). After that location, the magnitude of the radial velocities keeps decreasing near the centerline because the flow is almost completely axial and is

accelerating in that direction (Figure 8.2) which characterizes the jet flow. As the fluid moves downstream (z > 1.0 D) positive values of radial velocity can be observed indicating the flow in the jet reattaching to the region near the wall of the pipe, where the recirculation phenomenon is taking place. When the fluid approaches the outlet of the section (z > 5.0 D) the radial velocities gets very close to zero since a fully developed flow is been formed again as confirmed by the axial velocity profiles in Figure 8.2.
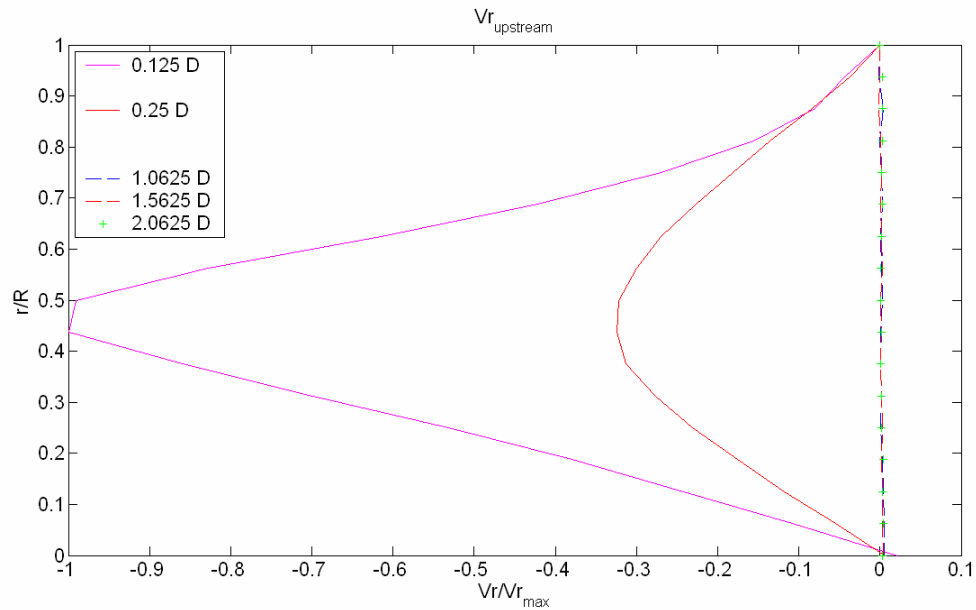
Figure 8.3. Radial Velocity profiles upstream the orifice-plate for N_{Re}=110,000.
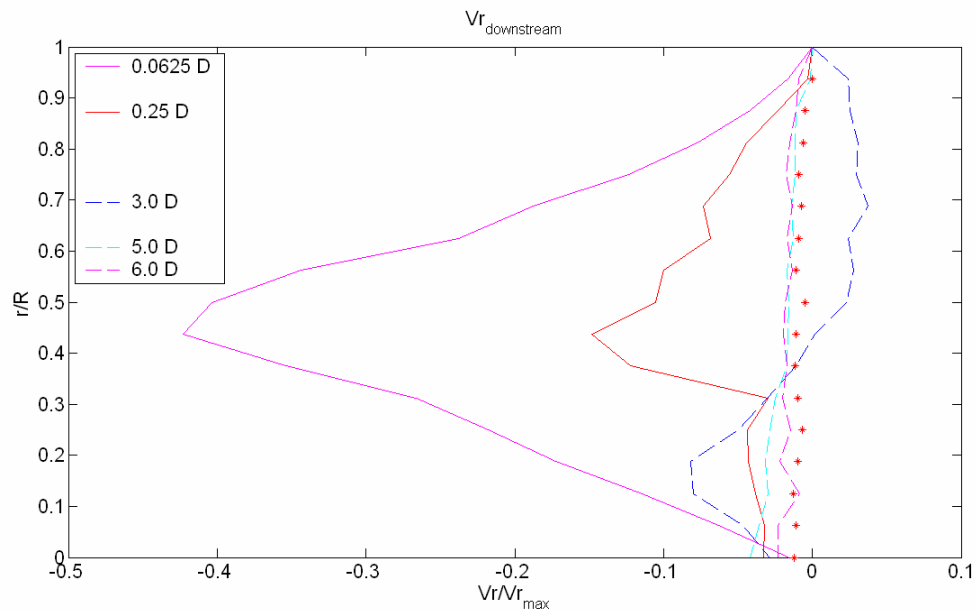
Figure 8.4. Radial Velocity profiles downstream the orifice-plate for N_{Re}=110,000.

The flow field represented by the vector plot near the orifice plate is shown in Figure 8.5. The sections of the flow immediately upstream and downstream the orifice plate can be observed, which contain the most relevant information. The velocity vectors are normalized by the largest velocity found along the axis of the pipe. Therefore, the size of the arrows indicates the magnitude of the velocity with respect to the rest of the flow domain.
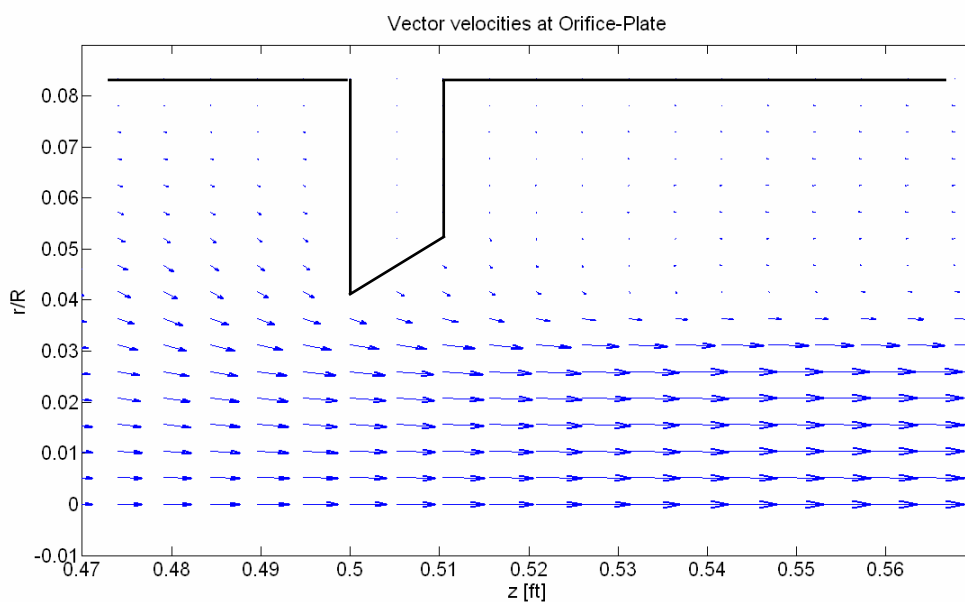
Figure 8.5. Vector velocities near the orifice-plate for N_{Re} =110,000.
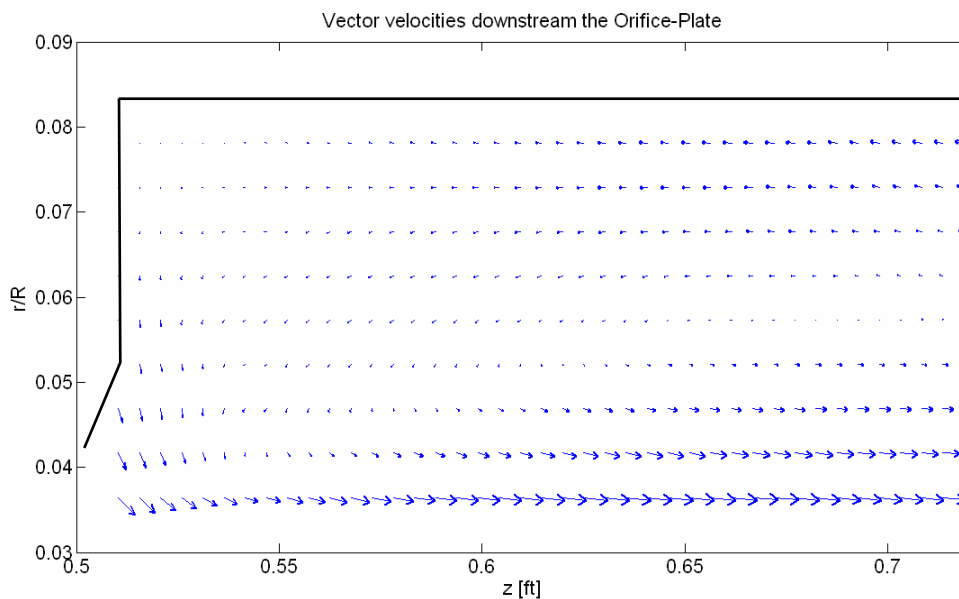
Figure 8.6. Vector velocities downstream the orifice-plate for N_{Re} =110,000.

As the flow approaches the orifice, the velocity vectors near the wall turn in the radial direction. Additionally, this momentum is transferred as the fluid accelerates in the axial direction near the centerline as it flows through the bore. The radial turning and axial acceleration creates a narrow orifice jet flow in the region from the axis of the pipe to r/R =0.25 as shown before in Figure 8.2. The vena contracta is located where the highest speed orifice jet occurs downstream the plate and the velocity profiles are very nearly flat. A large recirculation zone can be appreciated downstream the plate between the jet and the pipe wall, which is represented by the backflow taken place in the region. This phenomenon is magnified in Figure 8.6 where only the zone behind the plate and close to the wall is represented and a large eddy is appreciated as a feature of the turbulent flow that is occurring.

Figure 8.7 presents the streamwise distribution of the shear stress at the pipe wall. This plot is very important in determining the location where the flow changes direction by virtue of the sign change. It is clear that the first change in sign corresponds to the location of the plate and this is where the backflow starts to occur. Most importantly, the location where the sign changes for the second time indicates the end of the back flow and therefore defines the extension of the recirculation region. For this particular case the backflow ends 2.44 pipe diameters downstream the plate as shown in the figure below.
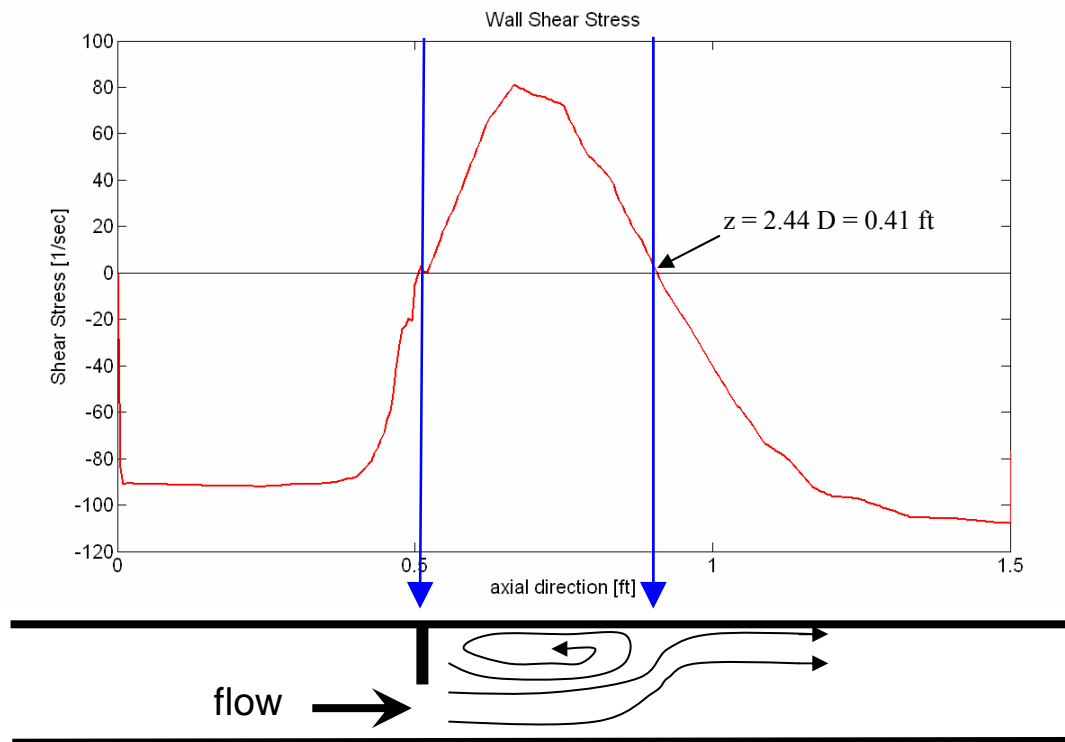
Figure 8.7. Wall Shear Stress for N_{Re} =110,000.

The distribution of pressure along the wall is represented by the dashed black line in the upper plot of Figure 8.8, while the solid blue line corresponds to the pressure along the axis of the pipe. It can be appreciated how both lines superimposed from the inlet of the section to z = -1.0625 D where the fluid starts deviating from a fully developed flow as shown before in Figures 8.1 and 8.3. After that location, a pressure drop occurs as a response of the constriction imposed by the orifice plate. Then, the pressure rises again, and a sudden increase is observed where the jet flow reattaches to the flow field in the recirculation region. For z > 4.0 D, the pressure distributions start superimposing again as the fluid is again approaching a fully developed flow and the radial variation in pressure is negligible. The minimum centerline pressure (16.18 psia) occurs at z = 0.1878 D. The wall pressure distribution serves the purposes to determine the flow rate by means of the AGA-3 equation (2.15) for any particular choice of pressure taps.
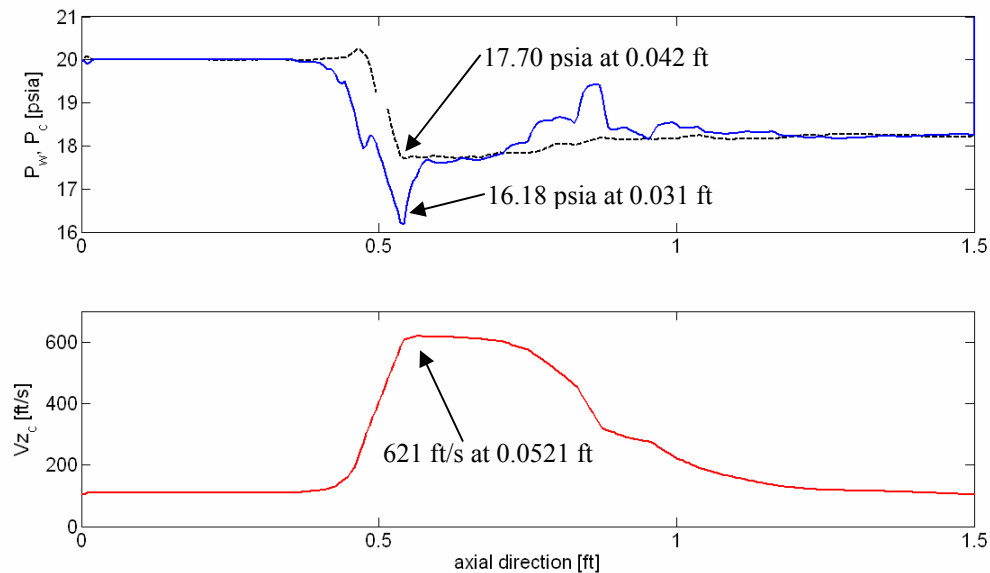
Figure 8.8. Axial distribution of Pressure and Velocity for N_{Re} =110,000.

Figure 8.8 presents the distribution of axial velocity along the axis of the pipe. It is clear how the velocity remains fairly constant from the inlet to 0.18 ft upstream the plate (z = -1.0625 D) where the fluid starts deviating from a fully developed flow as explained before. At this point, a sudden increase occur due to the reduction of area, and this acceleration continues through the orifice and reach a maximum of 621 ft/s at z = 0.3126 D, which corresponds to the location of the vena contracta. It is important to address the fact that the location of minimum wall pressure (z = 0.25 D) and maximum axial velocity along the axis of the pipe do not coincide as assumed by the

AGA-3 equation (2.15). This phenomenon can be explained by recognizing the two-dimensional nature of the pressure field which is neglected by the AGA-3 equation. In order for the minimum wall pressure to occur at the same location as the maximum centerline axial velocity, $\partial p / \partial r$ should be zero, but the fact that a recirculation phenomenon takes places there introduces radial and axial variations in both the velocity and the pressure. Therefore, the minimum wall pressure and maximum centerline axial velocity should not be expected to occur at the same location.

Figure 8.9 presents density profiles at different locations upstream the plate. Note that for illustration purposes, the x-axis represents the magnitude of the density and the y-axis corresponds to the normalized radial distance. It is very clear how from the inlet of the section to z = -1.0625 D the density remains almost constant through the radius of the pipe. This is consistent with the fact that a fully developed flow occurs at these locations as predicted by the velocity profiles (Figure 8.1 and 8.3). As the fluid moves downstream, the density decreases in the region near the axis of the pipe. This is also expected in order have conservation of mass in the axial direction since the fluid accelerates in that regions as it is approaching the orifice.
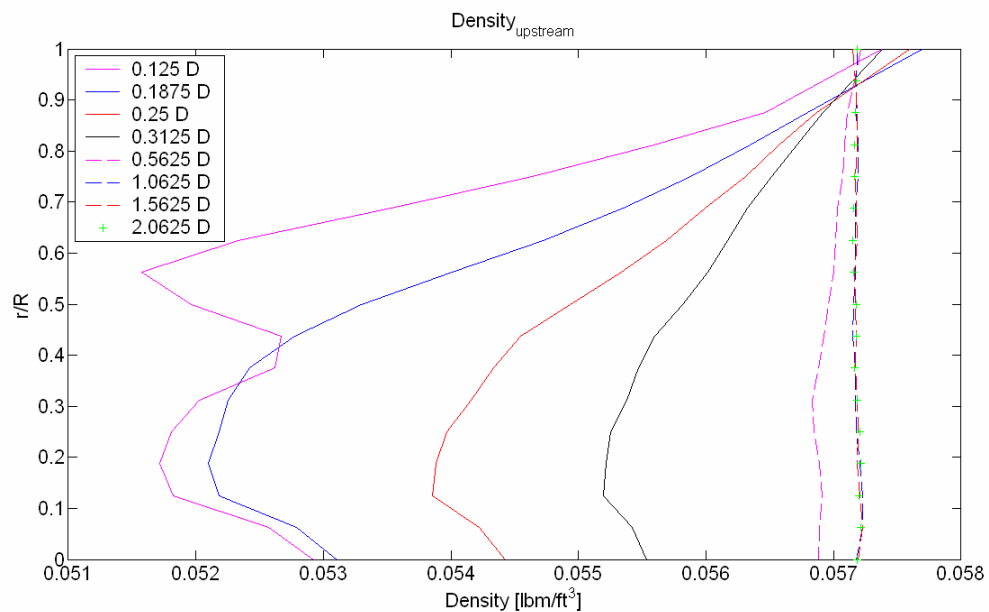
Figure 8.9. Density profiles upstream the orifice-plate for N_{Re}=110,000.

The values of density are contoured near the orifice-plate in Figure 8.10. We can see how the density values are lower where fluid achieve maximum velocities downstream the orifice, which is the location of the jet flow. The region of lower density continues where the recirculation zone

and orifice jet intersects. This can be attributed to the fact that a large velocity gradient takes place in that region increasing the turbulence effects.
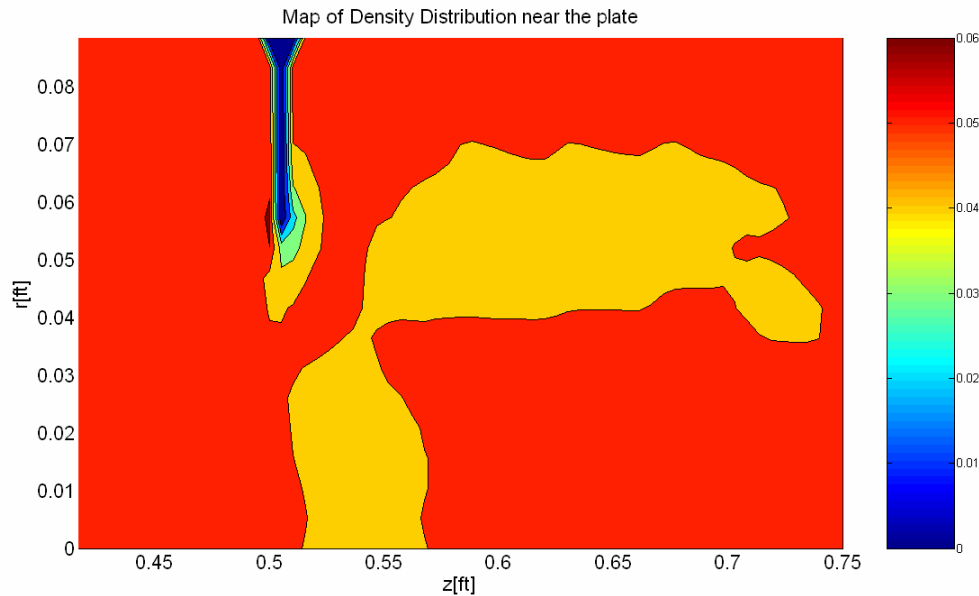
Figure 8.10. Contour plot of Density near the orifice-plate for N_{Re}=110,000.

The axial distribution of the temperature along the wall is represented by the dashed black line in Figure 8.11. The solid blue line corresponds to the temperature along the axis of the pipe. In consistency with the results presented for the other flow variables, from the inlet of the section to $z = -1.0625$ D no variation of the temperature in the radial direction can be appreciated since a fully developed flow occurs. After that location, a sudden decrease in temperature to a minimum of 50ºF can be observed due to the compression effect caused by the fluid entering a section of reduced area. The fluid cools down as it accelerates in the jet orifice. When the fluid reaches the maximum velocity and it starts decelerating, the temperature suddenly increases again due to the expansion that is taking place. As the fluid moves downstream, an additional increase in temperature is observed where the jet flow reattaches to the flow field in the recirculation region. This phenomenon was also observed for the pressure in Figure 8.8. For $z > 4.0$ D, the temperature distributions start superimposing again as the fluid is again approaching a fully developed flow and the radial variation in temperature is greatly reduced.
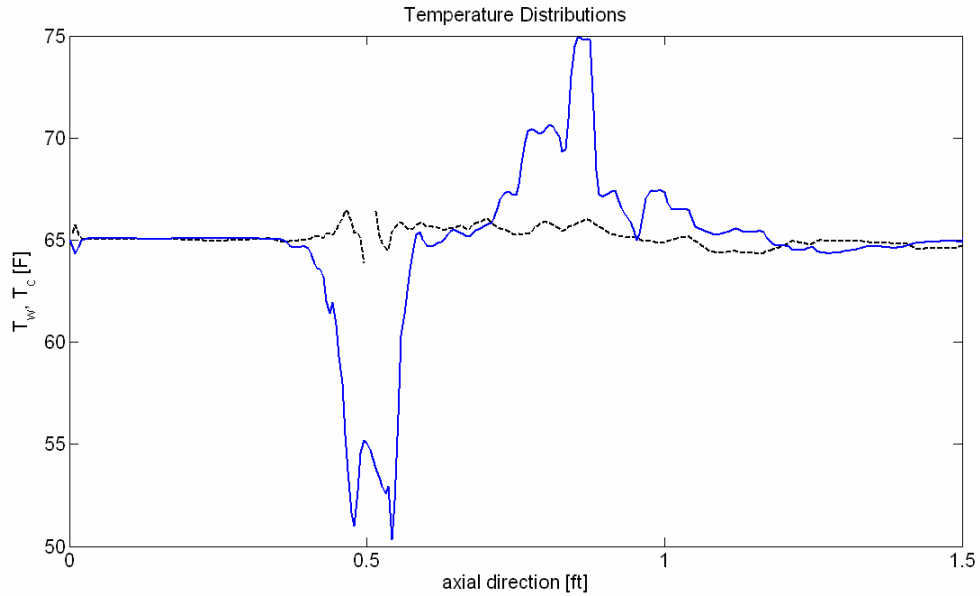
Figure 8.11. Axial distribution of Temperature for N_{Re} =110,000.

8.1.1. Flow Rate Calculation

The flow rate predicted by the model was computed by numerical integration of the axial velocity at a cross section located downstream the plate where a fully developed flow has been achieved (z = 5.0 D). The radial numerical integration was calculated as follows:

$$Q = \int_0^R V_z(r).2\pi r.dr$$

$$Q = 2\pi \sum_{j=1}^{nr-1}[(V_z(I,j)r(j)) + (V_z(I,j+1)r(j+1))]\frac{dr}{2} \qquad (8.1)$$

Note that "I" represents the location in the axial direction. The volume obtained from the previous expression was for the existing pressure and temperature. In order to determined such flow rate at standard conditions, the pressure and temperature where computed at the specific cross section. The values were obtained integrating numerically in the radial direction as:

$$\bar{p} = \frac{\int_0^R p(I,j).2\pi r.dr}{\int_0^R 2\pi r.dr} = \frac{\sum_{j=1}^{nr-1}[p(I,j)r(j) + p(I,j+1)r(j+1)]dr}{R^2} \qquad (8.2)$$

$$\bar{T} = \frac{\int_0^R T(I,j).2\pi r.dr}{\int_0^R 2\pi r.dr} = \frac{\sum_{j=1}^{nr-1}[T(I,j)r(j) + T(I,j+1)r(j+1)]dr}{R^2} \qquad (8.3)$$

Now, the volumetric flow rate at standard conditions is calculated as:

$$Q_{sc} = \frac{Q.\bar{p}.T_{sc}}{p_{sc}.\bar{T}.z} \qquad (8.4)$$

For this case, the flow rate calculated by the model was 221.208 MSCF/D. Comparing this value with the imposed flow rate at the inlet (222.600 MSCF/D) the error is 0.63%. Moreover, with the values of pressure predicted by the model at the flange tap locations, a pressure drop of 2.2657 psig was determined and together with the pressure at the flange upstream the plate (20.0288 psia) and the rest of the specifications mentioned at the beginning of this chapter, a flow rate of 231.575 MSCF/D was estimated using the AGA-3 equation (2.15). The difference between this model and the AGA-3 equation is of 4.47 %.

The analysis just presented, applies for all the other cases, which are summarized in Tables 8.1 to 8.3. For the sake of brevity, similar plots for all the cases predicted by the model will be omitted, and only the relevant graphs for the parametric study that follows are presented in this chapter.

The integrated velocity profiles were obtained using linear interpolation between two points. A higher order polynomial interpolation could be used to obtain the velocity profiles and ultimately calculated the flow rate. However, after trying second and third order polynomial interpolation only a very small variation in the flow rate calculations was observed; for some cases, the values are higher while for others they are lower than the value produced by the linear interpolation. For consistency purposes, and due to the fact that fully turbulent profiles are essentially flat compared

to laminar flow, all the results presented in this study were obtained using linear interpolation. Sensitivity studies can be performed in the future to determine which order of polynomial may give a better flow rate estimates.

8.2. Parametric Study

Figures 8.5 and 8.6 illustrate the overall features of the flow field in orifice meter. Phenomena such as the turning of the fluid towards the orifice upstream the plate, the separation of the flow from the edge of the plate, the formation of a jet flow, and the recirculation zone behind the plate can be appreciated. These features are the same for all the possible cases, and the fact that the results in Figures 8.1 to 8.4 are normalized, allows for generalization. In the following sections a parametric study varying the Reynolds number, the specific gravity of the fluid, and the Beta ratio is presented.

8.2.1. Reynolds Number

The effect of the Reynolds number is presented here. Note that only plots for the $N_{Re} = 67,000$ and 21,000 cases are presented here, because the ones that correspond to the $N_{Re} = 110,000$ case are included in Section 8.1 of this study. The variation of the Reynolds number was achieved through a change in the fluid velocity without making any other change to the computational model or solution procedure. Table 8.1 summarizes the cases predicted.

Table 8.1. Specifications for Reynolds Number parametric study.

Case	Reynolds Number	$V_{z,inlet}$ [ft/s]
1.1	21,000	17.68
1.2	67,000	53.19
1.3	110,000	87.34

Figures 8.12 and 8.13 present the wall shear stress for the cases of $N_{Re} = 67,000$ and 21,000 respectively. Recall that Figure 8.6 show the same results for the case of $N_{Re} = 110,000$. As mentioned before, the location where the sign changes for the second time indicates the end of the back flow and therefore defines the extension of the recirculation region. For the $N_{Re} = 110,000$

case, the recirculation phenomenon ended 2.44 pipe diameters downstream the plate, while for the cases of 67,000 and 21,000, this recirculation region extends to 2.09 and 2.03 pipe diameters downstream the plate, as shown in Figures 8.12 and 8.13 respectively. From these results one can conclude that the larger the Reynolds number, the larger the extension of the recirculation region which is caused by the turbulent effects of the flow.

Another parameter that can be analyzed is the minimum centerline pressure which for the N_{Re} = 110,000 case is 16.18 psia and occurs at z = 0.1878 D (Figure 6.8). For the N_{Re} = 67,000 and 21,000 cases, Figures 8.14 and 8.15 show minimum pressures of 16.96 and 19.74 psia respectively. As expected the larger the Reynolds number, the larger the pressure drop caused by the plate. Additionally, as the Reynolds number increases, the maximum velocity which occurs at the location of the vena contracta also increases. For N_{Re} = 110,000, the maximum velocity is 621 ft/s, and for the N_{Re} = 67,000 and 21,000 cases at the vena contracta the velocities are equal to 365 ft/s and 111 ft/s respectively. For all the cases, the location of minimum wall pressure and maximum axial velocity along the axis of the pipe do not coincide. As explained before, this is because the present model considers the 2-D effects of the flow, which are neglected by the AGA-3 equation (2.15).
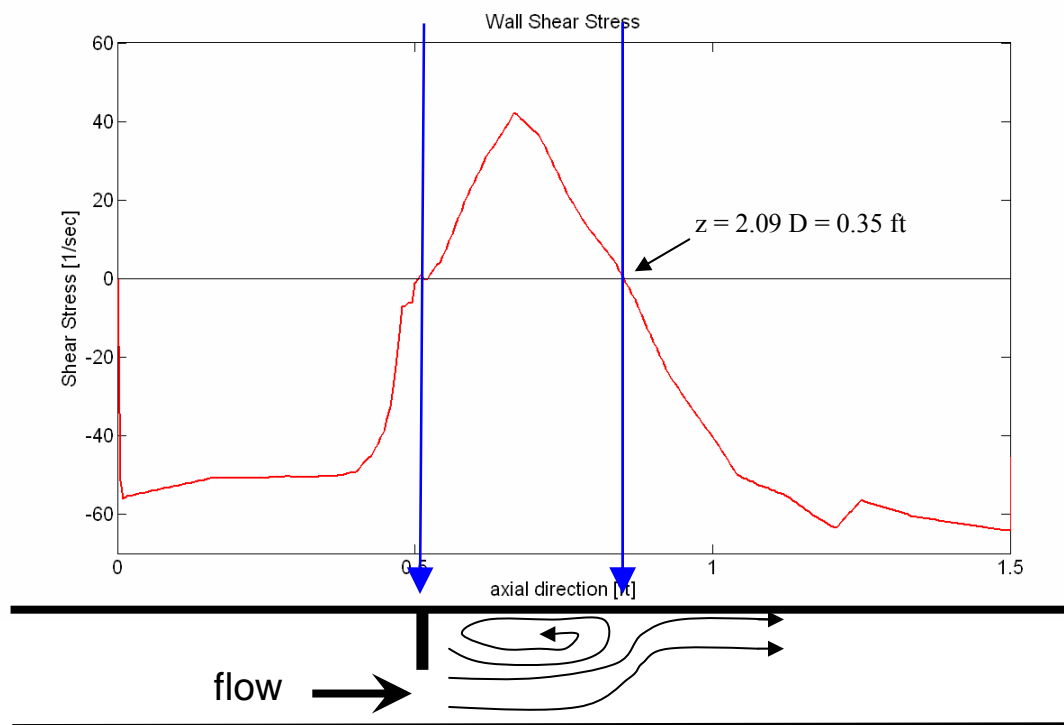
Figure 8.12. Wall Shear Stress for N_{Re} =67,000.
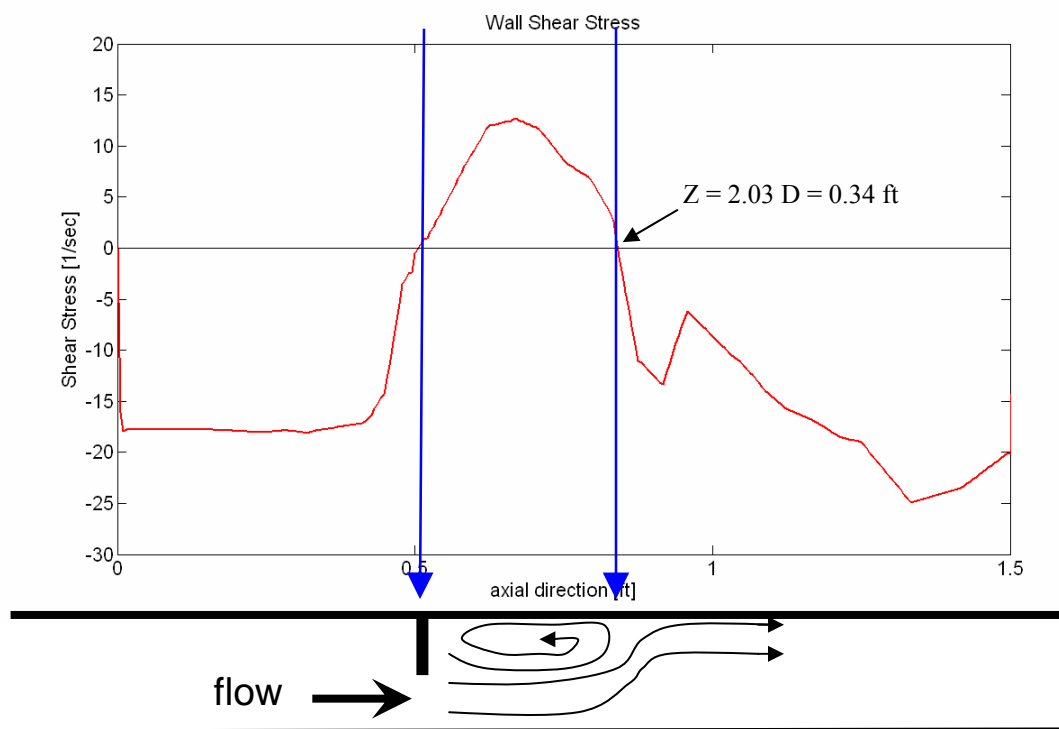
Figure 8.13. Wall Shear Stress for N_{Re} =21,000.
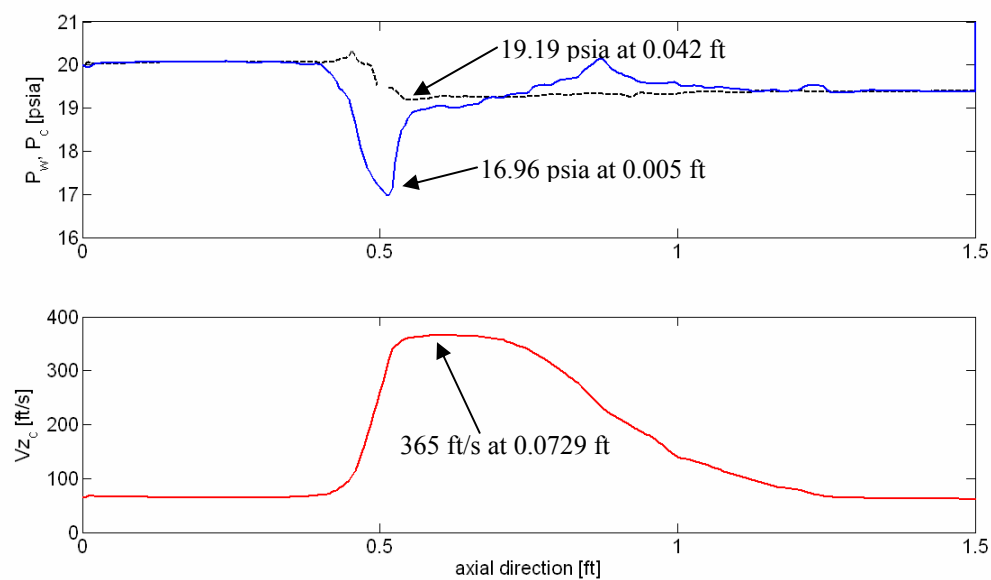
Figure 8.14. Axial distribution of Pressure and Velocity for N_{Re} =67,000.
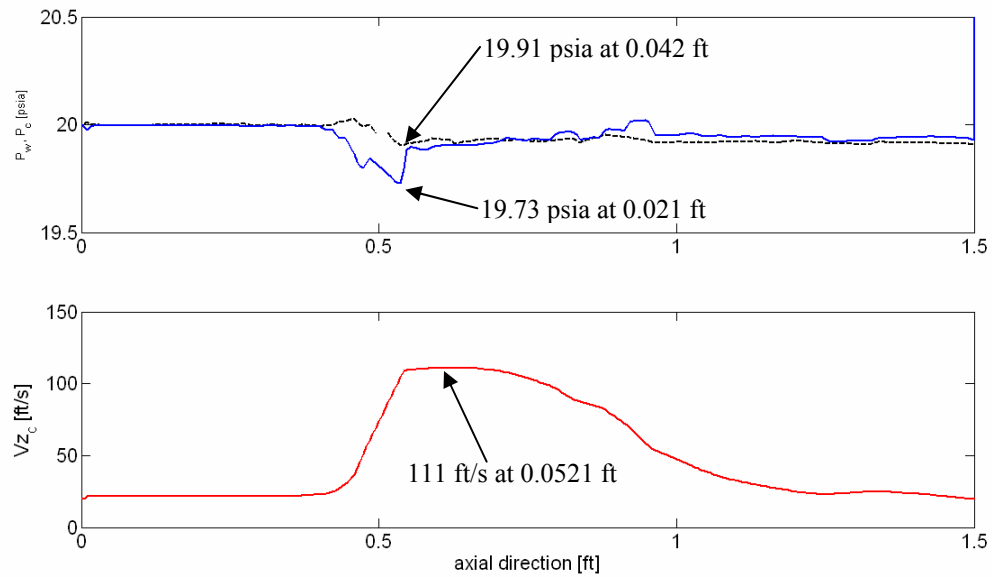
Figure 8.15. Axial distribution of Pressure and Velocity for N_{Re} =21,000.

Figures 8.16 and 8.17 show the temperature profiles along the pipeline for the cases of N_{Re} = 67,000 and 21,000 respectively. The main difference between the three cases is in the temperature drop that takes place at the plate, which for the N_{Re} = 110,000 case was shown to be 15ºF in Figure 8.11, and for the cases of N_{Re} = 67,000 and 21,000 they are 2ºF and 1.2ºF respectively (Figures 8.16 and 8.17). Additionally, the temperature drop seems to grow exponentially as the Reynolds number increases.
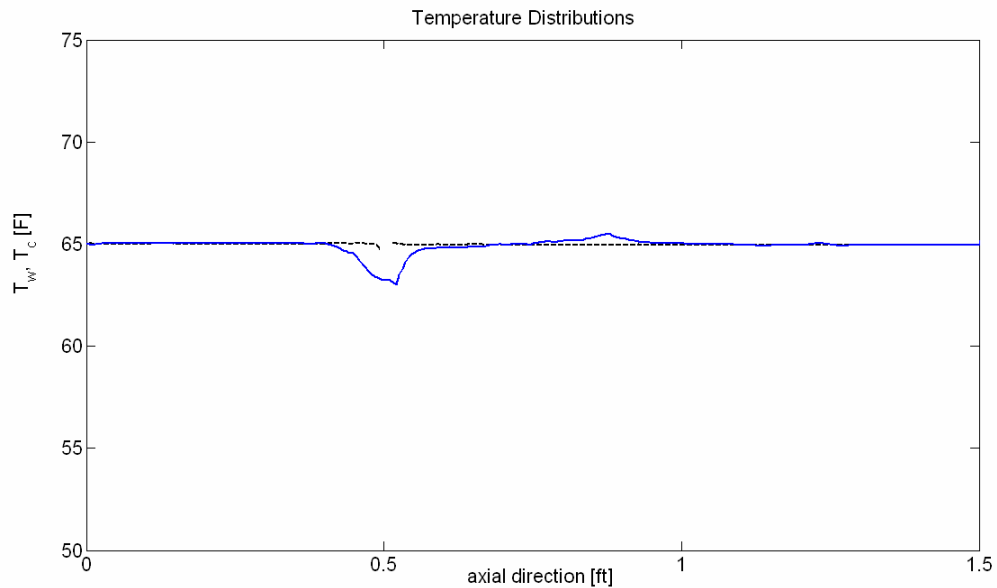
Figure 8.16. Axial distribution of Temperature for N_{Re} =67,000.
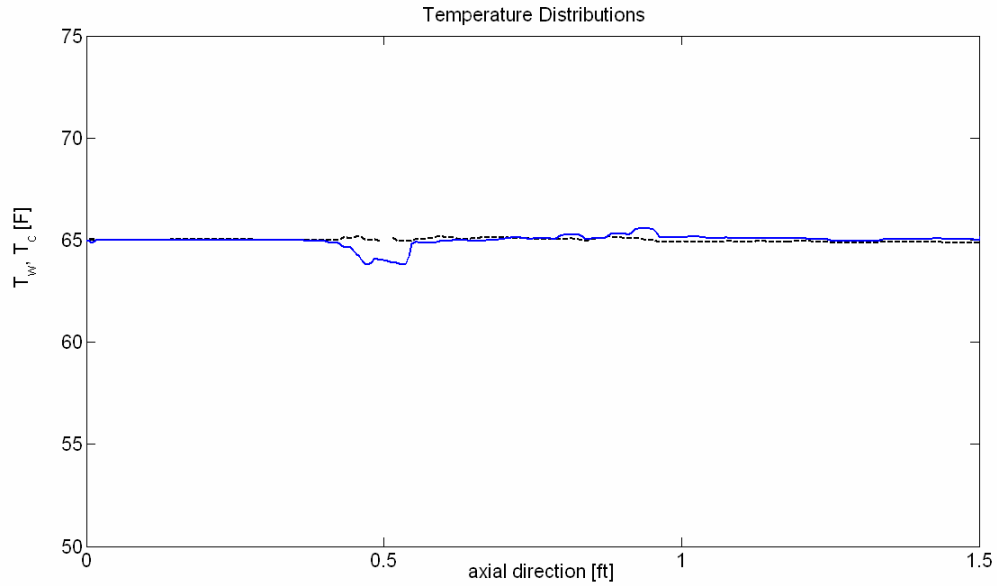
Figure 8.17. Axial distribution of Temperature for N_{Re} =21,000.

Table 8.2 presents the flow rate calculated by the model using numerical integration of the axial velocity at a given location, and it was also determined using the AGA-3 equation with the pressure drop across the plate, the pressure at the flange upstream the plate and the rest of the specifications mentioned in Section 2.9.1 of the present study. The maximum error between the specified flow rate at the inlet and the predicted value is 5.83% for the case of N_{Re} = 21,000, while the maximum error produced by the AGA-3 equation is 4.57% for the same case. For the other cases the error generated by our model is below 3%, and the error produced by AGA-3 is above 4%.

Table 8.2. Predicted Flow rate and Error for Reynolds number parametric study.

Case	Q [MSCF/D]			Error using this model [%]	Error using AGA-3 [%]
	Specified at the inlet	Predicted by this model	AGA-3		
1.1	42.500	45.130	40.559	5.83	-4.57
1.2	135.550	139.269	142.756	2.67	5.32
1.3	222.600	221.208	231.575	-0.63	4.03

8.2.2. Specific Gravity

This section presents how the specific gravity of the fluid affect the remaining flow variables. Table 8.3 summarizes the composition of the fluids for the cases predicted. The Reynolds number was maintained constant at 110,000. Only the plots for the $\gamma = 0.65$ and 0.77 cases are included here because the ones for the $\gamma = 0.55$ were presented in Section 8.1 of this study.

Table 8.3. Specifications for Specific Gravity parametric study.

Case	Composition	Specific Gravity	$V_{z,inlet}$ [ft/s]
2.1	100% CH_4	0.55	87.34
2.2	80% CH_4 and 20% C_2H_6	0.65	80.70
2.3	70% CH_4, 15% C_2H_6 and 15% C_3H_8	0.77	72.25

To keep the Reynolds number constant, the inlet flow rate was decreased as the density of the fluid was increased. Recall from Figure 8.8 that the maximum velocity which occur at the location of the vena contracta for the $\gamma = 0.55$ case was 621 ft/s. Figures 8.18 and 8.19 show maximum centerlines velocities equivalent to 574 ft/s and 514 ft/s respectively. This trend was expected in order to maintain an invariable Reynolds number. With respect to the centerline pressure, represented by the solid blue line, for the $\gamma = 0.55$ case, the minimum is 16.18 psia and occurs at z = 0.1878 D (Figure 6.8). For the $\gamma = 0.65$ and 0.77 cases, Figures 8.18 and 8.19 show minimum pressures of 16.28 and 16.54 psia respectively. This results show a very small variation of the pressure drop with respect to the change in specific gravity of the fluid, which confirms the fact that this factor is more dependent of the Reynolds number rather than to the other parameters. Notice again that for all the cases, the location of minimum wall pressure and maximum axial velocity along the axis of the pipe do not coincide (0.01 ft difference), as would be predicted by the AGA-3 equation.
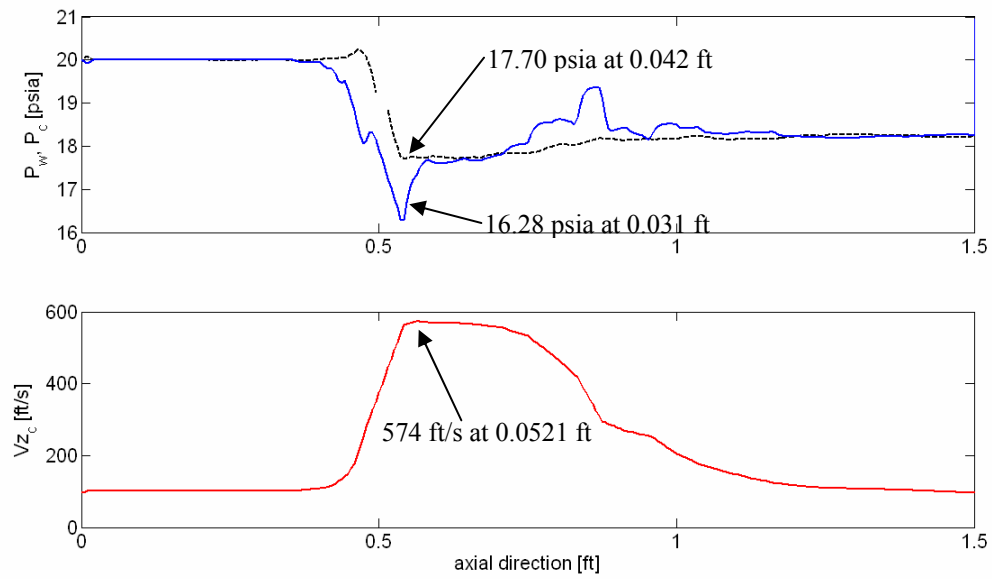
Figure 8.18. Axial distribution of Pressure and Velocity for γ=0.65.
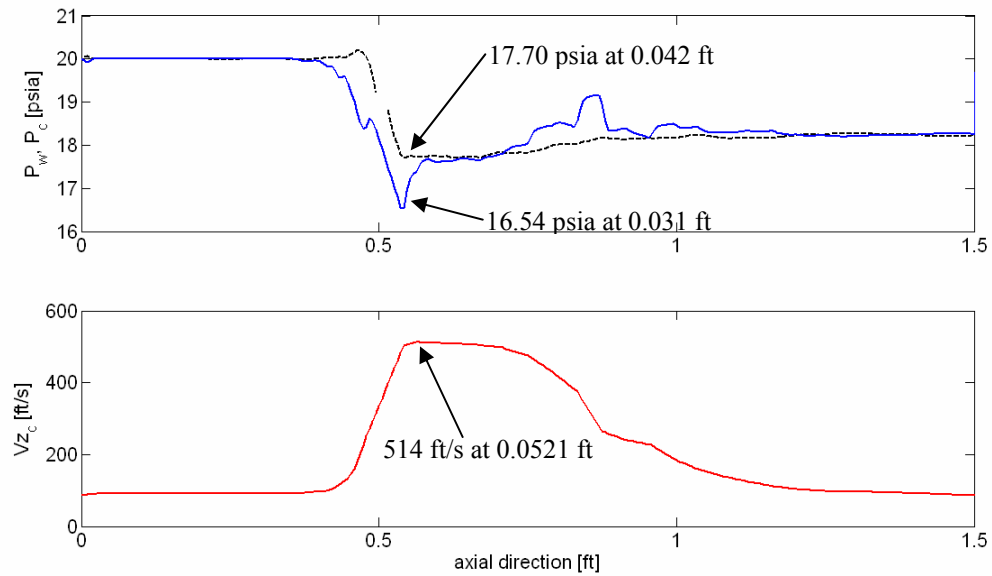
Figure 8.19. Axial distribution of Pressure and Velocity for γ=0.77.

Figures 8.20 and 8.21 show the temperature profiles along the pipeline for the cases of γ = 0.65 and 0.77 respectively. Recall from Figure 8.11 that the temperature drop for the γ = 0.55 case was shown to be 15ºF, while for the γ = 0.65 and 0.77 cases, they are 13ºF and 9ºF respectively. Therefore, it is clear that for a fixed Reynolds number, fluids with larger density will produce smaller temperature drop across the plate.
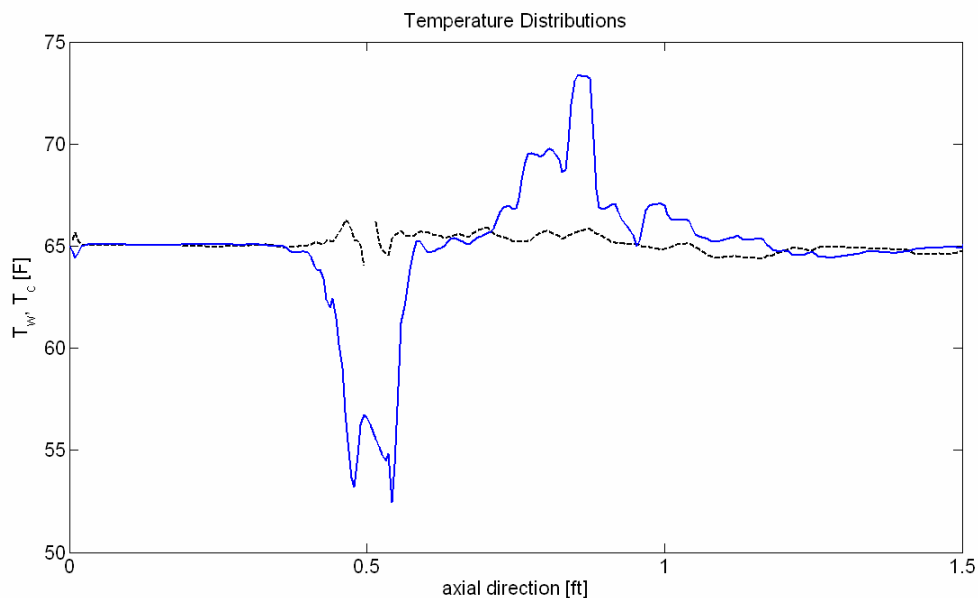
Figure 8.20. Axial distribution of Temperature for γ=0.65.
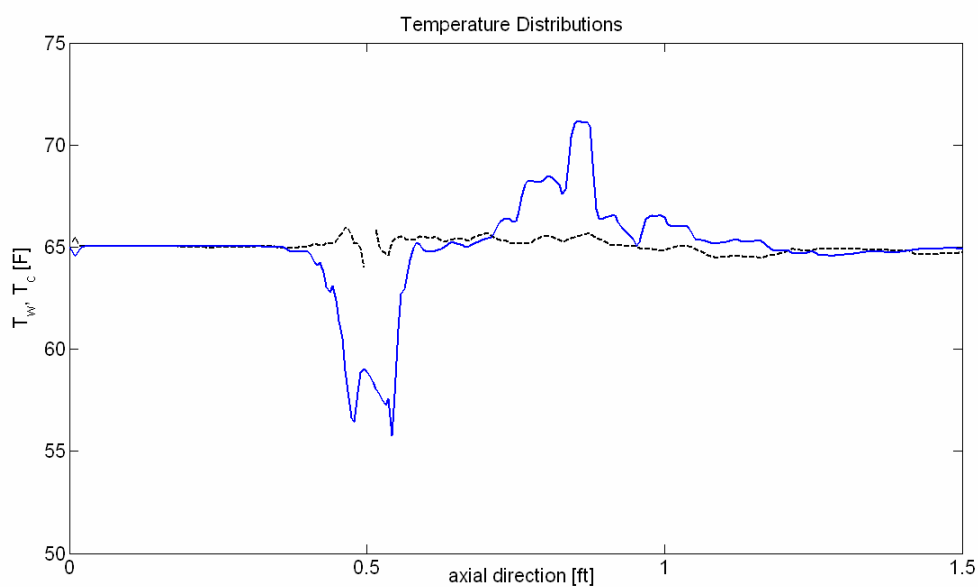
Figure 8.21. Axial distribution of Temperature for γ=0.77.

Table 8.4 presents the flow rate calculated by the model using numerical integration of the axial velocity at a given location, and it was also determined using the AGA-3 equation. The maximum error between the imposed flow rate at the inlet and the predicted value is 0.93%. Moreover, the maximum error produced by the AGA-3 equation is above 6%.

Table 8.4. Predicted Flow rate and Error for Specific Gravity parametric study.

Case	Q [MSCF/D]			Error using this model [%]	Error using AGA-3 [%]
	Specified at the inlet	Predicted by this model	AGA-3		
2.1	222.600	221.208	231.575	-0.63	4.03
2.2	205.950	204.393	213.650	-0.76	3.74
2.3	184.700	183.004	196.543	-0.93	6.41

8.2.3. Beta Ratio

In this section, the effect of the Beta ratio in the flow variables is presented. Two cases are compared in this section, for Beta = 0.5 and 0.75, although all the figures presented here correspond to the last case because for Beta = 0.5 they are included in Section 8.1 of this chapter for the N_{Re} = 110,000 case. The specific gravity of the fluid in both cases is 0.55 and the Reynolds number is 110,000. Table 8.5 summarizes the cases predicted.

Table 8.5. Specifications for Beta Ratio parametric study.

Case	Beta ratio	$V_{z,inlet}$ [ft/s]
3.1	0.50	87.34
3.2	0.75	87.34

Figure 8.22 presents the radial profiles of the axial velocity at different locations upstream the plate. Comparing these results with the ones generated for the Beta = 0.50 case (Figure 8.1), it can be appreciated that there is almost no variation between the inlet of the pipe and -0.5625 D (pipe diameters) upstream the plate for both cases, indicating that the influence of the plate in the flow field depends mostly on the location of the plate and not the diameter of the orifice. When approaching the plate, the axial velocities increased significantly in the region near the axis of the pipe while close to the wall it start to decrease since the fluid is turning towards the orifice. Then, very close to the plate at z = -0.125 D the highest velocity is reached at the centerline as the fluid is now entering the bore, which also causes the values of velocity to approach zero near the wall of the pipe. For the case of Beta = 0.75, the normalized maximum velocity is 0.65 compared to 0.49 in the Beta = 0.5 case, which implies that for a larger orifice diameter compared to the pipe diameter, the fluid accelerates more upstream the plate.

Figure 8.23 shows the radial distribution of the normalized axial velocities at different locations downstream the plate. It can be clearly seen how velocities increase significantly as the fluid exits the orifice (from z=0.065 D to 0.25 D). At these locations, the velocity remains approximately constant from the centerline to r/R = 0.60, showing a nearly flat profile. However, near the wall of the pipe (from r/R = 0.75 to 1.0), negative values of velocities can be observed which characterize the backflow that takes place behind the plate due to the recirculation phenomenon.

As the fluid moves downstream, the flow starts spreading as the velocity near the centerline decreases but still negative velocities are observed up to a location of z = 1.0 D compared to z = 3.0 D in the Beta = 0.5 case, which indicates that the extension of the recirculation zone is smaller as the Beta ratio increases. For the profiles located at z > 1.0 D no more negative velocities can be observed which indicates that no more backflow takes place. Additionally, the velocity profiles flatten out as they approach a fully developed flow at z = 5.0 D. This location coincide with the one in the Beta = 0.75 case confirming the fact that the influence of the plate in the flow field is not strongly related with the Beta ratio.

The radial distributions of the normalized radial velocity at various locations upstream the plate are plotted in Figure 8.24. Between the inlet and z = -0.5625 D, the radial velocity component is mainly zero since a fully developed flow takes place which is not influenced by the orifice plate. In the cross sections closer to the plate (z > -0.5625 D), the values of radial velocity become negative across the entire pipe, which indicates how the fluid is turning towards the bore. Note that these are the same locations where the axial velocity increases (Figure 8.22) as the fluid is rapidly converging toward the centerline before entering through the orifice. Very close to the orifice, at z = -0.125 D, the minimum value of radial velocity is obtained near the edge of the plate, which represents how the fluid is actually entering the bore. For this case the location is r/R = 0.7 compared to r/R = 0.45 in the Beta = 0.5 case (Figure 8.3).
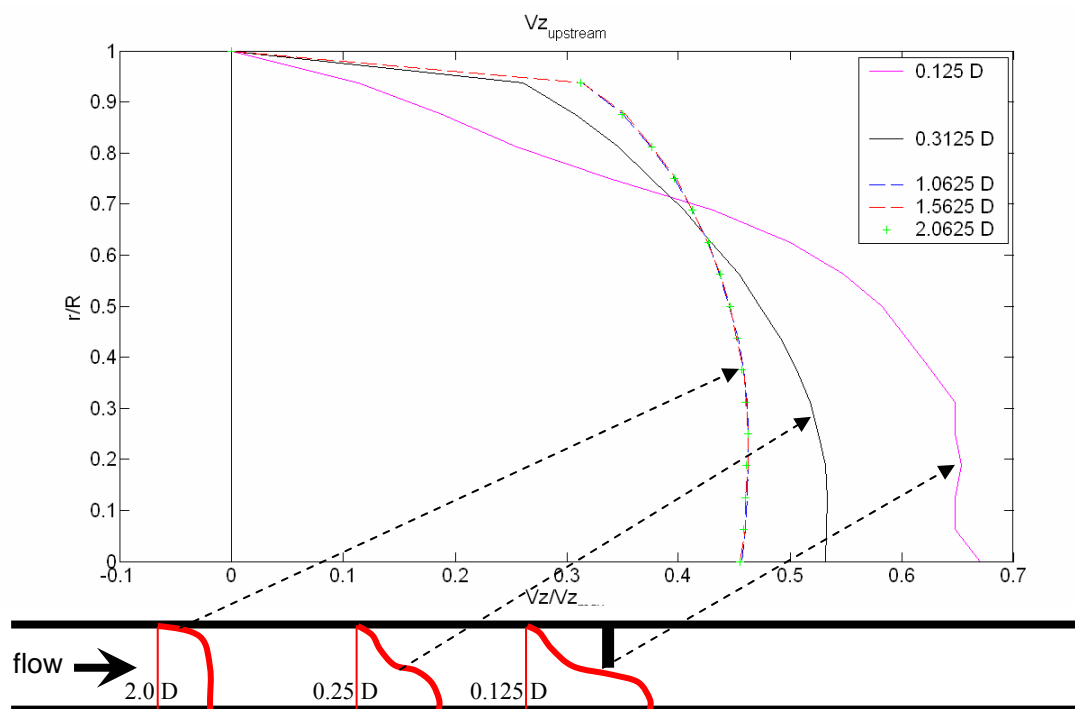
Figure 8.22. Axial Velocity profiles upstream the orifice-plate for Beta = 0.75.
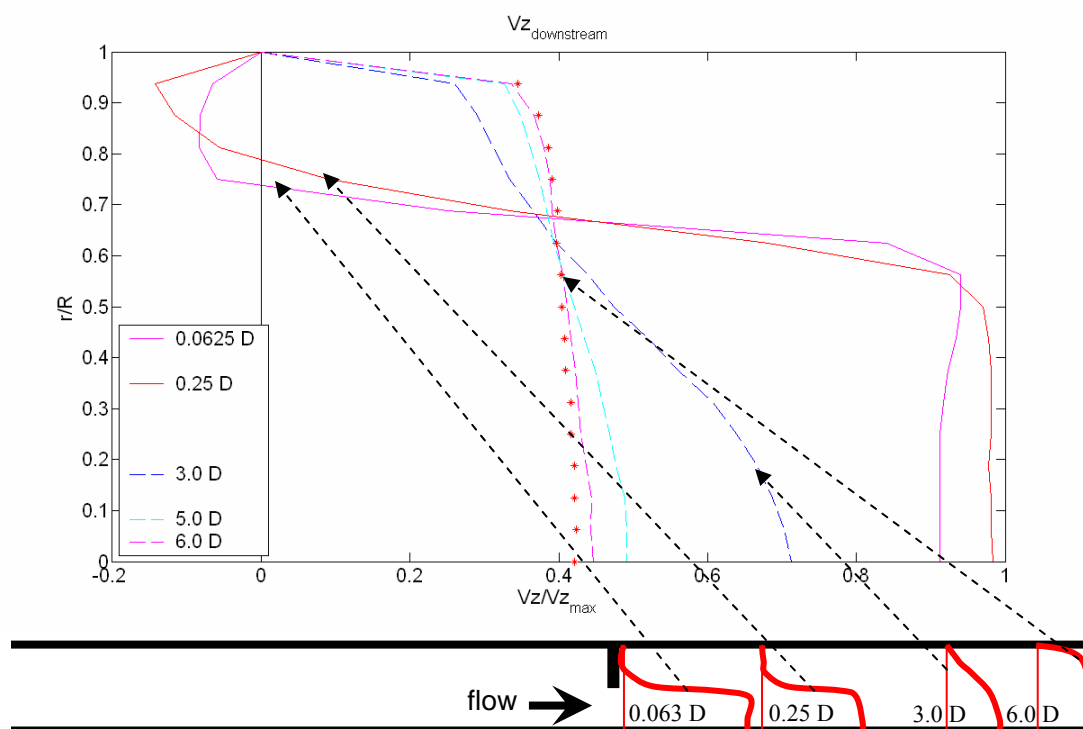
Figure 8.23. Axial Velocity profiles downstream the orifice-plate for Beta = 0.75.

Figure 8.25 shows how just downstream the plate the radial components of the velocity reduce to half of the values observed upstream the orifice (compare $V_r/V_{r,max}$=-1.0 at z=-0.125 D with $V_r/V_{r,max}$=-0.42 at z=0.0625 D). After that location, the magnitude of the radial velocities keeps decreasing near the centerline because the flow is almost completely axial and is accelerating in that direction (Figure 8.23) which characterizes the jet flow. As the fluid moves downstream (z > 1.0 D) positive values of radial velocity can be observed indicating the flow in the jet reattaching to the region near the wall of the pipe, where the recirculation phenomenon is taking place. When the fluid approaches the outlet of the section (z > 5.0 D) the radial velocities gets very close to zero since a fully developed flow is been formed again as confirmed by the axial velocity profiles in Figure 8.23.
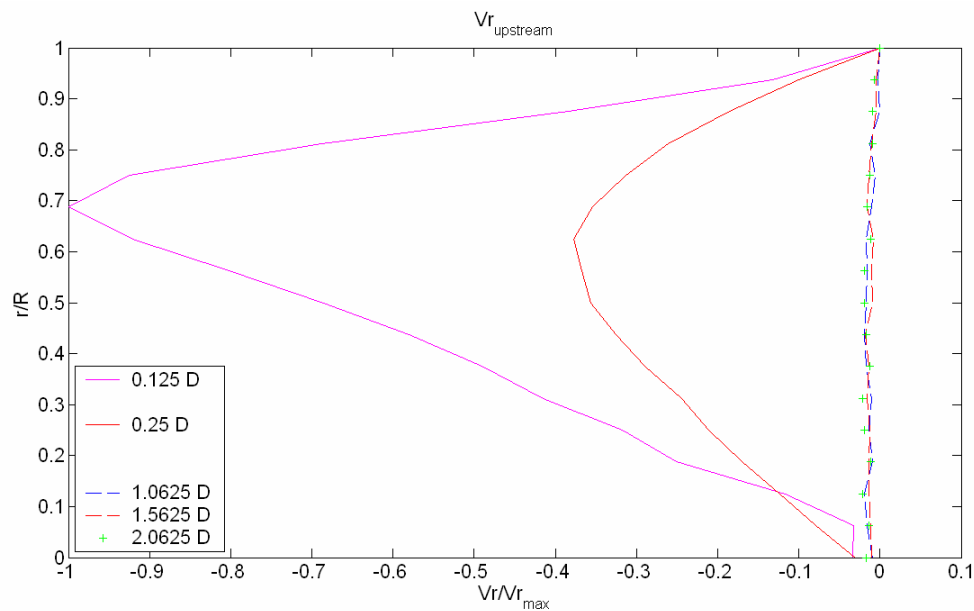
Figure 8.24. Radial Velocity profiles upstream the orifice-plate for Beta = 0.75.

The flow field represented by the vector plot near the orifice plate is shown in Figure 8.26. The sections of the flow immediately upstream and downstream the orifice plate can be observed, which contain the most relevant information. A large recirculation zone can be appreciated downstream the plate between the jet and the pipe wall.
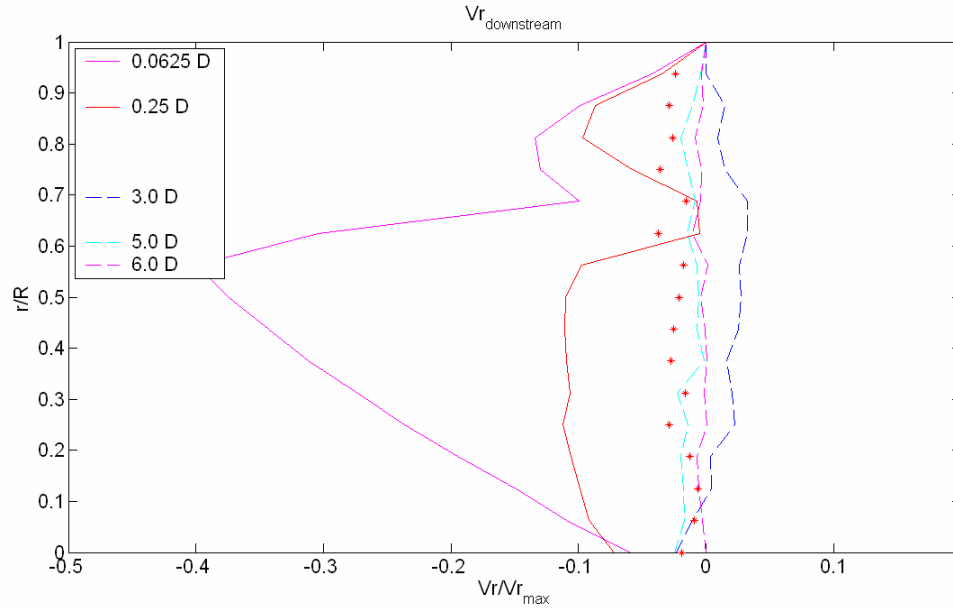
Figure 8.25. Radial Velocity profiles downstream the orifice-plate for Beta = 0.75.
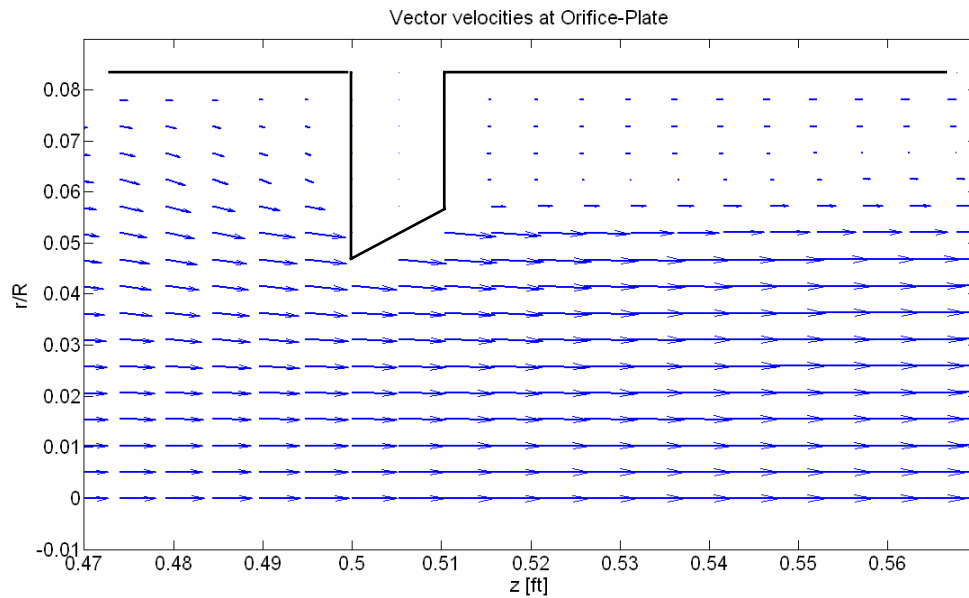
Figure 8.26. Vector velocities near the orifice-plate for Beta = 0.75.

Figure 8.27 presents the streamwise distribution of the shear stress at the pipe wall. The location where the sign changes for the second time indicates the end of the back flow and therefore defines the extension of the recirculation region. For this particular case the backflow ends 0.84 pipe diameters downstream the plate as shown in the figure below. Comparing that to the 2.44 D

for the case of Beta = 0.75, it is clear that the larger the Beta ratio, the shorter the extension of the recirculation region.

Recall from Figure 8.8 that the maximum velocity, which occurs at the location of the vena contracta, for the Beta = 0.5 case was 621 ft/s. Figure 8.28 shows a maximum centerline velocity equivalent to 228 ft/s. It is clear that the larger the diameter of the bore, the smaller the acceleration of the orifice jet which conclude with a lower maximum velocity. With respect to the centerline pressure, for the Beta = 0.5 case, the minimum is 16.18 psia and occurs at z = 0.1878 D (Figure 6.8). For the Beta = 0.75, Figure 8.28 shows a minimum pressure of 19.69 psia. Therefore, it can be concluded that the larger the diameter of the constriction, the smaller the pressure drop caused by it. It can be noted also for this case, that the location of minimum wall pressure and maximum axial velocity along the axis of the pipe do not coincide as stated before.
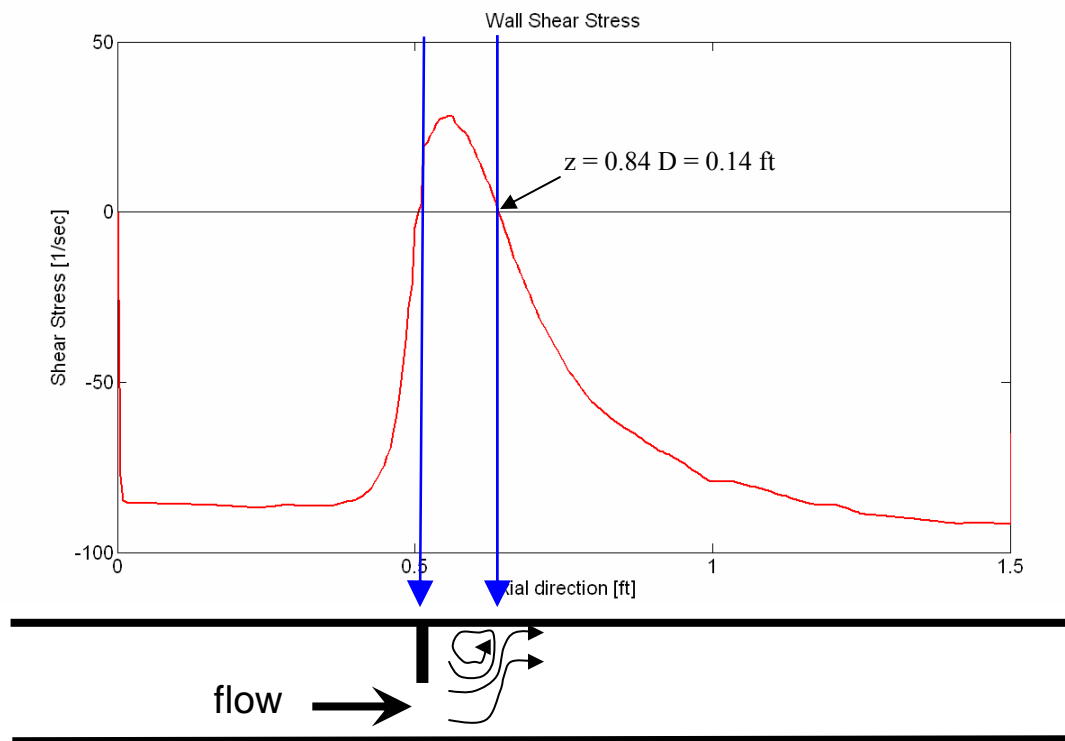
Figure 8.27. Wall Shear Stress for Beta = 0.75.
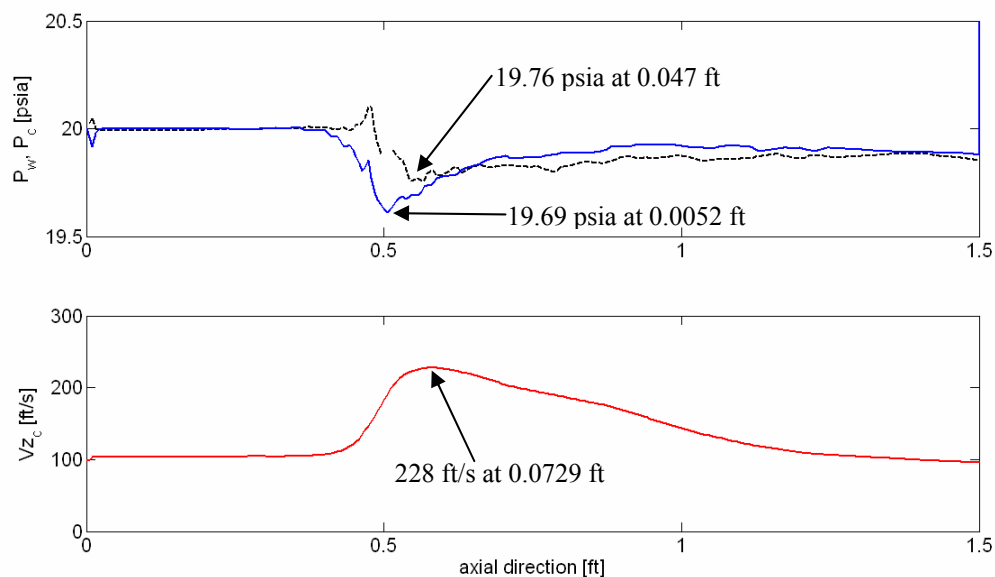
Figure 8.28. Axial distribution of Pressure and Velocity for Beta = 0.75.

Figure 8.29 shows the temperature profile along the pipeline for the case of Beta = 0.75. Recall from Figure 8.11 that the temperature drop for the Beta = 0.5 case was shown to be 15ºF, while for the present case it is only 1.9ºF. Since the fluid compresses less for a larger Beta ratio, the temperature drop across the plate is highly reduced.
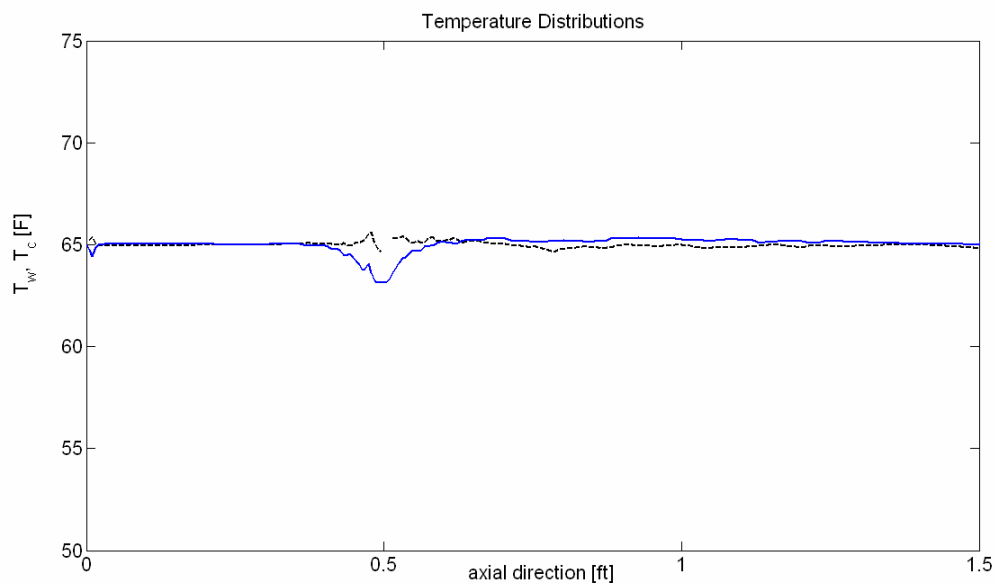
Figure 8.29. Axial distribution of Temperature for Beta = 0.75.

Finally, Table 8.6 presents the flow rate calculated by the model using numerical integration of the axial velocity at a given location, and it was also determined using the AGA-3 equation. The maximum error between the model prediction and the flow rate specified at the inlet is below 1%, while the maximum error generated by the AGA-3 equation is above 4%.

Table 8.6. Predicted Flow rate and Error for Specific Gravity parametric study.

Case	Q [MSCF/D]			Error using this model [%]	Error using AGA-3 [%]
	Specified at the inlet	Predicted by this model	AGA-3		
3.1	222.600	221.208	231.575	-0.63	4.03
3.2	208.400	210.375	198.724	0.93	-4.64

From the obtained results, it is important to point out that comparing with the imposed flow rate at the inlet, the present fundamental model produces better predictions than the AGA-3 equation. For the majority of the cases the maximum error of this model is 0.93% while AGA-3 deviates up to 6.41%. The only exception is the case for $N_{Re} = 21,000$ where this model predicts with an error of 5.83% and the AGA-3 deviates 4.57%.

8.3. Pressure Comparison

During the experiments only the pressure at the inlet of the section and at the outlet of the sections were measured. The proposed model uses the inlet pressure as a boundary condition and for additional verification, the error between the measured pressure and predicted value at the outlet are presented in Table 8.7.

Table 8.7. Error in outlet pressure predictions.

	Reynolds Number		
Outlet Pressure [psia]	91,100	54,700	18,400
Experimental	17.99	19.06	19.54
Numerical	17.73	18.74	19.19
Difference	0.26	0.32	0.35
Error [%]	1.45	1.68	1.79

Note that the error in pressure predictions is within 2% at the outlet of the section. Additionally, it is clear the error increases as the Reynolds Number decreases which is the same behavior observed for the flow rate predictions.

The error in pressure presented in Table 8.7 is added to the pressure drop caused by the plate and used in the AGA-3 equation in order to give a rough conversion of the error in pressure to an error in flow rate. Table 8.8 show the translated errors of flow rate for all the cases modeled and it is clear that they are all within 1%, which is consistent with the error generated when comparing with the flow rate imposed at the inlet of the section of the pipe.

Table 8.8. Translation of Pressure Error into Flow Rate Error

Case	ΔP [psia]	AGA-3	AGA-3 $_{w/\ Pcorr}$	ΔP $_{error}$ [%]	Q $_{error}$ [%]
1.1	0.063	40.559	40.199	-1.79	-0.90
1.2	0.816	142.756	141.685	-1.68	-0.76
1.3, 2.1 and 3.1	2.266	231.575	230.025	-1.45	-0.67
2.2	2.267	213.65	212.220	-1.45	-0.67
2.3	2.277	196.543	195.228	-1.45	-0.67
3.2	2.160	198.724	197.306	-1.45	-0.72

8.4. Calibration Curves

For field application purposes, the proposed solver can be used to generate calibration curves in order to correct the estimate value given by the AGA-3 equation. Using the values calculated during the parametric study, three calibration curves are generated.

Figure 8.30 presents a curve for fixed values of specific gravity and beta ratio, and a variety of Reynolds Numbers. On the top of the plot, the equation that fits the data is included.

Calibration Curve for S.G. = 0.55, Beta = 0.5 and different Reynolds Number

$$Q_{This\ Model} = 7E\text{-}09xQ_{AGA\text{-}3}^{2} + 0.9198xQ_{AGA\text{-}3} + 7811$$
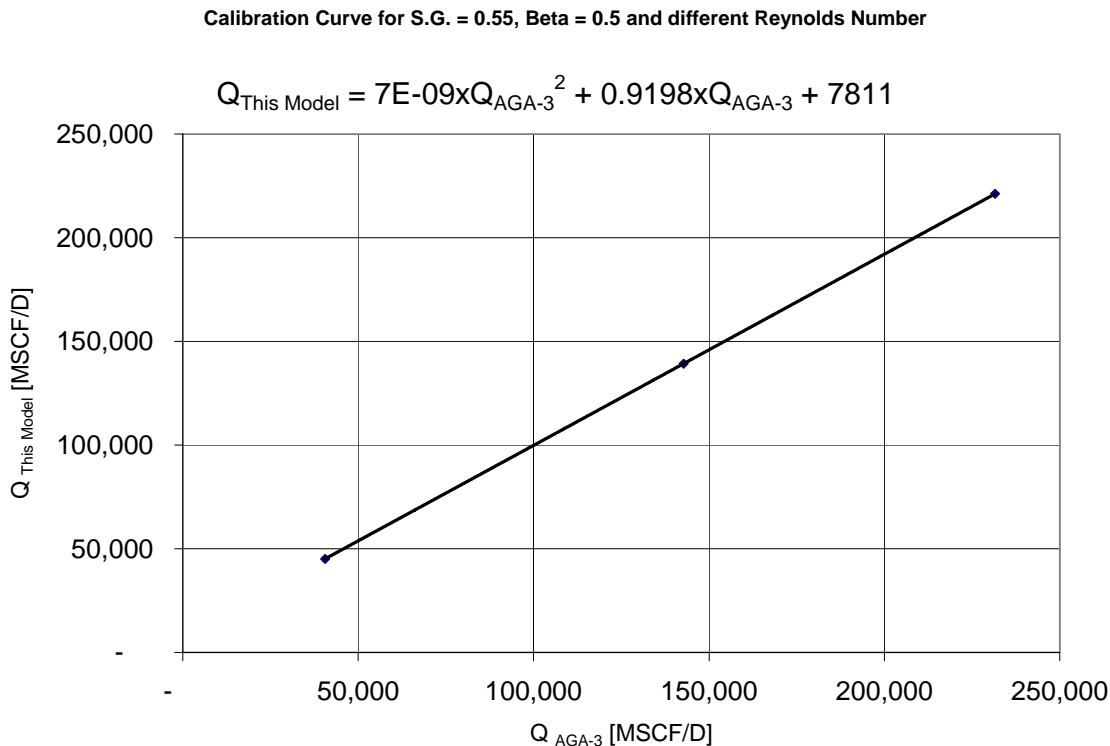
Figure 8.30. Calibration Curve for S.G. = 0.55, Beta Ratio = 0.5 and different Reynolds Numbers.

Figure 8.31 shows a curve for fixed Reynolds number and beta ratio. The calibration curve can be used for different values of specific gravity. Again, the equation that fits the data is included on the top of the plot.

Finally, in Figure 8.32 a curve for fixed Reynolds number and specific gravity is presented. The calibration curve can be used for different values of Beta ratio, by the means of the equation that fits the data and is included on the top of the plot.

It is clear the potential of the proposed solver as tool able to produce a great deal of data and then generate calibration curves that can be easily used in the field to obtain corrections for the estimates given by the AGA-3 equations.

Calibration Curve for N_{Re} = 110,000, Beta = 0.5 and different Specific Gravity

$$Q_{This\ Model} = -9E\text{-}06xQ_{AGA\text{-}3}{}^2 + 4.9063xQ_{AGA\text{-}3} - 436994$$
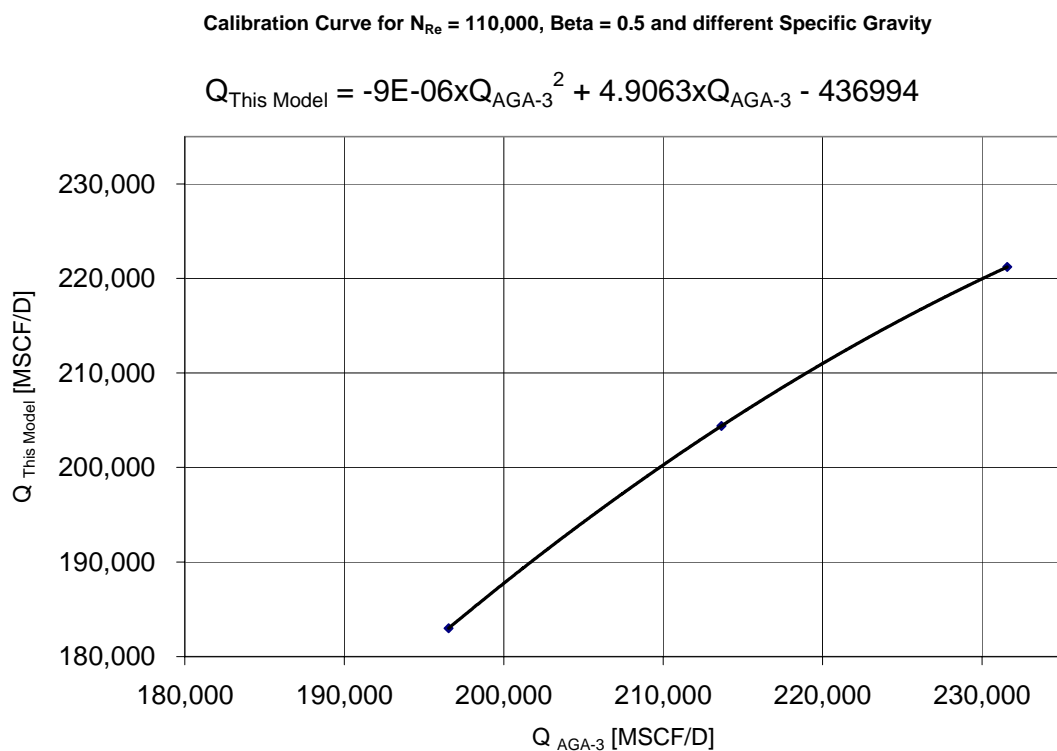
Figure 8.31. Calibration Curve for NRe = 110,000, Beta Ratio = 0.5 and different Specific Gravity.

Calibration Curve for Nre = 110,000, S.G.=0.55 and different Beta ratios

$$Q_{This\ Model} = 0.3899xQ_{AGA\text{-}3} + 130921$$
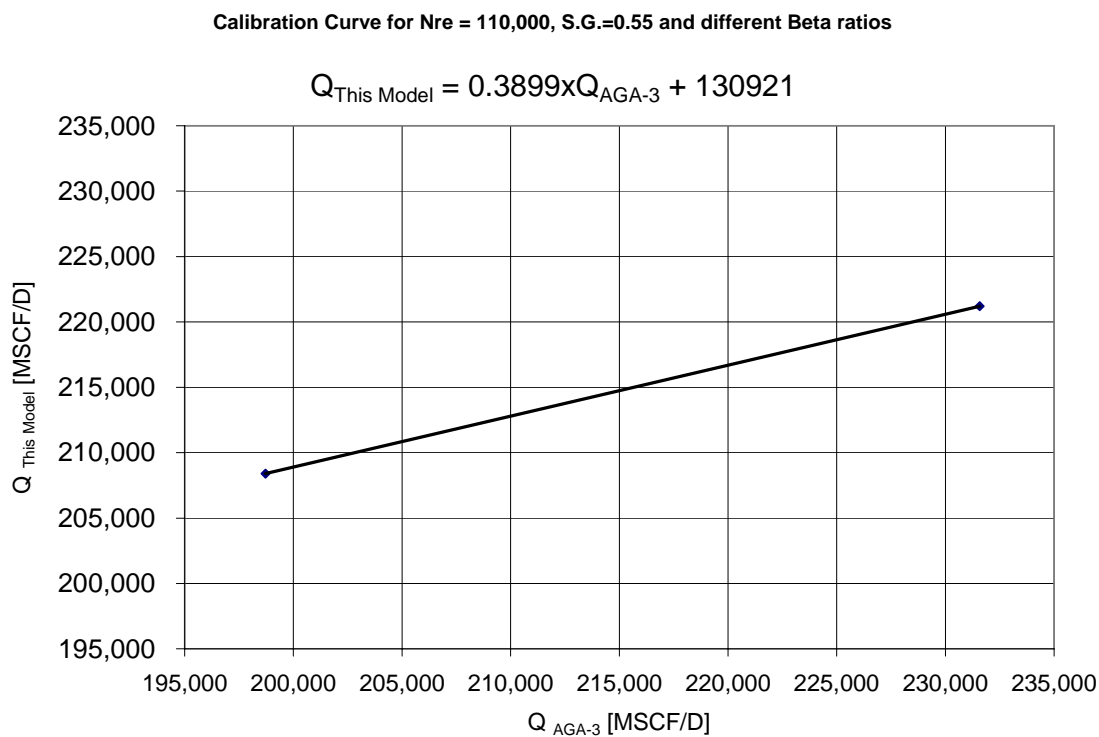
Figure 8.32. Calibration Curve for N_{Re} = 110,000, S.G. = 0.55 and different Beta Ratio.

Chapter 9

CONCLUSIONS AND RECOMMENDATIONS

9.1. Conclusions

An efficient and transportable generalized solver for 2-D hyperbolic PDEs has been developed. The system of homogenous PDEs is solved using the ENO Scheme while the system of ODEs that accounts for the forcing functions is solved using a high-order accurate Runge-Kutta Method. The capability of the numerical methods was assessed by solving a great deal of benchmark problems found in the literature, which have all the essential characteristic of the problem of interest and have exact solutions for comparison purposes.

A robust and reliable model has been developed to simulate natural gas flow through an orifice meter. This study has demonstrated that the Large Eddy Simulation approach combined with the wall model provide an accurate description of the main features of turbulent compressible flow through an axi-symmetric orifice-plate.

The initial conditions for the transient model are generated using a new protocol proposed by this study that includes the pressure derivatives into the fluxes of the momentum and energy equations in order to avoid ill-posed problems.

The study proposed a procedure to obtain the eigenstructure of the system. This technique allows us to remove the traditional assumptions of ideal gas, and the use of the caloric equation of state. Therefore, any equation of state can be used when calculating the eigenvalues and corresponding eigenvectors of the system of the hydrodynamic equations.

Three case studies were solved for a single pipeline. The first one solved the sudden valve closure problem using the one-dimensional model, where main features of the inviscid Euler's equations can be observed in the solution. The second case study simulated two-dimensional flow until steady state conditions are achieved and a fully developed turbulent flow can be appreciated in the downstream section of the pipe. The final case solved the sudden valve closure problem, but

using the two-dimensional model and a qualitative comparison of averaged profiles and the solutions given by the one-dimensional model is presented. The effects caused by the viscous flow can be appreciated in the solution produced by the Navier-Stokes equations. Finally, the model was successfully validated by matching experimental data of the velocity field for air flow through an orifice meter at different Reynolds numbers in the range of turbulent regime. The maximum error in the axial velocity upstream the orifice-plate between the experimental data and the numerical results is within 3.5%. Moreover, a cross plot for the comparison downstream the plate shows a very satisfactory match between the measured data and the numerical predictions.

Numerical predictions for natural gas flowing through the orifice meter were generated using the validated model. The results obtained include radial and axial distribution of the velocity components of the fluid, as well as other flow variables in the domain such as pressure, temperature and density.

The stream wise distribution of the axial velocity downstream the plate show that the location of the maximum velocity at the axis of the pipe, which is the vena contracta, do not coincide with the minimum wall static pressure, contrary to the assumption made by the Bernoulli equation. This phenomenon can be explained by recognizing the two-dimensional nature of the pressure field which is neglected by the AGA-3 equation. In order for the minimum wall pressure to occur at the same location as the maximum centerline axial velocity, $\partial p / \partial r$ should be zero, but the fact that a recirculation phenomenon takes places there introduces radial and axial variations in both the velocity and the pressure. Therefore, the minimum wall pressure and maximum centerline axial velocity should not be expected to occur at the same location.

Plots of the velocity vectors show the recirculation zone located in the downstream corner of the plate. The extension of the recirculation region is determined by means of the change in sign of the wall shear stress which indicates the end of backflow. The fact that the model is able to capture and represent the recirculation phenomenon is crucial because this is one of the main sources of errors introduced in the flow rate estimates from the AGA-3 equation, which neglects this effect. Additionally, the existence and size of this recirculation zone is a potential cause of difficulty for measurement using the flange taps. This conclusion is based on the fact that the flange taps are always located one inch from the orifice plate and therefore do not scale with the pipe specifications and fluid properties.

The produced results allow analyzing and comparing the flow variables by a parametric study that shows the effects of the Reynolds number, the specific gravity of the fluid, and the Beta ratio. The flow rate predicted by the model was computed by numerical integration of the axial velocity at a cross section located downstream the plate where a fully developed flow has been achieved (z = 5.0 D). Moreover, for comparison purposes using the values of pressure predicted by the model at the flange tap locations, the pressure drop was determined, and together with the pressure at the flange upstream the plate and the rest of the pipe and fluid specifications, the flow rate was estimated using the AGA 3 equation.

The extension of the recirculation region increases as the Reynolds number rises which is caused by the turbulent effects of the flow. As expected the larger the Reynolds number, the larger the pressure drop caused by the plate. Another important result is the temperature drop that takes place at the plate, which grows exponentially as the Reynolds number increases. Additionally, comparing the flow rates calculated by the model with the values specified at the inlet, the maximum error is 5.83% for the case of N_{Re} = 21,000, while for all the other cases is less than 1%. However, the error produced by the AGA-3 equation is 4.57% for the case of N_{Re} = 21,000, and for the other cases is above 4% which indicates that the results generated by this model are more accurate than those produced by the semi-empirical equation, with only one exception.

The minimum centerline pressure shows a very small variation as the density of the fluid changes. The pressure drop caused by the plate is almost constant for the different values of specific gravity of the fluid, which confirms the fact that such a differential pressure is more dependent of the Reynolds number rather than to the other parameters. Additionally, it is clear that for a fixed Reynolds number, the temperature drop across the orifice decreases as the density of the fluid is increased. For all the cases, the maximum error between the predictions and the values imposed at the inlet is within 1%, while the maximum error between the flow rate estimated by the AGA-3 equation and this model is above 6%.

It can be concluded that the size of the recirculation area is smaller for greater Beta ratios. Examining the axial velocity profiles, it is evident that there is almost no variation between the inlet of the pipe and -0.5625 D pipe diameters upstream the plate for both Beta ratios (0.5 and 0.75), indicating that the influence of the plate in the flow field depends mostly on the location of the plate and not the diameter of the orifice. The same applies for the axial velocity profiles downstream the plate, which shows a fully developed turbulent flow after 5 pipe diameters for

both orifice diameters. Another conclusion is that for a larger ratio of diameters, the fluid accelerates more in the section upstream the plate. Additionally, the larger the diameter of the constriction, the smaller the pressure drop caused by it. Moreover, since the fluid compresses less for a larger Beta ratio, the temperature drop across the plate is highly reduced. In addition, the maximum error between the predicted and imposed flow rate is 0.93%, while the maximum error produced by the AGA 3 equation is close to 6%.

From the obtained results, it is important to point out that comparing with the imposed flow rate at the inlet, the present fundamental model produces better predictions than the AGA-3 equation. This confirms the fact that assumptions of one-dimensional, steady, incompressible, frictionless flow made in the derivation of the semi-empirical equation neglects many of the important effects of this kind of flow causing errors when estimating the flow rate.

9.2. Recommendations

The proposed generalized solver could be used as a computational laboratory to obtain the solution of many problems that are represented by a system of 2-D hyperbolic PDEs, avoiding the need of programming a new computer code for each specific problem. One of the applications could be modeling natural gas flow trough pipelines with blockages. Eltohami (1999) developed a 1-D model for symmetrical blockage detection by generating transient pulses at the inlet. Since this model accounts for two spatial dimensions, a better prediction can be expected and we will be able to handle non-symmetrical blockages.

The transient nature of the model and the fact that the orifice-meter model presented in this study accounts for many of the effects neglected by the AGA-3 equation, should encourage future research in calculating flow rate through a pipeline computationally. New techniques to determine the volume of gas flowing through the pipe can be studied based on measured data.

Considering that the assumptions made by the AGA-3 equation does not account for the backflow that takes place downstream the plate, and the fact that this effect introduces an error to the flow rate estimations, the present model could be used to make predictions to determine the appropriate location of the pressure taps in order to avoid them to be placed where the recirculation phenomenon occurs, and therefore guarantee a more accurate measurement of static

pressure. Another solution to this problem can be achieved by generating new correlations or factors to include the effect of the presence of a recirculation region downstream the plate.

This study recommends extending the model to three dimensions in order to allow flow in the angular direction. This extension will allow to model swirl flow which is an integrated feature of "non-ideal" installations where the orifice meter is not preceded by a straight section of pipeline long enough to guarantee the formation of a fully developed turbulent flow upstream the plate. The configuration of such installations includes elbows, and non-horizontal sections of pipeline. Additionally, a three-dimensional model will allow predicting and analyzing the splitting phenomena in branching conduits, and also simulate flow through other metering devices such as venturi meters, turbine meters and flow nozzles.

Considering that the transient model takes between 12 to 48 hours to achieve steady-state, depending on the Reynolds number and the number of components of the gas mixture, and since the solution required to calculate the flow rate is the steady-state distribution, it is recommended that a steady-state model is developed for natural gas flow through an orifice meter. Comparisons should be made with the actual transient model for validation purposes.

Future work should also consider enhancing the model to include two-phase flow. Considering the fact that the AGA-3 equation was developed assuming single-phase flow, the formation of liquid is one of the source of errors caused by the empirical equation derived from Bernoulli's equation. A two-phase model will allow to determine the effect of liquid in the pressure measurements an ultimately the error caused in the estimates of flow rate. In order to account for a second phase, additional continuity and momentum equations should be included into the model. Moreover, a major challenge will be the mass transfer calculation between the phases at each block and it will require a great deal of research in order to account for this effect.

Additionally, a multi-dimensional two-phase flow model will allow the computational study of flow patterns. Comparison between the flow pattern maps, generated experimentally, and the numerical predictions will allow the generation of a complete database and the analysis of a great deal of configurations that, due to the time constraints, are very unlikely to be analyzed experimentally.

REFERENCES

Adebiyi, G.A.: *Formulations for the Thermodynamic Properties of Pure Substances*, Journal of Energy Resources Technology, Vol. 127, pp 83-87, 2005.

Allen, J.S.: *Numerical Solutions of the Compressible Navier-Stokes Equations for the Laminar Near Wake in Supersonic Flow,* Princeton University, PhD Dissertation, New Jersey, 1968.

Allievi, L.: *Teoria Generale del Moto Perturbato dell' Acqua Nei Tubi in Pressione,* Annali Della Societa Ingegneri ed Architertti Italiani, Milan, 1903.

Allievi, L.: *Teoria del colpo D Ariete,* Atti del Collegio Degli Ingegneri ed Architertti Italiani, Milan, 1913.

Allievi, L.: *Theory of Water Hammer,* (translated by E.E. Halmos), Annali Della Societa Ingegneri ed Architertti Italiani, Milan, 1925.

American Gas Association: *Orifice metering of natural gas and other related hydrocarbon fluids;* AGA Report No. 3, Second Edition, Alternatively named ANSI/API-2530, Arlington, Virginia, 1985.

American Gas Association Committee Report No. 3, *Orifice Metering of Natural Gas and other related Hydrocarbon Fluids,* Third Edition, 1992a.

American Gas Association Committee Report No. 3, *Orifice Metering of Natural Gas and other related Hydrocarbon Fluids, Part 2 - Specification and Installation Requirements*, Fourth Edition, 2000.

American Gas Association Committee Report No. 8, *Compressibility Factors of Natural Gas and Other Related Hydrocarbon Gases,* Second Edition, 1992b.

American Petroleum Institute: *Manual of Petroleum Measurement Standards 3rd Edition;* Chapter 14, Section 3, Part 1, Washington, D.C., 1990.

Anderson, J.D.: *Computational Fluid Dynamics, The Basics with Applications*, McGraw-Hill, Inc., Singapore, 1995.

Ayala, L.F.: *A unified two-fluid model for multiphase flow in natural gas pipelines,* MS Thesis, The Pennsylvania State University, University Park, Pennsylvania, 2001.

Bardina, J., Ferziger, J.H. and Reynolds, W.C.: *Improved Turbulence Models based on large Eddy Simulation of Homogeneous, Incompressible, Turbulent Flows*, Technical Report No TF-19, Department of Mechanical Engineering, Stanford University, 1983.

Barry, J.J., Sheikholeslami, M.Z., and Patel, B.R.: *Numerical Simulation of Flow through Orifice Meters – Final Report,* Creare Research and Development, Inc., Prepared for: Gas Research Institute, U.S. Department of Commerce, National Information Service, Report Number: PB93-124121, 1992.

Boriyantoro, N.H.: *An integrated single/multi phase flow model for gas condensate pipelines,* MS Thesis, The Pennsylvania State University, University Park, Pennsylvania, 1994.

Brill, J.P. and Arirachakaran, S.J.: *State of the Art in Multiphase Flow,* Journal of Petroleum Technology, 538-541, May 1992.

Cash, J. R. and Karp, A. H.: *A Variable Order Runge-Kutta Method for Initial Value Problems with Rapidly Varying Right-Hand Sides,* ACM Trans. Math. Softw., Volume 16, 201-222, 1990.

Chen, N.H.: *An Explicit Equation for Friction Factor in Pipe,* Industrial & Engineering Chemistry Fundamentals, v. 18, No. 3, 296-297, 1979.

Comte, P. and Lesieur, M.: *Large-Eddy Simulations of Compressible Turbulent Flows*, von Karman Institute for Fluid Dynamics Lecture Series 1998-05, "Advances in Turbulence Modelling", Belgium 1998.

Courant, R., Friedrichs, K. O. and Lewy, H.: Uber die Partiellen Differenzengleichungen der Mathematischen Physik, Math. Ann., Volume 100, 32-74. (Translated to: *On the Partial Difference Equations of Mathematical Physics,* IBM J. Res. Dev., Volume 11, 215-234, 1967.

Crane Company: *Flow of fluids through valves, fittings, and pipe*. Technical Paper No. 410 (TP 410), 1988.

Davis, R.W. and Mattingly, G.E.: *Numerical Modeling of Turbulent Flow through thin Orifice Plates;* National Bureau of Standards Special Publications 484, Proceedings of the Symposium on Flow in Open Channels and Closed Conduits held at NBS, Gaithersburg, MD, pp. 491-522, February 23-25, 1977.

Dukhovnaya, Y.: *One-dimensional compositional modeling of gas and condensate flow in pipelines,* MS Thesis, The Pennsylvania State University, University Park, Pennsylvania, 1996.

Eaton, R.R. and Zumwalt, G.W.: *A Numerical Solution for the Flow Field of a Supersonic Cone-Cylinder Entering and Leaving a Blast Sphere Diametrically*, SC-CR-67-2532, Sandia Laboratories, Albuquerque, New Mexico, 1967.

Eltohami, E. S.: *Modeling Pressure Transient in Partially Blocked Pipelines,* M.S. Thesis, The Pennsylvania State University, University Park, PA, 1999.

Eltohami, E. S.: *Modeling of PCB Removal Processes from Natural Gas Transmission Lines,* PhD Thesis, The Pennsylvania State University, University Park, PA, 2003.

Erlebacher, G., Hussaini, M.Y., Speziale, C.G. and Zang, T.A.: *Toward the large-eddy simulation of compressible turbulent flows*, Journal of Fluid Mechanics, vol. 238, pp. 155-185, 1992.

Fehlberg, E.: *Classical Fifth-, Sixth-, Seventh-, and Eighth Order Runge-Kutta Formulas with Stepsize Control,* National Aeronautics and Space Administration (NASA), Washington, DC, 1968.

Fling, W.A.: *The API/PGA Orifice-Plate Data Base,* Journal of Petroleum Technology, 920-922, SPE Paper 15393, July 1988.

Furuwaka, H., Shoham, O., and Brill, J.P.: *Predicting Compositional Two-Phase Flow Behavior in Pipelines,* Journal of Energy Resources Technology, Transactions of ASME, v. 108, 207-210, September 1986.

Gatski, T.B.: *Modeling Compressibility Effects on Turbulence*, "New Tools in Turbulence Models", pp. 73-104 ,Les Editions de Physique – Springer, Les Houches 1996.

Germano, M.: *Turbulence: A filtering approach*, Journal of Fluid Mechanics, vol. 238, pp. 325-336, 1992

Godunov, S. K.: *A Finite Difference Method for the Computation of Discontinuous Solutions of the Equations of Fluid Dynamics,* Math Sb., Volume 47, 357-393, 1959.

Greenspan, D.: *Numerical Studies of Viscous, Incompressible Flow through an Orifice for Arbitrary Reynolds Number;* International Journal for Numerical Methods in Engineering, Vol. 6, 489-496, 1973.

Hagen, G.: *Über die Bewegung des Wassers in engen zylindrischen Röhren,* Pogg. Ann. 46, 423-442,1839.

Harten, A.: *High resolution schemes for hyperbolic conservation laws*, Journal of Computational Physics, Vol 49, 357-393, 1983.

Harten, A.: *On high-order accurate interpolation for non-oscillatory shock capturing schemes,* MRC Thecnical Summary Report No. 2829, University of Wisconsin-Madison, 1985.

Harten, A., Engquist, B.; Osher, S.; and Chakravarthy, S.: *Uniformly High Order Essentially Non-oscillatory Schemes, III,* Journal of Computational Physics, Vol 71, 231-303, 1987.

Harten, A., and Osher, S.: *Uniformly high-order accurate non-oscillatory scheme, I,* SIAM Journal of Numerical Analysis, Vol 24, 279-309, 1987.

Heath, M.: *Scientific Computing, An Introductory Survey,* McGraw-Hill, PA. Second Edition, 2002.

Hirsch, Ch.: *Numerical computation of internal and external flows, Volume 1*, John Wiley and Sons, New York, NY, 1988.

Hirsch, Ch.: *Numerical computation of internal and external flows, Volume 2*, John Wiley and Sons, New York, NY, 1988.

Hirt, C.W., Nichols, B.D. and Romero, N.C.: *SOLA – A Numerical Solution Algorithm for Transient Fluid Flows;* Los Alamos Scientific Laboratory Report LA-5852, US Printing Office, Washington D.C., 1975.

Ikoku, Ch.: *Natural Gas Production Engineering,* John Wiley and Sons, USA, 1984.

International Organization for Standardization: *Measurement of fluid flow by means of orifice plates, nozzles and venturi tubes inserted in circular cross-section conduits running full;* ISO 5167, First Edition, 1980.

International Organization of Standardization: *Measurement of fluid flow by means of pressure differential devices – Part 1: orifice plates, nozzles and Venturi tubes inserted in circular cross-section conduits running full;* ISO 5167-1, Geneva, 1991.

John, V.: *Large Eddy Simulation of Turbulent Incompressible Flow – Analytical and Numerical Results for a Class of LES Models*, Springer –Verlag, Germany 2004.

Kessler, T.J.: *Numerical Experiments of Plane Shock Diffraction from Two-Dimensional Rectangular Obstacles,* MM 68-5425-24, Bell Telephone Labs, Whippany, New Jersey, 1968.

Lax, P. D.: *Weak Solutions of Nonlinear Hyperbolic Equations and their Numerical Computation,* Comm. Pure. Appl. Math., Volume VII, 159-193, 1954.

Lax, P.D. and Wendroff, B.: *System of Conservation Laws*, Comm. Pure and Applied Mathematics, Volume 13, 217-237, 1960.

León, D.: *A Generalized Hyperbolic PDEs Solver for Conservation Laws,* MSc Thesis, The Pennsylvania State University, University Park, PA, 2004.

Leonard, A: *Energy cascade in large-eddy simulations of turbulent fluid flows,* Advances in Geophysics, vol. 18, pag. 237, 1974.

LeVeque, R.J.: *Numerical Methods for Conservation Laws,* Second Edition, Munich, 1992.

Lesieur, M.: *Turbulence in Fluids*, Second Revised Edition, Kluwer Academic Publishers, London 1990.

Liu, S., Meneveau, C. and Katz, J.: *On the properties of similarity subgrid-scale models as deduced from measurements in a turbulent jet*, Journal of Fluid Mechanics, vol. 275, pp. 83-119, 1994.

Mattingly, G.E. and Davis, R.W.: *Numerical Solutions for Laminar Orifice Flow;* ASME Publication, 77-WA/FE-13, 1977.

Mattingly, G.E., Spencer, E.A., and Klein, M.: Report of the: *Workshop on Fundamental Research Issues in Orifice Metering,* Sponsored by The Gas Research Institute in cooperation with The National Bureau of Standards and The National Engineering Laboratory, September 1984.

Mattingly, G.E. and Yeh, T.T.: *NBS' Industry-Government Consortium Research Program on Flowmeter Installation Effects: Summary Report with Emphasis on Research Period January-July 1988;* NISTIR 89-4080, April 1989.

Mattingly, G.E. and Yeh, T.T.: *Effects of pipe elbows and tube bundles on selected types of flowmeters;* Journal of Flow Measurement and Instrumentation, Vol. 2, 4-13, 1991.

Metais, O. and Ferziger, J.: *New Tools in Turbulence Models*, Les Editions de Physique – Springer, Les Houches 1996.

Mills, R.D.: *Numerical Solutions of Viscous Flow through Pipe Orifice at Low Reynolds Numbers;* Journal of Mechanical Engineering Science, Vol. 10, Issue 2, 133-140, 1968.

Moin, P., Squires, K., Cabot, W. and Lee, S.: *A dynamic subgrid-scale model for compressible turbulence and scalar transport*, Physics of Fluids A, vol. 3, No. 11, pp. 2746-2757, 1991.

Morrison, G.L.: *3-D Laser Anemometer Study of Compressible Flow through Orifice Plates*, Gas Research Institute, Report Number GRI – 90/0036, November 1989.

Morrison, G.L.: *Personal communication on January* 2006.

Morrison, G.L., DeOtte, R.E. Jr, Nail, G.H., and Panak, D.L.: *Mean Velocity and Turbulence Fields Inside a β=0.5 Orifice Flowmeter;* AIChE Journal, Vol. 39, No. 5, 745-756, May 1993.

Morrison, G.L., Hauglie, J, and DeOtte, R.E. Jr.: *Beta ratio, axisymmetric flow distortion and swirl effects upon orifice flow meters;* Journal of Flow Measuremet and Instrumentation, Vol. 6, Number 3, 207-216, July 1995.

Mucharam, L.: *One-dimensional compositional modeling of gas and condensate flow in pipelines,* PhD Thesis, The Pennsylvania State University, University Park, PA, 1990.

Nail, G.H.: *A Study of 3-Dimensional Flow through Orifice Mesters*, PhD Thesis, Texas A&M University, May 1991.

Nichols, R.H. and Nelson, C.C.: *Wall Function Boundary Conditions Including Heat Transfer and Compressibility*, AIAA Journal, vol. 42, No. 6, pp. 1107-1114, 2004.

Panak, D.L.: *3-D Laser Doppler Velocimetry Study of Incompressible Flow through and Orifice Plate*, MS Thesis, Texas A&M University, May 1990.

Peng, D., and Robinson, D. B.: *A New Two-Constant Equation of State,* Industrial Engineering Chemical Fundamentals, v. 15, n. 1, 59-64, 1976.

Piomelli, U.: *Large-Eddy Simulation of Turbulent Flows*, von Karman Institute for Fluid Dynamics Lecture Series 1998-05, "Advances in Turbulence Modelling", Belgium 1998.

Piomelli, U.: *Large-Eddy and Direct Simulation of Turbulent Flows*, von Karman Institute for Fluid Dynamics Lecture Series 2000-04, "Introduction to the Modelling of Turbulence", Belgium 2000.

Poiseuille, J.: *Récherches expérimentalles sur le movement del liquids dans les tubes des très petits diamètres*, Comptes Rendus 11, 961-967 and 1041-1048, 1841.

Prandtl, L.: *Über Flüssigkeitsbewegung bei sehr kleiner Reibung,* Proceedings 3rd Intern. Math. Congr., Heidelberg, 1904.

Press, W.H., Teukolsky, S.A., Vetterling, W.T. and Flannery, B.P.: *Numerical Recipes in Fortran, The Art of Scientific Computing, Second Edition,* Cambridge University Press, second edition, New York, NY, 1994.

Reader-Harris, M.J. and Keegans, W.: *Comparison of Computation and LDV Measurement of Flow through Orifice and Perforated Plates, and computation of the effect of rough pipework on orifice plate*, Proceedings of the International Symposium of Fluid Flow Measurement, November 16-19, 1986.

Reader-Harris, M.J., Sattary, J.A., and Spearman, E.P.: *The orifice plate discharge coefficient equation – further work;* Journal of Flow Measurement and Instrumentation, Vol. 6, No. 2, 101-114, 1995.

Reynolds, O.: *An experimental investigation of the circumstances which determine whether the motion of water shall be direct or sinuos, and of the law of resistance in parallel channels,* Phil. Trans. Roy, Soc., London, 174, 935-982, 1883.

Roache, P.: *Fundamentals of Computational Fluid Dynamics,* Second Edition, Hermosa Publishers, USA, 1998.

Ruo, S.-Y.: *Evaluation of the Applicability of an Explicit Numerical Method to a plane, Turbulent, Low Velocity, Partially Confined Jet,* Oklahoma State University, PhD Thesis, Oklahoma, 1967.

Sagaut, P.: *Large Eddy simulation for Incompressible Flows – An Introduction*, Second Edition, Springer, Germany, 2002.

Sarkar, S., Erlebacher, G., Hussaini, M.Y. and Kreiss, H.O.: *The analysis and modeling of dilatational terms in compressible turbulence*, Journal of Fluid Mechanics, vol. 227, pp. 473-493, 1991.

Schilchting, H.: *Boundary-Layer Theory,* Sixth Edition, McGraw-Hill, USA, 1968.

Shu, Chi-Wang and Osher, S., *Efficient implementation of essentially non-oscillatory shock capturing schemes,* Journal of Computational Physics, Vol 77, 439-471, 1988.

Shu, Chi-Wang and Osher, S., *Efficient implementation of essentially non-oscillatory shock capturing schemes, II,* Journal of Computational Physics, Vol 83, 32-78, 1989.

Shu, Chi-Wang, *Preface to the Republication of "Uniformly High Order Essentially Non-oscillatory Schees, III" by Harten, Engquist, Osher, and Chakravarthy,* Journal of Computational Physics, Vol 131, 1-2, 1997.

Smagorinsky, J.: *Generical Circulation Experiments with the Primitive Equations,* Monthly Weather Review, Washington D.C. 1963.

Sod, G.A.: *A survey of several finite difference methods for systems of nonlinear hyperbolic conservation laws,* Journal of Computational Physics, vol. 27, p. 1-31, 1978.

Spalding, D.B.: *A Single Formula for the Law of the Wall*, Journal of Applied Mechanics, vol 28, no 3, pp 444-458, 1961.

Speziale, Ch.: *Galilean invariance of subgrid-scale stress models in the large-eddy simulation of turbulence*, Journal of Fluid Mechanics, vol. 156, pp. 55-62, 1985.

Starling, K.E., Jacobsen, R.T., Beyerlein, S.W., Fitz, C.W., Clarke, W.P., Lemmon, E., Che, Y.C. and Rondon, E.: *GRI High Accuracy Natural Gas Equation of State for Gas Measurement Applications – 1991 Revision of AGA No. 8 Equatio*, Technical Reference Document, GRI-91/0184, 1991

Tannehill, J. C., Anderson, D. A. and Pletcher, R. H.: *Computational Fluid Mechanics and Heat Transfer,* Taylor & Francys, Philadelphia, PA, Second Edition, 1997.

Toro, E.F.: *Riemann Solvers and Numerical Methods for Fluid Dynamics, A Practical Introduction*, Springer, Manchester – U.K. , Second Edition, 1999.

Vincent, P. A.: *One-Dimensional Compositional Modeling of Gas and Condensate Flow in Pipelines,* MS Thesis, The Pennsylvania State University, University Park, Pennsylvania, 1988.

Voke, P.R., Kleiser, L. and Chollet, J.P.: *Direct and Large Eddy simulation I – Selected papers from the First ERCOFTAC Workshop on Direct and Large-Eddy Simulation*, Kluwer Academic Publishers, 1994.

Vreman, A.W., Geurts, B.J. and Kuerten, J.G.M.: *Subgrid-modelling in LES of Compressible Flow*, "Direct and Large Eddy simulation I – Selected papers from the First ERCOFTAC Workshop on Direct and Large-Eddy Simulation", pp. 133-144, Kluwer Academic Publishers, 1994.

Wagner, D.: *The Riemann problem in two space dimensions for a single conservation law,* SIMA, Vol. 14, Issue 3, 1983.

White, F.M. and Christoph, G.H.: *A Simple Analysis of Compressible Turbulent Two-Dimensional Skin Friction Under Arbitrary Conditions*, US Air Force Flight Dynamics Lab, AFFDL-TR-70-133, 1971

Yeh, T.T., and Mattingly, G.E.: *Pipeflow downstream of a reducer and its effects on flowmeters;* Journal of Flow Measurement and Instrumentation, Vol. 5, Number 3, 181-187, 1994a.

Yeh, T.T., and Mattingly, G.E.: *Summary Report of NITS's Industry-Government Consortium Research Program on Flowmeter Installation Effects: The 45 Degree Elbow;* U.S. Department of Commerce, Technology Administration, NIST Technical Note 1408, 1994b.

Yoshizawa, A.: *Statistical theory for compressible turbulent shear flows, with the application to subgrid modeling*, Physics of Fluids, vol. 29, No. 7, pp. 2152-2164, 1986.

Zalesak, S.: *A preliminary comparison of modern shock-capturing schemes: linear advection*, in Adv. Conap. Meth. for PDE's, VI, R. Vichnevetsky and R. Stepleman (Eds.) IMACS, 1987.

Appendix A

PHASE BEHAVIOR MODELS

The analyses in reservoir and petroleum engineering applications require the prediction of the behavior of complex mixtures of hydrocarbons in the liquid and gas states. These applications include the present study, for which a reliable phase behavior model was built. This is a prediction tool that generates properties of the mixtures as a function of pressure and temperature using the so called equations of state (EOS), which are functions interrelating pressure, temperature and volume of the system. For the problem in place due to the continuous change in pressure and temperature along the pipeline, the state of the system always varies. In this sense, an EOS monitors these thermodynamic changes, and thus describes the volumetric behavior of the system. The package used in this study could choose between the Peng-Robinson EOS (Peng and Robinson, 1976) and the AGA Report No. 8 Equation (AGA, 1992). These two equation are described in the following sections.

A.1. PENG-ROBINSON EQUATION OF STATE

In 1976, Peng and Robinson proposed the following EOS (A.1) for multi-components hydrocarbon systems, which has been proved to be reliable for gas-condensate fluids.

$$p = \frac{RT}{\tilde{v} - b_m} - \frac{(a\alpha)_m}{\tilde{v}^2 + 2b_m\tilde{v} - b_m^2} \tag{A.1}$$

where:

$$(a\alpha)_i = 0.45724 \frac{R^2 T_{ci}^2}{p_{ci}} \left[1 + f(w_i)\left(1 - T_{ri}^{0.5}\right)\right]^2; \quad T_{ri} = \frac{T}{T_{ci}}$$

$$f(w_i) = 0.37464 + 1.54226 w_i - 0.26992 w_i^2; \quad b_i = 0.07780 \frac{RT_{ci}}{p_{ci}}$$

Then, equation (A.1) can be rewritten in terms of the compressibility factor $(Z = p\tilde{v} / RT)$ as the cubic polynomial [Equation (A.2)]:

$$Z^3 + a_1 Z^2 + b_1 Z + c_1 = 0 \tag{A.2}$$

where:

$$a_1 = -(1 - B); \quad b_1 = A - 3B^2 - 2B; \quad c_1 = -(AB - B^2 - B^3)$$

$$A = \frac{(a\alpha)_m p}{R^2 T^2}; \quad B = \frac{b_m p}{RT}$$

Here, $(a\alpha)_m$ and b_m are the mixture parameters, and they are calculated as a function of the properties of the pure components using the following mixing rules:

$$(a\alpha)_m = \sum_i^{n_c} \sum_j^{n_c} c_i c_j \sqrt{(a\alpha)_i (a\alpha)_j} (1 - k_{ij}); \quad b_m = \sum_i^{n_c} c_i b_i \tag{A.3}$$

A.2. THERMODYNAMIC PROPERTIES

A.2.1. Molecular Weight

Having the overall composition of the gas (y_i), the molecular weight of the mixture (MW_g) is calculated using the Kay's rule as a function of the molecular weight of the single components (MW_i) like:

$$MW_g = \sum_{i=1}^{n} y_i MW_i \tag{A.4}$$

A.2.2. Density

Using the real gas law the density of the mixture is calculated using the compressibility factor (Z_g) predicted by the Peng-Robinson EOS.

$$\rho_g = \frac{p}{RT}\left(\frac{MW_g}{Z_g}\right) \tag{C.5}$$

A.2.3. Enthalpy

In their paper, Peng and Robinson (1976) also proposed an equation for the enthalpy of departure of a mixture, which is:

$$\tilde{H} = H - H^* = RT(Z-1) + \frac{T\frac{d(a\alpha)_m}{dT} - (a\alpha)_m}{2\sqrt{2}b_m}\ln\left(\frac{Z+(\sqrt{2}+1)B}{Z-(\sqrt{2}-1)B}\right) \tag{A.6}$$

Note that the value of the enthalpy of the fluid (H) is obtained from the sum of the enthalpy of departure and the ideal enthalpy (H^*), which is a function of the temperature. This work use the correlation developed by Passut and Danner (1972) to get the ideal properties, including the ideal enthalpy:

$$H^* = A_{pd} + B_{pd}T + C_{pd}T^2 + D_{pd}T^3 + E_{pd}T^4 + F_{pd}T^5 \tag{A.7}$$

The coefficients $A_{pd}, B_{pd}, C_{pd}, D_{pd}, E_{pd}$ and F_{pd} used in equation (A.7) were given by Passut and Danner (1972) and some of them are included in Table A.1. Take into consideration that Equation (A.7) gives the ideal enthalpy of each component, and thus, the Kay's rule has to be applied to obtain the ideal enthalpy of the mixture.

$$H_m^* = \sum_{i=1}^{n} c_i H_i^* \tag{A.8}$$

The derivative $\dfrac{d(a\alpha)_m}{dT}$ is found to be:

$$\frac{d(a\alpha)_m}{dT} = -\frac{0.45724R^2}{2\sqrt{T}} \sum_i \sum_j c_i c_j (1-k_{ij}) \left[f(w_i) \left(\frac{\alpha_i^{0.5}T_{ci}}{P_{ci}^{0.5}}\right)\left(\frac{T_{cj}}{P_{cj}}\right)^{0.5} + f(w_i)\left(\frac{\alpha_j^{0.5}T_{cj}}{P_{cj}^{0.5}}\right)\left(\frac{T_{ci}}{P_{ci}}\right)^{0.5} \right]$$

(A.9)

It is also important to address that the enthalpy given by Equation (A.7) is expressed in BTU/lbm, therefore, an appropriate value of the Universal Gas Constant "R" must be used when using Equation (A.6).

Table A.1. Passut and Danner (1972) coefficients for ideal enthalpy computations.

Component	A_{pd}	B_{pd}	$C_{pd}(_x10^3)$	$D_{pd}(_x10^6)$	$E_{pd}(_x10^{10})$	$F_{pd}(_x10^{14})$
N_2	-0.68925	0.253664	-0.014549	0.012544	-0.017106	-0.008239
CO_2	4.77805	0.114433	0.101132	-0.026494	0.034706	-0.013140
C_1	-5.58114	0.564834	-0.282973	0.417399	-1.525576	1.958857
C_2	-0.76005	0.273088	-0.042956	0.312815	-1.389890	2.007023
C_3	-1.22301	0.179733	0.066458	0.250998	-1.247461	1.893509
i-C_4	13.28660	0.036637	0.349631	0.005361	-0.298111	0.538662
n-C_4	29.11502	0.002040	0.434879	-0.081810	0.072349	-0.014560
i-C_5	27.62342	-0.031504	0.469884	-0.098283	0.102985	-0.029485
n-C_5	27.17183	-0.002795	0.440073	-0.086288	0.081764	-0.019715
Neo-C_5	11.77146	0.004372	0.406465	-0.027646	-0.217453	0.468503
C_6	32.03560	-0.023096	0.461333	-0.097402	0.103368	-0.030643
C_7	30.70117	-0.023143	0.460981	-0.098074	0.104752	-0.031340
C_8	29.50114	-0.022402	0.459712	-0.098062	0.104754	-0.031355
C_9	28.56645	-0.021654	0.458518	-0.097973	0.104654	-0.031318
C_{10}	28.06989	-0.023837	0.461164	-0.099786	0.108353	-0.033074

In the case of the lumped-components used in Chapter 6, the Passut and Danner coefficients are included in Table A.2.

Table A.2. Passut and Danner (1972) coefficients for the lumped-gas system (Chapter 6).

Component	A_{pd}	B_{pd}	$C_{pd}(_x10^3)$	$D_{pd}(_x10^6)$	$E_{pd}(_x10^{10})$	$F_{pd}(_x10^{14})$
Lumped-1	-5.50834	0.56072	0.279430	0.41205	-1.50566	1.93289
Lumped-2	2.66938	0.21301	0.169826	0.23631	-1.22312	1.84605
Lumped-3	30.26330	-0.21654	0.458518	-0.09797	0.10465	-0.03132

A.3. AGA Report Number 8

The AGA Report Number 8 provides a method to compute compressibility factors and densities with high order of accuracy for natural gas mixtures. The method uses the natural gas composition as an input and it is called Detail Characterization Method (AGA, 1992).

The method works over a wide range of conditions for natural gas mixtures, pure hydrocarbon components, nitrogen and hydrogen. Additionally, heavier components can be handled as well as pure hydrogen sulfide and binary mixtures with hydrocarbon components, nitrogen and carbon dioxide. All the ranges of applicability for relative density, mole percent for each components and reference conditions are included in the AGA Report No. 8, 1992.

The equation of state is based on the method of Starling *et al* (1991) using a hybrid formulation that combines the features of the virial EOS for low density by the means of power series in density, and exponential functions for high density conditions, as an extension of the Benedict-Webb-Rubin equation.

A.3.1. General Equations

In this section the general equations used to calculate the compressibility factor, the molar density and mass density for natural gas are presented.

The molecular weight of the mixture is calculated from the composition using the Kay's mixing rule A.4. Then, the mass density is related to the molar density by the relation:

$$\rho = MW_g d \tag{A.10}$$

From the real gas law, the molar density can be expressed in terms of the compressibility factor as:

$$d = \frac{P}{ZRT} \tag{A.11}$$

The compressibility factor Z is obtained using the following equation:

$$Z = 1 + \frac{DB}{K^3} - D\sum_{n=13}^{18} C_n^* T^{-U_n} + \sum_{n=13}^{58} C_n^* T^{-U_n} (b_n - c_n k_n D^{k_n}) D^{b_n} \exp(-c_n D^{k_n}) \quad \text{(A.12)}$$

where:

Z : compressibility factor

B : second virial coefficient

K : mixture size parameter

D : reduced density

C_n^* : coefficients which are functions of compositions

T : absolute temperature

u_n, b_n, c_n, k_n : constants (n=13,14, etc.)

The reduced density is related to the molar density as:

$$D = K^3 d \qquad \text{(A.13)}$$

where:

d : molar density

K : mixture size parameter

The mixture size parameter is calculated with the equation:

$$K^5 = \left[\sum_{i=1}^{N} x_i K_i^{\frac{5}{2}} \right]^2 2\sum_{i=1}^{N-1} \sum_{j=i+1}^{N} x_i x_j (K_{ij}^5 - 1)(K_i K_j)^{\frac{5}{2}} \qquad \text{(A.14)}$$

where:

K_i : size parameter for i$^{\text{th}}$ component

K_j : size parameter for j$^{\text{th}}$ component

K_{ij} : binary interaction parameter for size

x_j : mole fraction of j$^{\text{th}}$ component

The second virial coefficient is calculated using the following equations:

$$B = \sum_{n=1}^{18} a_n T^{-u_n} \sum_{i=1}^{N} \sum_{j=1}^{N} x_i x_j E_{ij}^{u_n} (K_i K_j)^{\frac{3}{2}} B_{nij}^*$$ (A.15)

$$B_{nij}^* = (G_{ij} + 1 - g_n)^{g_n} (Q_i Q_j + 1 - q_n)^{q_n} (F_i^{\frac{1}{2}} F_j^{\frac{1}{2}} + 1 - f_n)^{f_n} (S_i S_j + 1 - s_n)^{s_n} (W_i W_j + 1 - w_n)^{w_n}$$ (A.16)

where:

B_{nij}^* : binary characterization coefficient

a_n, g_n, f_n, s_n, w_n : constants (n=1,2, etc)

T : absolute temperature

G_{ij} : binary orientation parameter

Q_i : quadrupole parameter for i^{th} component

Q_j : quadrupole parameter for j^{th} component

F_i : high temperature parameter for i^{th} component

F_j : high temperature parameter for j^{th} component

S_i : dipole parameter for i^{th} component

S_j : dipole parameter for j^{th} component

W_i : association parameter for i^{th} component

W_j : association parameter for j^{th} component

E_{ij} : second virial coefficient binary energy parameter

Note that W_i is zero for all components except water and that F_i is zero for all components except hydrogen. The binary parameters E_{ij} and G_{ij} are calculated as:

$$E_{ij} = E_{ij}^* (E_i E_j)^{\frac{1}{2}}$$ (A.17)

$$G_{ij} = \frac{G_{ij}^*(G_i G_j)}{2} \tag{A.18}$$

where:

E_i : characteristic energy parameter for ith component

E_j : characteristic energy parameter for jth component

E_{ij}^* : second virial coefficient energy binary interaction parameter

G_i : orientation parameter for ith component

G_j : orientation parameter for jth component

G_{ij}^* : binary interaction parameter for orientation

Note that all values of binary interaction parameters E_{ij}^* and G_{ij}^* are one except for the values in Table A.3. The coefficient C_n^* (n=13 to 58) are given by the equation:

$$C_n^* = a_n (G + 1 - g_n)^{g_n} (Q^2 + 1 - q_n)^{q_n} (F + 1 - f_n)^{f_n} U^{U_n} \tag{A.19}$$

where:

G : orientation parameter

Q : quadrupole parameter

F : mixture high temperature parameter

U : mixture energy parameter

The mixture parameters U, G, Q and F are calculated using the following equations:

$$U^5 = \left[\sum_{i=1}^{N} x_i E_i^{\frac{5}{2}} \right]^2 + 2 \sum_{i=1}^{N-1} \sum_{j=i+1}^{N} x_i x_j (U_{ij}^5 - 1)(E_i E_j)^{\frac{5}{2}} \tag{A.20}$$

$$G = \sum_{i=1}^{N} x_i G_i + \sum_{i=1}^{N-1} \sum_{j=i+1}^{N} x_i x_j (G_{ij}^* - 1)(G_i + G_j) \tag{A.21}$$

$$Q = \sum_{i=1}^{N} x_i Q_i \qquad \text{(A.22)}$$

$$F = \sum_{i=1}^{N} x_i^2 F_i \qquad \text{(A.23)}$$

where:

U_{ij} : binary interaction parameter for conformal energy

Note that all the values of the binary interaction parameters $K_{ij}, E_{ij}^*, G_{ij}^*$, and U_{ij} are one except for the values given in Table A.5.

During the computation of the compressibility factor, the composition of the gas, the pressure and temperature are known. A problem occurs when calculating the molar density using the EOS expression for pressure; therefore Equation A.12 is substitute into Equation A.11 to obtain:

$$P = dRT \left[1 + Bd - D \sum_{n=13}^{18} C_n^* T^{-U_n} + \sum_{n=13}^{58} C_n^* T^{-U_n} (b_n - c_n k_n D^{k_n}) D^{b_n} \exp(-c_n D^{k_n}) \right] \text{(A.24)}$$

Note that when the temperature, pressure and composition are known, the only unknown quantity is the molar density which is determined using iterative procedures. The EOS parameters are presented in Table A.3.

A.3.2. Algorithm for Compressibility Factors and Densities

The following steps are followed in order to obtain the compressibility factor of the natural gas mixture:

1) Knowing the input mole fractions of the components of the gas, the molecular gas of the mixture is calculated using Equation A.4.

2) Having the pressure and temperature for which the computation is desired, the coefficients B and C_n^* in the EOS are calculated using Equation A.15 to A.23. The constants required for this calculations are given in Tables A.3, A.4 an A.5.

3) Then the molar density is obtained iteratively from Equation A.24 using the Brent's method presented by Press *et al* (1986). The converge criterion is either agreement of the pressure calculated using Equation A.24 with the specified pressure or agreement of successive iterative values of molar density within an absolute relative deviation of 0.000001.

4) Now, the mass density is calculated using Equation A.10, and

5) Finally, the compressibility factor is obtained from Equation A.12.

Table A.3. Equation of State Parameters.

N	a_n	b_n	c_n	k_n	u_n	g_n	q_n	f_n	s_n	w_n
1	0.153832600	1	0	0	0.0	0	0	0	0	0
2	1.341953000	1	0	0	0.5	0	0	0	0	0
3	-2.998583000	1	0	0	1.0	0	0	0	0	0
4	-0.048312280	1	0	0	3.5	0	0	0	0	0
5	0.375796500	1	0	0	-0.5	1	0	0	0	0
6	-1.589575000	1	0	0	4.5	1	0	0	0	0
7	-0.053588470	1	0	0	0.5	0	1	0	0	0
8	0.886594630	1	0	0	7.5	0	0	0	1	0
9	-0.710237040	1	0	0	9.5	0	0	0	1	0
10	-1.471722000	1	0	0	6.0	0	0	0	0	1
11	1.321850350	1	0	0	12.0	0	0	0	0	1
12	-0.786659250	1	0	0	12.5	0	0	0	0	1
13	2.291290E-9	1	1	3	-6.0	0	0	1	0	0
14	0.157672400	1	1	2	2.0	0	0	0	0	0
15	-0.436386400	1	1	2	3.0	0	0	0	0	0
16	-0.044081590	1	1	2	2.0	0	1	0	0	0
17	-0.003433888	1	1	4	2.0	0	0	0	0	0
18	0.032059050	1	1	4	11.0	0	0	0	0	0
19	0.024873550	2	0	0	-0.5	0	0	0	0	0
20	0.073322790	2	0	0	0.5	0	0	0	0	0
21	-0.001600573	2	1	2	0.0	0	0	0	0	0
22	0.642470600	2	1	2	4.0	0	0	0	0	0
23	-0.416260100	2	1	2	6.0	0	0	0	0	0
24	-0.066899570	2	1	4	21.0	0	0	0	0	0
25	0.279179500	2	1	4	23.0	1	0	0	0	0
26	-0.696605100	2	1	4	22.0	0	1	0	0	0
27	-0.002860589	2	1	4	-1.0	0	0	1	0	0
28	-0.008098836	2	0	0	-0.5	0	1	0	0	0
29	3.150547000	2	1	1	7.0	1	0	0	0	0
30	0.007224479	2	1	1	-1.0	0	0	1	0	0
31	-0.705752900	2	1	2	6.0	0	0	0	0	0
32	0.534979200	2	1	2	4.0	1	0	0	0	0
33	-0.079314910	2	1	3	1.0	1	0	0	0	0
34	-1.418465000	3	1	3	9.0	1	0	0	0	0

35	-5.99905E-17	3	1	4	-13.0	0	0	1	0	0
36	0.105840200	3	1	4	21.0	0	0	0	0	0
37	0.034317290	3	1	4	8.0	0	1	0	0	0
38	-0.007022847	4	0	0	-0.5	0	0	0	0	0
39	0.024955870	4	0	0	0.0	0	0	0	0	0
40	0.042968180	4	1	2	2.0	0	0	0	0	0
41	0.746545300	4	1	2	7.0	0	0	0	0	0
42	-0.291961300	4	1	2	9.0	0	1	0	0	0
43	7.294616000	4	1	4	22.0	0	0	0	0	0
44	-9.936757000	4	1	4	23.0	0	0	0	0	0
45	-0.005399808	5	0	0	1.0	0	0	0	0	0
46	-0.243256700	5	1	2	9.0	0	0	0	0	0
47	0.049870160	5	1	2	3.0	0	1	0	0	0
48	0.003733797	5	1	4	8.0	0	0	0	0	0
49	1.874951000	5	1	4	23.0	0	1	0	0	0
50	0.002168144	6	0	0	1.5	0	0	0	0	0
51	-0.658716400	6	1	2	5.0	1	0	0	0	0
52	0.000205518	7	0	0	-0.5	0	1	0	0	0
53	0.009776195	7	1	2	4.0	0	0	0	0	0
54	-1.020487080	8	1	1	7.0	1	0	0	0	0
55	0.015573220	8	1	2	3.0	0	0	0	0	0
56	0.006862415	8	1	2	0.0	1	0	0	0	0
57	-0.001226752	9	1	2	1.0	0	0	0	0	0
58	0.002850908	9	1	2	0.0	0	1	0	0	0

Table A.4. Characterization Parameters.

CID	Comp.	M_r	E (K)	K	G	Q	F	S	W
1	CH_4	16.0430	151.318300	0.4619255	0.000000	0.000000	0.0	0.0000	0.0
2	N	28.0135	99.737780	0.4479153	0.027815	0.000000	0.0	0.0000	0.0
3	CO_2	44.0100	241.960600	0.4557489	0.189065	0.690000	0.0	0.0000	0.0
4	C_2H_6	30.0700	244.166700	0.5279209	0.079300	0.000000	0.0	0.0000	0.0
5	C_3H_8	44.0970	298.1183	0.5837490	0.141239	0.000000	0.0	0.0000	0.0
6	H_2O	18.0153	514.015600	0.3825868	0.332500	1.067750	0.0	1.5822	1.0
7	H_2S	34.0820	296.355000	0.4618263	0.088500	0.633276	0.0	0.3900	0.0
8	H	2.0159	26.957940	0.3514916	0.034369	0.000000	1.0	0.0000	0.0
9	CO	28.0100	105.534800	0.4533894	0.038953	0.000000	0.0	0.0000	0.0
10	O_2	31.9988	122.766700	0.4186954	0.021000	0.000000	0.0	0.0000	0.0
11	$i-C_4H_{10}$	58.1230	324.068900	0.6406937	0.256692	0.000000	0.0	0.0000	0.0
12	$n-C_4H_{10}$	58.1230	337.638900	0.6341423	0.281835	0.000000	0.0	0.0000	0.0
13	$i-C_5H_{12}$	72.1500	365.599900	0.6738577	0.332267	0.000000	0.0	0.0000	0.0
14	$n-C_5H_{12}$	72.1500	370.682300	0.6798307	0.366911	0.000000	0.0	0.0000	0.0
15	$n-C_6H_{14}$	86.1770	402.636293	0.7175118	0.289731	0.000000	0.0	0.0000	0.0
16	$n-C_7H_{16}$	100.2040	427.722630	0.7525189	0.337542	0.000000	0.0	0.0000	0.0
17	$n-C_8H_{18}$	114.2310	450.325022	0.7849550	0.383381	0.000000	0.0	0.0000	0.0
18	$n-C_9H_{20}$	128.2580	470.840891	0.8152731	0.427354	0.000000	0.0	0.0000	0.0
19	$n-C_{10}H_{22}$	142.2850	489.558373	0.8437826	0.469659	0.000000	0.0	0.0000	0.0
20	He	4.0026	2.610111	0.3589888	0.000000	0.000000	0.0	0.0000	0.0
21	Ar	39.9480	119.629900	0.4216551	0.000000	0.000000	0.0	0.0000	0.0

Table A.5. Binary Interaction Parameter Values.

CID(i)	CID(j)	Component Pair		E_{ij}^*	U_{ij}	K_{ij}	G_{ij}^*
ID Number							
1	2	CH_4	N	0.971640	0.886106	1.003630	
	3		CO_2	0.960644	0.963827	0.995933	0.807653
	4		C_2H_6				
	5		C_3H_8	0.994635	0.990877	1.007619	
	6		H_2O	0.708218			
	7		H_2S	0.931484	0.736833	1.000080	
	8		H	1.170520	1.156390	1.023260	1.957310
	9		CO	0.990126			
	10		O_2				
	11		$i\text{-}C_4H_{10}$	1.019530			
	12		$n\text{-}C_4H_{10}$	0.989844	0.992291	0.997596	
	13		$i\text{-}C_5H_{12}$	1.002350			
	14		$n\text{-}C_5H_{12}$	0.999268	1.003670	1.002529	
	15		$n\text{-}C_6H_{14}$	1.107274	1.302576	0.982962	
	16		$n\text{-}C_7H_{16}$	0.880880	1.191904	0.983565	
	17		$n\text{-}C_8H_{18}$	0.880973	1.205769	0.982707	
	18		$n\text{-}C_9H_{20}$	0.881067	1.219634	0.981849	
	19		$n\text{-}C_{10}H_{22}$	0.881161	1.233498	0.980991	
2	3	N	CO_2	1.022740	0.835058	0.982361	0.982746
	4		C_2H_6	0.970120	0.816431	1.007960	
	5		C_3H_8	0.945939	0.915502		
	6		H_2O	0.746954			
	7		H_2S	0.902271	0.993476	0.942596	
	8		H	1.086320	0.408838	1.032270	
	9		CO	1.005710			
	10		O_2	1.021000			
	11		$i\text{-}C_4H_{10}$	0.946914			
	12		$n\text{-}C_4H_{10}$	0.973384	0.993556		
	13		$i\text{-}C_5H_{12}$	0.959340			
	14		$n\text{-}C_5H_{12}$	0.945520			
3	4	CO_2	C_2H_6	0.925053	0.969870	1.008510	0.370296
	5		C_3H_8	0.960237			
	6		H_2O	0.849408			1.673090

	7		H$_2$S	0.955052	1.045290	1.007790	
	8		H	1.281790			
	9		CO	1.500000	0.900000		
	10		O$_2$				
	11		i-C$_4$H$_{10}$	0.906849			
	12		n-C$_4$H$_{10}$	0.897362			
	13		i-C$_5$H$_{12}$	0.726255			
	14		n-C$_5$H$_{12}$	0.859764			
	15		n-C$_6$H$_{14}$	0.855134	1.066638	0.910183	
	16		n-C$_7$H$_{16}$	0.831229	1.077634	0.895362	
	17		n-C$_8$H$_{18}$	0.808310	1.088178	0.881152	
	18		n-C$_9$H$_{20}$	0.786323	1.098291	0.867520	
	19		n-C$_{10}$H$_{22}$	0.765171	1.108021	0.854406	
4	5	C$_2$H$_6$	C$_3$H$_8$	1.022560	1.065173	0.986893	
	6		H$_2$O	0.693168			
	7		H$_2$S	0.946871	0.971926	0.999969	
	8		H	1.164460	1.616660	1.020340	
	9		CO				
	10		O$_2$				
	11		i-C$_4$H$_{10}$		1.250000		
	12		n-C$_4$H$_{10}$	1.013060	1.250000		
	13		i-C$_5$H$_{12}$		1.250000		
	14		n-C$_5$H$_{12}$	1.005320	1.250000		
5	8	C$_3$H$_8$	H	1.034787			
	12		n-C$_4$H$_{10}$	1.004900			
7	15	H$_2$S	n-C$_6$H$_{14}$	1.008692	1.028973		
	16		n-C$_7$H$_{16}$	1.010126	1.033754		
	17		n-C$_8$H$_{18}$	1.011501	1.038338		
	18		n-C$_9$H$_{20}$	1.012821	1.042735		
	19		n-C$_{10}$H$_{22}$	1.014089	1.046966		
8	9	H	CO	1.1			
	10		O$_2$				
	11		i-C$_4$H$_{10}$	1.3			
	12		n-C$_4$H$_{10}$	1.3			

Appendix B

ALGORITHMS FOR SCALAR PDE

Inductive recipes to obtain divided differences of the flux, and ultimately the numerical flux to the desired order of accuracy were given in Chapter 3. Due to the complexity of the procedures, only the algorithms were presented there, but for most interested readers step-by-step explanations are included here.

B.1. ENO-Roe Algorithm

Here we present a complete explanation of the algorithm for a third-order accurate scheme. The steps are as follows:

1. Compute the Newton divided difference table of F as:

$$F[U(x_l)] = F\big(U(x_l)\big)$$

$$F[U(x_l),U(x_{l+1})] = \frac{F[U(x_l)] - F[U(x_{l+1})]}{U(x_l) - U(x_{l+1})}$$

$$F[U(x_l),U(x_{l+1}),U(x_{l+2})] = \frac{F[U(x_l),U(x_{l+1})] - F[U(x_{l+1}),U(x_{l+2})]}{U(x_l) - U(x_{l+2})}$$

$$F[U(x_l),U(x_{l+1}),U(x_{l+2}),U(x_{l+3})] = \frac{F[U(x_l),U(x_{l+1}),U(x_{l+2})] - F[U(x_{l+1}),U(x_{l+2}),U(x_{l+3})]}{U(x_l) - U(x_{l+3})}$$

(B.1)

2. Now let l be the grid-point of interest, and calculate:

$$H[x_{l-\frac{1}{2}},x_{l+\frac{1}{2}}] = F[U(x_l)]$$

$$H[x_{l-\frac{1}{2}},x_{l+\frac{1}{2}},x_{l+1+\frac{1}{2}}] = \frac{1}{2}F[U(x_l),U(x_{l+1})]$$

$$H[x_{l-\frac{1}{2}}, x_{l+\frac{1}{2}}, x_{l+1+\frac{1}{2}}, x_{l+2+\frac{1}{2}}] = \frac{1}{3} F[U(x_l), U(x_{l+1}), U(x_{l+2})]$$

$$H[x_{l-\frac{1}{2}}, x_{l+\frac{1}{2}}, x_{l+1+\frac{1}{2}}, x_{l+2+\frac{1}{2}}, x_{l+3+\frac{1}{2}}] = \frac{1}{4} F[U(x_l), U(x_{l+1}), U(x_{l+2}), U(x_{l+3})] \qquad \text{(B.2)}$$

3. If $\bar{a}_{i+\frac{1}{2}} \geq 0$, then

$$k_{\min}^{(1)} = i$$

else

$$k_{\min}^{(1)} = i+1$$

4. Compute:

$$Q^{(1)}(x) = H[x_{k_{\min}^{(1)} - \frac{1}{2}}, x_{k_{\min}^{(1)} + \frac{1}{2}}](x - x_{k_{\min}^{(1)} - \frac{1}{2}}) \qquad \text{(B.3)}$$

5. Having $k_{\min}^{(1)}$ and $Q^{(1)}(x)$ both defined, there are two choices. In the case $k_{\min}^{(1)} = i$

$$a^{(2)} = H[x_{i-\frac{1}{2}}, x_{i+\frac{1}{2}}, x_{j+1+\frac{1}{2}}] \qquad \text{(B.4)}$$

$$b^{(2)} = H[x_{i-1-\frac{1}{2}}, x_{i-\frac{1}{2}}, x_{i+\frac{1}{2}}] \qquad \text{(B.5)}$$

i. If $\left| a^{(2)} \right| \geq \left| b^{(2)} \right|$, then

$$c^{(2)} = b^{(2)}, \quad k_{\min}^{(2)} = k_{\min}^{(1)} - 1 = i-1 \qquad \text{(B.6)}$$

otherwise

$$c^{(2)} = a^{(2)}, \quad k_{\min}^{(2)} = k_{\min}^{(1)} = i \qquad \text{(B.7)}$$

Note that, there is also the case for $k_{\min}^{(1)} = i+1$

ii. Form:

$$Q^{(2)}(x) = Q^{(1)}(x) + c^{(2)}[(x - x_{i-\frac{1}{2}})(x - x_{i+\frac{1}{2}})] \qquad \text{(B.8)}$$

6. Having $k_{\min}^{(2)}$ and $Q^{(2)}(x)$ both defined, there are three choices. Lets take the case $k_{\min}^{(2)} = i$

$$a^{(3)} = H[x_{i-\frac{1}{2}}, x_{i+\frac{1}{2}}, x_{i+1+\frac{1}{2}}, x_{i+2+\frac{1}{2}}] \tag{B.9}$$

$$b^{(3)} = H[x_{i-1-\frac{1}{2}}, x_{i-\frac{1}{2}}, x_{i+\frac{1}{2}}, x_{i+1+\frac{1}{2}}] \tag{B.10}$$

    i.   If $\left| a^{(3)} \right| \geq \left| b^{(3)} \right|$, then

$$c^{(3)} = b^{(3)}, \quad k_{\min}^{(3)} = k_{\min}^{(2)} - 1 = i - 1 \tag{B.11}$$

otherwise

$$c^{(3)} = a^{(3)}, \quad k_{\min}^{(3)} = k_{\min}^{(2)} = i \tag{B.12}$$

Note that, there are also the cases for $k_{\min}^{(2)} = i - 1$ and $k_{\min}^{(2)} = i + 1$

    ii. Form:

$$Q^{(3)}(x) = Q^{(2)}(x) + c^{(3)}[(x - x_{i-\frac{1}{2}})(x - x_{i+\frac{1}{2}})(x - x_{i+1+\frac{1}{2}})] \tag{B.13}$$

7. Having $k_{\min}^{(3)}$ and $Q^{(3)}(x)$ both defined, there are four choices. Lets work for the case $k_{\min}^{(3)} = i$

$$a^{(4)} = H[x_{i-\frac{1}{2}}, x_{i+\frac{1}{2}}, x_{i+1+\frac{1}{2}}, x_{i+2+\frac{1}{2}}, x_{i+3+\frac{1}{2}}] \tag{B.14}$$

$$b^{(4)} = H[x_{i-1-\frac{1}{2}}, x_{i-\frac{1}{2}}, x_{i+\frac{1}{2}}, x_{i+1+\frac{1}{2}}, x_{i+2+\frac{1}{2}}] \tag{B.15}$$

    i.   If $\left| a^{(4)} \right| \geq \left| b^{(4)} \right|$, then

$$c^{(4)} = b^{(4)}, \quad k_{\min}^{(4)} = k_{\min}^{(3)} - 1 = i - 1 \tag{B.16}$$

otherwise

$$c^{(4)} = a^{(4)}, \quad k_{\min}^{(4)} = k_{\min}^{(3)} = i \tag{B.17}$$

Note that, there are also the cases for $k_{\min}^{(3)} = i - 2$, $k_{\min}^{(3)} = i - 1$ and $k_{\min}^{(3)} = i + 1$

ii. Form:

$$Q^{(4)}(x) = Q^{(3)}(x) + c^{(4)}[(x - x_{i-\frac{1}{2}})(x - x_{i+\frac{1}{2}})(x - x_{i+1+\frac{1}{2}})(x - x_{i+2+\frac{1}{2}})] \tag{B.18}$$

8. At this point, we have:

$$Q_{i+\frac{1}{2}}(x) = Q^{(4)}(x) \tag{B.19}$$

9. And finally, we take:

$$\hat{F}_{i+\frac{1}{2}} = \frac{d}{dx} Q_{i+\frac{1}{2}}(x)\bigg|_{x=x_{i+\frac{1}{2}}} = \frac{Q_{i+\frac{1}{2}}(x_{i+\frac{1}{2}} + \varepsilon_x) - Q_{i+\frac{1}{2}}(x_{i+\frac{1}{2}})}{\varepsilon_x}, \tag{B.20}$$

$$\text{where } \frac{dx}{8} \leq \varepsilon_x \leq dx$$

B.2. ENO-LLF Algorithm

The acronym LLF stands for local Lax-Friedrichs. The main difference between this and the previous algorithm is the evaluation of two divided difference tables. Here we present a complete explanation of how they are constructed for a third-order-accurate scheme.

1. Compute the divided difference tables of F and U as:

$$F[U(x_l)] = F\big(U(x_l)\big)$$

$$F[U(x_l), U(x_{l+1})] = \frac{F[U(x_l)] - F[U(x_{l+1})]}{U(x_l) - U(x_{l+1})}$$

$$F[U(x_l), U(x_{l+1}), U(x_{l+2})] = \frac{F[U(x_l), U(x_{l+1})] - F[U(x_{l+1}), U(x_{l+2})]}{U(x_l) - U(x_{l+2})}$$

$$F[U(x_l), U(x_{l+1}), U(x_{l+2}), U(x_{l+3})] = \frac{F[U(x_l), U(x_{l+1}), U(x_{l+2})] - F[U(x_{l+1}), U(x_{l+2}), U(x_{l+3})]}{U(x_l) - U(x_{l+3})}$$

$$\tag{B.21}$$

$$U[x_l] = U(x_l)$$

$$U[x_l, x_{l+1}] = \frac{U[x_l] - U[x_{l+1}]}{x_l - x_{l+1}}$$

$$U[x_l, x_{l+1}, x_{l+2}] = \frac{U[x_l, x_{l+1}] - U[x_{l+1}, x_{l+2}]}{x_l - x_{l+2}}$$

$$U[x_l, x_{l+1}, x_{l+2}, x_{l+3}] = \frac{U[x_l, x_{l+1}, x_{l+2}] - U[x_{l+1}, x_{l+2}, x_{l+3}]}{x_l - x_{l+3}} \qquad \text{(B.22)}$$

2. Now calculate:

$$H^+[x_{i-\frac{1}{2}}, x_{i+\frac{1}{2}}] = \frac{1}{2}\left(F[U(x_i)] + \alpha_{i+\frac{1}{2}}U[x_i]\right)$$

$$H^+[x_{i-\frac{1}{2}}, x_{i+\frac{1}{2}}, x_{i+1+\frac{1}{2}}] = \frac{1}{2} \cdot \frac{1}{2}\left(F[U(x_i), U(x_{i+1})] + \alpha_{i+\frac{1}{2}}U[x_i, x_{i+1}]\right)$$

$$H^+[x_{i-\frac{1}{2}}, x_{i+\frac{1}{2}}, x_{i+1+\frac{1}{2}}, x_{i+2+\frac{1}{2}}] = \frac{1}{3} \cdot \frac{1}{2}\left(F[U(x_i), U(x_{i+1}), U(x_{i+2})] + \alpha_{i+\frac{1}{2}}U[x_i, x_{i+1}, x_{i+2}]\right)$$

$$H^+[x_{i-\frac{1}{2}}, x_{i+\frac{1}{2}}, x_{i+1+\frac{1}{2}}, x_{i+2+\frac{1}{2}}, x_{i+3+\frac{1}{2}}] = \frac{1}{4} \cdot \frac{1}{2}\left(F[U(x_i), U(x_{i+1}), U(x_{i+2}), U(x_{i+3})] + U[x_i, x_{i+1}, x_{i+2}, x_{i+3}]\right)$$

$$\text{(B.23)}$$

$$H^-[x_{i+\frac{1}{2}}, x_{i+1+\frac{1}{2}}] = \frac{1}{2}\left(F[U(x_{i+1})] - \alpha_{i+\frac{1}{2}}U[x_{i+1}]\right)$$

$$H^-[x_{i+\frac{1}{2}}, x_{i+1+\frac{1}{2}}, x_{i+2+\frac{1}{2}}] = \frac{1}{2} \cdot \frac{1}{2}\left(F[U(x_{i+1}), U(x_{i+2})] - \alpha_{i+\frac{1}{2}}U[x_{i+1}, x_{i+2}]\right)$$

$$H^-[x_{i+\frac{1}{2}}, x_{i+1+\frac{1}{2}}, x_{i+2+\frac{1}{2}}, x_{i+3+\frac{1}{2}}] = \frac{1}{3} \cdot \frac{1}{2}\left(F[U(x_{i+1}), U(x_{i+2}), U(x_{i+3})] - \alpha_{i+\frac{1}{2}}U[x_{i+1}, x_{i+2}, x_{i+3}]\right)$$

$$H^-[x_{i+\frac{1}{2}}, x_{i+1+\frac{1}{2}}, x_{i+2+\frac{1}{2}}, x_{i+3+\frac{1}{2}}, x_{i+4+\frac{1}{2}}] = \frac{1}{4} \cdot \frac{1}{2}\left(F[U(x_{i+1}), U(x_{i+2}), U(x_{i+3}), U(x_{i+4})] + U[x_{i+1}, x_{i+2}, x_{i+3}, x_{i+4}]\right)$$

$$\text{(B.24)}$$

where:

$$\alpha_{i+\frac{1}{2}} = \max_{u_i \le u \le u_{i+1}} |F'(U)| \qquad \text{(B.25)}$$

3. For H^+, $k_{min}^{(1)} = i$, then repeat steps (4)-(7) in Algorithm ENO-Roe to get $Q_+^{(4)}(x)$. And let:

$$Q_{i+\frac{1}{2}}^+(x) = Q_+^{(4)}(x) \tag{B.26}$$

4. For H^+, $k_{min}^{(1)} = i+1$, then repeat steps (4)-(7) in Algorithm ENO-Roe to get $Q_-^{(4)}(x)$. And let:

$$Q_{i+\frac{1}{2}}^-(x) = Q_-^{(4)}(x) \tag{B.27}$$

5. Finally, we have:

$$
\begin{aligned}
\hat{F}_{i+\frac{1}{2}} &= \frac{d}{dx}Q_{i+\frac{1}{2}}^+(x)\Big|_{x=x_{i+\frac{1}{2}}} + \frac{d}{dx}Q_{i+\frac{1}{2}}^-(x)\Big|_{x=x_{i+\frac{1}{2}}} \\
&= \frac{Q_{i+\frac{1}{2}}^+(x_{i+\frac{1}{2}} + \varepsilon_x) - Q_{i+\frac{1}{2}}^+(x_{i+\frac{1}{2}})}{\varepsilon_x} + \frac{Q_{i+\frac{1}{2}}^-(x_{i+\frac{1}{2}} + \varepsilon_x) - Q_{i+\frac{1}{2}}^-(x_{i+\frac{1}{2}})}{\varepsilon_x}
\end{aligned} \tag{B.28}
$$

where $dx\big/8 \leq \varepsilon_x \leq dx$

Appendix C

ADDITIONAL FIGURES
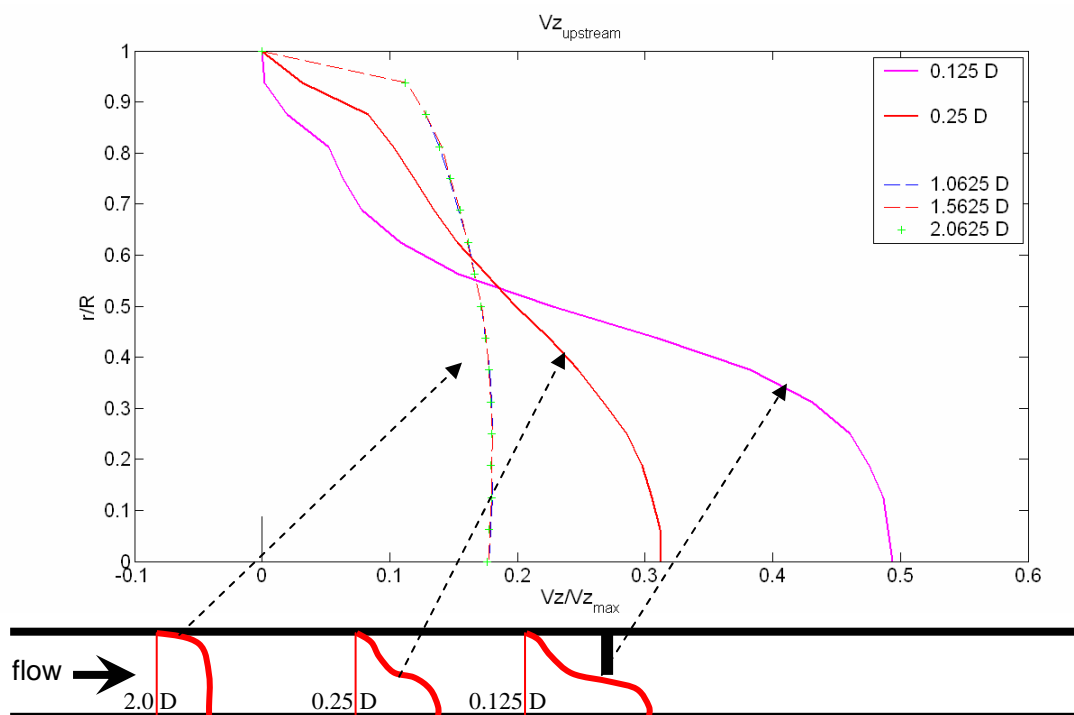
Figure C.1. Axial Velocity profiles upstream the orifice-plate for N_{Re} =54,700.
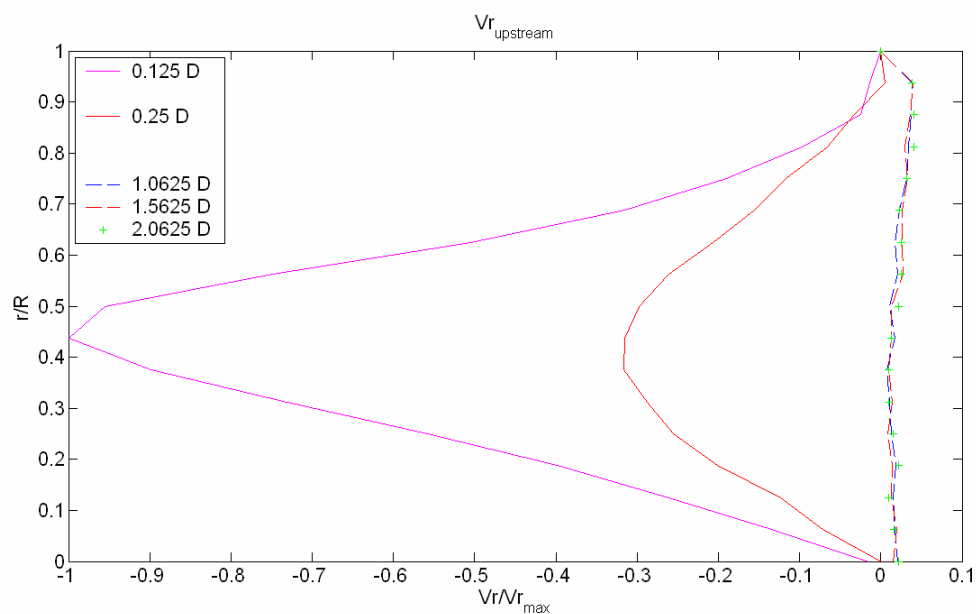
Figure C.2. Radial Velocity profiles upstream the orifice-plate for N_{Re} =54,700.
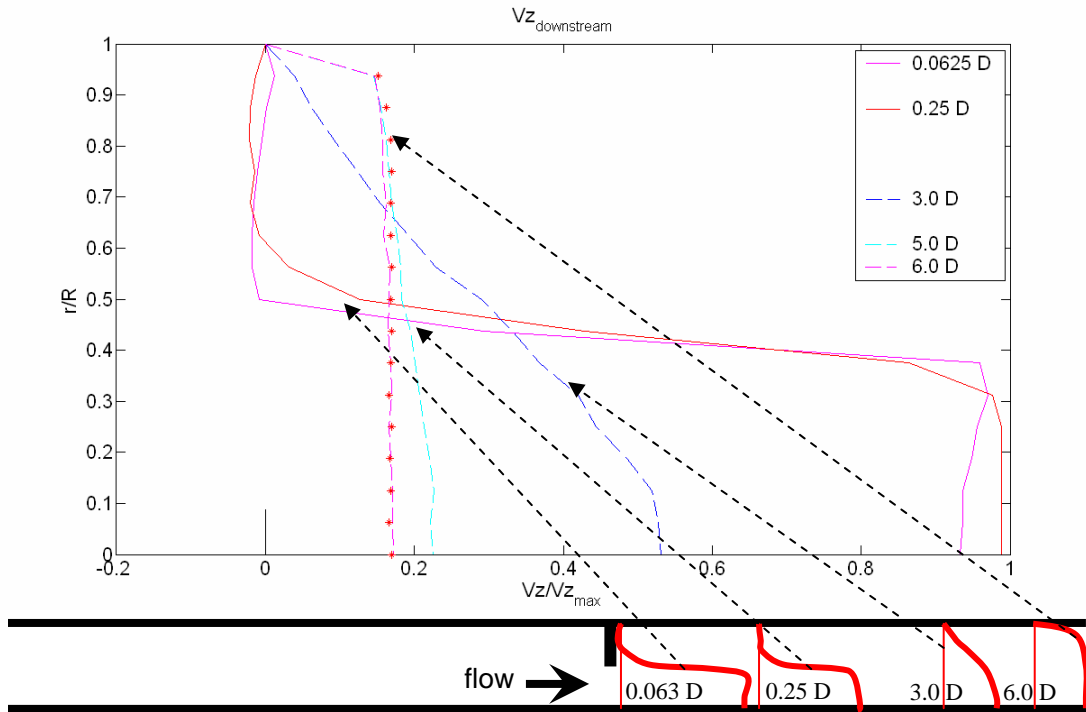
Figure C.3. Axial Velocity profiles downstream the orifice-plate for N_{Re} =54,700.
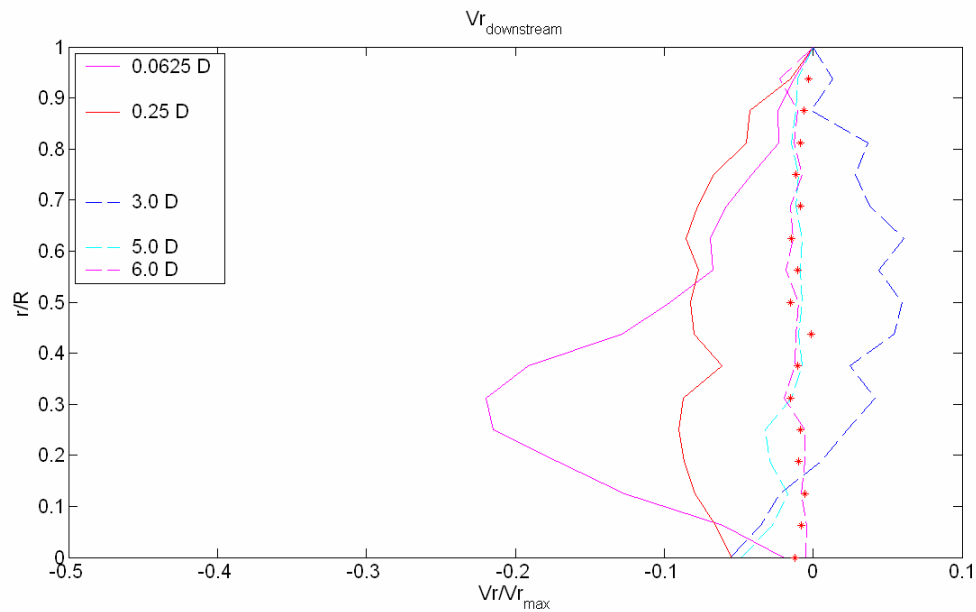
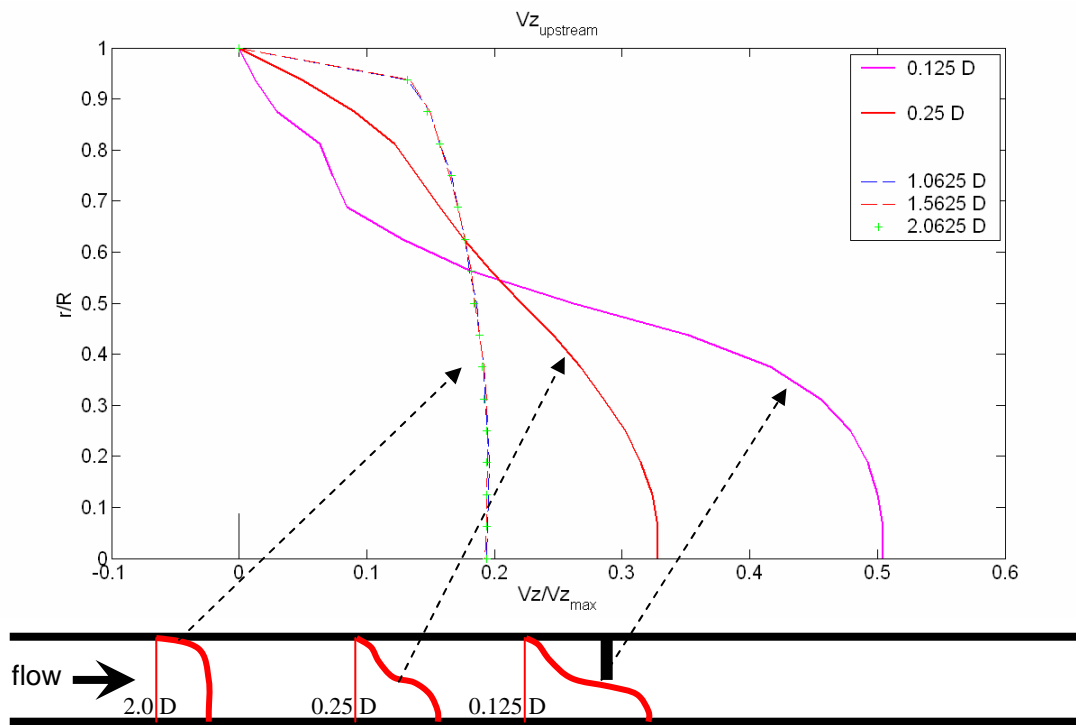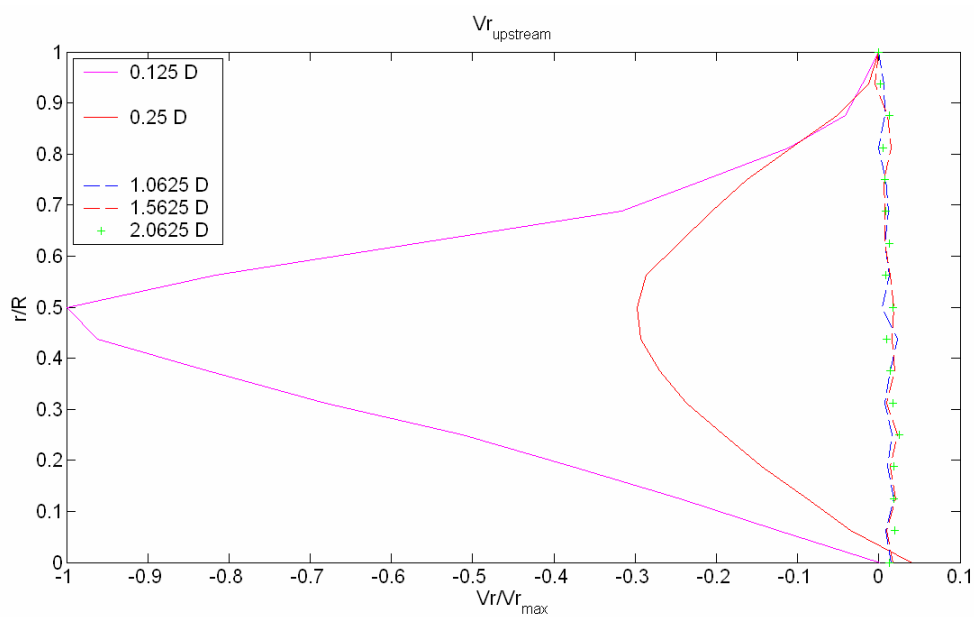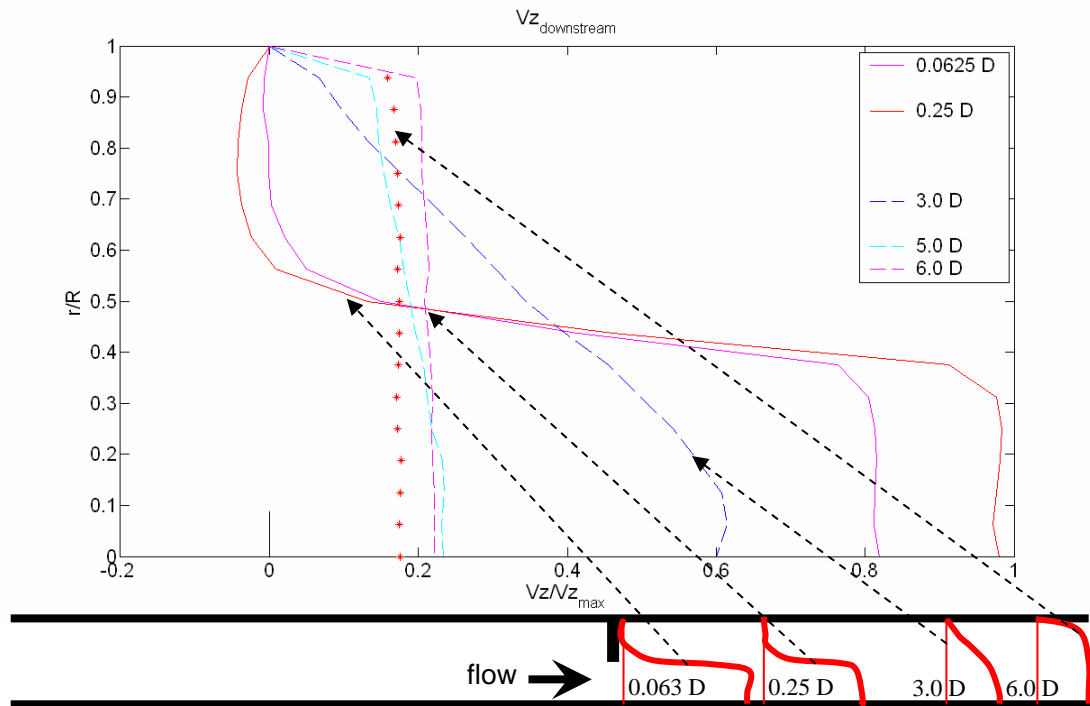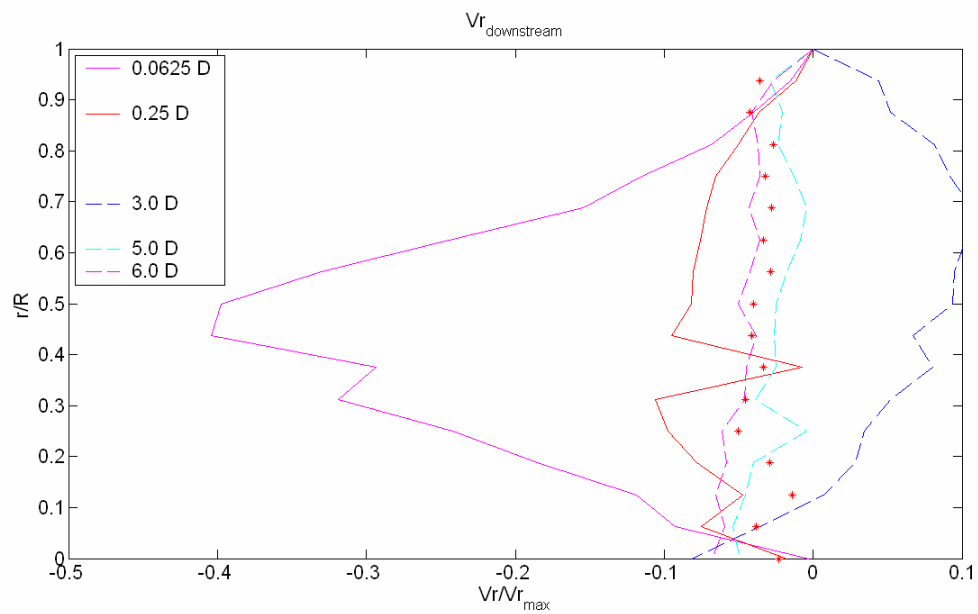Figure C.4. Radial Velocity profiles downstream the orifice-plate for N_{Re} =54,700.
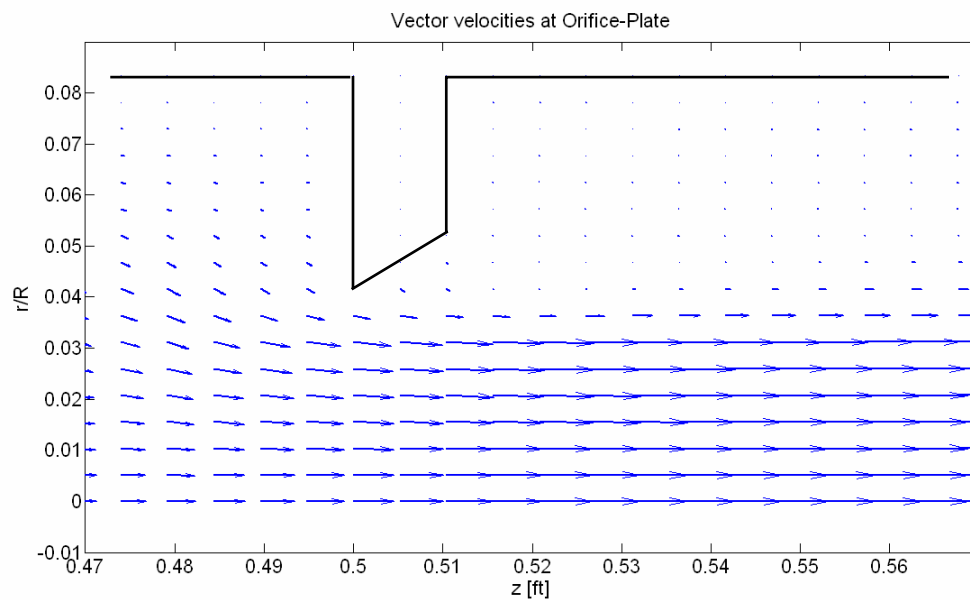
Figure C.5. Vector velocities near the orifice-plate for N_{Re} =54,700.
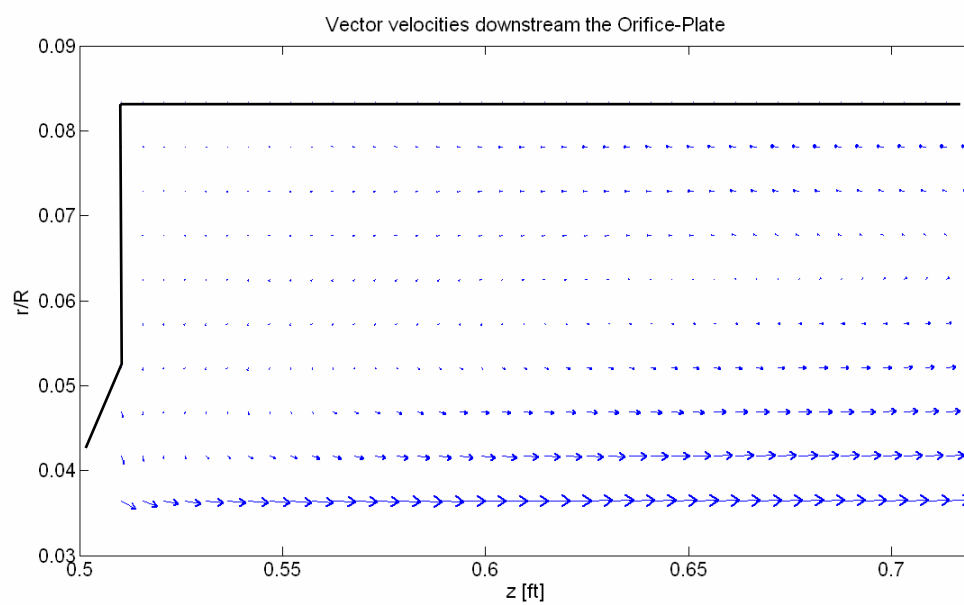
Figure C.6. Vector velocities downstream the orifice-plate for N_{Re} =54,700.
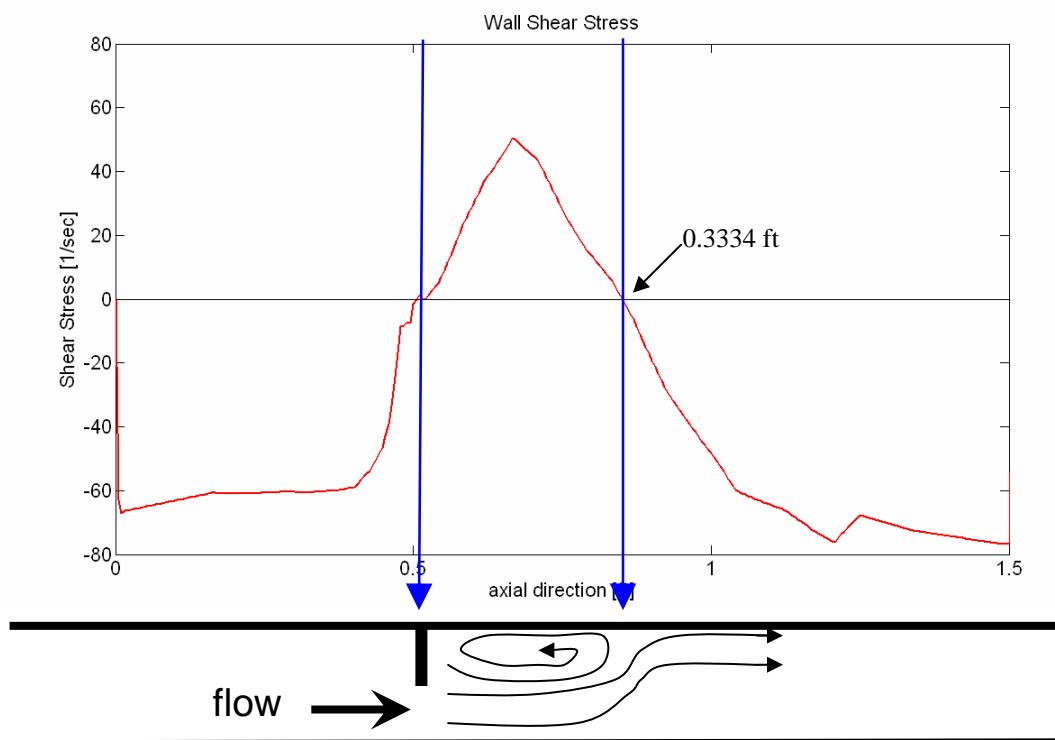
Figure C.7. Wall Shear Stress for N_{Re} =54,700.
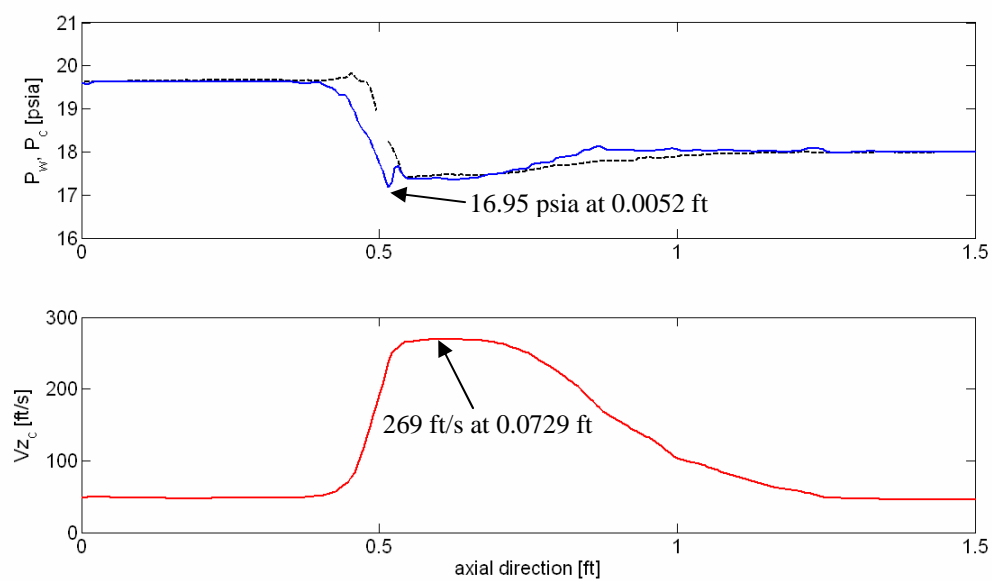
Figure C.8. Axial distribution of Pressure and Velocity for N_{Re} =54,700.

Figure C.9. Axial Velocity profiles upstream the orifice-plate for N_{Re} =18,400.

Figure C.10. Radial Velocity profiles upstream the orifice-plate for N_{Re} =18,400.

Figure C.11. Axial Velocity profiles downstream the orifice-plate for N_{Re} =18,400.

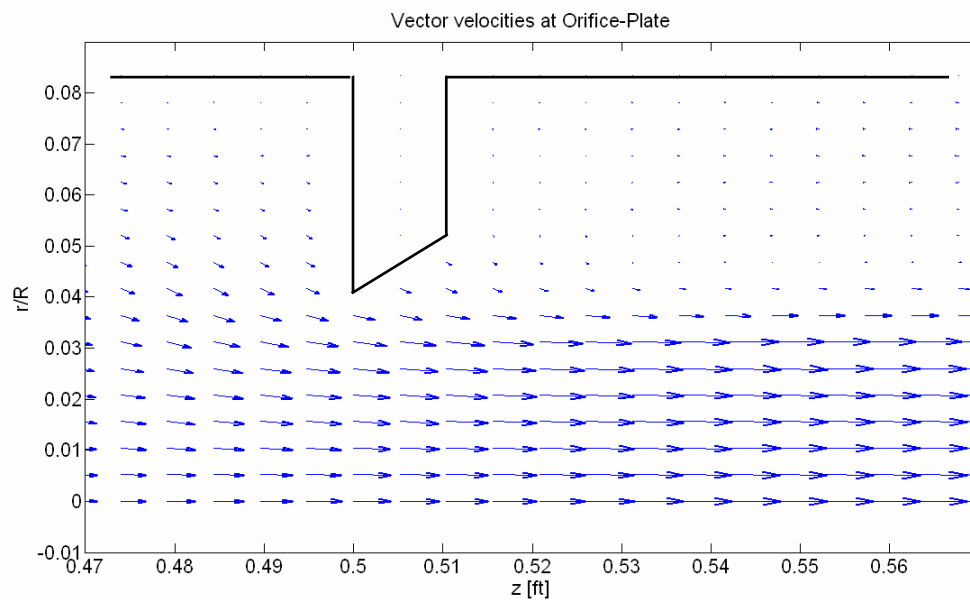Figure C.12. Radial Velocity profiles downstream the orifice-plate for N_{Re} =18,400.

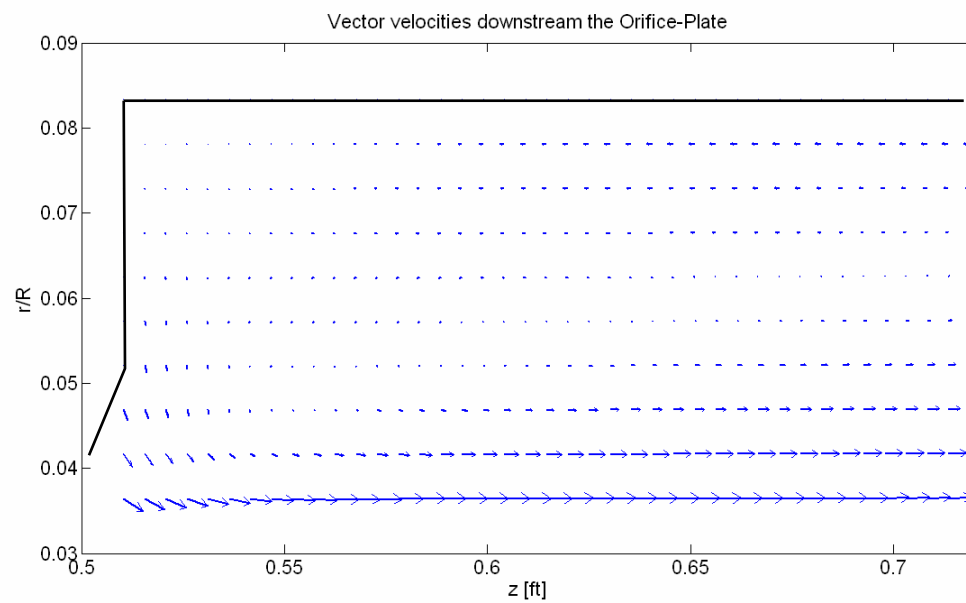Figure C.13. Vector velocities near the orifice-plate for N_{Re} =18,400.

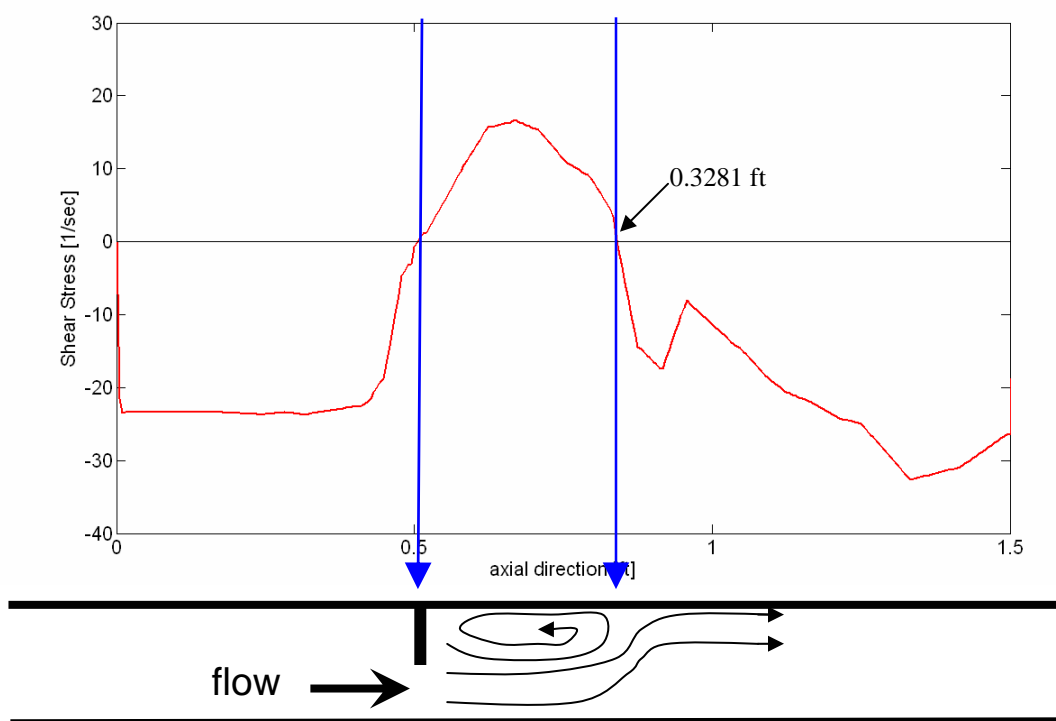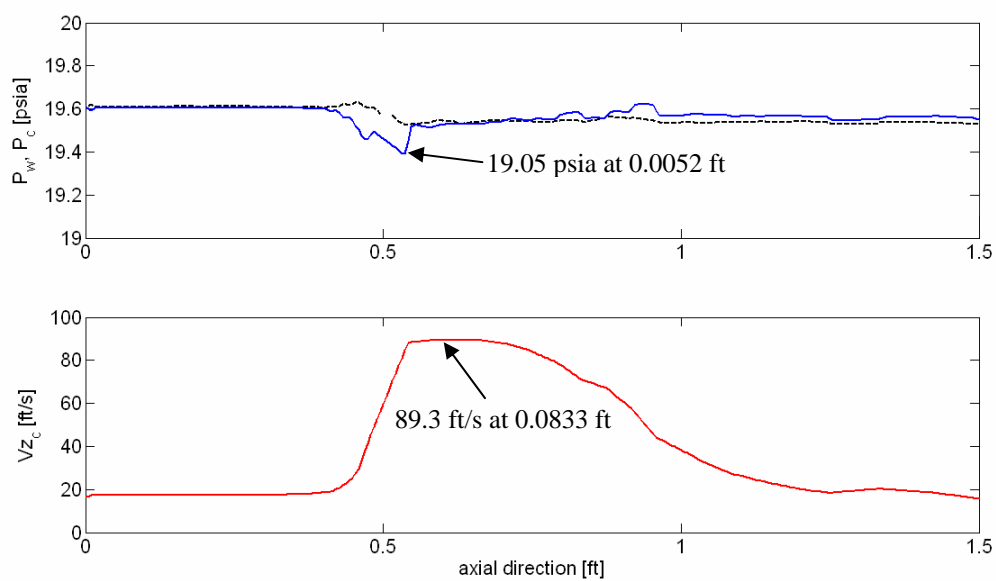Figure C.14. Vector velocities downstream the orifice-plate for N_{Re} =18,400.

Figure C.15. Wall Shear Stress for $N_{Re} =18,400$.

Figure C.16. Axial distribution of Pressure and Velocity for $N_{Re} =18,400$.

VITA

Daniel Eduardo León Echeverría

Daniel Eduardo León was born in Caracas, Venezuela, on October 19th, 1979. In 2002, he received a B.Sc. degree from Universidad Central de Venezuela as the first student ever to complete the program in four years from the College of Engineering and the Department of Petroleum Engineering. After graduating, Mr. León started his graduate studies in Petroleum and Natural Gas Engineering at The Pennsylvania State University in the United States of America. Daniel completed his Master of Science degree in 2004, and then he continued pursuing his doctoral studies at the same institution. At Penn State, he received the 2003-2004 Graduate Student Merit Award from the Petroleum and Natural Gas Engineering Program, 2005-2006 Rnulf I. Muan Graduate Fellowship for Excellence from the College of Earth and Mineral Sciences and 2005-2006 Centennial Research Award in Earth and Mineral Sciences. Daniel also won the Second Place of the Doctoral Division in the 2006 Regional SPE student paper/presentation contest. Mr. León is a member of the Society of Petroleum Engineers and of Colegio de Ingenieros de Venezuela.